

**UNIVERSIDADE FEDERAL DE UBERLÂNDIA**  
**FACULDADE DE ENGENHARIA MECÂNICA**  
**PÓS-GRADUAÇÃO EM ENGENHARIA MECÂNICA**

**Gustavo Henrique Nazareno Fernandes**

**Development, application, and validation of a new  
cooling technique applied for Inconel 718<sup>®</sup> machining**

**UBERLÂNDIA**  
**2023**

GUSTAVO HENRIQUE NAZARENO FERNANDES

**Development, application, and validation of a new cooling  
technique applied for Inconel 718<sup>®</sup> machining**

Proposal of a doctoral thesis submitted to the post-graduate program in Mechanical Engineering of the Federal University of Uberlândia.

**Concentration Area:** Materials and manufacturing processes

**Supervisor:** Dr. Álisson Rocha Machado

**Co-supervisor:** Dr. Paulo Sérgio Martins

**Uberlândia**

**2023**

Ficha Catalográfica Online do Sistema de Bibliotecas da UFU  
com dados informados pelo(a) próprio(a) autor(a).

F363 Fernandes, Gustavo Henrique Nazareno, 1986-

2023 Development, application, and validation of a new cooling technique applied for Inconel 718® machining [recurso eletrônico] / Gustavo Henrique Nazareno Fernandes. - 2023.

Orientador: Álisson Machado.

Coorientador: Paulo Martins.

Tese (Doutorado) - Universidade Federal de Uberlândia,  
Pós-graduação em Engenharia Mecânica.

Modo de acesso: Internet.

Disponível em: <http://doi.org/10.14393/ufu.te.2023.356>

Inclui bibliografia.

1. Engenharia mecânica. I. Machado, Álisson, 1956-, (Orient.). II. Martins, Paulo, 1976-, (Coorient.). III. Universidade Federal de Uberlândia. Pós-graduação em Engenharia Mecânica. IV. Título.

CDU:621

Bibliotecários responsáveis pela estrutura de acordo com o AACR2:

Gizele Cristine Nunes do Couto - CRB6/2091

Nelson Marcos Ferreira - CRB6/3074



## UNIVERSIDADE FEDERAL DE UBERLÂNDIA

Coordenação do Programa de Pós-Graduação em Engenharia Mecânica  
Av. João Naves de Ávila, nº 2121, Bloco 1M, Sala 212 - Bairro Santa Mônica, Uberlândia-MG, CEP 38400-902  
Telefone: (34) 3239-4282 - www.posmecanicaufu.com.br - secposmec@mecanica.ufu.br



### ATA DE DEFESA - PÓS-GRADUAÇÃO

Programa de Pós-Graduação em:	Engenharia Mecânica				
Defesa de:	Tese de Doutorado Acadêmico, nº 365, PPGEM				
Data:	15/08/2023	Hora de início:	08:00	Hora de encerramento:	12:00
Matrícula do Discente:	11923EMC003				
Nome do Discente:	Gustavo Henrique Nazareno Fernandes				
Título do Trabalho:	Development, application and validation of a new cooling technique applied for Inconel 718® machining				
Área de concentração:	Materiais e Processos de Fabricação				
Linha de pesquisa:	Processos de Fabricação (Usinagem e Soldagem)				
Projeto de Pesquisa de vinculação:	Desenvolvimento, aplicação e validação de uma nova técnica de refrigeração interna do inserto de metal duro via galerias internas produzidas por EDM na usinagem de materiais metálicos				

Reuniu-se por meio de videoconferência a Banca Examinadora, designada pelo Colegiado do Programa de Pós-graduação em Engenharia Mecânica, assim composta: Professores Doutores: Márcio Bacci da Silva - FEMEC/UFU; Rosemar Batista da Silva - FEMEC/UFU; Carlos Eiji Hirata Ventura - UFSCAR; Amauri Hassui - UNICAMP; Paulo Sérgio Martins - UNA e Álisson Rocha Machado - FEMEC/UFU, orientador do candidato.

Iniciando os trabalhos, o presidente da mesa, Dr. Álisson Rocha Machado, apresentou a Comissão Examinadora e o candidato, agradeceu a presença do público, e concedeu ao Discente a palavra para a exposição do seu trabalho. A duração da apresentação do Discente e o tempo de arguição e resposta foram conforme as normas do Programa.

A seguir o senhor(a) presidente concedeu a palavra, pela ordem sucessivamente, aos(às) examinadores(as), que passaram a arguir o(a) candidato(a). Ultimada a arguição, que se desenvolveu dentro dos termos regimentais, a Banca, em sessão secreta, atribuiu o resultado final, considerando o(a) candidato(a):

Aprovado.

Esta defesa faz parte dos requisitos necessários à obtenção do título de Doutor.

O competente diploma será expedido após cumprimento dos demais requisitos, conforme as normas do Programa, a legislação pertinente e a regulamentação interna da UFU.

Nada mais havendo a tratar foram encerrados os trabalhos. Foi lavrada a presente ata que após lida e achada conforme foi assinada pela Banca Examinadora.



Documento assinado eletronicamente por **Paulo Sérgio Martins, Usuário Externo**, em 15/08/2023, às 14:23, conforme horário oficial de Brasília, com fundamento no art. 6º, § 1º, do [Decreto nº 8.539, de 8 de outubro de 2015](#).



Documento assinado eletronicamente por **Carlos Eiji Hirata Ventura, Usuário Externo**, em 15/08/2023, às 19:22, conforme horário oficial de Brasília, com fundamento no art. 6º, § 1º, do [Decreto nº 8.539, de 8 de outubro de 2015](#).



Documento assinado eletronicamente por **Amauri Hassui, Usuário Externo**, em 15/08/2023, às 21:16, conforme horário oficial de Brasília, com fundamento no art. 6º, § 1º, do [Decreto nº 8.539, de 8 de outubro de 2015](#).



Documento assinado eletronicamente por **ALISSON ROCHA MACHADO, Usuário Externo**, em 16/08/2023, às 15:22, conforme horário oficial de Brasília, com fundamento no art. 6º, § 1º, do [Decreto nº 8.539, de 8 de outubro de 2015](#).



Documento assinado eletronicamente por **Marcio Bacci da Silva, Professor(a) do Magistério Superior**, em 16/08/2023, às 16:17, conforme horário oficial de Brasília, com fundamento no art. 6º, § 1º, do [Decreto nº 8.539, de 8 de outubro de 2015](#).



Documento assinado eletronicamente por **Rosemar Batista da Silva, Professor(a) do Magistério Superior**, em 16/08/2023, às 23:19, conforme horário oficial de Brasília, com fundamento no art. 6º, § 1º, do [Decreto nº 8.539, de 8 de outubro de 2015](#).



A autenticidade deste documento pode ser conferida no site [https://www.sei.ufu.br/sei/controlador\\_externo.php?acao=documento\\_conferir&id\\_orgao\\_acesso\\_externo=0](https://www.sei.ufu.br/sei/controlador_externo.php?acao=documento_conferir&id_orgao_acesso_externo=0), informando o código verificador **4663868** e o código CRC **2994CE7E**.

*"Studying is not spent. It is an investment. In fact, it is the best, the cheapest, and the longest-lasting investment. When you educate someone, it is forever."  
(Luís Inácio Lula da Silva)*

---

## Acknowledgment

---

I feel thankful for the invaluable contributions of my esteemed professors, Dr. Wisley Falco Sales (*in memoriam*), Dr. Álisson Rocha Machado, and Dr. Paulo Sérgio Martins. They are inspiring researchers who have dedicated their lives to the advancement of machining manufacturing. Their unwavering support and guidance have been instrumental in my growth and development.

To: the University of South Australia (UniSA), its staff, including Dr. Mohammad Uddin, Dr. Anthony Roccisano, Bob Chivel, Dr. Colin Hall, and especially Dr. André About Hatem, from the Future Institute.

To: the teachers of my basic training and technical course in Electronics of the Federal Center of Technological Education of Minas Gerais - CEFET - MG; my master's advisor, Prof. Dra. Antonella L. Costa; in particular, to Professor Carlos Eduardo (*in memoriam*), who taught me to like and love physics and inspired me in the search for knowledge.

To my lovely friends M.Sc. Pedro Henrique Pires França, M.Sc. Augusto César Peixoto, and M.Sc. Lucas Melo, for the sublime contributions to this work, without which much of this would not be a reality, for generosity, good mood, smiles, and company.

To colleagues of the School of Mechanical Engineering of Federal University of Uberlandia – FEMEC/UFU.

To FEMEC staff and lecturers, specially for Dr. Márcio Bacci da Silva and Dr. Éder Silva Costa and Cláudio Gomes do Nascimento, technician of Laboratory of Teaching and Research in Machining - LEPU, for availability, friendship, advice, rides and much more.

To my dear friends, part of my life, for the laughter and advice: Thiago (Wisk), Pedro (PêPê), Fernando (Chis), Gustavo (Gugu), Augusto (Boldão), Rafael, Fábio Côrrea (Fabinho), Iuri (Bimbo), Alexander (Jubas), Wiviany (WWivvi), Rainier (Cigano), Leandro (Lê Berola), Ormindá (Catu), Ana Luiza (Aninha), André (Dezão), Adriana (Dri), Jackson (Jackinho), Gabriel (Terê), Pedro (Pirex), Lucas Melo (Memelo), Augusto Peixoto (Augustin), Isabela (Bebela), Maria Paula (Mary Paul), Tatiane (Tati), among many others who have gone through my life and, somehow, today is part of me by the experiences exchanged.

To NipoTec – Special Tools, Walter Tools, Villares Metals SA, Ceratiziti, Mapal Brasil, Oerlikon Balzers, Petronas, Fuchs, and Stellantis Latam, all Brazilian companies, for supplying materials and services, without which this work could not be developed.

To all those who somehow, directly, or indirectly, helped me in this conquest.

To my parents, Levy Afonso and Maria das Graças, for my life; to my brother, Stanley Levi, for encouragement and academic example; to those people who have been part of my life, in the small and big details; and to the Brazilian people who, with the sweat of their work, were able to offer me the opportunity to study at a good public university.

Finally, I dedicate this thesis to Dr. H.c. Luís Inácio Lula da Silva for his struggle for education, his fight against hunger, his defense of social equality, his resistance to the ostentatious political-judicial-media persecution, his dignity, and for his thirty-five titles of honorary doctor.

---

## Abstract

---

Elevated temperatures can have detrimental effects on the quality of the machined output, including loss of dimensional tolerance, surface integrity issues and reduced tool life. Traditionally, the main method to avoid these problems is the application of Cutting Fluids in Abundance (CFA). However, this technique presents sustainability challenges in the social, environmental, and economic dimensions. Researchers have been exploring alternative cooling methods that aim to reduce or eliminate reliance on these inputs. This project sought to develop and test a new cooling method for machining, focusing on the turning of Inconel 718, a high-value superalloy. Coated tungsten carbide tools were used: TiNAl and a double coating, AlCrN over TiNAl, referred to as AlCrN+. They were integrated into an adapted tool holder with internal channels for circulation of a cooling fluid. An Design of Experiment (DoE) was employed, involving three atmospheres: internally cooled tools (ICTs), dry machining (DM) and the conventional use of abundant cutting fluids (CFA). Temperature analysis, conducted using a thermocamera and the tool-part thermocouple method, identified the speed ( $v_c$ ) and depth of cut ( $a_p$ ), as well as feed ( $f$ ), atmospheres (ICT, DM and CFA), in addition to coatings (TiNAl and AlCrN+) as the main input variables that affect temperature. In this case, the TiNAl coating together with the ICTs contributed significantly to the temperature reduction. However, the temperature at the interface between the chip and the tool increased with the basic machining parameters ( $v_c$ ,  $a_p$ ,  $f$ ) and was significantly affected by the atmosphere, with the ICTs demonstrating excellent performance. In terms of cutting forces, roughness and tool life, this research revealed that TiNAl together with ICTs outperformed CFA, removing 27% more material and an impressive 262% more than DM. AlCrN+ together with CFA, presented superior performance, providing a 46% increase in material removal compared to ICTs and a 306% increase in relation to DM. The TiNAl coating contributed to the increase in cutting forces, while other variables were not significant. Roughness was mainly influenced by coating, with no significant differences observed between atmospheres. Analyzes of wear mechanisms showed that abrasion, adhesion, oxidation and diffusion were observed regardless of coating or atmospheric conditions. Notably, the AlCrN+ coating showed a smoother and more uniform wear pattern, with a prevalence of flank and crater wear. In summary, internally cooled tools offer an innovative and environmentally friendly solution for machining operations. They excel in their heat dissipation capabilities, outperforming the CFA in some situations and significantly outperforming the DM. However, continuous efforts are needed to improve the lack of lubricity of the lubrication system and possible leakage problems.

**Keywords:** Inconel 718 machining, cooling, internally cooled tools, eco-friendly machining, sustainability



---

## Resumo

---

Temperaturas elevadas podem ter efeitos prejudiciais na qualidade da saída usinada, incluindo perda de tolerância dimensional, problemas de integridade da superfície e redução da vida útil da ferramenta. Tradicionalmente, o principal método para evitar esses problemas é aplicação Fluidos de Corte em Abundância (FCA). No entanto, essa técnica apresenta desafios de sustentabilidade nas dimensões social, ambiental e econômica. Os pesquisadores têm explorado os métodos alternativos de resfriamento que visam reduzir ou eliminar a dependência desses insumos. Este projeto buscou desenvolver e testar um novo método de resfriamento para usinagem, com foco no torneamento do Inconel 718, uma superliga de alto valor. Foram utilizadas ferramentas de carboneto de tungstênio revestidas: TiNAl e um revestimento duplo, AlCrN sobre TiNAl, referido como AlCrN+. Elas foram integradas a um porta-ferramentas adaptado com canais internos para circulação de um fluido de resfriamento. Foi empregado um planejamento experimental (*DoE*), envolvendo três atmosferas: ferramentas refrigeradas internamente (FRIs), usinagem a seco (US) e o uso convencional de fluidos de corte em abundância (FCA). A análise de temperatura, conduzida usando uma termocâmara e o método de termopar ferramenta-peça, identificou a velocidade ( $v_c$ ) e a profundidade de corte ( $a_p$ ), assim como o avanço ( $f$ ), atmosferas (FRI, US e FCA), além dos revestimentos (TiNAl e AlCrN+) como as principais variáveis de entrada que afetam a temperatura. Neste caso, o revestimento TiNAl junto com as FRIs contribuíram significativamente para a redução da temperatura. No entanto, a temperatura na interface entre o cavaco e a ferramenta aumentou com os parâmetros básicos de usinagem ( $v_c$ ,  $a_p$ ,  $f$ ) e foi significativamente afetada pela atmosfera, com as FRIs demonstrando excelente desempenho. Quanto às forças de corte, rugosidade e vida útil das ferramentas, esta pesquisa revelou que o TiNAl em conjunto com as FRIs superou o FCA, removendo 27% mais material e impressionantes 262 % a mais do que a US. Já o AlCrN+ junto com FCA, o apresentou desempenho superior, proporcionando um aumento de 46 % na remoção de material em comparação com as FRIs e um aumento de 306 % em relação a US. O revestimento TiNAl contribuiu para o aumento das forças de corte, enquanto outras variáveis não foram significativas. A rugosidade foi influenciada principalmente pelo revestimento, sem diferenças significativas observadas entre as atmosferas. As análises dos mecanismos de desgaste mostraram que abrasão, aderência, oxidação e difusão foram observadas independentemente do revestimento ou das condições de atmosfera. Notavelmente, o revestimento AlCrN+ apresentou um padrão de desgaste mais suave e uniforme, com prevalência de desgaste de flanco e cratera. Em resumo, as ferramentas resfriadas internamente oferecem uma solução inovadora e ecologicamente correta para operações de usinagem. Elas se destacam em suas capacidades de dissipação de calor, superando o FCA em algumas situações e superando significativamente o DM. No entanto, são necessários esforços contínuos para melhorar a falta de capacidade lubrificante do sistema lubrificação e possíveis problemas de vazamento.

**Palavras-chave:** usinagem, Inconel 718, refrigeração, ferramentas refrigeradas internamente, usinagem ecológica, sustentabilidade.

---

## Table of contents

---

Acknowledgment .....	vii
Abstract.....	viii
Resumo .....	ix
Table of contents .....	x
List of Figures .....	xii
List of Tables .....	xvii
List of Abbreviations and Acronyms .....	xix
Nomenclature .....	xxii
Chapter 1 : Introduction .....	25
<b>1.1. Introduction.....</b>	<b>25</b>
<b>1.2. Work objectives.....</b>	<b>27</b>
<b>1.3. Specific objectives.....</b>	<b>27</b>
Chapter 2 : Literature review .....	30
<b>2.1. Heat and temperature in machining.....</b>	<b>30</b>
<b>2.1.1. Temperature measurement via infrared radiation .....</b>	<b>37</b>
<b>2.1.2. Temperature measurement via thermo-couple tool-work .....</b>	<b>40</b>
<b>2.2. Machining Cooling Techniques.....</b>	<b>43</b>
<b>2.2.1. Wet Machining.....</b>	<b>45</b>
2.2.1.1. Cutting Fluid in Abundance - CFA .....	45
<b>2.2.2. Dry Machining - DM.....</b>	<b>53</b>
<b>2.2.3. Tools Indirectly Cooled – TIC.....</b>	<b>56</b>
2.2.3.1. Internally Cooled Shim – ICS .....	57
2.2.3.2. Heat pipes and heat sinks .....	65
2.2.3.3. Internally Cooled Tools – ICT .....	79
<b>2.3. Nickel (Ni) and nickel-based super alloys.....</b>	<b>86</b>
<b>2.3.1. Inconel 718 ®.....</b>	<b>92</b>
2.3.1.1. General overview of Inconel 718® .....	92
2.3.1.2. Inconel 718® machinability .....	96
2.3.1.3. Wear mechanisms & types for Inconel 718® .....	98

2.3.1.4. Tools materials for Inconel 718 <sup>®</sup> machining	107
2.3.1.5. Lubri-cooling techniques - Inconel 718 <sup>®</sup>	111
2.3.1.6. Surface integrity - Inconel 718 <sup>®</sup>	117
Chapter 3 : Experimental procedures .....	119
<b>3.1. Logical sequencing of experimental procedures</b> .....	<b>119</b>
<b>3.1.1. Cooling system &amp; Internally Cooled Tools – ICT</b> .....	<b>120</b>
<b>3.1.2. Inconel 718 characterization</b> .....	<b>126</b>
<b>3.1.3. Machine tool &amp; Fluids</b> .....	<b>128</b>
<b>3.1.4. Temperature measurements</b> .....	<b>130</b>
<b>3.1.5. Machining and wear mechanisms analysis</b> .....	<b>136</b>
Chapter 4 : Results and Discussions .....	141
<b>4.1. Cutting temperatures</b> .....	<b>141</b>
<b>4.1.1. Temperature results <i>via</i> thermocamera</b> .....	<b>141</b>
<b>4.1.2. Temperature results via tool-work thermocouple</b> .....	<b>148</b>
<b>4.2. Cutting forces</b> .....	<b>156</b>
<b>4.3. Roughness results</b> .....	<b>162</b>
<b>4.4. Tools life</b> .....	<b>175</b>
<b>4.5. Wear mechanisms analysis</b> .....	<b>182</b>
Chapter 5 : Conclusions.....	193
<b>5.1. Conclusions</b> .....	<b>193</b>
<b>5.2. Further works proposals</b> .....	<b>197</b>
References .....	198
Appendix A – Composition of various nickel and nickel-based alloys [110] .....	212
Appendix B - Mechanical properties (at room temperature) characteristics and applications of nickel-based alloys[110] .....	214
Appendix C - Physical properties (at room temperature) of various nickel-based alloys [110].....	218
Appendix D - Tool Spec Sheet SNMG120412 -NRT WS10.....	220
Appendix E - Tool Holder Spec Sheet DSSNR2525X12-P .....	223
Appendix F - Technical drawing of the SNMG 120408EN-M34 CTPX710 Tool adapted with internal cooling channels.....	227

---

## List of Figures

---

Figure 2-1: Heat sources in the orthogonal cutting.....	31
Figure 2-2: Chip formation on tool rake face .....	33
Figure 2-3: Representation and an orthogonal cut heat transfer model .....	34
Figure 2-4: Temperature as a function of feed and cutting speed when turning the Inconel 718. ....	39
Figure 2-5: Infrared photograph of the cutting process ( $v_c = 750$ m/min) .....	39
Figure 2-6: (a) Representative schematic of tool-work thermocouple using a rotating tailstock; (b) Thermoelectric tool-thermocouple system using a rotating tailstock.....	40
Figure 2-7: Schematic representation of the tool-work thermocouple system with a physical compensation element. ....	41
Figure 2-8: Classification of the machining environments according to the possible forms of lubrication and cooling.....	44
Figure 2-9: General classification of cutting fluids.....	45
Figure 2-10: Evolution of <i>Metal Working Fluids Consumption - MWF</i> (including FCs) globally .....	46
Figure 2-11: Relationship between metal temperature and friction coefficient for various contour and EP lubricating additives.....	47
Figure 2-12: Influencing factors in choosing a machining process.....	53
Figure 2-13: System proposed by Minton et al. (2013). (a) Internally cooled tool carrier, (b) Cooling block cut- A-A sight, (c) Pyrometer position, (d) Assembly of machine tool-part .....	58
Figure 2-14: Tool (left) and shim (right) with relief optimized to improve thermal efficiency.....	59
Figure 2-15: Shim and refrigerated inserts indirectly. (a, b) computational design. (c, d) optimized. (e, f) not optimized. (g, h) conventional. ....	60
Figure 2-16: Experimental results for optimized, non-optimized and conventional tools proposed by Li et al. (2018). (a) Temperature and (b) flank wear.....	61
Figure 2-17: Indirect cooling system proposed by Rozzi et al. (2011) . (a) Heat exchanger. (b) Internal view of the heat exchanger. (c) Complete set.....	62
Figure 2-18: Indirect cooling system of the tool carrier proposed by Neto et al. (2015): (a) Cut view of the tool holder and parts; (b) diagram of the refrigeration system; (c) tool carrier with displaced tool.....	63

Figure 2-19: Results for each condition and cooling method: a) Average temperature in thermocouple 1; b) Volume of removed material; (c) maximum depth of crater wear; d) Resulting force .....	64
Figure 2-20: Results of temperature measurements with the proposed system. (a) Heat pipes are used. (b) No heat pipes (c) Temperature in thermocouples ....	66
Figure 2-21: Orthogonal cutting scheme with heatsink. ....	67
Figure 2-22: Numerical results with different HS capacity. (a) Temperature on the main slack surface, (b) Flank wear .....	67
Figure 2-23: Numerical results, $q_{HS} = 45 \text{ W/mm}^2$ , varying the HS distance (a) Temperature on the main slack surface (b) Flank wear.....	68
Figure 2-24: Results of numerical temperature simulations at the chip/tool interface for three distinct conditions.....	69
Figure 2-25: a) Illustration of a drill with internal channel to insert the heat tube proposed by Jen et al. (2002) (b) Physical representation of an ideal heat tube .....	70
Figure 2-26: Temperature results for six different conditions simulating a drill in drilling condition. ....	70
Figure 2-27: Conventional drill (a) and drill with heat tubes (b) simulated with FEM proposed by Zhu et al. (2009).....	71
Figure 2-28: Tool Indirectly Cooled - TIC by heat pipes proposed by Chiou et al. (2007) . (a) Illustration of heat flux;(b) Illustration of simulation with ANSYS; (c) Experimental assembly; (d) Illustration of the fixation of thermocouples	73
Figure 2-29: Dry chip formation (a) with HT (b) dry and tool wear (c) dry and (d) HT.....	73
Figure 2-30: Temperature distribution simulation, dry (above) and with heat tube (below) .....	74
Figure 2-31: Temperature measurement by thermocouple, $v_c = 29.9 \text{ m/min}$ (above) and $v_c = 40.94 \text{ m/min}$ (below) .....	74
Figure 2-32: Tool Cooled Indirectly - TIC by internal cooling channels in the tool carrier and heat pipes proposed by Shu et al. (2011). ....	75
Figure 2-33: Conventional device (a), adapted with heat tube (b), simulation of the conventional (c) and (d) simulation of the heat tube. ....	76
Figure 2-34: Measured temperature without heat pipes in different positions experimentally (left) and by simulation (right), ( $v_c = 175.84 \text{ m/min}$ , $a_p = 0.7 \text{ mm}$ and $f = 0.1 \text{ mm/rev}$ ).....	77
Figure 2-35: Temperature at tool/chip interface depending on cutting speed .....	77
Figure 2-36: Chip morphology for experiments with heat (a) and dry tubes (b),...	78

Figure 2-37: Internally Cooled Tool - ICT with drawing and real photos .....	79
Figure 2-38: Indirect cooling device with proposed Peltier cells.....	80
Figure 2-39: Draw of Internally Cooled Tools -ICT with refrigeration system.....	82
Figure 2-40: Schematic of a chiller and its components .....	82
Figure 2-41: PCBN Internally cooled tool used by Barbosa (2021) .....	83
Figure 2-42: Internally cooled tool used by Bazon (2020) and França (2021).....	84
Figure 2-43: Standard Heat Treatment Diagram of the Inconel 718 (precipitated and aged) .....	94
Figure 2-44: Raw structure of Inconel 718 (a) (2,000x); structure after solubilization treatment (b) (500x) (1,095°C 1h/AA) and after aging (c) (500x) (955 1h/AA).....	95
Figure 2-45: Physical-chemical phenomena of tool wear: adhesion (a); abrasion (b); diffusion (c); oxidation (d).....	98
Figure 2-46: Wear mechanisms depending on machining parameters and temperature. ....	99
Figure 2-47: Abrasion and support details in Inconel 718 machining with uncoated PCBN tool .....	100
Figure 2-48: Types of abrasive wear caused by particles.....	101
Figure 2-49: Details of diffusion mechanism (smooth surface) on S20 carbide tool after machining Inconel 718 with CFA.....	102
Figure 2-50: Oxidizing dark spot on the main flank face in a class K cemented carbide tool after grey cast iron machining.....	103
Figure 2-51: Wear forms on a turning cutting tool.....	104
Figure 2-52: Parameters for measuring wear of cutting tools according to standard (ISO 3685, 1993) .....	104
Figure 2-53: Application range by hardness of BALINITI® coating material AlCrN .....	109
Figure 2-54: Residual stresses in two directions (a) radial and (b) longitudinal, under different environments: dry, MQL, cryogenic and <i>CryoMQL</i> .....	112
Figure 2-55: Main machining forces under different environments and cutting speeds.....	114
Figure 2-56: Wear for speed $v_c = 120$ m/min, cutting time of 30 s, in different environments. a) Flank wear and b) Crater wear .....	115
Figure 2-57: Maximum temperature measured on chips generated under different environments.....	115

<b>Figure 3-1: Diagram of experimental procedures at three levels: before, during, and after machining of Inconel 718 .....</b>	<b>119</b>
<b>Figure 3-2: Details of the components of the cooling system .....</b>	<b>120</b>
<b>Figure 3-3: Tool holder set, and cemented carbide insert made by EDM. ....</b>	<b>121</b>
<b>Figure 3-4: Tool and tool holder set. ....</b>	<b>122</b>
<b>Figure 3-5: Side view of the original tool holder (above) and adapted (below)...</b>	<b>124</b>
<b>Figure 3-6: (a) Side-cut view of AlCrN coating (BALINIT® ALNOVA) with thickness of 4 <math>\mu\text{m}</math> on hard metal substrate and (b) micro-abrasion marks until reveal the substrate.....</b>	<b>125</b>
<b>Figure 3-7: Microstructure of Inconel 718® VAT718 A produced by Villares Mettals. ....</b>	<b>127</b>
<b>Figure 3-8: A lathe and thermocamera experiment position .....</b>	<b>132</b>
<b>Figure 3-9: Experimental assembly diagram for temperature measurement .....</b>	<b>133</b>
<b>Figure 3-10: Modified mandril of the tailstock for capturing the signal of a rotating part used.....</b>	<b>134</b>
<b>Figure 3-11: Schematical draw of the calibration of the tool-workpiece thermocouple in an oven.....</b>	<b>135</b>
<b>Figure 3-12: Tool-work thermocouple calibration curve .....</b>	<b>135</b>
<b>Figure 3-13: Example of the cutting force (<math>F_c</math>) signal where the average was calculated .....</b>	<b>138</b>
<b>Figure 3-14: a) Photo of the force measurement experimental set up and b) schematical draw.....</b>	<b>139</b>
<b>Figure 3-15: Axial bar rotation for three different positions to assess roughness. ....</b>	<b>140</b>
<b>Figure 4-1: Chip-back temperature analysis with software.....</b>	<b>141</b>
<b>Figure 4-2: Temperature results in descending order via thermocamera .....</b>	<b>142</b>
<b>Figure 4-3: Pareto chart results for the cutting temperature measured by the thermocamera. ....</b>	<b>143</b>
<b>Figure 4-4: Tool-work thermocouple temperature results.....</b>	<b>149</b>
<b>Figure 4-5: Pareto Chart for tool-work thermocouple temperature, ICT x DM ...</b>	<b>150</b>
<b>Figure 4-6: Pareto Chart of the temperatures measured by the tool-workpiece thermocouple method, ICT x CFA .....</b>	<b>151</b>
<b>Figure 4-7: Pareto Chart of the temperatures measured by the tool-workpiece thermocouple method, CFA x DM .....</b>	<b>152</b>

<b>Figure 4-8: Cutting forces with different tool coatings and atmosphere conditions.</b>	<b>156</b>
<b>Figure 4-9: Pareto chart results for cutting forces considering different atmospheres, ICT x CFA (a), ICT x DM (b), CFA x DM (c)</b>	<b>158</b>
<b>Figure 4-10: Surface roughness <math>R_a</math> average (R1, R2, and R3) for various cutting atmospheres and tool coatings. <math>v_c = 45</math> m/min, <math>a_p = 0.5</math> and <math>f = 0.103</math> mm/rev</b>	<b>164</b>
<b>Figure 4-11: Surface roughness <math>R_z</math> average (R1, R2, and R3) for various cutting atmospheres and tool coatings. <math>v_c = 45</math> m/min, <math>a_p = 0.5</math> and <math>f = 0.103</math> mm/rev.</b>	<b>164</b>
<b>Figure 4-12: Surface roughness <math>R_q</math> average (R1, R2, and R3) for various cutting atmospheres and tool coatings. <math>v_c = 45</math> m/min, <math>a_p = 0.5</math> and <math>f = 0.103</math> mm/rev.</b>	<b>165</b>
<b>Figure 4-13: Pareto chart results for (a) <math>R_a</math>; (b) <math>R_z</math> and (c) <math>R_q</math> - ICT x CFA</b>	<b>168</b>
<b>Figure 4-14: Pareto chart results for roughness (a) <math>R_a</math>, (b) <math>R_z</math> and (c) <math>R_q</math>, respectively (from top to bottom) comparing ICT x DM</b>	<b>170</b>
<b>Figure 4-15: Pareto chart results for roughness (a) <math>R_a</math>, (b) <math>R_z</math> and (c) <math>R_q</math>, respectively (from top to bottom) comparing CFA x DM</b>	<b>173</b>
<b>Figure 4-16: Average (Replica 1, 2, and 3) for tool's life for each machining condition</b>	<b>175</b>
<b>Figure 4-17: Pareto's charts of the for tool's life results, (a) ICT x CFA, (b) ICT x DM and (c) CFA x DM.</b>	<b>178</b>
<b>Figure 4-18: Semi-quantitative graphic elements analysis at tools rake and flank faces</b>	<b>184</b>
<b>Figure 4-19: Perspective tool view for coating and atmosphere conditions</b>	<b>188</b>
<b>Figure 4-20: Lateral view (flank face) of the worn tools used under all cutting atmospheres tested. (a) 100 X, (b) 200 X and (c) 1 200 X</b>	<b>189</b>
<b>Figure 4-21: Top view (rake face) of the worn tools used under all cutting atmospheres tested (a) 100 X, (b) 200 X and (c) 1,200 X</b>	<b>190</b>
<b>Figure 4-22: Top view (rake face) EDS analysis on the worn tools used under several cutting atmospheres</b>	<b>191</b>
<b>Figure 4-23: Lateral view (flank face) EDS analysis on the worn tools used under several cutting atmospheres</b>	<b>192</b>



---

## List of Tables

---

<b>Table 2-1: Energy distribution during machining .....</b>	<b>35</b>
<b>Table 2-2: Cutting conditions used [93] .....</b>	<b>64</b>
<b>Table 2-3: Various uses of Nickel .....</b>	<b>86</b>
<b>Table 2-4: Influence of various chemical elements on the properties of superalloys .....</b>	<b>88</b>
<b>Table 2-5: Inconel 718 chemical composition .....</b>	<b>93</b>
<b>Table 2-6: Mechanical and physical properties of Inconel 718 AMS 5663M .....</b>	<b>93</b>
<b>Table 2-7: Studies of Inconel 718 with cutting parameters and response variables .....</b>	<b>96</b>
<b>Table 2-8: Summary of wear types and their causes in different machining processes of Inconel 718 .....</b>	<b>106</b>
<b>Table 2-9: Properties of different types of tool materials in Inconel 718 machining .....</b>	<b>108</b>
<b>Table 2-10: Various operations and results using BALINITI ® ALNOVA .....</b>	<b>110</b>
<b>Table 2-11: Lubri-cooling techniques used in the machining of Inconel 718 .....</b>	<b>116</b>
<b>Table 2-12: Several studies on the roughness of Inconel 718 .....</b>	<b>118</b>
<b>Table 3-1: Specifications of the cooling system.....</b>	<b>121</b>
<b>Table 3-2: Cemented carbide tool inserts specifications .....</b>	<b>123</b>
<b>Table 3-3: Toolholder specifications (in conjunction with Table 3-2) .....</b>	<b>123</b>
<b>Table 3-4: Coating specifications (BALINIT® ALNOVA &amp; Dragon Skin) .....</b>	<b>125</b>
<b>Table 3-5: Composition, mechanical and physical-chemical properties of Inconel 718.....</b>	<b>126</b>
<b>Table 3-6: ECOCOOL P 1977 BF specifications.....</b>	<b>129</b>
<b>Table 3-7: Properties of mono ethylene glycol.....</b>	<b>129</b>
<b>Table 3-8: Temperature fractionated DoE <math>2^5 - 1</math>.....</b>	<b>130</b>
<b>Table 3-9: Fractionated factorial experiment design <math>2 \times 25 - 1</math> .....</b>	<b>131</b>
<b>Table 3-10: Two full factorial Design of Experiment <math>2^2</math>.....</b>	<b>136</b>
<b>Table 3-11: Two full factorial Design of Experiment <math>2^2</math> .....</b>	<b>137</b>
<b>Table 3-12: Two Full factorial design 22 for roughness measurement.....</b>	<b>140</b>
<b>Table 4-1: Thermocamera temperature results .....</b>	<b>142</b>
<b>Table 4-2: Thermo camera temperature ANOVA.....</b>	<b>143</b>

<b>Table 4-3: Tool-work thermocouple temperature results .....</b>	<b>148</b>
<b>Table 4-4: ANOVA of the temperature measured by the tool-workpiece thermocouple method (ICT x DM).....</b>	<b>149</b>
<b>Table 4-5: ANOVA of the temperature measured by the tool-workpiece thermocouple method (ICT x CFA).....</b>	<b>150</b>
<b>Table 4-6: ANOVA of the temperature measured by the tool-workpiece thermocouple method (CFA x DM).....</b>	<b>151</b>
<b>Table 4-7: Cutting forces measured at the beginning of the tool's life .....</b>	<b>156</b>
<b>Table 4-8: Cutting Forces ANOVA.....</b>	<b>157</b>
<b>Table 4-9: Surface roughness <math>R_a</math> parameter .....</b>	<b>162</b>
<b>Table 4-10: Surface roughness <math>R_z</math> parameter.....</b>	<b>163</b>
<b>Table 4-11: Surface roughness <math>R_q</math> parameter .....</b>	<b>163</b>
<b>Table 4-12: Roughness <math>R_a</math>, <math>R_z</math>, and <math>R_q</math> ANOVA comparing ICT x CFA .....</b>	<b>166</b>
<b>Table 4-13: Roughness <math>R_a</math>, <math>R_z</math>, and <math>R_q</math> ANOVA comparing ICT x DM .....</b>	<b>169</b>
<b>Table 4-14: Roughness <math>R_a</math>, <math>R_z</math>, and <math>R_q</math> ANOVA comparing CFA x DM .....</b>	<b>172</b>
<b>Table 4-15: Tool's life for different machining conditions .....</b>	<b>175</b>
<b>Table 4-16: ANOVA of the tool life tests .....</b>	<b>176</b>
<b>Table 4-17: Semi-quantitative elements analysis at tools rake and flank faces... </b>	<b>183</b>

---

## List of Abbreviations and Acronyms

---

ADM	Absolute dry machining
ANOVA	Analysis of variance
APB	Anti-phase boundary
AZ	Adhesion zone
BCT	Body-centered tetragonal
BUE	Built-up edge
CA	Compressed air
CBN	Cubic boron nitride
CBT	centered body tetragonal
CCP	Central composite planning
CF	Cutting fluids
CFA	Cutting fluid in abundance
CFD	Computer fluid dynamics
CNC	Computer numerical control
CTI	Cooled tool indirectly
CVD	Chemical vapor deposition processes
DLC	Diamond-like carbon
DM	Dry machining
DoE	Design of Experiments
EDM	Electric discharge machine
EDS	Electron dispersion spectroscopy
EP	Extreme-pressure
FCC	Face-Centered Cubic
FEM	Finite element method
FZ	Flow zone
GMS	<i>Grupo de Manufatura Sustentável</i>
HLB	Hydrophilic-lipophilic balance
HP	Heat pipes
HPCF	High-pressure cutting fluid
HSM	High-speed machining

HSS	High-speed steels
HT	Heating tubes
ICCN	Internal cooled channels
ICCH	Internally cooled chamber
ICS	Internally cooled shim
ICT	Internally cooled tools
IR	Infrared
IRT	Infrared thermocamera
LEPU	<i>Laboratório de Ensino e Pesquisa em Usinagem</i> (Laboratory of Teaching and Research in Machining)
MQCL	Minimum quantity of cooled lubricant
MQL	Minimum quantity lubrication
MQSL	Minimum quantity of solid lubrication
MWF	Metal working fluids
NDM	Near dry machining
nMQL	Minimum quantity of nanoparticulate lubricant
PCC	Central Composite Planning
PCD	Polycrystalline diamond
PHE	Primary heat exchanger
PSZ	Primary shear zone
PTFE	Polytetrafluoroethylene
PVD	Physical vapor deposition processes
R&D	Research & development
SEM	Scanning electron microscope
SHE	Secondary heat exchanger
SL	Solid lubricants
SSZ	Secondary shear zone
TCB	Tetragonal Centered Body
TCP	Topologically Close-Packed
TIC	Tools indirectly cooled
TSZ	Tertiary shear zone
TT	Textured tools

UFU	Universidade Federal de Uberlândia
UN	United Nations
WEDM	Wire electrical discharge machining
WM	Wet machining

## Nomenclature

Description	Abbreviation	Unit
Asymmetry Factor of the Evaluated Profile (Skewness)	Rsk	
Average flank wear	V <sub>BB</sub>	mm
Average Temperature Obtained at the Chip-Tool Interface	T1	°C
Calibration constants	A, B, C	
Chip thickness ration	Rc	
Chip velocity	V <sub>chip</sub>	m/min
Constant radiation 1	C1	W.m <sup>2</sup>
Constant radiation 2	C2	mK
Cooling rate	CR	K/h
Crater wear	KT	mm
Cutting force	Fc	N
Cutting speed	vc	m/min
Cutting width	a <sub>w</sub>	mm
Deformation rates	$\bar{\epsilon}$	1/s
Density	$\rho$	kg / m <sup>3</sup>
Depth of Cut	ap	mm
Diameter of the Internal Cooling Channels	D	mm
E.M.F. Formed by the Connection of the Copper Wire And the Tool at the Temperature T2	E <sub>BF</sub>	e. m. f.
E.M.F. Generated Between The Workpiece and Material A at the Temperature T3	E <sub>PA</sub>	e. m. f.
E.M.F. That Is Generated Between the Insert and the Workpiece at Temperature T1	E <sub>F.P</sub>	e. m. f.
E.M.F. That Relates the Joint Between the Metal and the Copper Wire B for the Temperature T4	E <sub>AB</sub>	e. m. f.
Electrical Circuit of the Tool-Workpiece Thermocouple System	$\Delta E$	e. m. f.
Emissivity Coefficient of the Surface	r $\epsilon$	
Evaluation length	ln	
Feed	f	mm/rev
Flattening Factor of the Evaluated Profile (Kurtosis)	Rku	
Frictional force	Ff	N

Heat generation rate in the part	$\Gamma$	$J$
Heat generation rates given in the primary shear zone	$P_s$	$J$
Heat generation rates given in the secondary shear zone	$P_f$	$J$
Heating rate		$^{\circ}C/s$
Heatsink area	$A_{HS}$	$mm^2$
Heatsink contact length	$C_{HS}$	$mm$
Heatsink distance	$D$	$mm$
Horizontal dimension	$H$	$mm$
Ideal black body emissivity	$\epsilon\lambda$	
Initial workpiece temperature	$\theta_0$	$^{\circ}C$
Insert thickness	$T_i$	$mm$
Intensity of reading a real body	$L\lambda$	
Joint temperature formed by the contact of the element compensation in the tool	$T_2$	$^{\circ}C$
Machining force	$F_u$	$N$
Maximum chip temperature	$\theta_{max}$	$^{\circ}C$
Maximum flank wear	$V_{Bmax}$	$mm$
Maximum profile height	$R_z$	
Mean arithmetic deviation	$R_a$	
Normal force	$F_N$	$N$
Notch wear	$V_{BN}$	$mm$
Opposing force	$F_A$	$N$
Primary shear zone temperature increment	$\theta_s$	$^{\circ}C$
Quadratic mean deviation	$R_q$	
Radiation intensity of a black body	$E(\lambda, T)$	
Radiation intensity of an ideal black body	$L(\lambda, T)$	
Rate of energy generated in the cutting process	$P_m$	$J/s$
Real amount of energy detected	$E$	$J$
Rhomboid geometry	$W$	
Round	$R$	
Sampling length	$l_r$	
Secondary shear zone temperature increment	$\theta_m$	$^{\circ}C$
Small tooltip angles	$\epsilon_R$	$^{\circ}$
Specific heat	$c$	$J/kgK$

Square format	S	
Temperature of the object	T	K
Thermal dissipation capacity	$q_{HS}$	$W/mm^2$
Thermal flow	$q''$	$W/m^2$
Tool tip radius	$r_\epsilon$	mm
Total profile height	Rt	
Undeformed chip thickness	ac	mm
Vertical dimension	V	mm
Wavelength	$\lambda$	m



---

---

## Chapter 1: Introduction

---

---

### 1.1. Introduction

High heat generation with the consequent increase in temperature is still a limiting factor for productivity and quality in machining processes [1–3]. It is widely recognized that increasing the cutting speed reduces operating time and elevates the cutting temperature. This temperature rise has both positive and negative implications. On the positive side, it softens the material, reducing shear resistance and facilitating the cutting process. However, on the other hand, this elevated temperature accelerates wear progression, thereby compromising the tool's overall lifespan [4,5].

The standard method used industrially to circumvent heat generation and temperature rise in machining is applying a cutting fluid in abundance (CFA)[6,7]. In fact, it has been reported by Said et al. (2019) that the global consumption of non-biodegradable mineral-based cutting fluids reached approximately 13,726 million tons in 2016, with further projected increases [8]. Furthermore, Benedicto et al. (2017) have estimated that the global demand for lubricants could reach 43.9 million tons by 2022 [9].

Various alternative lubrication and cooling methods have been extensively researched and effectively implemented. These methods include minimum quantity lubrication (MQL), minimum quantity of cooled lubricant (MQCL), high pressure cutting fluid (HPCF), cryogenic fluids such as liquid nitrogen and CO<sub>2</sub>, solid lubricants, lubricants infused with nanoparticles, tool texturizations with lubricant impregnation, high-pressure coolant systems, refrigerated compressed air, among others [10–16].

For instance, the High-Pressure Cutting Fluid (HPCF) technique consists of injecting conventional cutting fluid over the tool/chip interface at high pressures, ranging from some Mega Pascal [17] can reach the 400 MPa [18]. HPCF reduces chip size and contact length with the tool, which reduces friction, heat generation, temperature, wear and thus improves tool life. Nandy et al. (2009) studied the chip/tool contact length in ti-6Al-4V machining and observed a reduction of almost 50% for HPCF than conventional machining [19]. Kaminski & Alvelid (2000) achieved cutting-edge temperature reduction from 40 to 45% in SS2541-03 steel turning with a coated carbide tool and fluid pressure

ranging from 70 to 360 MPa [20]. Ezugwu & Bonney (2005) life gain of coated carbide tool of almost 3.5 times in the finish of the Inconel 718 with HPCF (11 MPa) and cutting speed of 60 m/min [21].

The Minimum Amount of Lubricant – MQL is a method that consists of using compressed air line (5 ~ 15 *bar*) passing through a mixing chamber where, by venturi tube effect, a pressure differential sucks the lubricating oil from a reservoir and creates a mixture of air with atomized droplets. This mixture, also called mist, is then injected into the cutting zone by an injector nozzle, or nozzle, of an approximate diameter of  $\varnothing = 1 \text{ mm}$ , at rates of 50 *ml/h* ~ 2 *l/h* of and assist in the lubri-cooling of the cutting process [22]. Yazid et al. (2011) studied surface integrity in turning the Inconel 718, finishing operation using MQL, and dry machining [23]. For this, the authors varied the fluid flow rate of 50 and 100 *ml/h*. The analysis results by Scanning Electron Microscopy - SEM indicated severe plastic deformations that generated alterations in the subsurface layers of the part. The hardening working was evident with the microhardness profile measured. The authors also verified that the MQL conditions improve surface integrity results.

Despite the good results achieve in some instances, many of these alternative methods involve the use of inputs and the unavoidable generation of waste. For instance, when liquid nitrogen or CO<sub>2</sub> is used, they rapidly vaporize and disperse into the atmosphere, resulting in their loss. Similarly, in the case of MQL, although it consumes less volume, the oil is not recovered or reused, leading to its depletion. Consequently, these methods have environmental impacts, albeit relatively minor when compared to conventional cutting fluids, but they can still be significant when implemented on a large scale. Additionally, these alternative methods often have higher associated costs [7].

An important consideration is the negative impact of excessive use of cutting fluid. Although the cutting fluid helps protect the tool by reducing the temperature, it also affects the workpiece and chip [24]. The temperature rise in the workpiece/chip is advantageous for machining as it lowers the material's mechanical resistance, making it easier to cut and shear, thus reducing the required forces and power. Therefore, a hypothetical effective coolant system should focus majorly into reducing the tool's temperature trying to affect the minimum as possible the temperature increase of the chip and workpiece.

Indeed, the Research & Development (R&D) of a new cooling technique for machining holds significant promise. The focus of this technique should be on implementing a closed-loop concept, ensuring that there is no dispersion of fluids into the atmosphere while primarily targeting the cooling of the cutting tool. This proposal outlines the scope and objectives of the work, aiming to contribute to developing an environmentally friendly and efficient cooling method that optimizes the machining process.

## 1.2. Work objectives

The primary objective of the research was to develop and implement an innovative cooling technique. Inconel 718 was selected as the material of choice for this study due to its high relative mechanical properties, making it one of the most significant superalloys. The effectiveness of this technique was validated through comparative and statistical methods. The proposed approach involved the circulation of a coolant inside the tool, utilizing galleries created using electric discharge machining (EDM), specifically focusing on cooling the tool during the machining process.

## 1.3. Specific objectives

The specific objectives of this work include:

- Conduct a state-of-the-art literature review on alternative cooling methods in machining, including classifications (wet machining, near-dry machining, and dry machining), the main techniques, their characteristics, advantages, disadvantages, and their application in the machining of Inconel 718.
- Perform a literature and historical investigation of indirectly cooled tools, including the state of the art, aiming to create a timeline from the first historical record to the most recent research on the topic.
- Conduct a literature review on nickel-based alloys, focusing primarily on the superalloy Inconel 718. The review covered the general characteristics of Inconel 718, machinability, wear mechanisms, types, tools used in its machining, lubrication-cooling techniques, and surface integrity.
- To project and adapt a cooling system to cool water at  $\sim 0^\circ\text{C}$  and circulate it inside the carbide inserts with internal cooling channels manufactured by *electric discharge machining - EDM*.

- To conduct experimental comparisons between the internally cooled tools (ICT) system and the methods of dry machining and cutting fluid in abundance (CFA). The evaluation focused on various response variables, including surface roughness, cutting forces, cutting temperature, tool life, and wear mechanisms. These parameters were measured and analyzed to assess the performance and effectiveness of the ICT system compared to traditional approaches.
- This study aims to compare the performance of two coatings, TiNAl and AlCrN+, under three cutting atmospheres: ICT, CFA, and DM. Notably, the temperature analysis, conducted using thermocamera analysis, focuses specifically on the ICT and DM conditions. This investigation forms a crucial part of the research, shedding light on the thermal dynamics in these two machining environments.

#### 1.4. Relevance and originality

A recurring term in the leading international conferences convened by the United Nations - UN, such as Rio + 20, is "Sustainable Development." It was defined as: *"Sustainable development is one that meets the needs of the present without compromising the ability of future generations to meet their own needs"* [25]. Considering the environmental factor and the limitation of material resources, research on more effective manufacturing methods and technologies has significantly boosted in recent decades [2].

Within the industry, cutting fluids continue to pose a significant problem. Shashidhara & Jayaram (2010) estimate that approximately 80% of operator-related health issues are associated with cutting fluid poisoning [26]. These fluids often contain various additives, many of which are toxic, such as fungicides and bactericides. These additives can severely affect human health, including allergic reactions, respiratory problems, degenerative diseases, and even cancer [6,27].

In addition to their impact on human health, cutting fluids also cause environmental damage. They can contaminate soils, sewers, rivers, and water sources, harming ecosystems and water quality [28,29].

The cost of cutting fluids (CFs) is another drawback, especially as environmental regulations become more stringent and manufacturers are held accountable for the entire lifecycle of the product, from production to disposal [22,30]. Research suggests that CFs

alone can contribute from 7 to 17% of the total machining cost [31], and in exceptional cases, they can reach up to 30% [32].

In this work, the approach used was the closed-loop concept, which prevents fluid dispersion into the atmosphere and keeps the tool cool throughout the cutting process. The goal was to improve productivity through increased cutting parameters, longer tool life, enhanced surface integrity, and greater sustainability.

The decision to use Inconel 718 as the work material was based on its significance in the aeronautical industry, where economic quality and reliability are crucial. Despite its importance, machinability remains a significant challenge.

## 1.5. Work structure

This work was divided into five chapters, as follows:

**Chapter 1:** contains an introduction raising the problem and scientific gap for justifying the work, general and specific objectives, ending highlighting the relevance and originality of the work.

**Chapter 2:** presents the literature review of the main topics related to the work, including heat in the machining process and main temperature measurements techniques; cooling techniques such as wet machining, near dry machining, and dry machining; methods about tools indirectly cooled – TIC and machinability of Inconel 718.

**Chapter 3:** gives details of the methodology used in the experimental work, with equipment and all the procedures adopted, the internal cooling system design, and Inconel 718 characteristics.

**Chapter 4:** the main results for temperature, cutting forces, roughness tool's life, and wear mechanisms are presented and discussed in this chapter.

**Chapter 5:** presents the most relevant conclusions drawn from this work, as well as suggestions for future work.

---

---

## Chapter 2: Literature review

---

---

### 2.1. Heat and temperature in machining

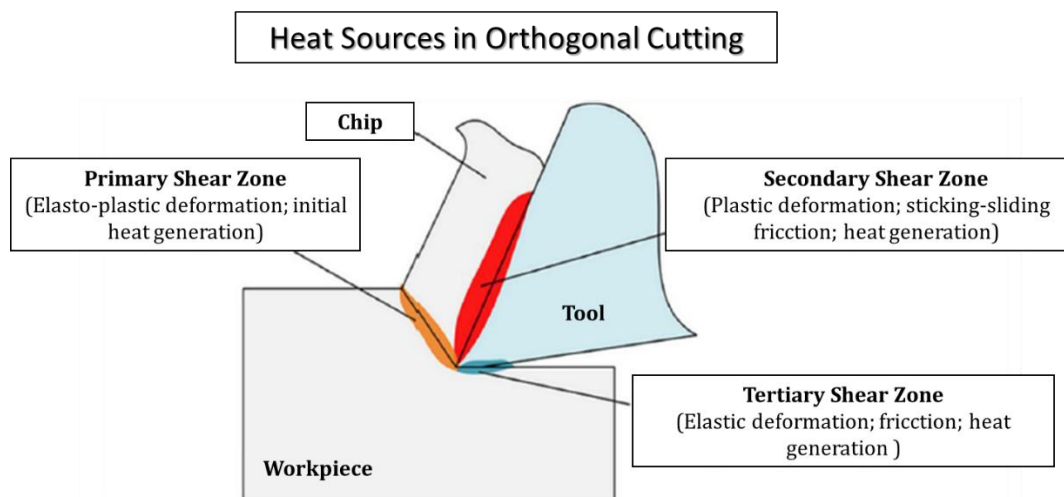
Machining is a complex operation still not fully comprehended, as it encompasses a thermomechanical process [4]. This process involves high pressures and temperatures in a small area at the interface between the tool and the chip. The energy generation during machining is primarily converted into heat, distributed among the workpiece, chip, tool, and surrounding environment [33,34].

Heat generation in machining is closely related to the process of chip formation. The chip formation begins with the initial contact between the tool and the workpiece, known as the initial engagement. The tool's cutting edge elastically deforms the workpiece's material during this stage. According to Knight & Boothroyd (2005), heat generation is minimal during this initial engagement because the material absorbs energy elastically [35].

The elastoplastic deformation plane comprises shear stresses, but compression and tensile stresses may also occur, or even their combination, culminating in the material's rupture. As the cutting process is dynamic, several deformation planes rapidly form parallel, which defines the primary shear zone - PSZ, as shown in **Figure 2-1**. In a second moment, material lamellae are wholly or partially separate, giving rise to a continuous or discontinuous chip [4,36].

Knight & Boothroyd (2005) developed a mathematical treatment of the average temperature, for orthogonal cutting, increase of the material ( $\theta_s$ ) when passing through the PSZ ( $P_s$ ) as a function of heat generation rate, with an energy's fraction being distributed to the part ( $\Gamma$ ) and the remainder distributed to the chip ( $[1 - \Gamma]P_s$ ) [35]. Firstly, the rate of energy generated in the cutting process ( $P_m$ ) is given by the product of the cutting speed ( $v_c$ ) and the cutting force ( $F_c$ ), Eq. (1):

$$P_m = F_c \cdot v_c \text{ [J/s]} \quad (1)$$



**Figure 2-1:** Heat sources in the orthogonal cutting

Source: [191]

The total heat generation rate ( $P_m$ ) in machining can be divided into the heat generation rates given in the primary ( $P_s$ ), secondary ( $P_f$ ) and tertiary zones. The tertiary zone is the contact between the workpiece and the flank face of the cutting tool and consumes a minimal amount of energy and thus can be ignored unless the tool is too worn out. So, Eq. (2) represents the simplified form of heat generation rate:

$$P_m = P_s + P_f \quad [J/s] \quad (2)$$

The heat generated in the primary shear zone can be determined by the equation of the average temperature increases in the workpiece at the PSZ ( $\theta_s$ ), given by Eq. (3):

$$\theta_s = \frac{[1 - \Gamma]P_s}{\rho c v_c a_c a_w} \quad (3)$$

Where:  $\rho$  is the density of the part [ $kg/m^3$ ];  
 $c$  is the specific heat of the part [ $J/kgK$ ];  
 $a_c$  is the undeformed chip thickness [ $mm$ ];  
 $a_w$  is the cutting width [ $mm$ ].

The heat generated in the secondary shear zone is given by Eq. (4):

$$P_f = F_f \cdot v_{chip} \quad (4)$$

Where:  $F_f$  is the frictional force [ $N$ ] on the rake face,

$v_{chip}$  is the chip velocity [m/min], that can be calculated by  $v_{chip} = vc/Rc$ ,  
 $Rc$  is the chip thickness ratio ( $Rc = v_{chip}/vc$ )

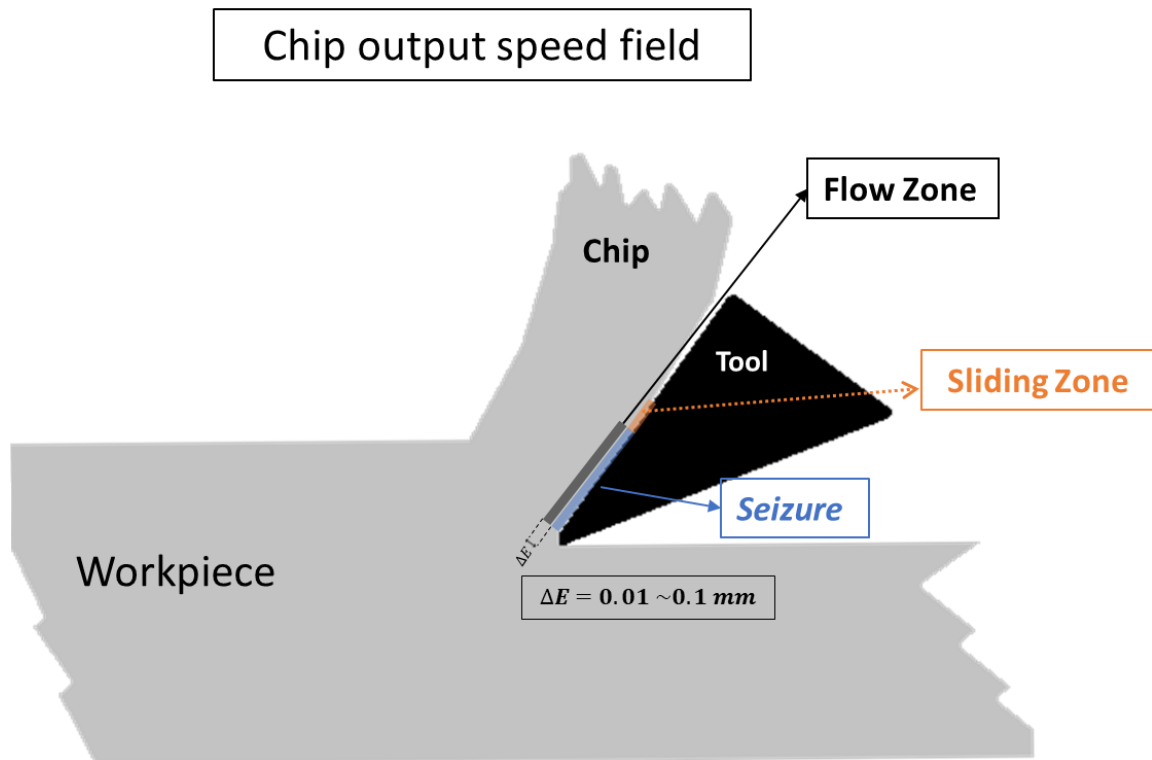
The second stage of heat generation occurs when the chip, under high temperature and pressure, is forced to slide over the tool's rake face, forming a material flow that forms the secondary shear zone - SSZ. The tribological characteristics of the chip/tool pair are essential in this step, as the chip must overcome the frictional forces that influence: the cutting force ( $\bar{F}_U$ ), the rate of material removal, heat generation, temperature increase, wear and tool life, and productivity [4,5].

The SSZ can be divided into two regions: adhesion and sliding zones. In certain conditions, the chip/tool contact pressure close to the cutting edge on the tool rake surface can reach as high as giga Pascal order, with temperatures above 1,000 °C, deformation rates ( $\dot{\epsilon} = 10^6/s$ ) with a theoretical heating rate of the order of ( $10^6 \text{ }^\circ\text{C}/s$ ) [37]. Under these conditions, the cutting region becomes extremely hot, softens the work material, and creates a condition for developing a flow zone - FZ in the adhesion zone - AZ.

Machado et al. (2015) comment that a common condition for machining steels in the industry is when the chip velocity ( $v_{chip}$ ) is of the order of 120 m/min with a small contact area of just 6 mm<sup>2</sup> [4]. Such high speed would prevent heat from being exchanged for conduction to the tool, forming an adiabatic process. However, the chip has a speed gradient, where the film of adhered material on the tool surface has  $\vec{V} = 0$  and grows continuously, featuring a flow zone - FZ, with thickness ranging from 0.01 to 0.10 mm, until it reaches the chip's full flow speed ( $\vec{V}_{max} = v_{cav}$ ), according to **Figure 2-2**. This phenomenon is vital since the chip when in direct and prolonged contact with the tool, allows heat transfer by conduction, with a consequent increase in temperature and wear.

In the sliding zone, the relative movement of the chip over the tool rake face occurs in the points of contact in a way known as stick-slip. It is characterized by an unstable dynamic condition and non-linear sliding [38], in which the movement of the chip involves adhesion and sliding. Heat under such conditions occurs by flashes when the contact points are broken.



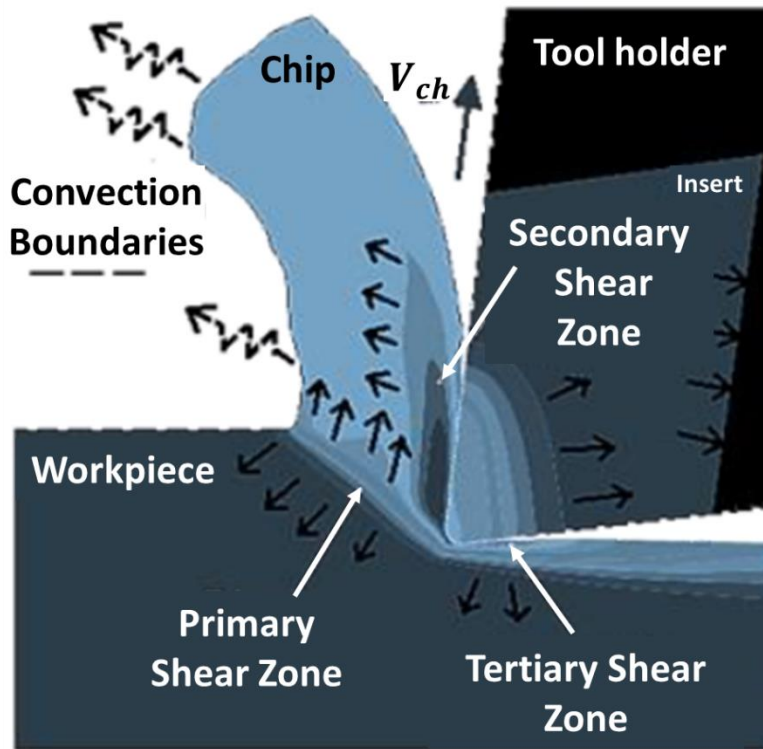


**Figure 2-2:** Chip formation on tool rake face

In the tertiary shear zone - TSZ, heat is generated by contact friction between the newly machined surface and the tool flank, where elastic deformation predominates [36]. The amount of heat generated in this region can be neglected if the tool is new (no flank wear) and a clearance angle ( $\alpha_0$ ) has been selected in a way that minimizes friction between the newly formed surface and the tool.

The heat generated in machining is dissipated from the primary, secondary, and tertiary zones through the chip, tool, workpiece, and environment, as illustrated in **Figure 2-3** [39].

Maximum chip temperature ( $\theta_{max}$ ) can be estimated by considering the SSZ temperature increment ( $\theta_m$ ) plus the initial workpiece temperature ( $\theta_0$ ) plus, the PSZ temperature increment ( $\theta_s$ ) given by Eq. 5, neglecting the TSZ [35].



**Figure 2-3:** Representation and an orthogonal cut heat transfer model

Source: [39]

$$\theta_{max} = \theta_m + \theta_s + \theta_0 \quad (5)$$

Where:  $\theta_m$  = temperature increase of the workpiece material after the SSZ;  
 $\theta_s$  = temperature increase of the PSZ;  
 $\theta_0$  = initial workpiece temperature.

The increase in chip temperature ( $\theta_m$ ) caused by heat generated in the SSZ is given by Eq. (6):

$$\theta_m = \frac{P_f}{\rho c v_c a_c a_w} \quad (6)$$

Due to the complex nature of the physical and chemical phenomena occurring during the cutting process and the inherent difficulties in directly measuring the chip-tool interface, there are discrepancies in the literature regarding energy distribution in the process [24]. Furthermore, the proportion of heat distributed among the workpiece, tool, chip, and environment can vary depending on several factors, such as the tool and workpiece material, cutting parameters, tool condition, machining operation type, and environmental conditions. In their extensive literature review, Fleischer et al. (2007) concluded that it is challenging to precisely determine the exact percentage of energy

distribution among the workpiece, chip, and tool. However, they could estimate percentage ranges, as presented in **Table 2-1** [24]. The heat going to the tool goes from 1 to 35 %.

**Table 2-1: Energy distribution during machining**

	<b>Drilling</b>	<b>Turning</b>	<b>Milling</b>
<b>Workpiece (%)</b>	5~15	2,1 ~18	5,3 ~10
<b>Tool (%)</b>	10 ~35	1.1 ~20	1.3 ~25
<b>Chip (%)</b>	55 ~75	74.6 ~96.3	65 ~74.6

Source: [24]

Numerous studies have highlighted the adverse effects of high temperatures on the machining process. These effects include reduced tool life, undesired deformations, increased surface roughness, excessive material hardening, thermal cracks, compromised dimensional accuracy, impaired surface integrity, elevated costs, and more [40–42].

Many decades ago, computer numerical control (CNC) machines emerged, featuring improved structural integrity and increased power compared to their predecessors. This technological advancement marked a significant milestone in metal cutting, revolutionizing machining operations [43,44]. This technology enabled a sharp increase in cutting parameters. Naturally, the elevation of these parameters increases the contact region at the tool/part interface, generating more friction, heat, and consequently, higher temperatures [5].

Various techniques are being employed to address the issue of high temperatures. One approach involves adjusting cutting parameters to optimize the process. Additionally, the use of increasingly robust tools, characterized by their thermal stability and high wear resistance, is gaining prominence [45]. Such tools include cemented carbide (coated or uncoated)[16], ceramics, cubic boron nitride (CBN), and polycrystalline diamond (PCD). However, it is worth noting that these advanced tools often come at a higher cost and are more fragile. Therefore, their usage is only when economically justified [22,30]. Another detail is that the use of these special tools demands new machinery and special fixing methods that do not generate strong vibrations, as these tools are very sensitive and break easily under these conditions [46].

The equations (1 to 6) presented in this chapter, along with the table of Energy Distribution during Machining, play a fundamental role in introducing the topic of heat and temperature in machining. While these equations are not directly applied for calculation purposes in this work, they serve a crucial role in establishing the necessary conceptual foundation to understand the importance of temperature throughout this study. Temperature is a primary variable in this field of research, and its impact will be addressed in various parts of this thesis.

### 2.1.1. Temperature measurement via infrared radiation

The infrared radiation measurement technique is based on the principle that any material surface with a temperature above absolute zero (- 273 °C) emits electromagnetic radiation in the infrared (IR) spectrum, with a wavelength ranging from 1 to 1,000 μm. This phenomenon was first observed by the English physicist William Herschel in 1,800 while measuring the temperature of a crystal's light spectrum using a mercury thermometer. Herschel noticed that the heat was more pronounced near the red-light spectrum, even though no visible light was present [47].

With significant technological advancements, infrared cameras with high-precision sensors have become widely used. This method offers several advantages: (i) it is non-intrusive, meaning it does not interfere with the machining operation; (ii) modern devices have high data acquisition rates, allowing for real-time temperature monitoring; (iii) it provides high measurement accuracy, typically within a range of approximately ± 2 °C; (iv) it enables temperature measurements in difficult-to-reach areas; (v) it is relatively easy to apply compared to other temperature measurement techniques; (vi) it provides temperature readings along the surface, offering a comprehensive view rather than just a single point measurement [48].

However, there are some limitations to consider: (i) obtaining accurate surface emissivity can be challenging; (ii) obstructions caused by chips or cutting fluids can obstruct the camera's view; (iii) proper camera positioning is crucial for accurate measurements; (iv) infrared cameras can only measure surface temperatures [49,50].

Meola & Carlomagno (2004) feature the calibration function of an infrared camera term (Eq. 7)[47]:

$$E = \varepsilon \frac{A}{(e^{B/T} - C)} \quad (7)$$

Where: *E* is the real amount of energy detected,

*ε* = emissivity coefficient of a surface;

*T* = is the temperature of the object through calibration constants *A, B, C*.

Planck's law gives the radiation intensity of a black body as a function of temperature (*T*) and wavelength (*λ*) (Eq. 8) [51]:

$$E(\lambda, T) = \frac{C_1}{\lambda^5 (e^{(C_2/\lambda T)} - 1)} \quad (8)$$

Where:  $\lambda$  = wavelength in m;

$T$  = is the temperature of the object in K;

$C_1$  and  $C_2$  = first and second constant radiation,

$C_1 = 1.191044 \times 10^{-16} \text{ Wm}^2$  and  $C_2 = 0.014388 \text{ m. K}$ .

However, a real body emissivity constitutes only a fraction of an ideal black body emissivity, considering an equal temperature and wavelengths, according to Eq. 9 [47].

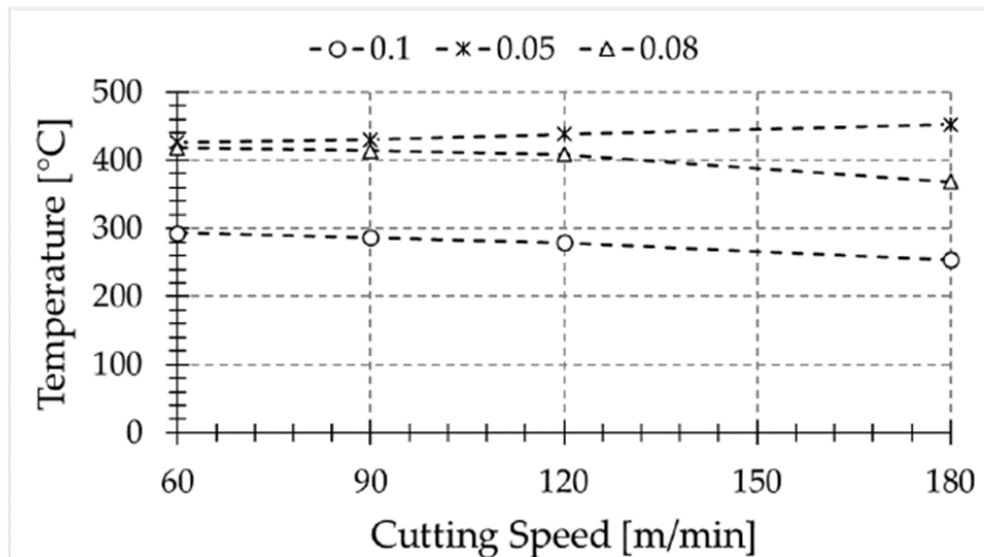
$$\varepsilon_\lambda = \frac{E_\lambda}{E_{(\lambda, T)}} \quad (9)$$

Where:  $E_\lambda$  = intensity of reading a real body;

$E_{(\lambda, T)}$  = radiation intensity of an ideal black body.

Zhao et al. (2018) used infrared radiation specially developed in a two-color pyrometer during the Inconel 718 turning [51]. They used ceramic tools reinforced with whiskers. According to the authors, this equipment eliminates the emissivity variation, increasing the accuracy of measurements. It has a range of 350 ~ 1,400 °C with a resolution of  $\pm 3$  °C. The cutting speed was varied in  $v_c = 60, 80, 100$  e  $120 \text{ m/min}$  reaching the maximum temperature for each of these speeds in  $T = 715, 750, 775, 800$  °C, respectively. Both feed and depth of cut were kept constant at  $0.085 \text{ mm/rev}$  and  $0.5 \text{ mm}$ , respectively.

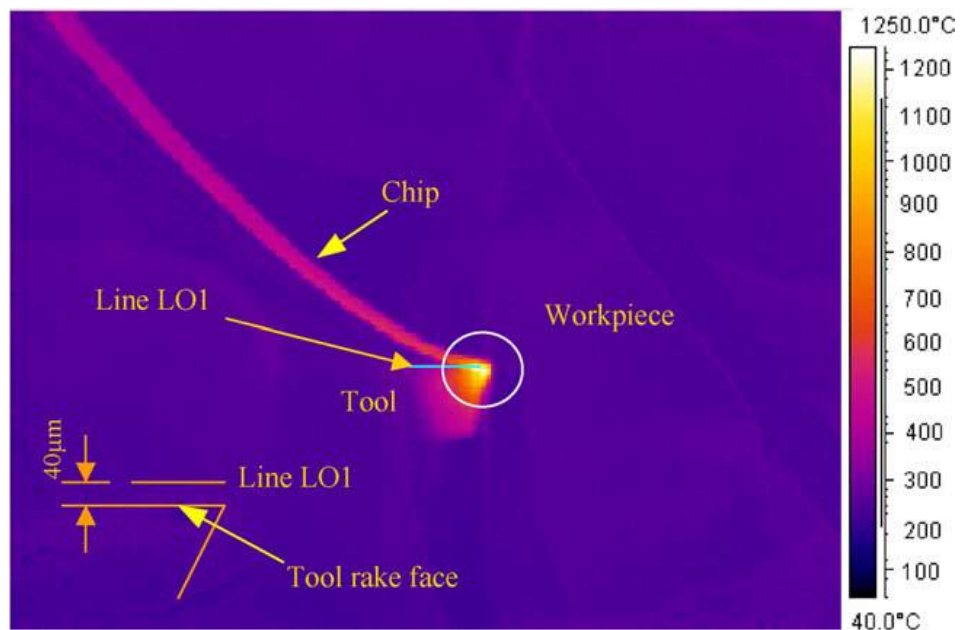
Vastly different temperatures were found by Díaz-Álvarez et al. (2017) in comparison to Zhao et al. (2018), showing that, even with modern equipment, it is still challenging to measure these variables accurately [51,52]. The authors also used the two-color pyrometer technique with optical fibre, measuring a range of 250 to 1,200 °C, turning the Inconel 718, varying the feed rate, and cutting speed ( $v_c$ ) and using uncoated carbide tools (TCMW16T308H13A). The feeds were  $f = 0.05, 0.08,$  and  $0.1 \text{ mm/rev}$ , cutting speeds have been  $v_c = 30, 60, 90, 120,$  and  $180 \text{ m/min}$  the depth of cut was kept constant at  $a_p = 2.0 \text{ mm}$ . Temperatures found, as a function of cutting speed and feed, are shown in **Figure 2-4**. However, the decrease in temperatures with an increase in cutting speed ( $v_c$ ) was not explained in the text.



**Figure 2-4:** Temperature as a function of feed and cutting speed when turning the Inconel 718.

Source: [52]

Abukhshim et al. (2006) performed several tests to measure the turning temperature of AISI 4140 steel using a high-speed machine,  $v_c = 750$  m/min,  $f = 0.15$  mm/rev and  $a_p = 0.1$  mm [36]. The IRT was used, and they could verify temperatures higher than 1,200 °C where the insert meets the workpiece, as shown in **Figure 2-5**.

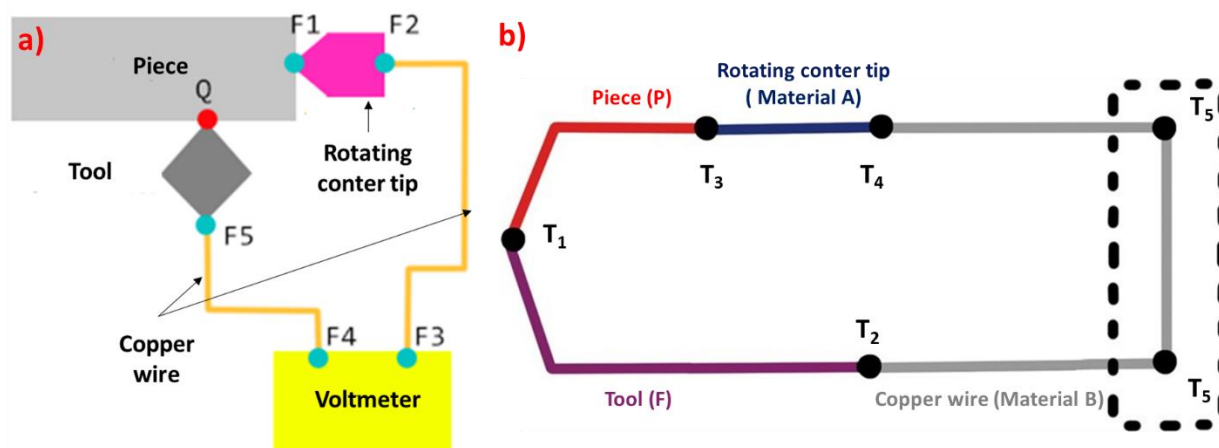


**Figure 2-5:** Infrared photograph of the cutting process ( $v_c = 750$  m/min)

Source: [36]

## 2.1.2. Temperature measurement via thermo-couple tool-work

The tool-workpiece thermocouple method utilizes a thermoelectric circuit consisting of multiple junctions formed by various elements, including the one created by the tool insert and the workpiece. **Figure 2-6** illustrates the basic configuration of a thermocouple tool-workpiece system [53].



**Figure 2-6:** (a) Representative schematic of tool-work thermocouple using a rotating tailstock; (b) Thermoelectric tool-thermocouple system using a rotating tailstock.

Source: [53]

The contact point between the tool and workpiece Q is the hot joint (in red), which reproduces the temperature generated during the machining operation, while F1, F2, F3, F4, and F5 represent the cold joints (in blue). In this configuration, a rotating tailstock transfers the electrical signal through mercury located internally to this component.

By interconnecting the electrical wires emerging from joints F5 (tool connection) and F2 (connection to the rotating dead center of the tailstock) at joints F3 and F4, it becomes feasible to measure the electrical signal of the system and determine the average temperatures at the chip-tool interface.

This method was described in publications such as França et al. (2022) and Klocke (2011) [6,37]. Referring to **Figure 2-6 (b)** and considering the clockwise direction, the electrical circuit of the tool-workpiece thermocouple system can be represented by Eq. (10):

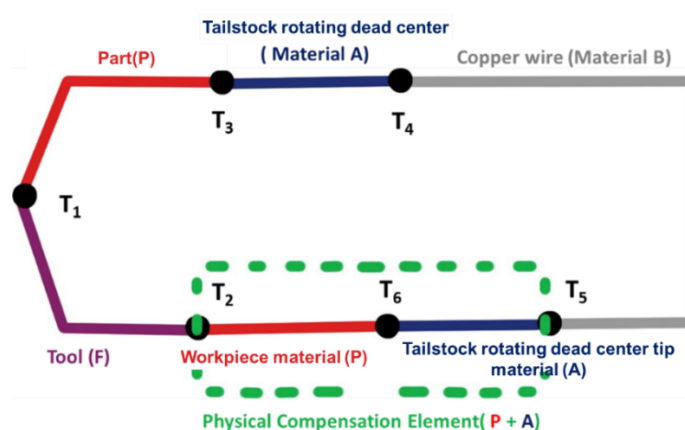
$$\Delta E = E_{FP} \cdot T_1 + E_{PA} \cdot T_3 + E_{AB} \cdot T_4 + E_{B.F.} \cdot T_2 \quad (10)$$



Each portion of the sum of this equation represents the electromotive force (e.m.f.) formed at each junction of their respective pairs, where this e.m.f. is a function of the temperature. The term  $E_{F,P}$  indicates the e.m.f. that is generated between the insert and the workpiece subjected to a temperature  $T_1$ .  $E_{PA}$  represents the e.m.f. generated between the workpiece and material A at the temperature  $T_3$ .  $E_{AB}$  the e.m.f. that relates the joint between the metal A and the copper wire B for the temperature  $T_4$  and finally, the last term of the equation  $E_{B,F}$  indicates the e.m.f. formed by the connection of the copper wire and the tool at the temperature  $T_2$ .

Analyzing equation (10) to find the temperature of interest of the hot joint  $T_1$ , it is necessary to know the e.m.f. that act on the other joints of the system [53]. Because different materials form them and generally have relative temperatures, secondary junctions generate e.m.f. that significantly influence the e.m.f. of the system.

To eliminate unwanted noises, the tool-workpiece thermocouple system with a physical compensation was proposed by Kaminise et al. (2014), which minimizes the effect of the e.m.f. of the cold joints [54]. The various cold joints generate this by adding a component formed by the two materials in the system that compose the standard measurement system: dead center material A and workpiece material P. It also allows calibration on the test bench, which on the other hand, in most cases, is carried out externally and may not adequately represent the system more realistically. **Figure 2-7** illustrates this circuit with the addition of the physical compensation.



**Figure 2-7:** Schematic representation of the tool-work thermocouple system with a physical compensation element.

Source: [53]

Analyzing the standard circuit with the addition of physical compensation (Eq. 11) is obtained:

$$\Delta E = E_{FP} \cdot T_1 + E_{PA} \cdot T_3 + E_{AB} \cdot T_4 - E_{AB} \cdot T_5 - E_{PA} \cdot T_6 - E_{F.P.} \cdot T_2 \quad (11)$$

When considering that the cold joints distant from the cutting zone do not consider temperature variations throughout the tests, the temperature relations will be  $T_3 = T_4 = T_5 = T_6$  (Eqs. 12 to 14):

$$E_{PA} \cdot T_3 = E_{PA} \cdot T_6 \text{ and } E_{AB} \cdot T_4 = E_{AB} \cdot T_5 \quad (12)$$

Thereby,

$$\Delta E = E_{FP} \cdot T_1 - E_{FP} \cdot T_2 = K (T_1 - T_2) \quad (13)$$

Finally, isolating  $T_1$  the final Eq. 14 will be given by:

$$T_1 = T_2 + \frac{\Delta E}{K} \quad (14)$$

Note that, by equation (14), it is possible to obtain the cutting temperatures by the voltage  $\Delta E$  measured by a voltmeter, where  $T_1$  is the average temperature obtained at the chip-tool interface,  $T_2$  is the joint temperature formed by the contact of the element compensation in the tool, and  $K$  is the Seebeck constant obtained in the system calibration [54]. The temperatures obtained in  $T_2$  can vary throughout the cutting process, mainly in the inserting processes [53]. Therefore, it is necessary to measure  $T_2$  in the calibration and execution of the tests and during the development of the final curve.

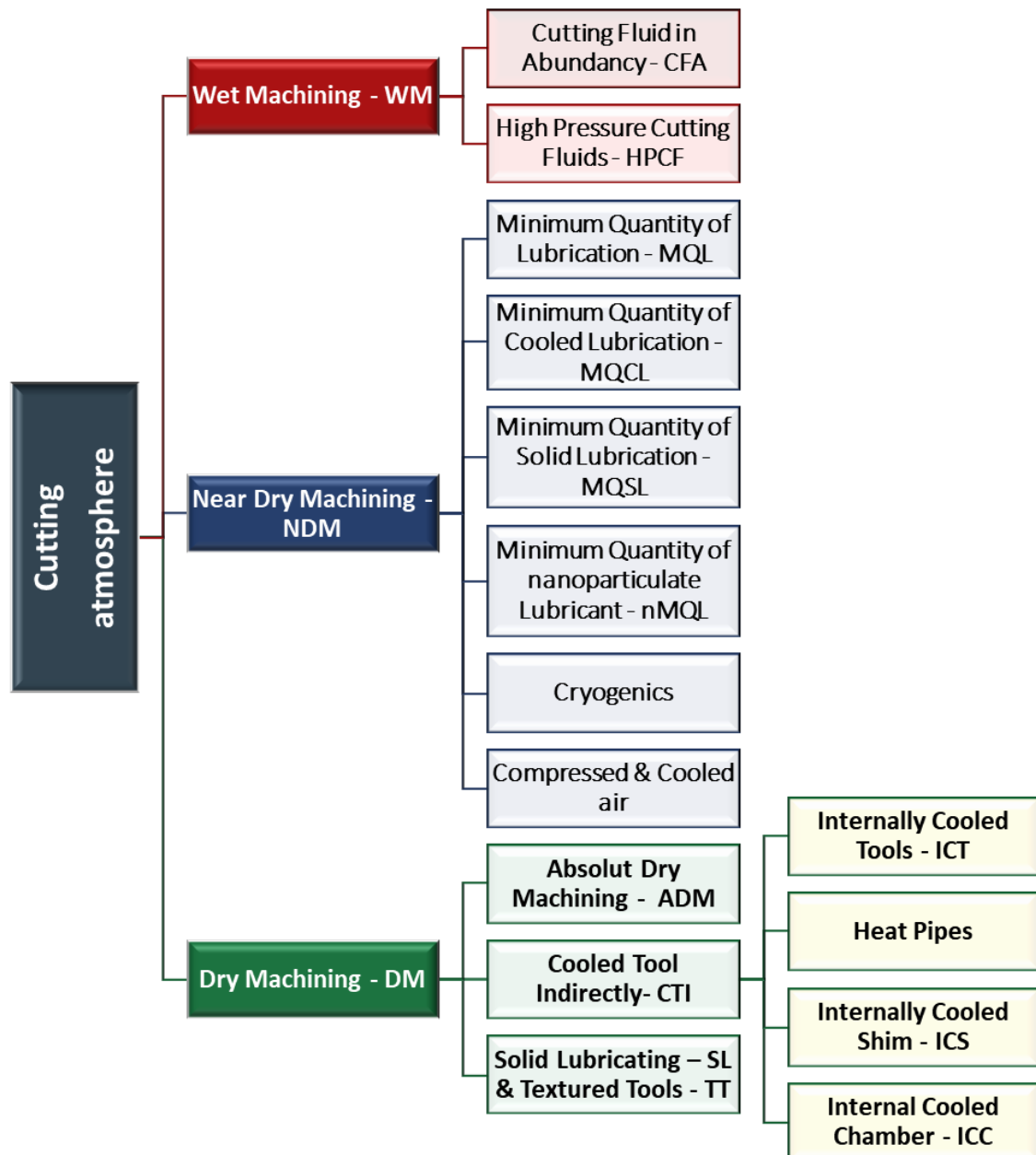
## 2.2. Machining Cooling Techniques

Researchers have studied thermal behavior during machining for over a century. In 1883, Frederick W. Taylor conducted studies to reduce the heat generated. He devised a system to supply a continuous plentiful flow of water saturated with soda and observed that it led to a significant increase in cutting speed, approximately 40% [55]. This groundbreaking work marked the inception of cutting fluids (CFs). Since then, extensive research and development efforts have been dedicated to achieving temperature control in machining processes [10,56,57].

Besides CFs, alternative strategies and lubrication-cooling methods have been studied and successfully applied [7]. Among them, there are minimum quantity of lubricants - MQL, minimum quantity of cooled lubricant - MQCL, high-pressure cutting fluid - HPCF, cryogenic fluids (nitrogen liquid), solid lubricants, nanoparticles, texturization, high-pressure and refrigerated compressed air, among others [10].

Several studies have employed hybrid lubrication-cooling techniques. For instance, Yildırım (2019) utilized sixteen different lubrication environments while turning Inconel 625, incorporating hBN and Al<sub>2</sub>O<sub>3</sub> nanoparticles [59]. Other researchers have also explored the inclusion of nanoparticles or solid particles in the lubricating oil used in minimum quantity lubrication (MQL) applications [60–62]. Another approach involves cooling the MQL air before blending it with atomized oil particles, a technique called the minimum quantity of cooled lubrication (MQCL).

Fernandes & Barbosa (2022) classified many lubri-cooling conditions in machining into three main groups: **wet machining (WM)**, which is the traditional method and its variations; **near dry machining (NDM)**, which utilizes fluids (liquids or gases) in minimal amounts; and **dry machining (DM)**, which can be performed without any coolant, with the use of solid lubricants, or through indirect cooling techniques like internally cooled tools. **Figure 2-8** provides a visual representation of this division of lubri-cooling methods.



**Figure 2-8:** Classification of the machining environments according to the possible forms of lubrication and cooling

Source: [7]

In pursuing more sustainable processes, dry machining is considered an ideal approach. However, this practice can encounter technical challenges that necessitate using coolant, especially regarding temperature. As a result, despite ongoing efforts to explore more environmentally friendly machining methods, the prevailing lubri-cooling condition is still the application of cutting fluids in abundance (CFA). Further information about this technique will be described in the following sections.

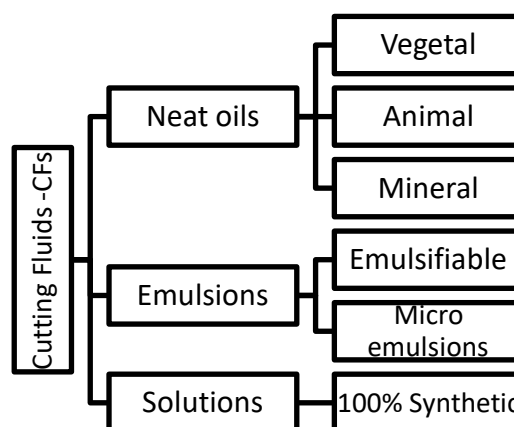
## 2.2.1. Wet Machining

In the upcoming subchapter, an extensive exploration of cutting fluids will be conducted. The initial focus will be on the traditional approach known as Cutting Fluid in Abundance (CFA). This comprehensive analysis will provide profound insights into historical practices and their wide-ranging implications within the field of machining processes. It will encompass various aspects, including types of cutting fluids, market dynamics, the role of additives, advantages and disadvantages, and sustainability considerations, among other pertinent factors.

### 2.2.1.1. Cutting Fluid in Abundance - CFA

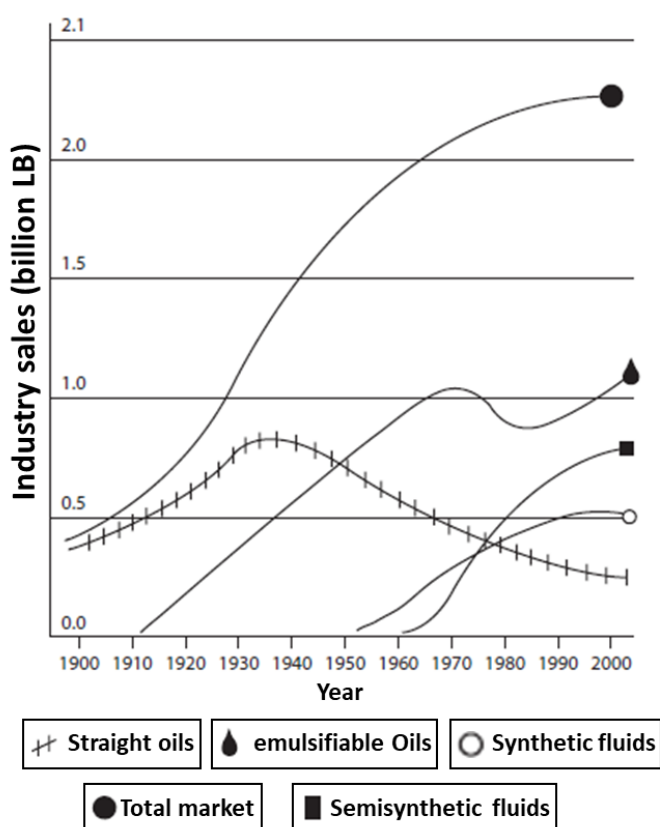
Metal working fluids (MWF) are liquid or gaseous chemical elements used in metal processing for material removal or forming. Cutting fluids serve various functions, including lubrication, cooling, anti-oxidation, and chip removal. An adequate cutting fluid alters the tribological system at the tool/chip interface, reducing friction and temperature and thereby facilitating cutting and preserving the integrity of both the part and the tool. Additionally, these fluids help to protect the machinery by preventing oxidation and the accumulation of debris between moving parts [4].

Cutting fluids can be categorized into three main groups: neat oils, emulsions (emulsifiable or semi-synthetic), and solutions (synthetic). **Figure 2-9** provides detailed information about this classification [4].



**Figure 2-9:** General classification of cutting fluids

The most widely used CFs are emulsifiable fluids, also known as macro emulsions. These fluids are a heterogeneous mixture of water and oil, with particle sizes ranging from 2 to 5  $\mu\text{m}$  in diameter. The next category is semisynthetic fluids, also known as micro emulsions, which serve as an intermediate type between emulsifiable fluids and solutions. Typically, they contain less than 50% of neat oil and have particles ranging from 0.1 to 1  $\mu\text{m}$  in diameter. The third category comprises 100% synthetic fluids, forming a translucent water-based solution. Lastly, 100% neat oils can be derived from animal, vegetable, or mineral sources, but their usage has decreased over time [55]. **Figure 2-10** depicts the market share of each CF type throughout the 20<sup>th</sup> century.



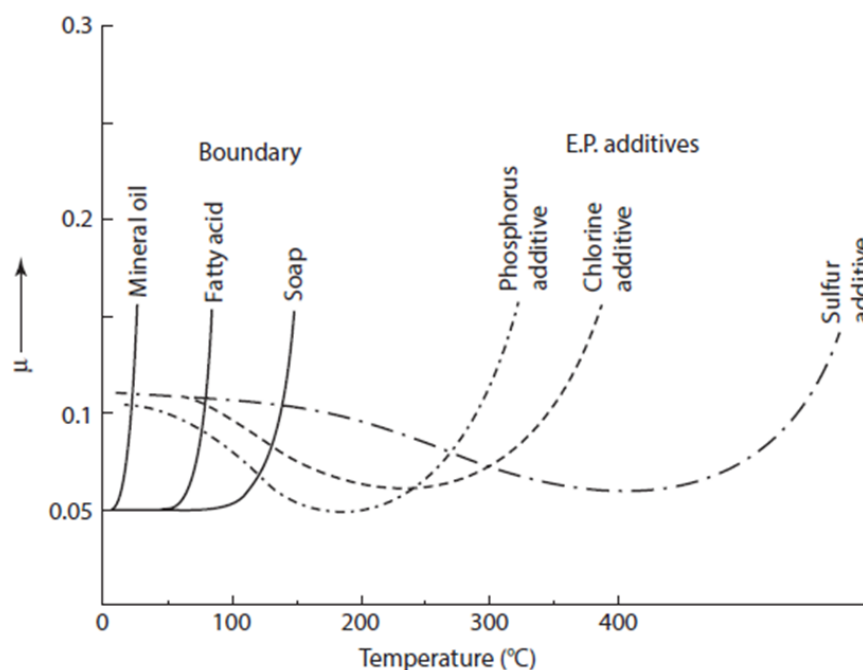
**Figure 2-10:** Evolution of *Metal Working Fluids Consumption - MWF* (including FCs) globally

Source: [55]

Cutting fluids are manufactured using different primary inputs, depending on their type and functional additives. A cutting fluid can consist of over ten additives, regardless of whether it is. Each additive has a specific role in the formulation, contributing to the

product's overall performance. Byers (2016) explains the various types of additives and their respective functions [55]:

- **Lubricants:** can be of two distinct types, boundary or extreme-pressure - EP. They are incorporated to enhance the lubricating performance of the fluid, as mineral oil and water alone do not possess this property. These additives undergo chemical activation based on the operating temperature (**Figure 2-11**); It is worth noting that due to environmental concerns, chlorine-based additives are becoming less common as they contribute to the greenhouse effect.



**Figure 2-11:** Relationship between metal temperature and friction coefficient for various contour and EP lubricating additives

Source: [55,192]

- **Corrosion inhibitors:** The corrosive action of free hydrogen ions in water ( $H^+$ ) tends to corrode metals, so additives that inhibit this action are necessary. They form a protective film on the surface of the metal.
- **Metal deactivators:** Non-ferrous materials are prone to staining when they meet certain elements, such as sulfur. Additives with hydrophilic and polar structures are used to address this issue, forming a protective layer on the metal surface. It is important to note that aluminum alloys can compromise their protective oxide

layer when exposed to alkaline solutions with a pH above 9.0.

- **Alkaline Reserve:** works with corrosion inhibitors to maintain the fluid's alkalinity and prevent acid contamination. They play a crucial role in ensuring the fluid remains in an optimal condition with its primary and functional characteristics. A cutting fluid with a low alkaline reserve is vulnerable to fungal and bacterial contamination. The pH level of the fluid is typically an excellent indicator of its quality, with an ideal pH of around 9 for most types of cutting fluids, particularly synthetic and semisynthetic ones. When the pH level decreases, the alkaline reserve is increased to correct the imbalance.
- **Emulsifiers (surfactants):** are compounds responsible for dispersing oil droplets in water, resulting in the formation of an emulsion (macroemulsion) or a semisynthetic mixture (microemulsion). They contain a long hydrocarbon chain (lipophilic) interacting with the oil phase and a polar structure (hydrophilic) interacting with the water phase. To assess the emulsifier's affinity for water, the hydrophilic-lipophilic balance (HLB) system was developed by William C. Griffin in 1951. This system assigns a value on a scale from 1 to 20, with 20 indicating complete solubility and 1 indicating poor dispersibility in water. The HLB value allows evaluation of the emulsifier's quality and effectiveness in forming stable emulsions.
- **Coupler agents:** work with emulsifiers to stabilize the emulsion and prolong its shelf life. They play a crucial role in maintaining the stability and homogeneity of the emulsion over time, preventing phase separation and degradation. By enhancing the interaction between the oil and water phases, coupling agents contribute to the overall stability and longevity of the emulsion.
- **Antifoams:** as the name suggests, they function by inhibiting the formation of foams. Foams are created when the air becomes trapped within the cutting fluid, typically due to their interaction. Foam generation can be particularly troublesome in high-speed cutting operations or when using high-pressure cutting fluids, as these processes tend to introduce more air into the system. Antifoaming agents are typically not utilized in whole oils due to their viscosity.



- **Anti-fog:** is responsible for inhibiting fog formation during the machining process. These agents consist of long and heavy molecular chain polymers that increase the fluid's viscosity, enabling it to withstand the stresses it encounters better. They are vital in formulating fluids designed explicitly for minimum-quantity lubrication applications.
- **Antioxidants:** are additives that serve as inhibitors for oxidative processes, particularly in fluids exposed to high temperatures and working pressures. These additives are commonly employed in neat oils and play a crucial role in protecting the entire assembly of the machine, workpiece, and tool from the harmful effects of oxidation. By preventing or reducing oxidation, antioxidants help maintain the stability and integrity of the cutting fluid, ensuring optimal performance and prolonging the lifespan of the machining equipment.
- **Dyes:** are utilized to provide a uniform coloration to the fluid, which aids in distinguishing one product from another. Additionally, they enhance the visual appeal of the fluid, making it more aesthetically pleasing.
- **Wetting:** is employed to lower the surface tension of cutting fluids and enhance their ability to wet metals. They contribute in two ways: first, by assisting in the formation of a protective film on the metal surface, and second, by aiding in the removal of chips from the machining process. Wetting agents help to ensure proper coverage and contact between the cutting fluid and the metal, promoting efficient lubrication and chip flushing.
- **Biocidal:** in cutting fluids consist of two types: antibacterial and fungicidal agents. Water-based cutting fluids are susceptible to various types of contamination, resulting in the growth of microorganisms that decompose the fluid and create unpleasant odors, thereby compromising the work environment. Biocides are incorporated into the cutting fluids to prevent such issues, inhibiting the growth and proliferation of microorganisms and ensuring the fluid remains stable and free from degradation.

It is important to note that using chlorine in lubricating additives at high temperatures should be cautiously approached. Chlorine tends to decompose, forming

dioxins and highly flammable substances, which can lead to uncontrollable burning. Furthermore, these compounds pose risks to human health and the environment. Consequently, chlorine-containing cutting fluids can only be disposed of in specialized incinerators, significantly increasing the overall cost [63,64]. Additionally, these compounds are not recommended for machining certain materials like titanium alloys due to their corrosive properties [65]. As a result, the use of chlorine-containing cutting fluids is becoming increasingly restricted in several countries.

Regarding neat oils, Gajrani & Sankar (2020) explain that they primarily consist of oils, and Klocke (2011) states that approximately 90% are mineral-based [37,66]. Neat oils also incorporate other additives to enhance their chemical stability, lubrication properties, wear protection, oxidation resistance, durability, and foaming characteristics. These oils are typically utilized in low-speed but high-severity machining operations, such as gear milling [8].

There is a significant trend toward substituting mineral-based oils with vegetable-based oils. This shift is driven by several advantages of vegetable-based oils, including a low evaporation temperature, high flash point, biodegradability, and reduced harm to operator health [14,67]. Additionally, vegetable-based oils have lower viscosity, allowing for improved tool/chip interface penetration and enhancing lubrication performance. However, it is essential to note that vegetable-based oils are generally more expensive than their mineral-based counterparts. Nevertheless, increasing demand for sustainable alternatives and stricter regulations governing manufacturers' responsibilities, from production to disposal, have made these oils more competitive.

Water-based cutting fluids are typically formulated as emulsions or solutions. Emulsions consist of a mixture of water and oils, usually of mineral or vegetable origin, with a ratio ranging from 1:99 to 1:10. These emulsions are biphasic compounds, and like neat oils, they incorporate additives based on the specific functions required for the cutting fluid. Due to their water content, paying particular attention to the pH level is crucial, which should ideally be maintained between 8 and 9 to prevent corrosive effects. Emulsions rely on essential additives called emulsifiers or surfactants, which are polar agents responsible for dispersing the oil into fine droplets throughout the water phase [4,37].

Emulsions are particularly vulnerable to contamination by microorganisms, including bacteria and fungi. This contamination can decrease pH, adversely affecting the mixture's lubrication, cooling, and anti-oxidation properties. Moreover, it promotes fluid instability, resulting in the formation of sludge deposits that can potentially clog the pumping system. Contamination also gives rise to unpleasant odors in the workplace. Biocides at a concentration of approximately 0.15% are recommended to mitigate these issues. Semisynthetic fluids, classified as microemulsions, are composed of chemicals with oil content ranging from 5% to 50% (mineral or vegetable oil) miscible in water. These fluids incorporate significant amounts of emulsifier additives [55].

Lastly, solutions are considered homogeneous single-phase mixtures. Since they are already diluted in water, there is no need for the use of emulsifiers. Solutions are translucent, which allows for better visualization during cutting processes. They do not contain added oils, making them less toxic to the environment and operators' health. However, they incorporate various additives such as organic and inorganic minerals, antioxidants, lubricants, biocides, etc. Solutions are particularly suitable for high-speed cutting operations due to their excellent coolant properties, especially when generating significant heat. Nevertheless, the cost of these fluids remains a restricting factor [68].

Numerous studies have highlighted the technical advantages of cutting fluids (CFs), as many machining operations rely heavily on their use. In a study conducted by Vieira et al. (2001), various CF types, including mineral emulsion, semi-synthetic, and synthetic fluids, were investigated during the face milling of AISI 8640 steel using a coated carbide tool [69]. The researchers measured tool life, energy consumption, surface roughness, and temperature to assess the cooling effectiveness of the CFs. Comparatively, dry conditions exhibited the highest temperatures, followed by synthetic fluid, mineral emulsion, and semisynthetic CF.

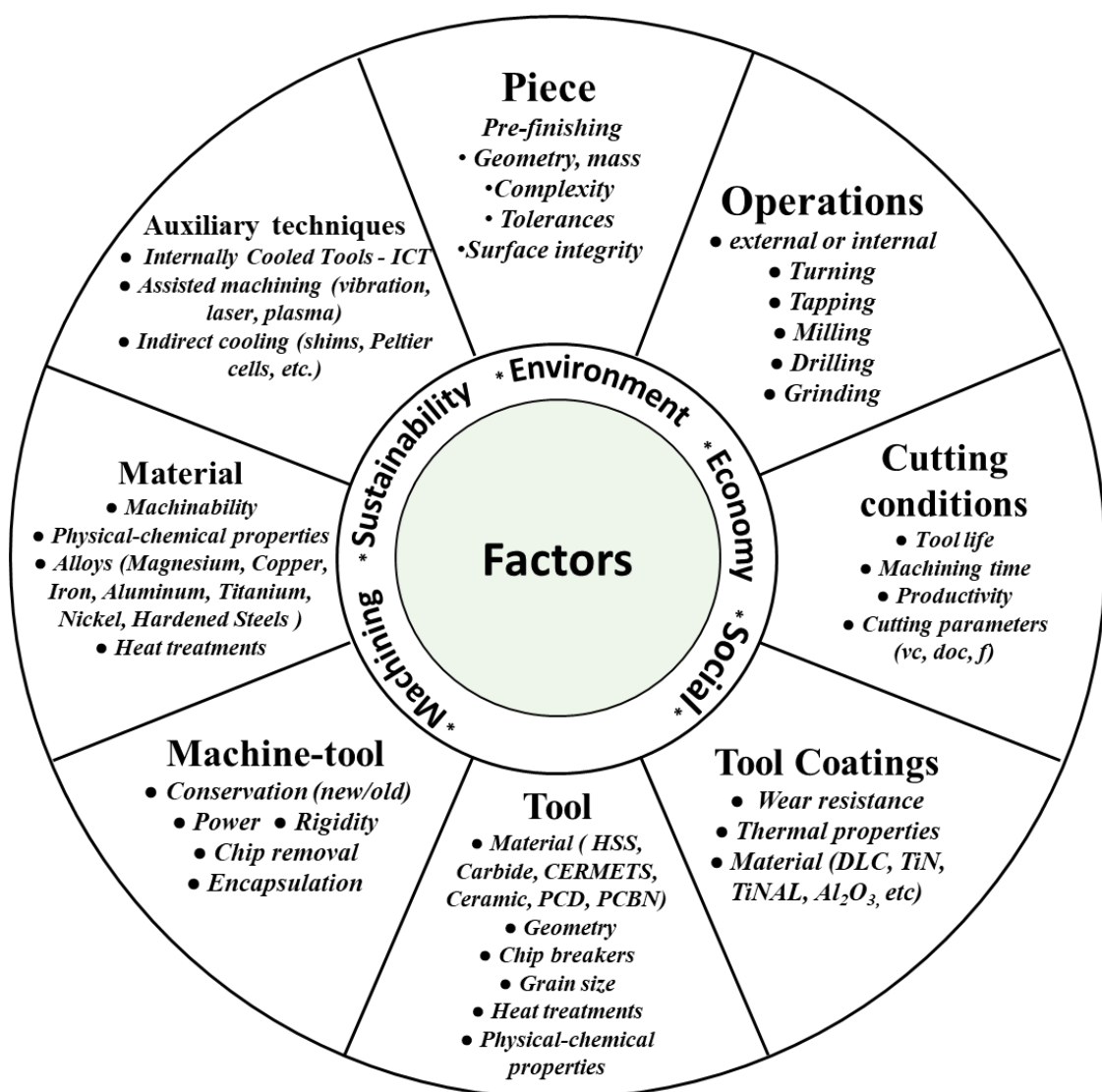
In a study conducted by Iturbe et al. (2016), the machining of Inconel 718 in a finishing turning operation was carried out to compare the performance of two different lubri-cooling techniques: minimum quantity lubrication with cryogenics and cutting fluids in abundance [70]. The researchers analyzed tool wear and the surface integrity of the workpiece, explicitly focusing on roughness and microhardness. The findings

indicated that using CFA improved tool life and roughness during continuous machining in comparison to MQL with cryogenics.

While cutting fluids offer various advantages, they pose significant challenges within the production chain, primarily regarding costs, environmental impact, and human health. Numerous research studies have been conducted to minimize or eliminate their usage. These investigations have successfully demonstrated the technical benefits of alternative techniques. However, the cost factor remains a significant limitation in many situations [2,9].

## 2.2.2. Dry Machining - DM

Like any other machining process, dry machining is influenced by various factors such as the work material, machine tool assembly, cutting parameters, type of operation, and the tools used, whether they are coated or not. **Figure 2-12** provides a schematic representation of these factors in detail. Choosing the appropriate combination of these variables is not simple and requires extensive prior experience. Additionally, it is essential to note that optimal selection may not be universally applicable but rather varies on a case-by-case basis.



**Figure 2-12:** Influencing factors in choosing a machining process.

Source: [172]

However, when the variables are chosen correctly, dry machining can be effectively applied to various materials and operations, including challenging materials such as titanium or nickel superalloys. This has been demonstrated in studies by Minton et al. (2013) and Zhang et al. (2012) [12,71].

Dry machining is more commonly employed when dealing with metal alloys that exhibit higher machinability, as it allows for efficient machining operations. Grey cast irons, which contain graphite in their composition, are often machined dry due to the self-lubricating action of the graphite [72]. Free-machining steels containing added inclusions, such as Pb, Bi, Te, Se, Sn, etc., act as lubricants at the chip-tool interface, reducing heat generation and cutting forces [73]. These alloys are typically well-suited for dry machining.

Easy-cutting materials like magnesium, aluminum, and copper alloys are also prime examples where dry machining is recommended. These materials possess low melting points, exhibit low shear resistance and hardness, and often produce short chips [74,75]. However, it is essential to note that certain materials warrant caution when considering dry machining. Ductile materials such as pure aluminum, copper, and low-carbon steels tend to adhere intensely to the cutting tool, making dry machining less suitable, especially in drilling processes [76].

Finally, titanium and nickel-based superalloys are virtually unviable materials machined industrially dry, with rare exceptions. For example, titanium alloys widely used as biomaterials can be machined dry to avoid contamination. These alloys are poor heat conductors, maintain their mechanical properties even at high temperatures, suffer excessive work hardening, have high hardness, chemical affinity, etc. [77–79]. All these make it exceedingly difficult to use DM when cutting them with cemented carbide tools, but there are studies in this sense in which the cutting factors were carefully selected to enable dry machining. The nickel-based superalloys can be machined with ceramic tools, and in this case, the recommendation is DM because of the poor thermal shock resistance of these tool materials.

Devillez et al. (2011) evaluated the surface integrity (microhardness and microstructure) of the Inconel 718 after turning with triple coated carbide tool (TiCN, Al<sub>2</sub>O<sub>3</sub>, TiN – CVD) under CFA and DM cutting conditions for several different cutting

speeds to determine the ideal for dry cutting [80]. The authors found that the optimum cutting parameters were  $v_c = 60$  m/min,  $a_p = 0.5$  mm, and  $f = 0.1$  mm/rev. They also concluded that regarding microhardness, microstructure, and residual stresses analyses dry machining presented results equivalent to CFA.

Ginting & Nouari (2009) studied the surface integrity (roughness and microhardness) of titanium alloy (Ti-6242S) in milling operation with coated (WC-Ti-Ta/Nb-C), (TiN/TiC/TiCN - CVD) and uncoated tools [81]. The results indicated that DM could be used for titanium with an uncoated carbide tool and limited to finishing and semi-finishing operations.

### 2.2.3. Tools Indirectly Cooled – TIC

The cutting fluid helps to protect the tool by lowering the average system temperature. However, it also acts on the workpiece and chip. The temperature elevation experienced by the workpiece and chip during machining is advantageous since it diminishes the material's mechanical strength. This temperature increase facilitates cutting by reducing the required force and power. Hence, an ideal cooling system should focus exclusively on cooling the tool, effectively lowering its temperature [7].

The idea of indirectly cooling the cutting tool during the machining process probably began in 1964 when Meyers (1964) obtained a patent for a thermoelectric system. In 1970, Jeffries & Zerkle (1970) proposed a mathematical thermal analysis of a tool indirectly cooled – TIC for orthogonal cutting considering new and worn ones [82,83]. Since then, many other attempts have been made to this meaning.

Studies conducted on tool indirectly cooled systems have demonstrated encouraging results so far [53,84–87]. However, it is essential to note that most of these studies have been conducted in a dry-cutting atmosphere, which deviates from the industrial reality where cutting fluid in abundance is commonly employed. Further studies are necessary to validate TIC's effectiveness in different machining scenarios. Yet in the literature there is no specific study on how coatings can help reduce the temperature in the ICT, for instance. In the following discussion, some of the prominent research efforts in the field of TIC will be explored.



### 2.2.3.1. Internally Cooled Shim – ICS

Among the various approaches developed for tool indirectly cooled (TIC) systems, indirect cooling through the shim is one commonly explored technique. This method has garnered significant attention due to its practicality, as cooling the shim is relatively easier than cooling the tool.

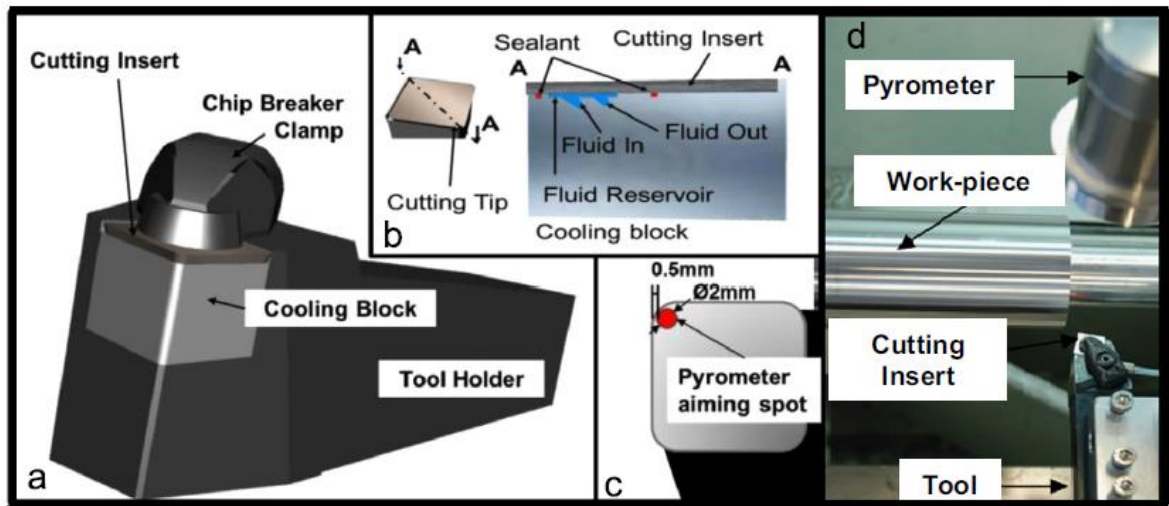
In 1964, Meyers patented a cooling system that utilized the concept of thermoelectricity [82]. This concept involves certain materials that exhibit a temperature difference when subjected to an electrical potential differential, with one terminal heating up while the other cools down. Meyers' idea was to apply this principle by placing the cold junction in contact with the cutting tool, thereby conducting heat away from the machining process. According to Meyers (1964), one advantage of this system was that cooling would occur only at critical points, thus minimizing energy waste and eliminating the need for cutting fluids in the process.

In 1970, Jeffries and Zerkle expanded on indirect cooling by introducing heat exchange surfaces within the tool shim, utilizing a phase-changing fluid [83]. They suggested that this method could offer a high heat removal capacity by harnessing the latent heat of vaporization. The authors conducted a thermal and mathematical analysis, considering dry environments and their proposed system. They examined the temperature distribution on the chip and the tool during orthogonal cutting, considering the scenarios of both new and worn tools.

Zerkle (1971) stated that the proposed system could achieve a heat reduction ranging from 1,000 to 20,000 Btu/hour.ft<sup>2</sup>. °F [88]. In contrast, the conventional cutting fluid typically has a heat removal capacity of 10 to 1,000 Btu/hour.ft<sup>2</sup>. °F. Zerkle further mentioned that this system could potentially lower the temperature by approximately 204 °C, whereas the temperature reduction with conventional cutting fluid is around 93 °C.

In a study conducted by Minton et al. (2013), a similar approach was employed, but instead of utilizing the cutting tool shim, they employed a cooling chamber (block) [89]. They implemented a closed-circuit system using nonethylene glycol at room temperature (~26 °C). The machining experiments were conducted on Titanium, specifically class 2,

using carbide inserts coated with polycrystalline diamond (PCD) through chemical vapor deposition (CVD). **Figure 2-13** provides further details.



**Figure 2-13:** System proposed by Minton et al. (2013). (a) Internally cooled tool carrier, (b) Cooling block cut- A-A sight, (c) Pyrometer position, (d) Assembly of machine tool-part

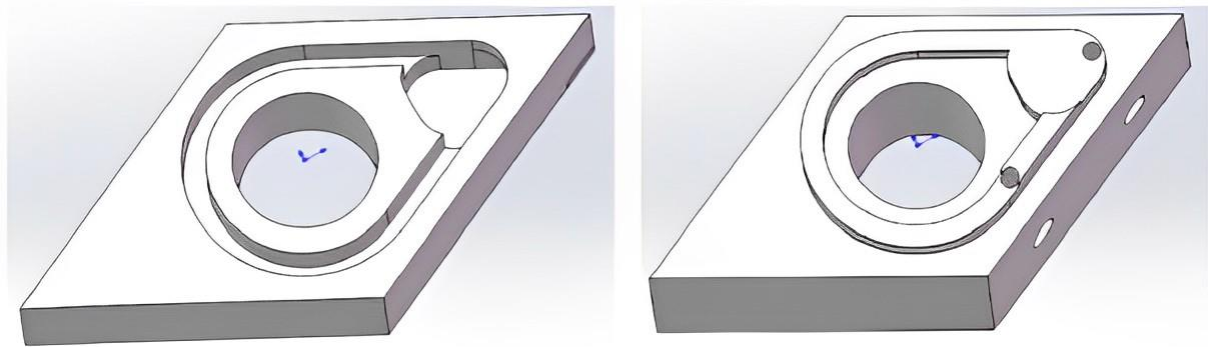
Source: [71]

The authors observed that the internal cooling system within the tool carrier demonstrated efficient performance. They noted that the PCD coating effectively dissipated heat from the surface, which was then removed through internal cooling. The refrigeration system employed in their experiment resulted in improved tool life and lower temperatures. The researchers achieved successful heat extraction from the tools, thereby preventing the activation of thermal oxidation between titanium and PCD. However, they acknowledged the need for further studies, mainly focusing on the superficial integrity of the machined surfaces.

Another study proposed by Li et al. (2017) conducted a three-step simulation study to determine the optimal geometry for the refrigerated tool indirectly [90]. Firstly, they performed a topological optimization for both the shim and the tool. The concept involved incorporating fluid flow inside the shim with relief to enhance the heat exchange area. In **Figure 2-14 (left)** there is the optimized design of the tool, and on the right the shim, both with protrusions that enhance the heat transfer.

In the second stage, thermal and mechanical simulations were carried out to assess the effectiveness of the internal cooling channels. Finally, computational analysis of the

structure and fluid was conducted at various speeds to check the thermal behavior.



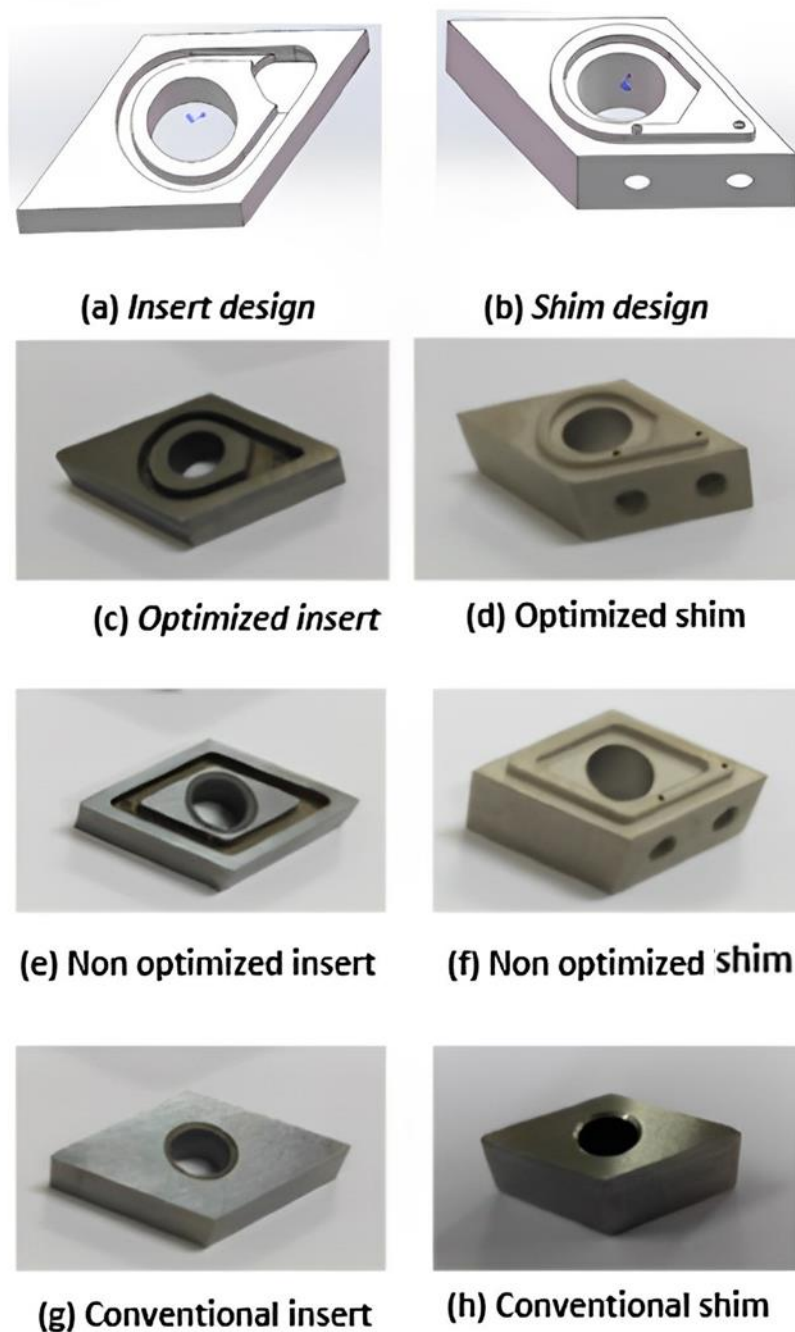
**Figure 2-14:** Tool (left) and shim (right) with relief optimized to improve thermal efficiency.

Source: [90]

In the simulations conducted by Li, three different designs were tested. A structural and mechanical analysis was performed using ANSYS software, with the AISI 1045 steel selected as the material for evaluation. The depth of the internal channels was adjusted to maintain the same material removal rate across the proposed designs. The results of the mechanical simulations revealed that the optimized tool exhibited 7.6% higher stresses than conventional tools, while the non-optimized tool demonstrated a higher stress level of 16.3%. Additionally, deformation was found to be lower for the optimized tool at 6.5%, while the non-optimized tool showed a higher deformation rate of 9.3%.

Li et al. (2017) concluded that the indirectly refrigerated tool with optimized relief exhibited superior temperature results [91]. They observed a temperature decrease of approximately 180 °C compared to a conventional tool and around 6 °C less than an indirectly refrigerated tool without topographic optimization.

Following their numerical investigations into the optimal topologies of shims and tools, Li et al. (2018) proceeded with experimental work centered around the studied system [92]. The authors conducted a performance evaluation of indirectly refrigerated tools, comparing the results between optimized and non-optimized relief designs during the turning process of AISI 1045 steel. The study focused on analyzing the heat transfer capacity and tool wear. **Figure 2-15** in the reference illustrates the designs of the tools employed in the experiments.

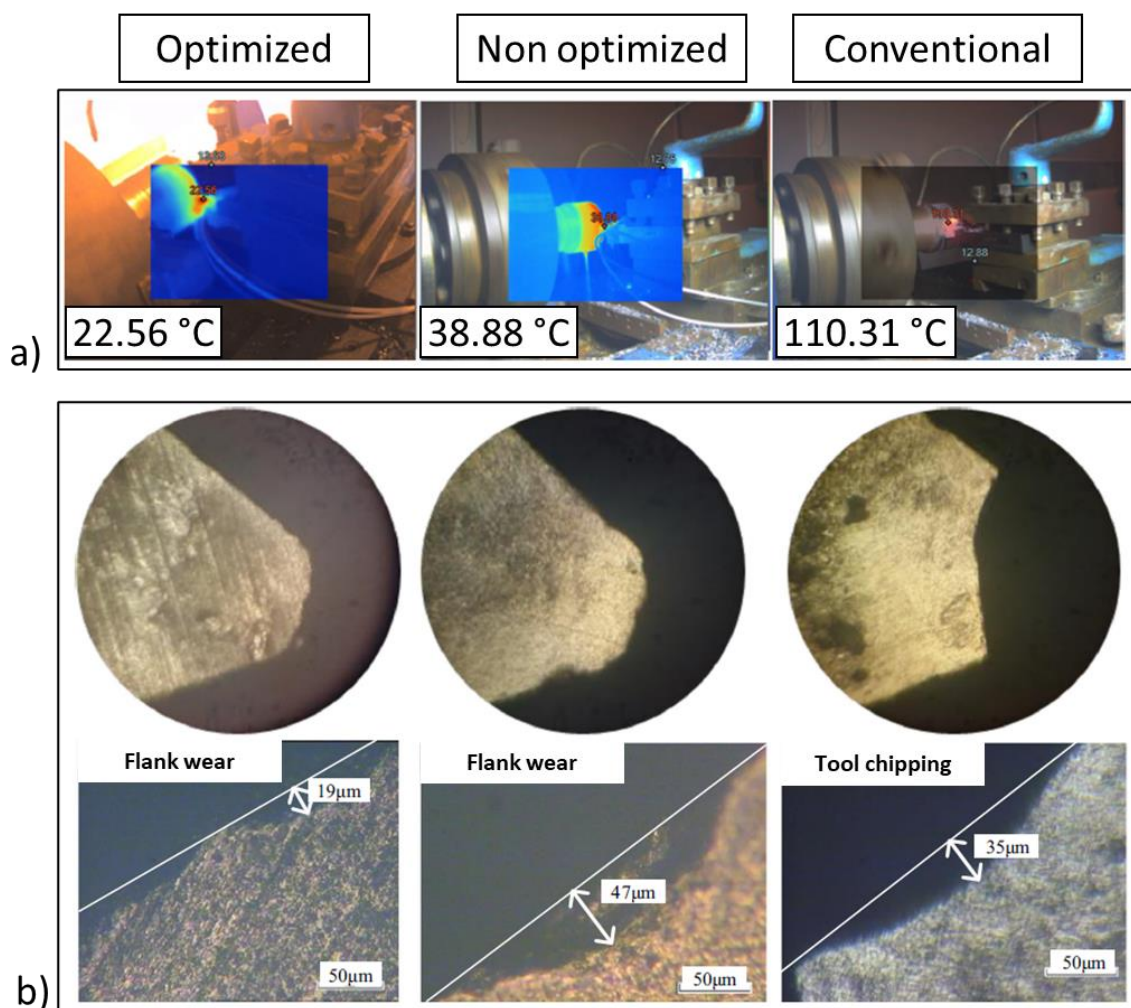


**Figure 2-15:** Shim and refrigerated inserts indirectly. (a, b) computational design. (c, d) optimized. (e, f) not optimized. (g, h) conventional.

Source: [92]

In the experimental study, the main parameters used included a cutting speed of 100 m/min, a feed of 0.16 mm/rev, and a depth of cut ( $a_p$ ) of 1.0 mm. The water flow rate was set at 1 mm/s with a temperature of 11°C. The key findings regarding temperature showed that the optimized tool exhibited a temperature of 22°C, the non-optimized tool

had a temperature of 56°C, and the conventional tool recorded a temperature of 110 °C, measured at the flank face. Regarding flank wear, the results indicated values of 19  $\mu\text{m}$ , 47  $\mu\text{m}$ , and 35  $\mu\text{m}$  for the optimized, non-optimized, and conventional tools, respectively. **Figure 2-16** in the reference showcases the results of both flank wear and temperature obtained from the experiments.

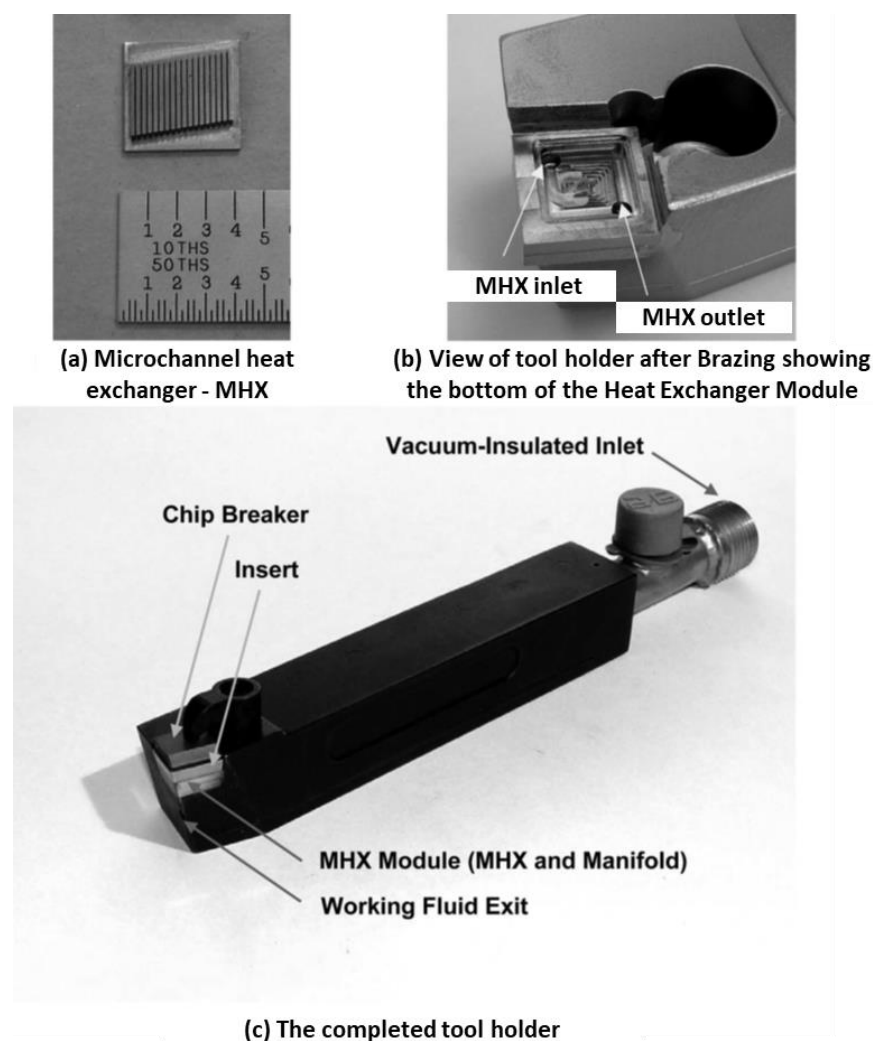


**Figure 2-16:** Experimental results for optimized, non-optimized and conventional tools proposed by Li et al. (2018). (a) Temperature and (b) flank wear

Source: [92]

To sum it up, the authors discovered that indirectly cooled tools with an optimized relief design on the shim have a considerable capacity for heat removal, resulting in lower temperatures and less wear. Furthermore, the tool with an optimized relief design exhibited superior performance in terms of deformation compared to the non-optimized relief design.

Another system developed by Rozzi et al. (2011) utilizes microchannels in the tool shim to exchange heat, which is cooled by circulating liquid nitrogen ( $\text{LN}_2$ ) [94]. This cooling technique can be used for both static and rotating tools. The authors created a numerical model to predict tool life based on different cutting speeds and cooling functions. They also conducted experiments to validate the model and compared the life of the indirectly refrigerated tool with CFA. The authors filed a patent application for this invention in at least ten countries, including Brazil, where it was accepted with the number BRPI1010317B1. Additionally, they registered a patent application in Brazil for the heat exchanger adapted for rotating tools, known as BRPI1013942B1. **Figure 2-17** provides details of the heat exchanger system.

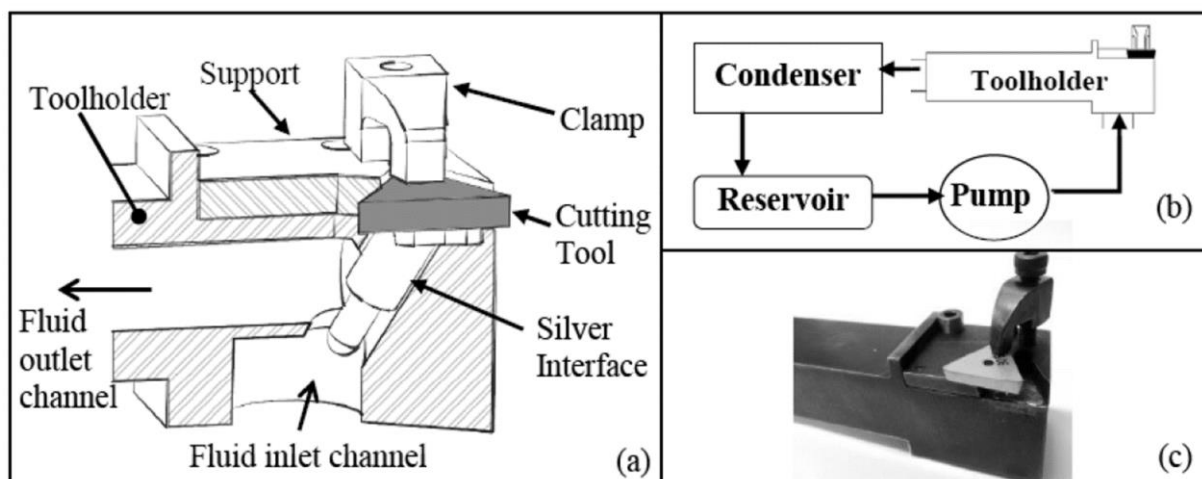


**Figure 2-17:** Indirect cooling system proposed by Rozzi et al. (2011) . (a) Heat exchanger. (b) Internal view of the heat exchanger. (c) Complete set

Source: [93]

In their study, Rozzi et al. (2011) concluded that the LN<sub>2</sub>-cooled microchannel heat exchanger system is a viable solution that can significantly enhance tool life compared to traditional flood cooling with cutting fluids. The proposed design effectively minimized pressure losses and leakage issues. Furthermore, the numerical model developed by the authors demonstrated good agreement with the experimental results in predicting tool life. As a final remark, the authors suggest that the system has the potential to be implemented on an industrial scale, offering improved sustainability in terms of social, environmental, and economic aspects by replacing conventional cutting fluids.

Neto et al. (2015) designed a unique internally cooled tool holder with a refrigerant fluid instead of the commonly used water [95]. The refrigerant fluid was in direct contact with an expansion chamber constructed from silver, as depicted in **Figure 2-18**. This system was patented in Brazil in 2016 under the patent of process number BR 102013018189-7 A2 [96].



**Figure 2-18:** Indirect cooling system of the tool carrier proposed by Neto et al. (2015): (a) Cut view of the tool holder and parts; (b) diagram of the refrigeration system; (c) tool carrier with displaced tool

Source: [95]

The authors conducted turning tests using the proposed system on SAE XEV-F, a type of stainless steel known for its low thermal conductivity (14.5 W/m·K), like Inconel 718. The tests employed triple-coated cemented carbide tools with TiN, TiCN, and Al<sub>2</sub>O<sub>3</sub> CVD coatings. The study considered three different input variables: cutting speed, feed rate, and the cutting environment, which included the internally cooled tool holder, dry cutting,

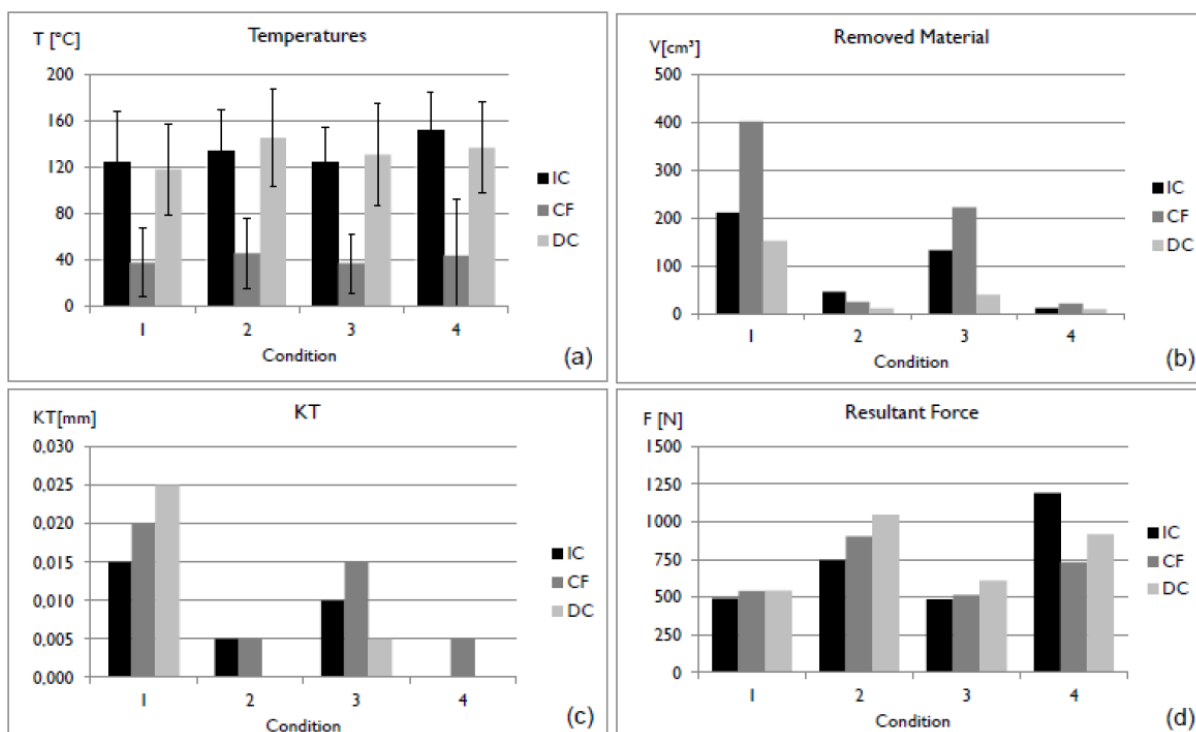
and cutting fluid. The depth of cut was maintained constant at 0.50 mm, and the specific variable conditions are outlined in **Table 2-2**.

**Table 2-2:** Cutting conditions used [95]

condition	$v_c$ [m/min]	$f$ [m/min]	$a_p$ [mm]	cutting atmosphere
1	80	0.20	0.50	(Internally Cooled), (Dry Cutting) or Cutting Fluid)
2	80	0.40	0.50	
3	100	0.20	0.50	
4	100	0.40	0.50	

Source: [95]

The study analyzed response variables: temperature, cutting forces, crater wear (KT), and tool life ( $V_{Bmax} = 0.6$  mm or  $V_{BB} = 0.3$  mm). The results obtained from the experiments are illustrated in **Figure 2-19**, providing insights into the effects of the different input variables on the response variables.



**Figure 2-19:** Results for each condition and cooling method: a) Average temperature in thermocouple 1; b) Volume of removed material; (c) maximum depth of crater wear; d) Resulting force

Source: [95]



### 2.2.3.2. Heat pipes and heat sinks

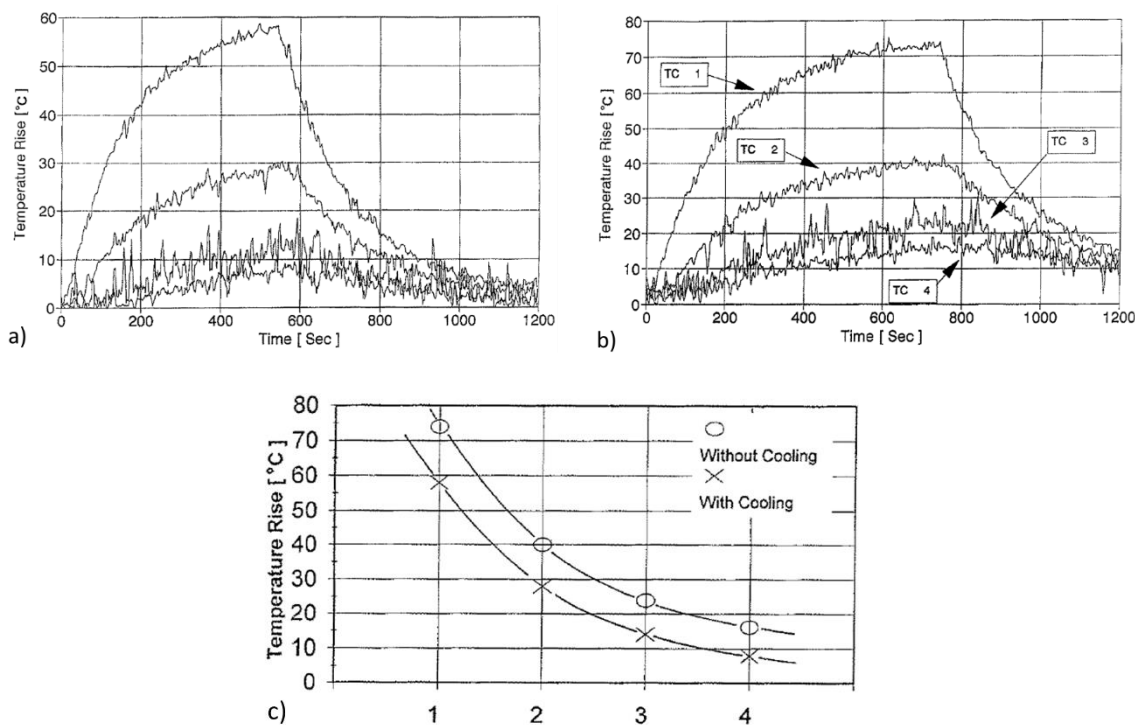
Heat pipes or heat tubes are devices constructed using highly conductive metals such as copper or silver. They are filled with a liquid, typically used for refrigeration purposes. When one section of the heat pipe is heated, the liquid absorbs heat until it reaches its vaporization point, acquiring latent heat. This causes a pressure differential within the tube, initiating the circulation of the fluid from the hottest region to the coldest one. In the coldest part, the system releases heat to the surrounding environment, causing the fluid to condense and complete the cooling cycle [7].

Judd et al. (1995) introduced an indirect cooling system that integrated heat pipes (HP) into the tool holder. The primary objective was maintaining refrigeration to prevent thermal expansion with [97] subsequent loss of dimensional tolerance. To evaluate its performance, the authors monitored the tool holder's temperature using thermocouples and employed millimeters to measure the thermal expansion during the turning process of AISI 1018.

A copper heat tube with a thermal exchange capacity of up to 200 W was employed, and the adapted tool holder was a boring bar with a diameter ( $\emptyset$ ) of 10 mm and an internal hole. Cold water ( $\sim 0^\circ\text{C}$ ) was circulated within the system by a centrifugal pump.

The input variables were the depth of cut ( $a_p = 1.25, 2.50, \text{ and } 3.75 \text{ mm}$ ), feed rate ( $f = 0.148 \text{ and } 0.230 \text{ mm/rev}$ ), and a fixed cutting speed of 45 m/min. The fluid flow rate inside the heat tube ranged from 150 ml/min to 300 ml/min, depending on the thermal intake received.

**Figure 2-20** depicts the primary outcomes derived from the thermocouple measurements conducted with and without coolant, as presented by Judd et al. (1995). The authors concluded that the heat pipes exhibited a remarkable thermal exchange capacity, effectively removing heat from the system. Ultimately, the authors emphasized the significant impact of the device and recommended further studies to enhance and refine the technique.

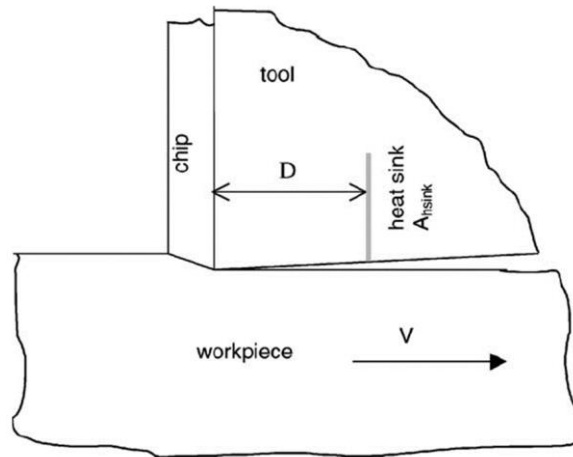


**Figure 2-20:** Results of temperature measurements with the proposed system. (a) Heat pipes are used. (b) No heat pipes (c) Temperature in thermocouples

Source: [97]

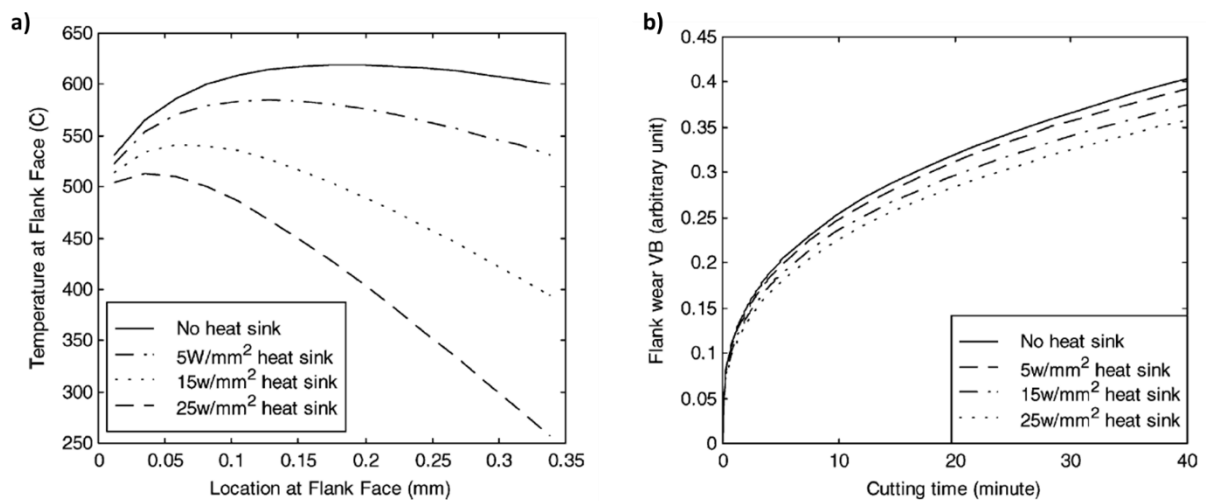
H. Zhao et al. (2002) conducted a numerical study investigating the influence of internal cooling on the flank wear of the tool by employing heatsinks [99]. Their research involved the development of a model that incorporated orthogonal cutting and considered the material's softening effects concerning temperature. To analyze the impact of the heatsink on tool temperature, the authors proposed and examined various geometries. **Figure 2-21** illustrates the proposed schematic representation of the study.

**Figure 2-22** provides an overview of the temperature and flank wear results obtained from a numerical simulation by H. Zhao et al. (2002) [98]. The simulation involved a rectangular plane heatsink with  $2.0 \times 2.0 \text{ mm}^2$  dimensions and a thermal dissipation capacity ( $q_{HS}$ ) ranging from zero (no heatsink) to  $25 \text{ W/mm}^2$ . The heatsink distance ( $D$ ) was fixed at 1.0 mm.



**Figure 2-21:** Orthogonal cutting scheme with heatsink.

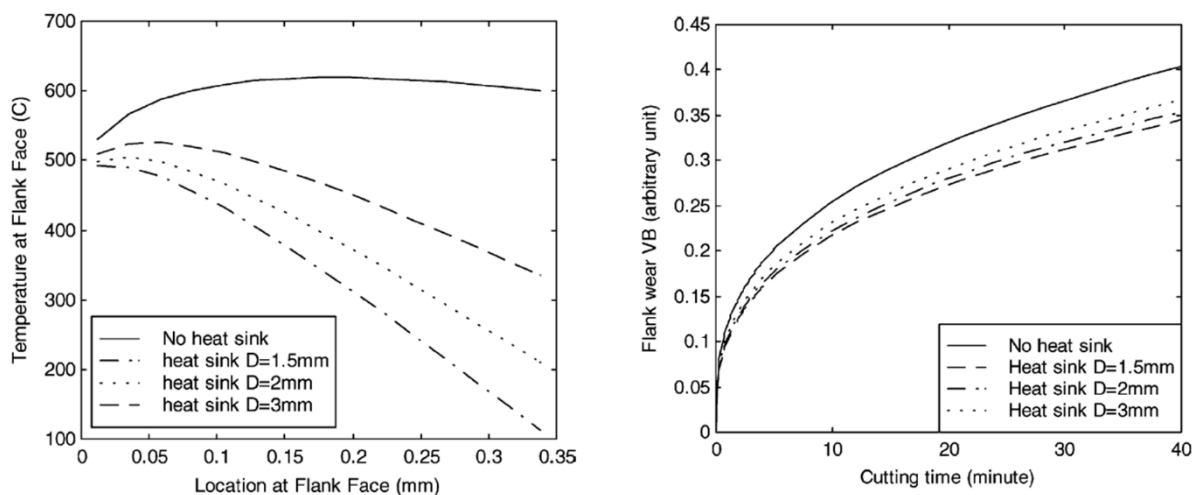
Source: [98]



**Figure 2-22:** Numerical results with different HS capacity.  
(a) Temperature on the main slack surface, (b) Flank wear

Source: [98]

In **Figure 2-23**, the outcomes of a second simulation are presented. This simulation employed a heatsink with identical dimensions ( $A_{HS} = 2.0 \times 2.0 \text{ mm}^2$ ) but with an increased thermal dissipation capability ( $q_{HS} = 45 \text{ W/mm}^2$ ). The heatsink distance ( $D$ ) varied between 1.5 and 3.0 mm. The authors emphasized that heatsinks in carbide tools can lead to an extension of tool life by up to 15% compared to a dry system.



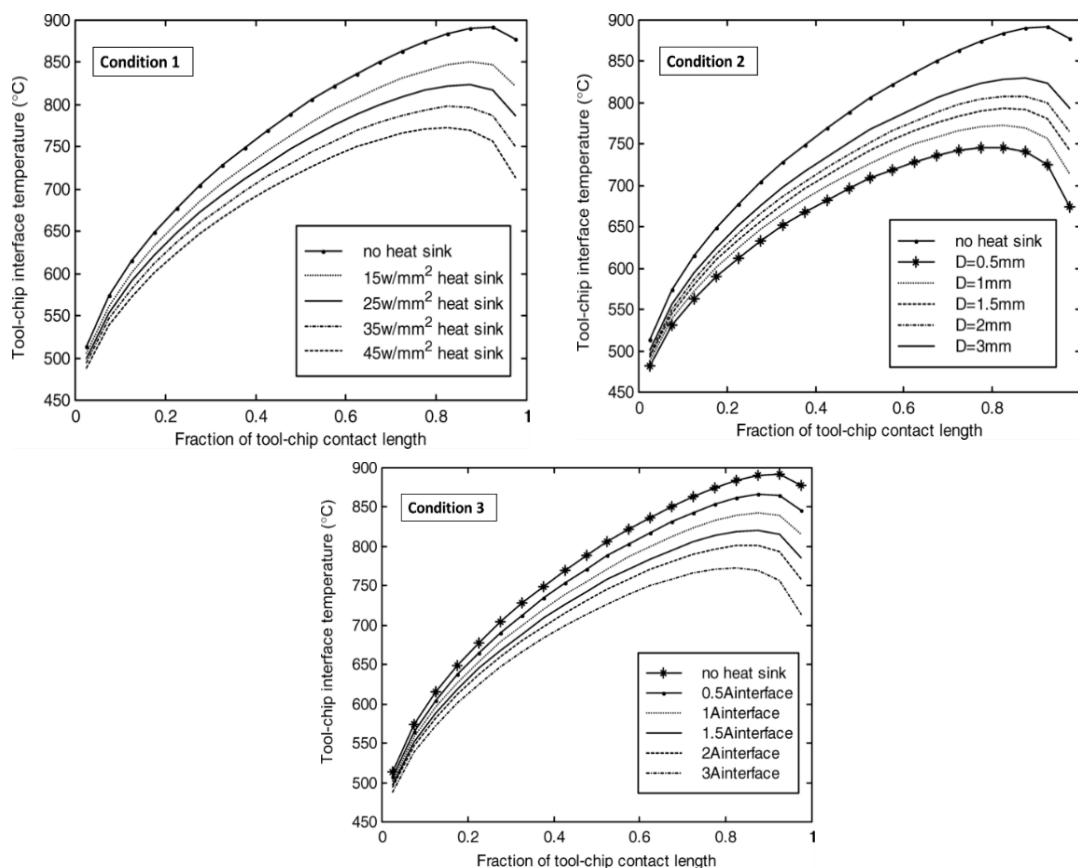
**Figure 2-23:** Numerical results,  $q_{HS} = 45 \text{ W/mm}^2$ , varying the HS distance  
 (a) Temperature on the main slack surface (b) Flank wear.

Source: [98]

In another study by Zhao et al. (2006), the researchers examined the impacts of employing various types, geometries, and capacities of heat sinks on the temperature at the tool/chip interface [100]. This research followed a similar approach to the previous study described earlier. The numerical analysis considered the chip, tool, and interface between them as semi-finite bodies.

The authors investigated the effects of varying the thermal dissipation capacity ( $q_{HS}$ ), distance ( $D$ ) of the heat sink in the tool, chip/tool contact length ( $C$ ), and heat sink area. They conducted numerical simulations, and **Figure 2-24** presents a compilation of the primary temperature results obtained in these simulations.

In their conclusion, Zhao et al. (2006) state that indirect cooling with heat sinks effectively removes heat from the chip/tool interface [100]. They observed a significant temperature decrease ranging from 40 to 150 °C. The researchers identified the heat sink capacity ( $q_{HS}$ ), the distance ( $D$ ) of the heat sink in the tool, and the heat sink area ( $A_{HS}$ ) as the most influential parameters in reducing the temperature at the chip/tool interface.



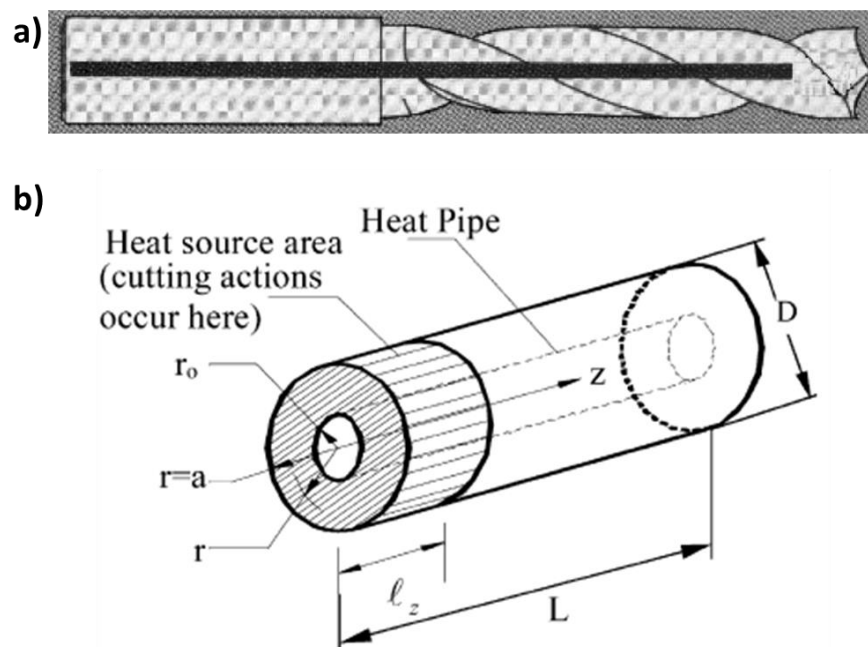
**Figure 2-24:** Results of numerical temperature simulations at the chip/tool interface for three distinct conditions

Source: [100]

In a study by Jen et al. (2002), a numerical analysis using the Finite Element Method (FEM) and experimental investigations were conducted on a Tool Indirectly Cooled (TIC) system [99]. This system involved the use of heat tubes inserted inside helical drills. The researchers aimed to determine the optimal design of the drill with the heat tube by conducting a parametric study.

The study focused on various dimensional parameters, such as the diameter of the drill and heat tube, the distance between the drill tip and the heat tube, and the type of contact between them. These factors were found to influence the thermal efficiency of the system significantly.

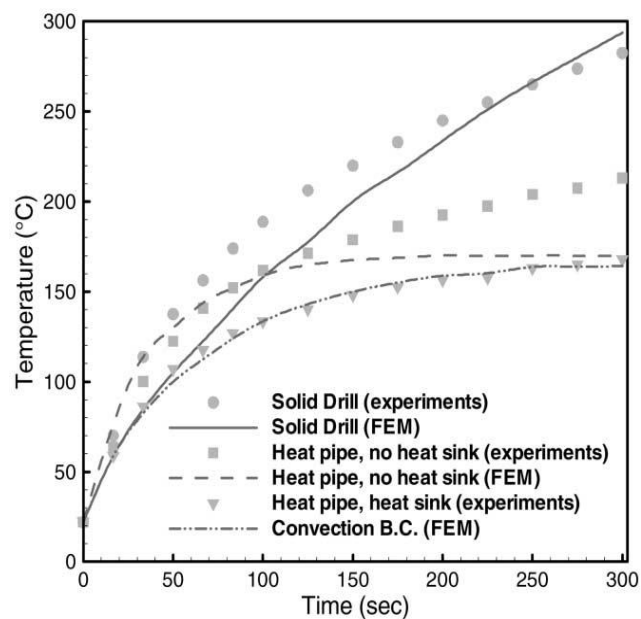
**Figure 2-25 (a)** illustrates the proposed tool, while **Figure 2-25 (b)** simplifies the heat tube and the drill as ideal cylinders for analysis. These visual representations aid in understanding the configuration and geometry of the TIC system under investigation.



**Figure 2-25:** a) Illustration of a drill with internal channel to insert the heat tube proposed by Jen et al. (2002) (b) Physical representation of an ideal heat tube

Source: [99]

The experiments and simulations were conducted in three different setups: solid drill, heat pipe without a sink; heat pipe with a sink; basic convection cylinder (BC). The temperature outcomes are presented in **Figure 2-26**.



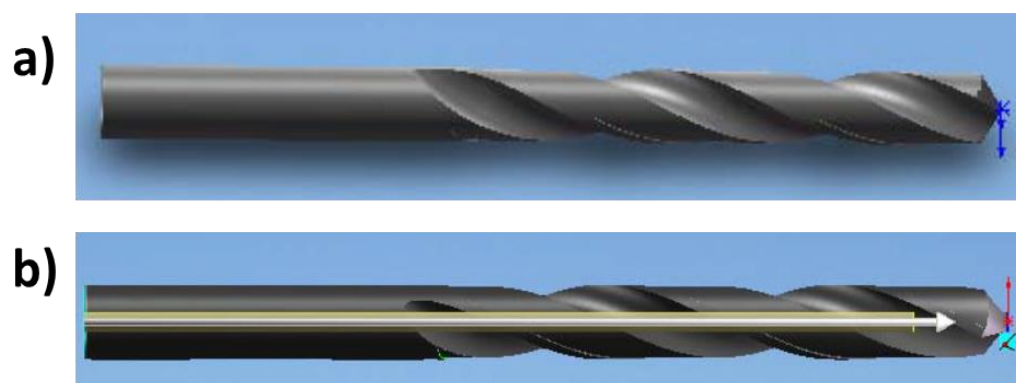
**Figure 2-26:** Temperature results for six different conditions simulating a drill in drilling condition.

Source: [99]

Jen et al. (2002) conducted experimental tests to validate the accuracy of their numerical model, and a strong correlation between them was observed [99]. The maximum temperature difference recorded was approximately 110 °C between the conventional drilling method (BC) and the heat pipe with dry cutting (HP with DC). In the case of experiments without a heat sink (HT or HP) and with a heat sink, the temperature difference was around 40 °C.

Once the numerical and experimental models were validated, the authors performed a parametric optimization study on the drill design with a heat tube. This study involved analyzing factors such as the distance between the cutting edge and the end of the heat tube, the impact of contact resistance, and the diameter of the heat tube. The authors concluded that heat pipes, especially when combined with heat sinks, are highly effective in maintaining a cool temperature for the drill.

In a subsequent and ongoing study on HP, Zhu et al., 2009, conducted finite element method (FEM) simulations to perform thermal, structural, static, and dynamic analyses of drills equipped with heat pipes to assess their practicality [101]. The researchers utilized COSMOS\works software to compare conventional drills (CD) with HP drills, both with and without CFA. **Figure 2-27** depicts the simulated device, resembling the one examined earlier in **Figure 2-25 (a)**.



**Figure 2-27:** Conventional drill (a) and drill with heat tubes (b) simulated with FEM proposed by Zhu et al. (2009)

Source: [101]

The maximum temperatures obtained from the experiments were as follows: 343 °C for conventional drilling (CD), 258 °C for conventional drilling with cutting fluid application (CD + CFA), 189 °C for heat pipe cooling (HP), and 173 °C for heat pipe cooling

with cutting fluid application (HP + CFA). The thermal stress analyses revealed 250 MPa for CD, 200 MPa for CD + CFA, 160 MPa for HP, and 130 MPa for HP + CFA. These findings demonstrate that heat pipes are highly effective in removing heat from the drilling process, resulting in significantly lower temperatures. A maximum temperature reduction of 153 °C was observed, and the thermal stress was reduced by 3x compared to conventional drilling methods.

Regarding stress and deformation analyses, the maximum stress values were found to occur in the drill channels. The maximum stress value for the drill with a heat pipe was  $3.401 \times 10^8$  Pa, while for the conventional drill, it was  $2.643 \times 10^8$  Pa. This indicates that the heat pipe (HP) configuration increased the stresses by approximately 30% due to the reduction in the hole. Consequently, the stresses in the HP drill were also higher, with maximum values of  $1.313 \times 10^{-3}$  Pa for the conventional drill (CD) and  $1.779 \times 10^{-3}$  Pa for the HP drill.

In the dynamic analysis, the authors found that the deformations in the HP drill were significantly larger, potentially leading to a loss of dimensional quality. However, it should be noted that the drills did not reach the point of failure, indicating that the structural performance was still within acceptable limits. The authors recommended future work to design reinforced drills, mainly focusing on the points of higher loads, to address the structural concerns identified.

In conclusion, the authors state that thermally, the heat pipes are highly efficient in cooling the drill, but structurally, the performance is affected, although they do not reach failure. The need for reinforced drill designs and further investigation into areas of high load is suggested for future research.

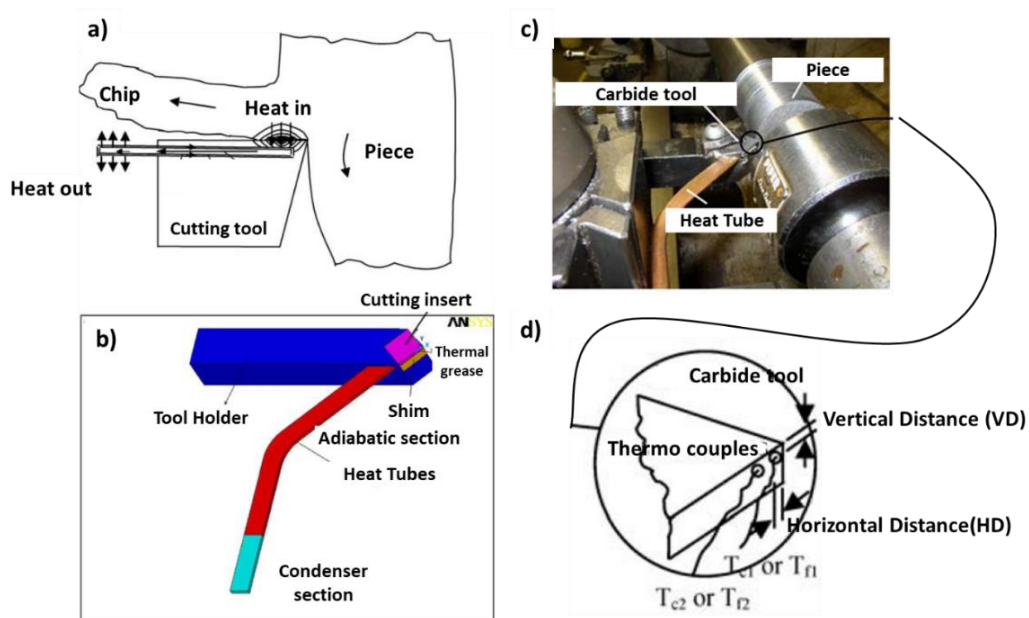
Chiou et al. (2007) studied the thermal behavior of carbide tools using Heating tubes (HT) for indirect tool cooling [102]. The HT device was designed to be attached between the tool and the shim, providing cooling to the tool. The authors performed numerical simulations using ANSYS as the finite element software to analyze the thermal behavior, and they also conducted experimental tests using AISI 1020 and 1040 in a turning operation.

**Figure 2-28** provides detailed information about the HT system, illustrating its



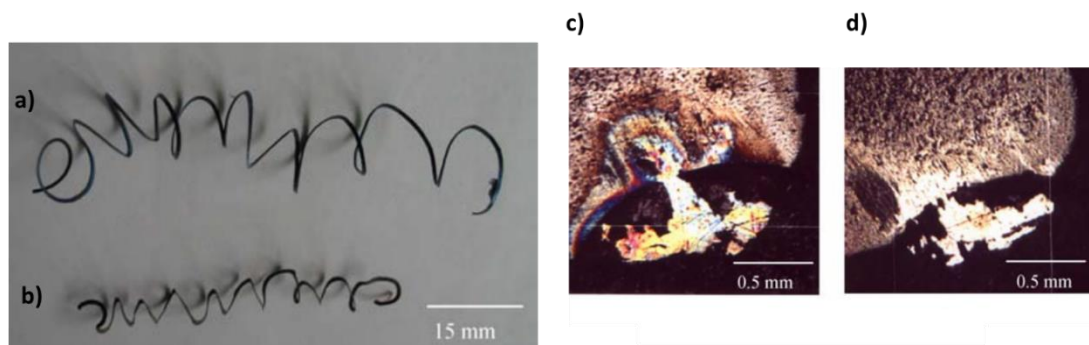
components and configuration. The study's main results are presented in **Figure 2-29**, **Figure 2-30**, and **Figure 2-31**. These figures showcase important temperature distribution, thermal stress, and tool life findings.

The numerical simulations and experimental tests allowed the authors to observe the effectiveness of the HT device in reducing temperatures and minimizing thermal stress on the carbide tools. The results demonstrate that the HT system successfully mitigated heat buildup, leading to lower temperatures and improved tool life [102].



**Figure 2-28:** Tool Indirectly Cooled - TIC by heat pipes proposed by Chiou et al. (2007). (a) Illustration of heat flux; (b) Illustration of simulation with ANSYS; (c) Experimental assembly; (d) Illustration of the fixation of thermocouples

Source: [102]



**Figure 2-29:** Dry chip formation (a) with HT (b) dry and tool wear (c) dry and (d) HT

Source: [102]

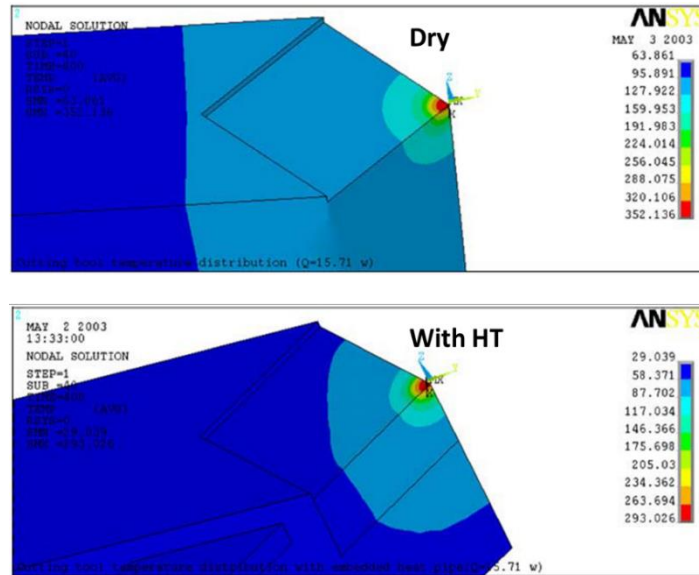


Figure 2-30: Temperature distribution simulation, dry (above) and with heat tube (below)

Source: [102]

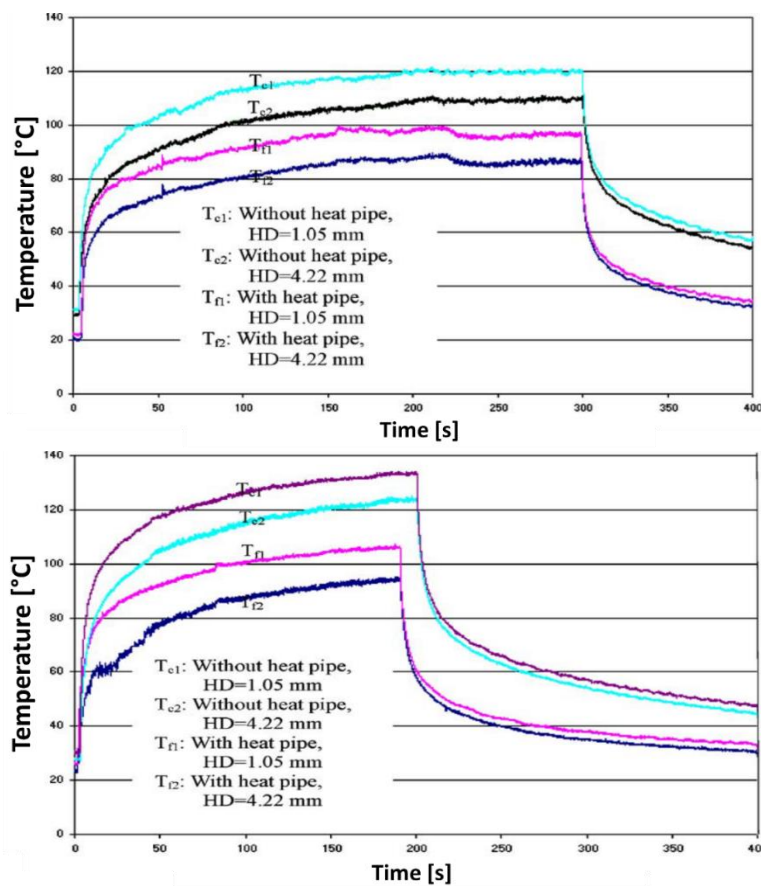


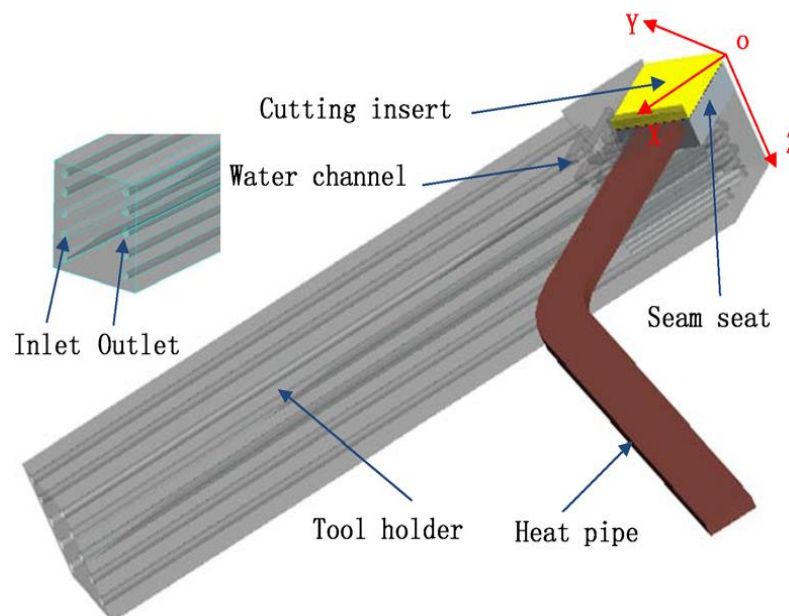
Figure 2-31: Temperature measurement by thermocouple,  $v_c = 29.9$  m/min (above) and  $v_c = 40.94$  m/min (below)

Source: [102]

According to the findings of Chiou et al. (2007), the use of HT at the tooltip resulted in a maximum temperature difference of 59 °C in the numerical simulations [102]. In the experimental measurements using a thermocouple, a maximum temperature difference of 28 °C was observed at 1.05 mm from the cutting edge.

In terms of chip morphology, as depicted in **Figure 2-29 (a) (b)**, dry cutting exhibited larger bending chips, indicating higher temperatures. The bluish coloration observed in the chips further suggests the activation of an oxidation mechanism at elevated temperatures. **Figure 2-29 (c) (d)** shows that a visual analysis indicates more prominent crater wear in dry cutting conditions when considering tool wear. Based on these results, the authors conclude that heat pipes effectively remove heat from the tool, preserving its service life.

It is interesting to note that additional research in this area was conducted by Shu et al. (2011), who used finite element analysis and ANSYS software to simulate a tool holder with internal cooling channels and heat pipes in the tool shim, as shown in **Figure 2-32** [103]. The authors conducted dynamic, static, thermal, and structural analyses to evaluate their proposed system's effectiveness.

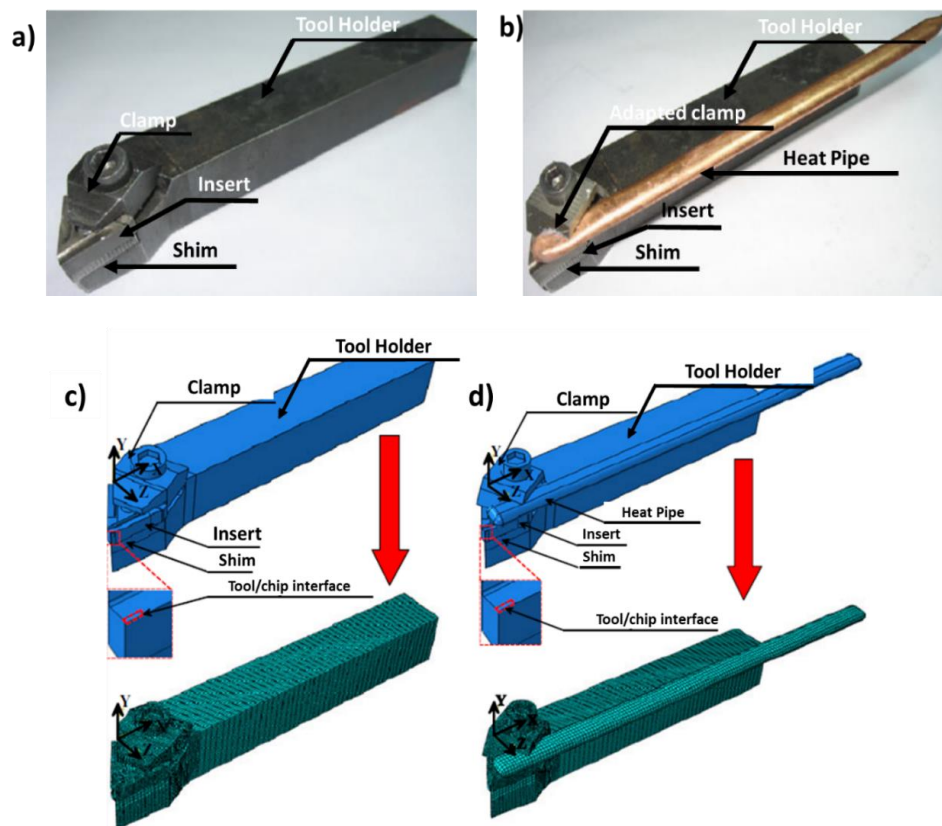


**Figure 2-32:** Tool Cooled Indirectly - TIC by internal cooling channels in the tool carrier and heat pipes proposed by Shu et al. (2011).

Source: [103]

The primary findings demonstrated that integrating internally cooled channels (ICCs) with heat tubes (HT) resulted in an approximately 81 °C reduction in the maximum tool temperature [103]. Additionally, deformation tests revealed that the conventional tool exhibited a deformation of 5.210  $\mu\text{m}$ , whereas the ICCs combined with heat pipes exhibited a deformation of 5.495  $\mu\text{m}$ . Ultimately, the authors concluded that the combined device is viable and represents the most efficient cooling method for the insert. Furthermore, the insertion of ICCs had a minimal structural impact on the tool holder.

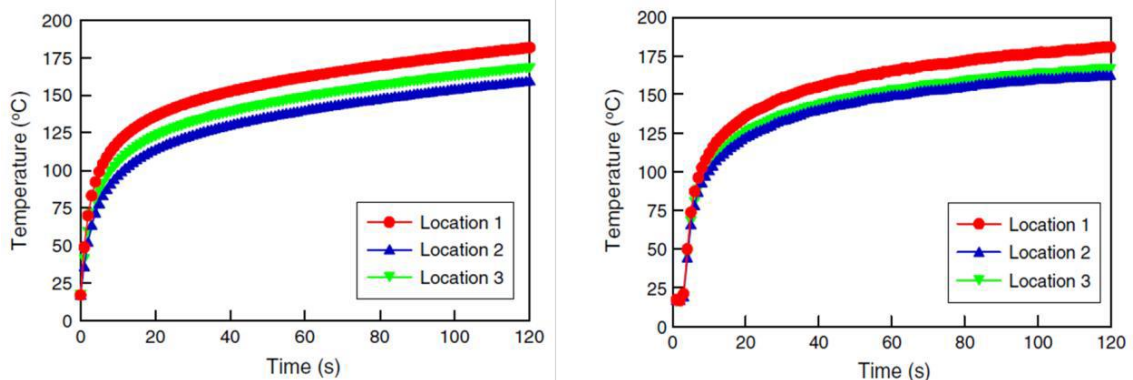
Liang et al. (2011) conducted numerical experiments and simulations to utilize inverse engineering methods and determine the temperature at the interface between the tool and chip [104]. To accommodate the heat pipe next to the tool, an adaptation was made to the clamp. **Figure 2-33** illustrates the details of the experimentally assembled and simulated device.



**Figure 2-33:** Conventional device (a), adapted with heat tube (b), simulation of the conventional (c) and (d) simulation of the heat tube.

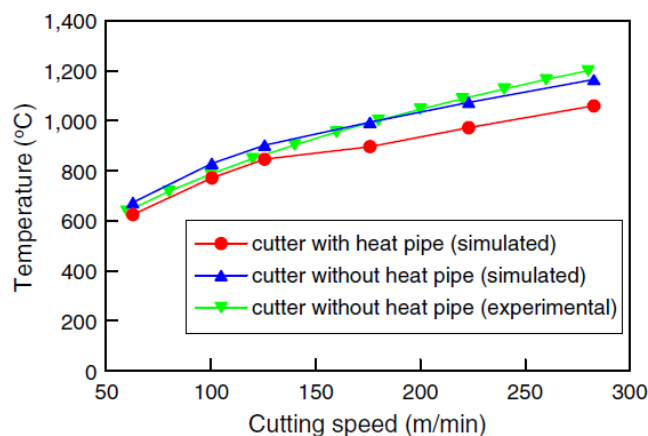
Source: [104]

The input variables in the study included cutting speed ( $v_c = 63$  to  $283$  m/min), feed rate ( $f = 0.7$  mm/rot and  $0.1$  mm/rot), cutting environment (dry and with heat pipes), and a constant depth of cut ( $a_p = 0.7$  mm). The output variables were chip temperature and morphology. To determine the tool/chip contact area, the authors applied black paint to the rake surfaces and measured the area revealed by chip drag after machining. Three K-type thermocouples were inserted into the tool to measure the temperature during AISI 1045 turning. **Figure 2-34** presents an example of the temperature measured experimentally and through simulation. Using this data, the thermal flow was estimated to be  $q'' = 2.95 \times 10^7$  W/m<sup>2</sup>, enabling the temperature simulation at the tool/chip interface using ABAQUS 6.8 software, as shown in **Figure 2-35**. **Figure 2-36** depicts the obtained chips. No significant difference was observed.



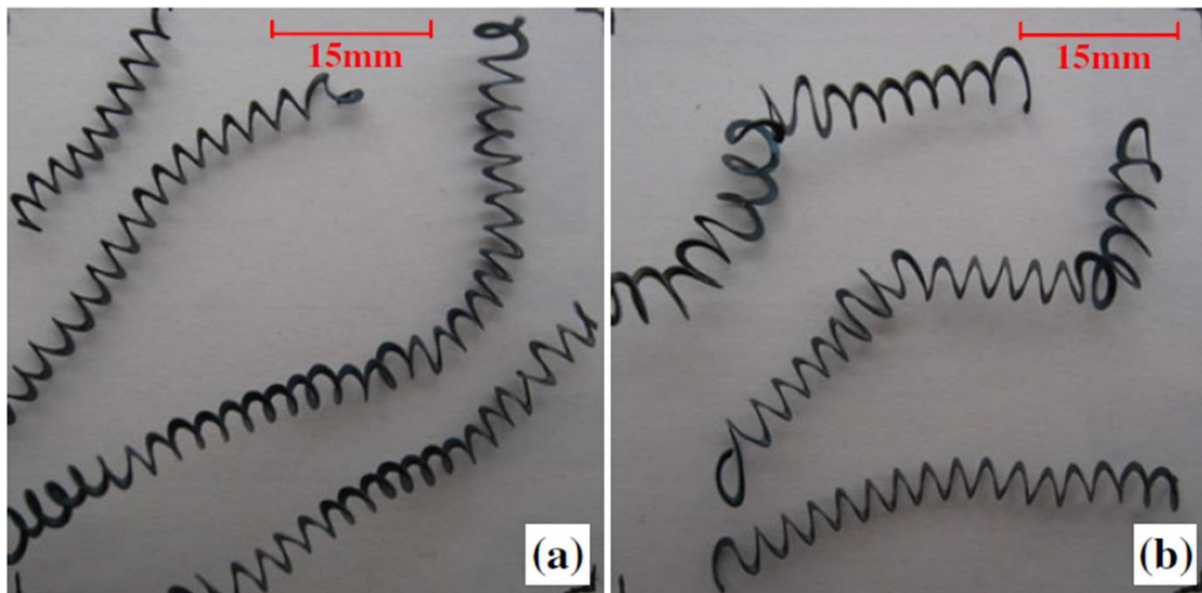
**Figure 2-34:** Measured temperature without heat pipes in different positions experimentally (left) and by simulation (right), ( $v_c = 175.84$  m/min,  $a_p = 0.7$  mm and  $f = 0.1$  mm/rev)

Source: [104]



**Figure 2-35:** Temperature at tool/chip interface depending on cutting speed (doc = 0.7 mm and  $f = 0.1$  min/rev, cutting time = 120 s)

Source: [104]



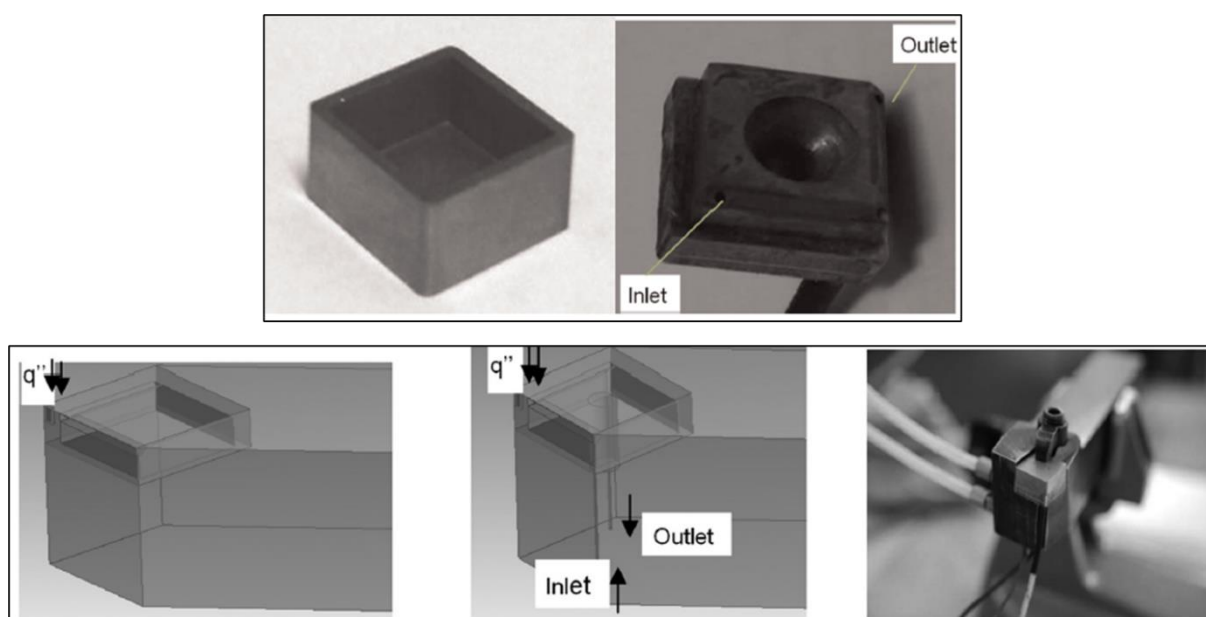
**Figure 2-36:** Chip morphology for experiments with heat (a) and dry tubes (b),  
( $v_c = 175.84$  m/min,  $a_p = 0.7$  mm and  $f = 0.1$  min/rev )

Source: [104]

### 2.2.3.3. Internally Cooled Tools - ICT

As the name suggests, internal cooling tools have internal channels through which a coolant fluid circulates. There are various methods for ensuring fluid circulation within the tool during machining. Additionally, the geometry of the internal galleries is a factor that undergoes optimization studies to determine the most efficient design for removing heat.

Sun et al. (2012) introduced an internally cooled tools (ICT) system, which featured internal channels that passed directly through the insert and were located near the cutting edge [105]. The authors employed the Taguchi DoE to simulate the optimal cooling structure near the cutting edge. In addition to simulations, the system was also tested experimentally. **Figure 2-37** illustrates the proposed ICT system.



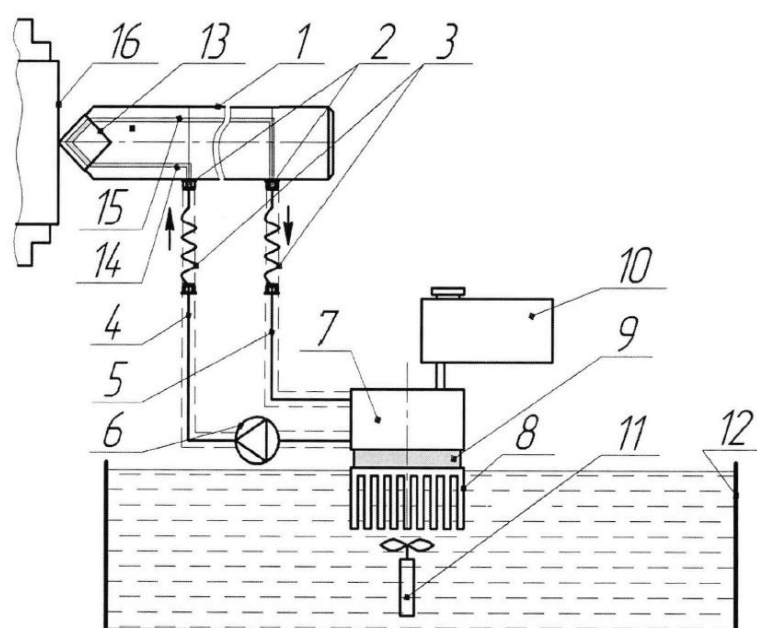
**Figure 2-37:** Internally Cooled Tool - ICT with drawing and real photos

Source: [105]

Initially, Sun et al. (2012) utilized computer fluid dynamics (CFD), ANSYS, and FLUENT software to simulate the thermal behavior of the ICT system. They employed a carbide tool and pure water at room temperature ( $\sim 25^{\circ}\text{C}$ ) with a flow rate of 0.15 m/s for the simulations. The theoretical results indicated a temperature reduction of  $35^{\circ}\text{C}$  within the ICT. The subsequent phase of the study involved optimizing the tool geometry for efficient heat exchange. The variables considered in the optimization process included insert

thickness (T), vertical dimension (V), horizontal dimension (H), and diameter of the internal cooling channels (D). The results indicated that the diameter of the channels (D) insert thickness (T) and vertical (V) dimension are significant variables concerning thermal exchange efficiency.

Two similar patents of internally refrigerated tools were requested in Russia, having the same authors. In the first one, Pavlovich et al. (2017) explain that it consists of a cooling device for turning cutting inserts with two heat exchangers, one with Peltier cells inserted into a coolant tank [107]. Further details are shown in **Figure 2-38**.



**Figure 2-38:** Indirect cooling device with proposed Peltier cells

Source: [107]

As per Pavlovich et al. (2017) in **Figure 2-38**, the system comprises several components. These include an adapted tool door (1) and a corresponding cutting tool (13) connected via a duct for a cold coolant inlet (14) and a hot fluid outlet duct (15). The purpose of these connections is to remove heat generated during the machining process. Quick coupling valves (3) are utilized and connected by thermally insulated fluid inlet (4) and outlet (5) ducts. A pump (6) is employed to facilitate the forced circulation of fluid within the system. A heat exchanger, such as a refrigerant (7), is connected to a heatsink (8) in contact with Peltier thermoelectric cells (9). An expansion tank (10) is designed to compensate for variations in coolant volume resulting from heating or cooling (12). Inside



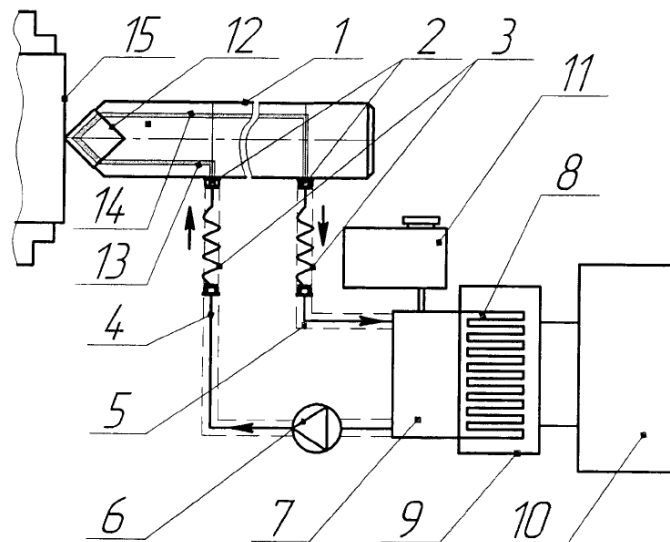
a cooling tank (12), an agitator (11) is present to promote convection. Lastly, the workpiece is denoted as (16).

The authors did not provide specific experimental results or simulations in their study. However, they claim that the device can potentially increase tool life by 1.5 times and improve productivity by 25%. They acknowledge a couple of challenges associated with the device. Firstly, they note that the cooling capacity of the Peltier cells is limited to the size of the tool holder. Additionally, they mention that the external system required for the device is complex to assemble, involving numerous connections, which could lead to longer tool change times. The authors did not provide any specific information regarding the manufacturing of these channels.

In the second patent by Pavlovich et al. (2017), the authors introduce a system similar to the previous one [106]. However, instead of utilizing Peltier cells, they propose using a refrigeration machine. The system is illustrated in **Figure 2-39**.

According to Pavlovich et al. (2017) in **Figure 2-39**, the system comprises the following components: an adapted tool holder (1) and a corresponding cutting tool (12) connected via a duct for cold coolant input (14) and a hot fluid outlet duct (15) to extract heat generated during the machining process. Quick coupling valves (3) are connected by thermally insulated fluid inlet (4) and outlet (5) ducts. A pump (6) is utilized to force fluid circulation within the system. A heat exchanger, such as a coolant (7), is connected to a heatsink (8), which is in contact with a cooling chamber (9). The system also incorporates a refrigeration machine (10) for cooling purposes. An expansion tank (11) is designed to accommodate variations in coolant volume resulting from heating or cooling. The workpiece is denoted as (15).

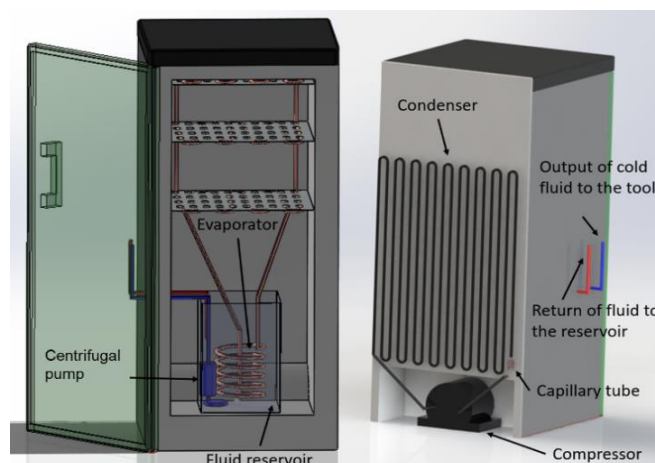
According to Pavlovich et al. (2017), implementing cooling on both the bottom and top of the tool at -15 °C can effectively reduce wear [106]. This approach enables the device to enhance tool life and increase productivity by allowing higher cutting parameters while eliminating the need for cutting fluids.



**Figure 2-39:** Draw of Internally Cooled Tools -ICT with refrigeration system

Source: [106]

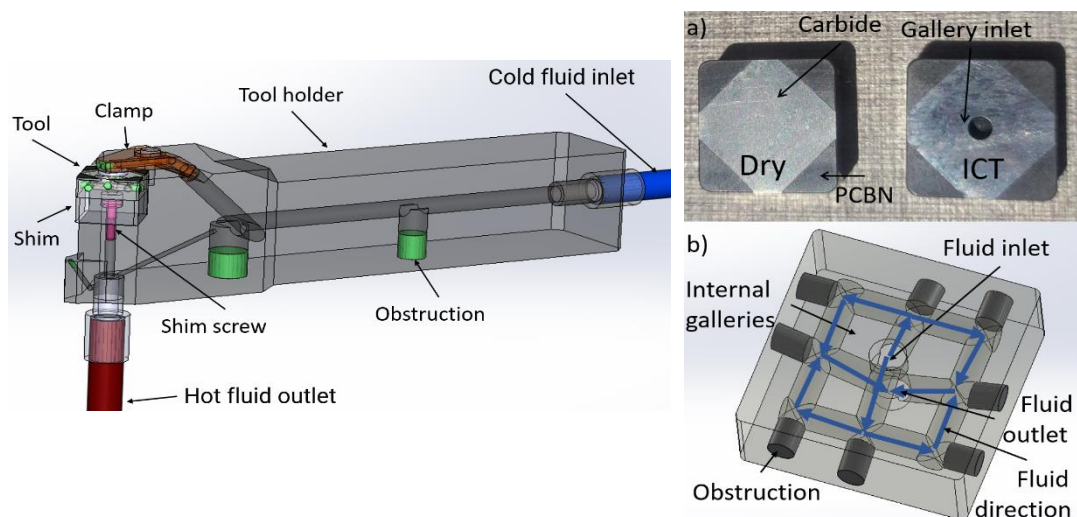
The Group of Sustainable Manufacturing (GSM) at the Federal University of Uberlândia in Minas Gerais State, Brazil, has developed another important proposal for an ICT system. The major improvement from the previous works is the design of the galleries and the tool holder, enhancing cooling capacity. In their proposal, a chiller is used to cool a water mixture solution with an antioxidant and pump it into the internally cooled tools during machining. It was constructed using an adapted conventional refrigerator, specifically a *Prosdocimo* brand model 04180CBC201, with a power rating of 146 W. The freezer unit consists of thermal insulation, a compressor, a condenser, an expansion device, and an evaporator, as depicted in **Figure 2-40** [108].



**Figure 2-40:** Schematic of a chiller and its components

Source: [108]

In a study conducted by Barbosa (2021), the aforementioned internally cooling system was tested on polycrystalline cubic boron nitride (PCBN) tools. The system involved circulating a closed-circuit mixture of water and ethylene glycol. The tests were carried out during the turning operation of D6 hardened steel and compared with dry machining. The study's main findings demonstrated that the internally cooled tool (ICT) system had a notable impact on reducing the temperature of the tool's rake surface, as evidenced by thermographic camera measurements. **Figure 2-41** presents the tools that were utilized in the experiments.



**Figure 2-41:** PCBN Internally cooled tool used by Barbosa (2021)

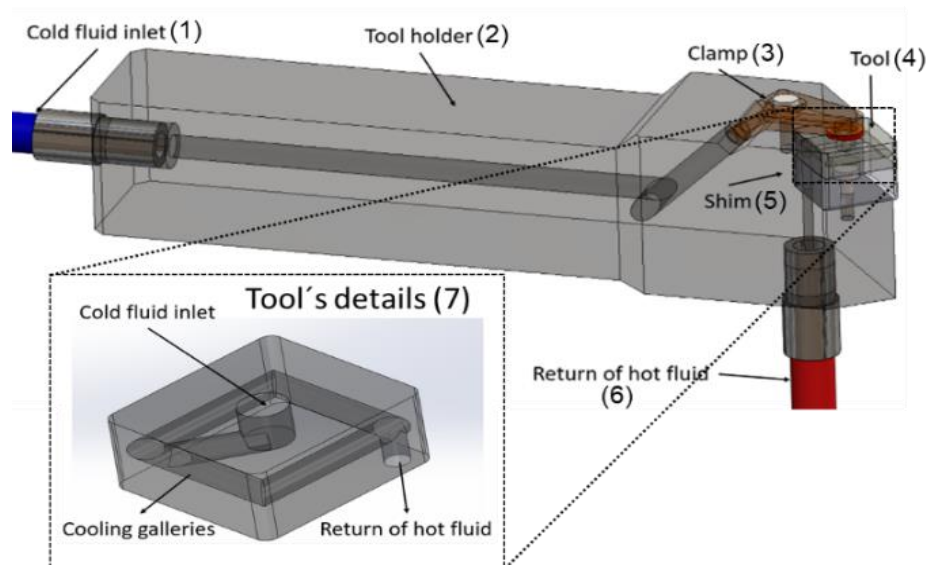
Source: [108]

Regarding tool life tests, the ICT system consistently showed an extended tool life in all analyzed scenarios compared to dry machining, with cutting speed being the most influential factor. The feed rate primarily influenced the cutting force due to the increased cutting area, followed by the cooling system. The ICT system exhibited higher forces due to the lowered cutting temperature.

Conversely, the roughness was predominantly affected by the edge geometry condition, where a worn tool resulted in a better surface finish. Both flank and crater wear were observed, with crater wear being more pronounced in dry machining due to higher cutting temperatures. The predominant wear mechanisms identified were abrasion and diffusion.

With the same cooling system varying the tool's design, **Figure 2-42**, and workpiece material, Fernandes et al. (2023) and França et al. (2022) studied an ICT proposal for the

gray cast iron turning [53,84]. The former studied cutting forces, surface integrity (roughness, microhardness, workpiece metallography), and wear mechanisms, while the latter studied the temperature by tool-workpiece thermocouple system.



**Figure 2-42:** Internally cooled tool used by Bazon (2020) and França (2021)

Source: [159,165]

According to Fernandes et al. (2023), the ICT exhibited a remarkable heat removal capacity. The analysis of the subsurface microhardness of the grey cast iron confirmed that both ICT and CFA processes led to the expected work hardening of the material. Notably, the ICT method displayed higher microhardness, potentially attributed to the absence of a lubricating effect. Adhesion and abrasion were identified as the primary wear mechanisms, with some plastic deformation explicitly observed concerning the ICT method [85].

In their study, França et al. (2022) concluded that ICTs demonstrated high efficiency in controlling temperatures at the chip-tool interface compared to dry machining processes. Internally cooled tools effectively reduced the temperature up to 21.52%. Additionally, ICTs significantly impacted the thermal gradient across the machining area.

Furthermore, the study concluded that ICTs have the potential to be a promising method with reduced ecological harm. This is due to their ability to minimize or eliminate the need for cutting fluids, resulting in significant savings in their usage.

Despite conducting an extensive search in renowned journal databases such as Web of Science, Clarivate, Scopus, and Science Direct, no prior studies were discovered that have investigated the application of an internally cooled system (ICT) in the machining of Inconel 718. This notable absence indicates a significant research gap in this area.

### 2.3. Nickel (Ni) and nickel-based super alloys

Nickel (Ni) is a chemical element with an atomic number of 28. It possesses a melting point of 1,455°C and a density of 8,908 kg/m<sup>3</sup>. With its face-centered cubic structure (FCC), nickel falls into the category of transition metals and exhibits a desirable combination of hardness and ductility. It is the fifth most copious metal in the Earth's crust [109].

Exploration of ancient artifacts, including weapons, tools, jewelry, coins, and decorative items, reveals the historical utilization of nickel in varying proportions, although the precise extent of its usage during that era remains uncertain. Chinese manuscripts refer to the use of nickel in copper alloys between 1,700 and 1,400 BC, known as Baitong (白銅 in Chinese, meaning "copper white"). However, due to its silver-like appearance, there are indications that miners may have mistaken nickel for silver as early as 4,000 BCE, suggesting its potential utilization since then (ASM International, 1990; Marques, 2015) [110,111]. Currently, nickel is primarily incorporated into metal alloys, as depicted in **Table 2-3**.

**Table 2-3:** Various uses of Nickel

	Stainless Steel	Steel alloys	Nickel-based alloys	Copper-based alloys	Galvanization	Casting	Others
Percentage usage Nickel (%)	57	9.5	13	2.3	10.4	4.4	3.3

Source: [110,111]

Nickel (Ni) exhibits remarkable versatility as an element, as it can readily combine with a wide range of metals to form various alloys that find diverse applications. Some notable examples include nickel-chromium, nickel-chromium-iron, stainless steels, iron-nickel-chromium, nickel-iron, and iron-nickel alloys. When combined with copper, nickel forms a fully soluble mixture, the foundation for many nickel-based superalloys. Appendix A, B, and C provide detailed information on various nickel-containing alloys, encompassing their compositions, mechanical properties, characteristics, applications, and physical properties. These alloys can be classified into five distinct groups, as outlined below [112,113]:

- **Group A - Pure nickel alloys:** Nickel-containing alloys typically have a nickel content of over 95%. These alloys exhibit moderate mechanical strength and hardness. The hardness ranges from 115 to 388 HV, with the potential for higher values in exceptional cases when subjected to heat treatment. The rupture limit varies between 345 and 1,170 MPa, as observed in the case of Duranickel 301.
- **Group B - nickel-copper alloys:** The nickel-containing alloys within this range typically consist of nickel ranging from 29 to 63%, with copper content between 27 to 34%. These alloys, known as group B, exhibit higher resistance than those in group A but have a lower hardness. The hardness values range from 111 to 303 HV, and the tensile rupture limit falls between 385 and 1,100 MPa. An example of such an alloy is the k-500 alloy, which achieves hardening through precipitation.
- **Group C - Nickel-chromium or nickel-chromium-iron alloys:** The nickel-containing alloys within this composition range typically consist of nickel ranging from 44 to 78%, chromium from 5 to 25%, and iron from 1 to 21%. These alloys exhibit similarities to stainless steel, including their machinability. They possess excellent mechanical properties, even at high temperatures. The hardness of these alloys ranges from 115 to 388 HV, and the tensile rupture limit varies from 620 to 1,310 MPa. An example of such an alloy is the Inconel 718, which achieves hardening through precipitation.
- **Group D - Iron-nickel-chromium alloys:** The nickel-containing alloys within this range are primarily hardened by aging. They consist of iron from 22 to 40%, nickel from 20 to 46%, and chromium from 19 to 23%. These alloys exhibit high hardness, ranging from 95 to 342 HV, and possess a tensile rupture limit between 550 and 1,210 MPa. An example is the 925 alloy, which is thermally treated, and precipitation hardened.
- **Group E - Monel R-405:** The described alloy is a nickel-copper alloy containing a minimum of 63% nickel and a copper content ranging from 28 to 34%. Its hardness range of 115 to 142 HV, and a tensile strength limit of 550 MPa. One of its notable features is its good machinability, which allows for efficient processing with minimal restrictions. This attribute contributes to higher productivity. The controlled addition of sulfur plays a crucial role in achieving these characteristics. The sulfur acts as a natural solid lubricant, aiding chip

breaking and control during machining.

**Table 2-4** contains the most constituent elements of nickel alloys and their influence over the microstructural phases' stability.

**Table 2-4:** Influence of various chemical elements on the properties of superalloys

Effect	Iron-based	Cobalt-based	Nickel-Based
Solid-solution trainers	Cr,Mo	Nb,Cr,Mo,Ni,W,Ta	Co,Cr,Fe,Mo,W,Ta,Re
FCC matrix stabilizers	C,W,Ni	Ni	***
Carbide Formers			
MC	Ti	Ti	W,Ta,Ti,Mo,Nb,Hf
M <sub>7</sub> C <sub>3</sub>	***	Cr	Cr
M <sub>23</sub> C <sub>6</sub>	Cr	Cr	Cr,Mo,W
M <sub>6</sub> C	Mo	Mo, W	Mo,W,Nb
Carbonitrides: M(CN)	C,N	C,N	C,N
Carbide precipitation promoters	P	***	***
Formers $\gamma'$ Ni <sub>3</sub> (Al, Ti)	Al, Ni, Ti	***	Al, Ti
Former retarders de Ni <sub>3</sub> Ti	***	***	Co
Precipitate and/or intermetallic builders	Al,Ti,Nb	Al,Mo,Ti,W,Ta	Al,Ti,Nb
Oxidation resistance	Cr	Al, Cr	Al,Cr,Y,La,Ce
Resistance to hot corrosion	La,Y	La,Y,Th	La,Th
Sulfur resistance	Cr	Cr	Cr, Co, Si
Creep resistance	B	***	B, Ta
Tear resistance	B	B, Zr	B
Grain refiners	***	***	B,C,Zr,Hf
Workability	***	Ni <sub>3</sub> Ti	***

Source: [114,115]

A typical microstructure present in nickel superalloys is composed of three different phases, as below [111,115–118]:

- **Gamma ( $\gamma$ ) phase:** it is formed by a continuous face-centered cubic structure (FCC) or austenitic phase, being the base structure (matrix) for the other phases. It has reinforcement elements with an atomic radius close to that of nickel, dispersed in a solid solution. These elements are cobalt, iron, chromium, ruthenium, rhenium, and molybdenum.
- **Gama ( $\gamma'$ ) precipitate:** it consists of precipitate elements of the gamma phase ( $\gamma$ ), type Ni<sub>3</sub>(Al, Ti), also with FCC structure. It is rich in titanium, tantalum, and aluminum.
- **Gama ( $\gamma''$ ) precipitate:** in nickel-iron alloys rich in niobium or tantalum, there is the formation of the  $\gamma''$  to the detriment of  $\gamma'$ . The phase  $\gamma''$  forms a compact and



strongly bonded structure of type  $\text{Ni}_3(\text{Nb, Ta})$  Tetragonal Centered Body (TCB), with few planes of slipping, low weight, and confers mechanical resistance even at high temperatures, as in the case of Inconel 718.

- **Delta ( $\delta$ ) phase:** is an orthorhombic structure that forms in prolonged exposure to temperatures above  $650^\circ\text{C}$  and consists of  $\text{Ni}_3\text{Nb}$  where the metastable phase ( $\gamma''$ ) dissolution occurs into a delta phase ( $\delta$ ). Stable, plate-shaped that is inconsistent with the  $\gamma$  matrix. This phase is present in leagues of Inconel 718. It can be favorable to inhibit grain growth and strengthen the alloy in small amounts. Large quantities can weaken the material.
- **Carbides and borides:** there is the formation of carbides, generally responsible for abrasive wear on carbide tools. Carbon can vary within the structure from 0.05 to 0.2%, forming primary precipitates of the MC type, where M is the metal element that joins the carbon. These precipitates are created by binding elements such as titanium, tantalum, and hafnium. The mechanical work can promote the decomposition of precipitates of the MC type, forming  $\text{M}_{23}\text{C}_6$  or  $\text{M}_6\text{C}$  that are formed next to the grain boundaries and are responsible for work hardening.

Ezugwu et al. (1999) mentioned that heat treatment has developed to form grain boundaries  $\gamma'$  precipitates to inhibit the spread of cracks and thus ensure highest resistance to breakage [119]. According to Reed (2008), some types of aged superalloys, such as Inconel 718, form intermetallic phases, such as the Topologically Close-Packed structure (TCP) present in the phases  $\mu$ ,  $\sigma$ , laves, etc., which may cause weakening and loss of creep resistance, so it should be avoided [120].

Reed (2008) cites that strengthening a superalloy is crucial to ensure a microstructure that guarantees the desired mechanical properties. These are strongly associated with the morphology of grain boundaries that is influenced by the phases discussed above, such as  $\gamma'$ ,  $\gamma''$ , carbides, borides, etc. Ezugwu et al. (1999) explained at least three processes for strengthening the microstructure of superalloys.

- **Strengthening by solid solution:** consists of adding elements whose atomic radius can range from 1 to 13% of the nickel, ensuring creep resistance. These elements form a substitutional solid solution, hardening the crystalline network, and must have good solubility in the matrix ( $\gamma$ ) and a high melting point. Typical

elements include cobalt, iron, chromium, titanium, vanadium, molybdenum, tungsten, and aluminum.

- **Hardening by Precipitation:** this hardening mechanism occurs mainly by the precipitation of the  $\gamma'$  within the Gamma matrix ( $\gamma$ ). The hardening level is causally related to the amount of  $\text{Ni}_3(\text{Al, Ti})$  dispersed, the volume fraction, their size, and the anti-phase boundary – APB energy. APB energy is given depending on the level of organization of the structure of the  $\gamma'$  particulates. When there is a network failure of this structure, it creates a high-deformation zone that makes dislocations challenging to move. To deform, it is necessary to overcome the strength of APB.  $\text{Ni}_3$  elements (Al, Ti) make cracks challenging to propagate in grain boundary regions. Carbides or borides are not as effective in this hardening mechanism because of their low volume fraction. However, they play an essential role in creep and fatigue resistance. If the  $\gamma'$  phase is saturated with niobium, titanium, or tantalum, the structure may transform. For example,  $\text{Ni}_3\text{Ti}$  in a metastable eta phase ( $\eta$ ) of a compact hexagonal structure can interfere with the mechanical properties of the material. Also, if niobium saturation occurs, there will be the transformation of the metastable eta phase ( $\eta$ ) for a  $\gamma''$  phase of a centered body tetragonal structure (CBT) until it reaches  $\text{Ni}_3\text{Nb}$  equilibrium with an orthorhombic structure.
- **Hardening by carbide dispersion:** at high temperatures, the  $\gamma'$  precipitates tend to solubilize, forming a new stable phase insoluble in the matrix. One way to contain this change is by using oxides homogeneously dispersed in the matrix. Carbides are also used in dispersion hardening, formed by structures  $\text{M}_6\text{C}$ ,  $\text{M}_7\text{C}_3$ , and  $\text{M}_{23}\text{C}_6$ . These structures tend to form and concentrate in the grain boundary regions, hindering the propagation of cracks and increasing the material strength. However, due to the high hardness and stability, in excess, they can weaken the material. Therefore, there must be strict control to ensure the best possible mechanical properties in the casting process of nickel alloys.

Heat treatment is another relevant aspect of ensuring the good mechanical properties of nickel-based superalloys. Ezugwu et al. (1999) further explain that three main processes are:

- **Annealing or softening:** it is indicated for alloys subject to hardening by mechanical work and usually hardened alloys with a solid solution. It aims to promote the recrystallization of grains, increase their size, and relieve microstructure stress. It makes the material more ductile and tougher but less resistant. This process should be done in a controlled manner to avoid the complete solubilization of the precipitate's phases,  $\gamma'$ , carbides, etc.
- **Treatment by solution:** aims at solubilizing or dissolving the phases of the  $\gamma'$  precipitates, carbides, borides, etc., before reheating or aging. Each treatment will depend on the precipitates' solubility temperature, the grains' annealing, the quantity, etc. Thinner grains, or refined crystalline structures, provide better fatigue and tensile resistance, hardness, etc., while coarser structures ensure better resistance to flow.
- **Aging or precipitation hardening:** this treatment promotes the precipitation of harder phases. The main goal is usually to increase the mechanical properties of tensile strength, hardness, fatigue, etc., to the detriment of ductility and toughness. Promotes the formation of more heterogeneous microstructures with the precipitation of the  $\gamma'$ ,  $\gamma''$  phases, carbides, and borides.

Finally, in the words of the authors in Ezugwu et al. (1999), the importance of the development of the mechanical properties of nickel superalloys is given as follows:

*“(i) solid solution reinforcement  $\gamma$ ; (ii) increase the percentage in a volume of  $\gamma'$ ; (iii) increase the power of the fault of  $\gamma'$ ; (iv) hardening of a solid solution of  $\gamma'$ ; (v) reduction in the formation of  $\eta$ ,  $Ni_3Nb$ , Laves, and  $\sigma$  phases; (vi) carbide formation control to avoid grain boundary films with  $M_{23}C_6$  and cellular structures (for tensile strength); and (vii) carbide control and  $\gamma''$  (grain size, etc.) to increase resistance to breakage”.*

Among the nickel-based superalloys, especially nickel-chromo-iron grades, group C, the Inconel 718® stands out. The details will be discussed in the following section.

### 2.3.1. Inconel 718®

In the upcoming subchapters, a comprehensive examination awaits. This scholarly journey commences with a meticulous exploration of Inconel 718®, a superlative superalloy of substantial scientific and industrial significance. This expedition begins with a systematic exposition of the alloy's overarching attributes and multifarious applications. Subsequently, the intricate terrain of machining Inconel 718® shall be navigated, dissecting the intricate challenges inherent in this process. The expedition further extends to the domain of wear mechanisms, with a particular focus on those germane to Inconel 718®. The aim is to contribute sagacious insights, deeply rooted in rigorous research, to this scholarly discourse.

#### 2.3.1.1. General overview of Inconel 718®

Inconel 718 belongs to group C and is a nickel-chromium-iron alloy containing significant amounts of niobium, molybdenum, titanium, and tantalum. It was originally developed in the late 1950s by H.L Eiselstein for use as a jet engine turbine disc by General Electric (GE), and it was patented by the International Nickel Corporation [111,118]. This material possesses good mechanical, corrosion, and creep resistance, even at temperatures up to 700 °C. Through aging and precipitation heat treatment, it achieves a high hardness of approximately 388 HV [112]. In manufacturing, it exhibits exceptional weldability, forging, casting, and brazing capabilities [121,122]. However, it is essential to note that Inconel 718 has lower machinability than stainless steel and aluminum, which are approximately 75% and 94% easier to machine, respectively [123].

By the beginning of the 21<sup>st</sup> century, it accounted for nearly 50% of all superalloys used worldwide. Its versatility and performance have led to its widespread applications in sectors such as medical (orthopedic prostheses and dentistry), aeronautics (gas turbines, combustion chambers, screws, housings, exhaust systems, turbines, blades), as well as in space, naval, defense, petrochemical (structural elements, screws, fans, valves, cryogenic vessels), and electronics and nuclear industries [111,124].

For reference, the chemical composition of Inconel 718 is presented in **Table 2-5**, while **Table 2-6** provides information on its physical and mechanical properties.

**Table 2-5:** Inconel 718 chemical composition

		Composition (wt.%) <sup>(a)</sup>															
		Ni	Cr	Fe	Co	Mo	W	Nb	Ti	Al	C	Mn	Si	B	Cu	S	Outros
Min		50	17	bal	1.0	2.8	***	4.75	0.65	0.20	0.08	0.35	0.35	0.006	0.3	***	***
Max		55 <sup>(b)</sup>	21			3.3		5.5 <sup>(c)</sup>	1.15	0.80							

a) Single values are maximum values unless otherwise indicated.  
b) Nickel plus cobalt content.  
c) Niobium plus tantalum content.

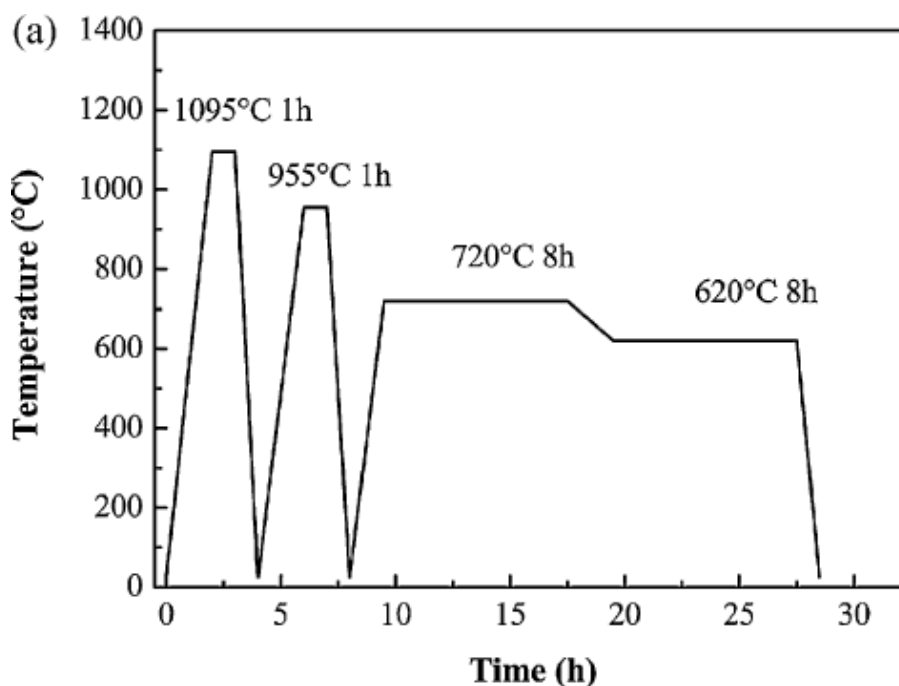
Source: adapted from [112]

**Table 2-6:** Mechanical and physical properties of Inconel 718 AMS 5663M

Temperature [°C]	Ultimate tensile strength [MPa]	Young modulus (0.2%) [MPa]	Density [kg/m <sup>3</sup> ]	Melting point [°C]	Thermal Conductivity [W/m <sup>2</sup> K]
Ambient	1594	1926	8190	1300	11,2
600	1366	1596			

Source: [125]

Inconel 718 is commercially available predominantly in two conditions: annealed for softening and stress relief. In a most recent advancement, it can also be found by additive manufacturing more related to specific applications [126]. Also, it can be precipitated and aged to enhance its mechanical strength. As mentioned earlier, during precipitation hardening, the formation of the  $\gamma'$  phase occurs, which is primarily composed of  $\text{Ni}_3(\text{Al}, \text{Ti})$  and contains significant amounts of titanium and aluminum. However, when this phase reaches saturation, a structural transformation may occur, forming a metastable eta ( $\eta$ ) phase with a compact hexagonal structure, typically composed of  $\text{Ni}_3\text{Ti}$ . Furthermore, with niobium saturation, the metastable phase undergoes a transformation from eta ( $\eta$ ) to a highly hardened  $\gamma''$  phase with a centered body tetragonal structure, eventually achieving a balance with the formation of  $\text{Ni}_3\text{Nb}$ , which exhibits an orthorhombic structure. These structural transformations contribute significantly to the hardening of Inconel 718. Other alloying elements, such as molybdenum and tantalum, contribute to solid precipitation hardening. Additionally, carbon and boron facilitate hardening by forming carbides and borides [119].

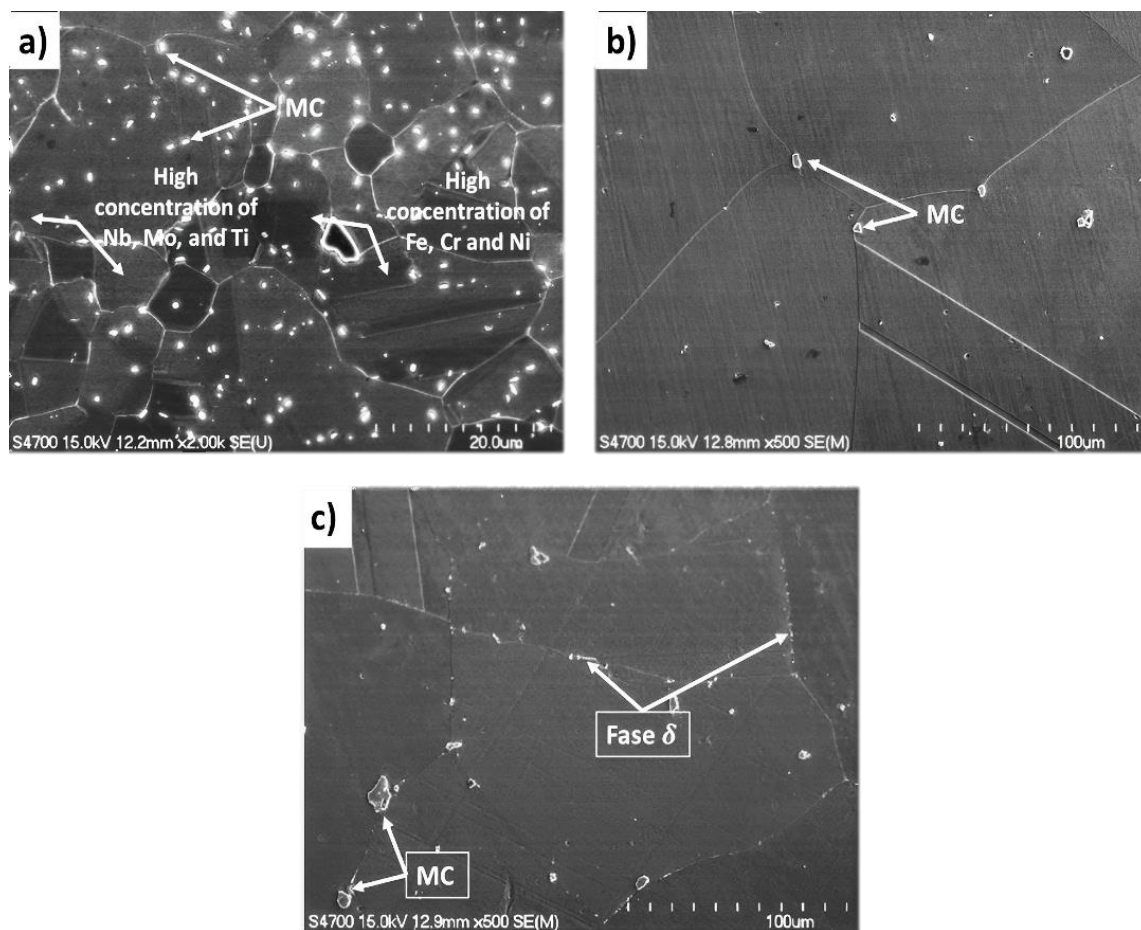


**Figure 2-43:** Standard Heat Treatment Diagram of the Inconel 718 (precipitated and aged)

Source: [127]

Kuo et al. (2009) explained the standard heat treatment process for producing Inconel 718, which involves solubilization and aging steps, as depicted in **Figure 2-43** of the heat treatment diagram [127]. The first step is solubilization, where the alloy is heated to a temperature of 1,095 °C and then cooled for 1 hour in atmospheric air (AA) until it reaches room temperature. This process allows for the dissolution of carbides and the Laves phase back into the Gamma matrix ( $\gamma$ ). The aging process occurs in two stages. In the first stage, the alloy is heated to 955 °C and then cooled to room temperature for 1 hour in atmospheric air (AA). During this stage, precipitation of the  $\delta$  phase takes place, which occurs along the grain boundaries. This precipitation hinders the growth of the grain boundaries, leading to the refinement and strengthening of the microstructure.

In the second stage of aging, the alloy undergoes a heat treatment where the precipitation of the  $\gamma'$  and  $\gamma''$  hardened phases occurs. Inconel 718 is heated to 720 °C and held at this temperature for 8 hours. Subsequently, it is cooled in a furnace with a cooling rate of 57 K/h until it reaches 620 °C for 8h, then it is cooled in atmospheric air (AA) [127]. **Figure 2-44** displays the microstructure of Inconel 718 at different stages of the heat treatment process, highlighting the presence of carbide and  $\delta$  phases.



**Figure 2-44:** Raw structure of Inconel 718 (a) (2,000x); structure after solubilization treatment (b) (500x) (1,095°C 1h/AA) and after aging (c) (500x) (955 1h/AA)

Source: [127]

### 2.3.1.2. Inconel 718® machinability

Inconel 718 poses several challenges arise during cutting [128]. These include: i) high hardness that persists even at elevated temperatures; ii) continuous hardening due to mechanical work; iii) high shear resistance; iv) low thermal conductivity, which concentrates heat in the tool-workpiece contact area; v) elevated temperatures that accelerate tool wear; vi) limited cutting speeds (typically 40 to 50 m/min) with carbides. As these values fall within the range where build-up edge (BUE) formation can occur; vii) the presence of abrasive carbide particles within the microstructure; viii) chemical affinity that promotes diffusive wear, especially at high temperatures; ix) material adherence to the tool surface due to high cutting temperature and pressure; x) formation of long chips that are difficult to control due to the high mechanical strength of Inconel 718 [77,79,128]. These factors, combined with the complex extraction and casting processes (attributed to the alloy's high melting point), significantly hinder the competitiveness of these alloys, limiting their use to exceptional cases.

A summary of studies conducted on Inconel 718 and the developed cutting parameters can be found in **Table 2-7**.

**Table 2-7:** Studies of Inconel 718 with cutting parameters and response variables

Reference	Cutting Speed (m/min)	Feed (mm/rev)	Depth of cut (mm)	Remarks
(He et al., 2016)	60; 40; 80	0.3; 0.2; 0.10	0.7; 0.5; 0.3	Residual stresses of compression
(Iturbe et al., 2016)	70	0.2	0.2	Surface Integrity and Tool wear
(Kumar et al., 2017)	30; 50; 70; 90; 110	0.075; 0.10; 0.125; 0.150; 0.175	0.20	Surface roughness
(Shokrani et al., 2017)	60	0.05	20 e radial 1	Tool wear, surface roughness, and tool life
(Paturi et al., 2016)	60; 80; 100	0.1; 0.2; 0.3	0.01; 0.075; 0.1	Surface roughness
(Yazid et al., 2011)	90; 120; 150	0.10; 0.15	0.30 e 0.50	Surface integrity
(Kitagawa et al., 1997)	30; 50; 100; 150; 200; 250; 300	0.19	0.50	Tool Wear and Temperature
(Jafarian et al., 2016)	75; 100; 125; 150	0.015; 0.025; 0.035; 0.045	0.15; 0.25; 0.35; 0.45	Surface roughness and Tool wear
(Thirumalai et al., 2012)	25; 35; 45	0.10; 0.15; 0.20	1.0; 1.25; 1.50	Surface roughness and Tool wear

Source: [79]

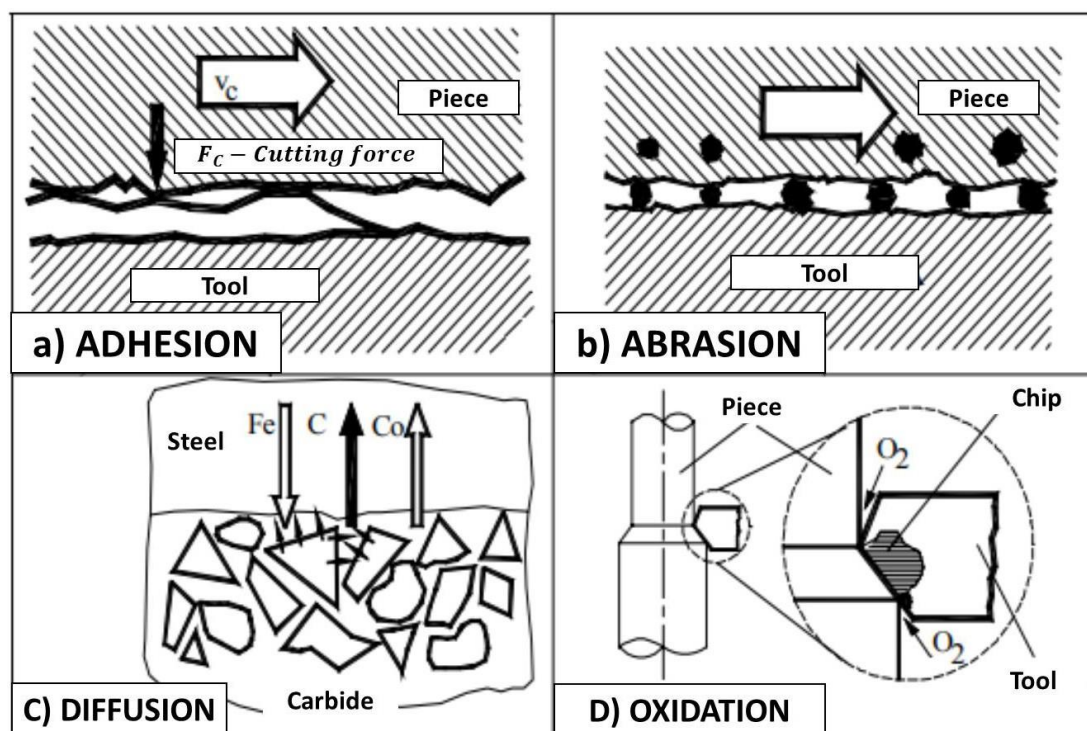


Roy et al. (2018) comprehensively reviewed the machinability of Inconel 718 regarding processes, environment, tool wear, temperature, and surface integrity. In the author's words, the main conclusions observed were:

- *“The abrasive wear at the trailing machining edge was found to be the most vital wear mechanism of the cutting tool. Coated tools generated a better surface finish than uncoated tools during high-speed machining operations. The tool's wear was found to be mainly dependent on the machining speed followed by feed and depth of cut.*
- *Notch wear, chipping of tool tip, flank and crater wear were noticed main types of tool failure in various machining operations.*
- *It was found that during machining operation most of the heat was generated at the rake face of the tool around the cutting edge and by proper application of coolant can drastically reduce the heat generated during machining. It was found that cutting speed was the most dominating factor for wear of the tool followed by machining temperature.*
- *Enhanced surface finish was achieved by increasing the cutting speed and reducing the feed rate and depth of cut during machining operation of super alloy.”*

### 2.3.1.3. Wear mechanisms & types for Inconel 718®

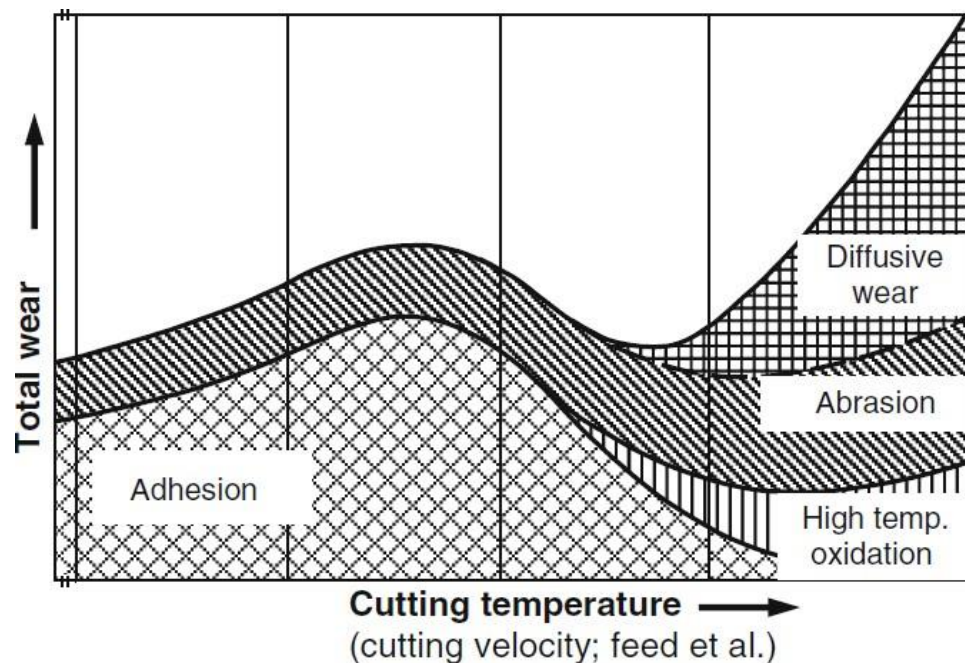
The tool wear process can be divided into two main categories: mechanisms and types of wear. In their study, Machado et al. (2015) identified some phenomena contributing to wear mechanisms, as depicted in **Figure 2-45**. It is worth noting that the intensity of these phenomena and their impact on tools are closely linked to the process's temperature (cutting speed), as illustrated in **Figure 2-46**. The literature has extensively described these four physical-chemical wear phenomena [4,37,129,130].



**Figure 2-45:** Physical-chemical phenomena of tool wear: adhesion (a); abrasion (b); diffusion (c); oxidation (d)

Source: [37]

- **Adhesion:** adhesion is a wear phenomenon that occurs at the grain level on the rake and clearance surfaces, both primary and secondary. A rough and non-uniform appearance characterizes it and is more common at low cutting speeds, as depicted in **Figure 2-47**. However, it can also occur at higher speeds, particularly in areas with irregular material flow. During adhesion, small contact areas experience significant forces, resulting in high stresses that can reach the GPa level and temperatures exceeding 1,000 °C. These conditions

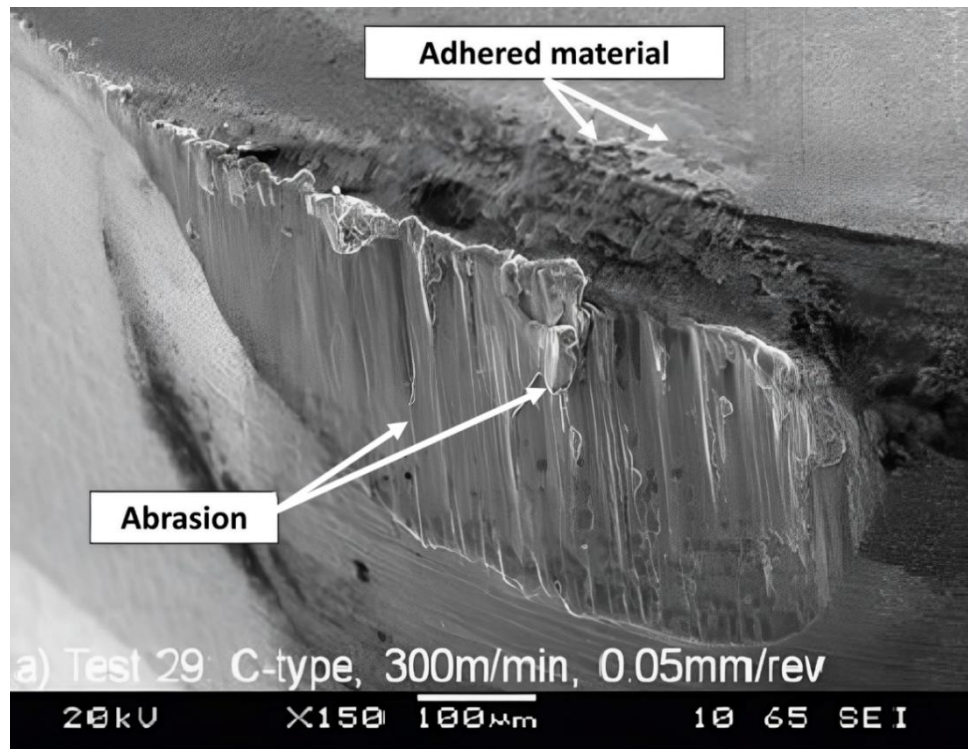


**Figure 2-46:** Wear mechanisms depending on machining parameters and temperature.

Source: [37,129]

promote the formation of strong chemical bonds by exchanging thermally activated free electrons or even mechanical junctions in cases of excessive plastic deformation. Electrons thermally activate diffusion or mechanical junction (notching) if there is too much plastic deformation [130].

The material/tool combination's specific characteristics influence the adhesion's strength. The dynamics of wear through adhesion involve several stages: the initial formation of micro weld points to create the bond, followed by reinforcement of the bond through the flow of compressed chip material onto the tool surface, and ultimately the detachment of the bond due to the flow of the chip itself, as illustrated in **Figure 2-45 (a)**. This wear mechanism is particularly prevalent in the sliding zone (refer to **Figure 2-2**) but can be mitigated in some instances, especially when using effective lubrication and cooling methods [4]. Adhesion is a significant challenge in machining superalloys due to high temperatures, pressures, and chemical affinity, such as Inconel 718. **Figure 2-47** provides an example of adhesive wear with a rough surface.

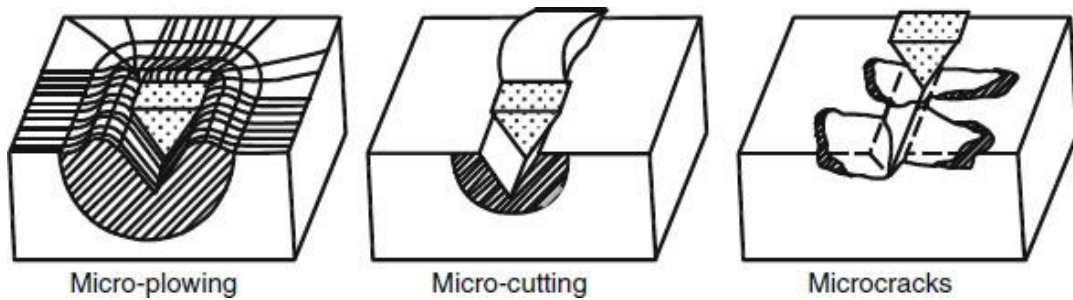


**Figure 2-47:** Abrasion and support details in Inconel 718 machining with uncoated PCBN tool  
 ( $v_c = 300$  m/min,  $f = 0.05$  mm/rev,  $a_p = 0.2$  mm)

Source: [193]

- **Abrasion:** occurs at the grain level, regardless of cutting speed, and is characterized by a uniformly rough surface with parallel grooves aligned in the direction of material flow. It results from the relative movement or sliding between two or more bodies, such as chip/tool or chip/tool/hard particles. Loose particles in this process form a tribological system involving three bodies. Abrasion is commonly observed on the rake surfaces, primarily, and on the clearance surfaces (both primary and secondary) [4]. The mechanism typically begins with the sliding motion between two bodies, where the hard phases in the microstructure, such as oxides, carbides, nitrides, borides, etc., meet the cutting tool. These hard phases eventually loosen and form particles, forming a tribological system involving three bodies.

The type of abrasive wear can vary depending on the material. It can occur through plastic deformation or brittle fracture, with the harder material rubbing against the softer one. Micro-plowing, micro-cutting, or microcracks are some examples of the different types of abrasive wear, as illustrated in **Figure 2-48**.



**Figure 2-48:** Types of abrasive wear caused by particles

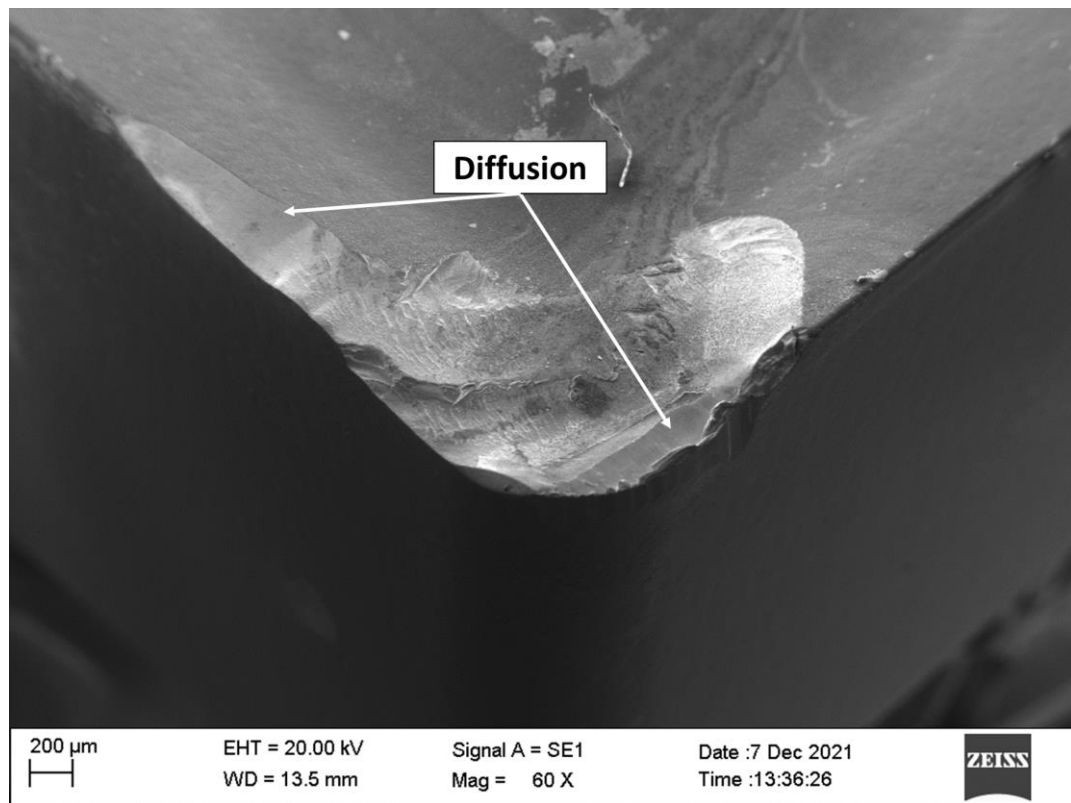
Source: [37]

In the case of micro-plowing, the wear mechanism involves the formation of lateral grooves characterized by elastoplastic deformation without material pull-out. This differs from micro-cutting, where the worn material is removed as a chip. Fragile materials can experience the formation of micro-cracks or erosion. **Figure 2-47** illustrates the details of abrasive wear, showing the orientation of the grooves in the direction of sliding between the workpiece and the tool. This mechanism is prominently observed in the machining of Inconel 718, primarily due to hard phases such as carbides,  $\gamma'$ ,  $\gamma''$ , and  $\delta$  [7].

- **Diffusion** occurs at the interatomic level on the tool's output and clearance surfaces (primary and secondary). It has a smooth appearance and is activated at high temperatures, specifically at high cutting speeds. The type of interaction, or affinity, between the workpiece and the tool influences this wear mechanism, considering factors like solubility, atom size, type of solution, and interatomic, interstitial, or substitutional exchange.

The process involves the formation of the adhesion zone (AZ). At the point of contact with the tool, the chip velocity is zero, creating conditions for diffuse exchanges that require some time. The adhesion zone is continuously renewed as the existing zone detaches and a new one forms. Without this renewal process, the adhesion zone would act as a protective layer for the tool [4]. Although the amount of material worn from the tool is relatively low due to this mechanism, the main concern is the weakening of the tool due to the diffusion of specific alloying elements, such as Cobalt, in the case of carbide tools. This weakening grows exponentially with increasing temperature, posing a challenge for superalloys that experience high temperatures near the cutting edge, such as

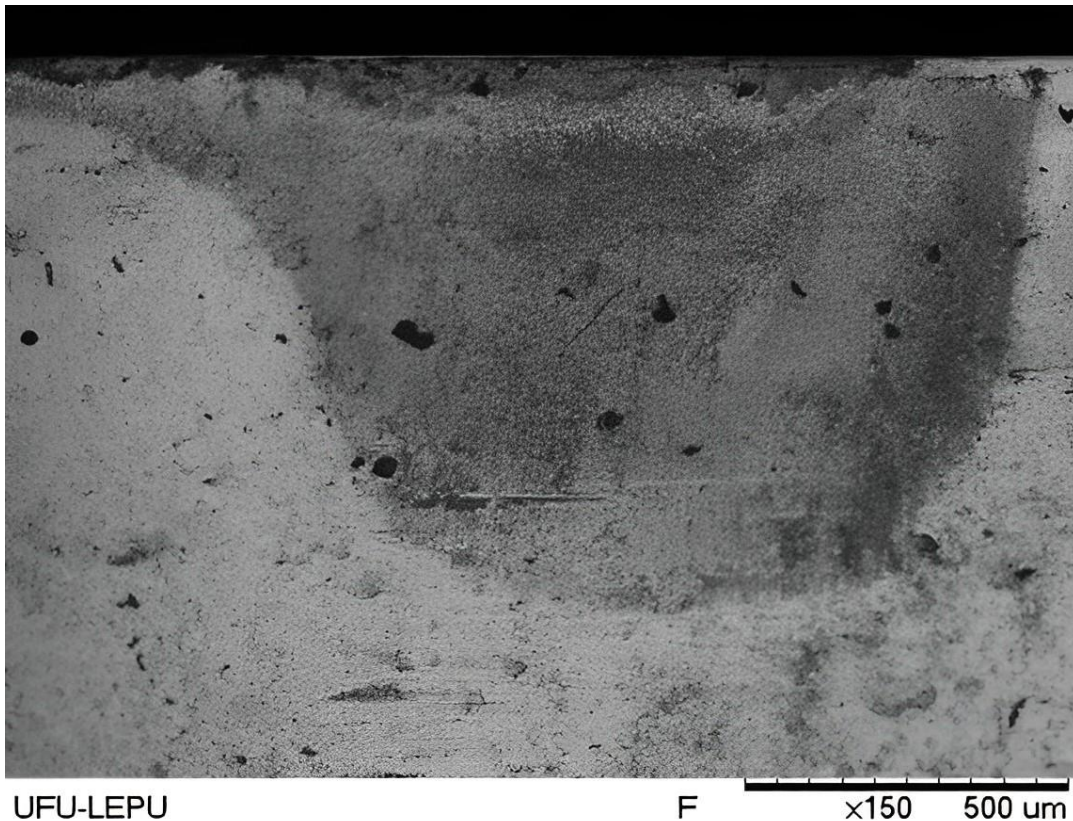
Inconel 718. **Figure 2-49** illustrates the details of diffusion in carbide tool wear during the machining of the Inconel 718 superalloy.



**Figure 2-49:** Details of diffusion mechanism (smooth surface) on S20 carbide tool after machining Inconel 718 with CFA

**Oxidation:** occurs at the interatomic level on the tool's output and clearance surfaces (primary and secondary). It is characterized by a rough appearance and a stain and is activated by both friction and high temperatures, particularly at high cutting speeds. The nature of the interaction or affinity between the workpiece and the tool plays a significant role in chemical wear. Ceramic and ultrahard materials are generally chemically inert or resistant to this type of wear. However, materials such as high-speed steel and carbide can be significantly affected [4].

The dynamics of the chemical wear process involve an oxi-reduction reaction, where one of the materials involved in the wear yields electrons from its valence layer. The resulting oxidizing layer can carry the material flow or adhere to the tool, forming a coating. Chemical wear is commonly observed near the cutting zone, where thermal activation is present. In **Figure 2-50**, the dark spot indicates the presence of the oxidizing layer on the chip, which was not removed during the cutting process.



**Figure 2-50:** Oxidizing dark spot on the main flank face in a class K cemented carbide tool after grey cast iron machining.

According to Trent & Wright (2000) additional mechanisms are plastic deformation by shearing at high temperatures and plastic deformation under compressive stresses. Notch wear and oxidation are also considered part of the wear mechanisms by these authors. On the other hand, Klocke (2011) identifies five wear mechanisms, with one being separate from the main four. This additional mechanism is surface damage caused by the tribological alternating state of stresses.

Continuous wear mechanisms acting on tools give rise to various wear shapes. As depicted in **Figure 2-51**, these wear types include crater wear (A), notches (B, C, E), flank wear (D), and plastic deformation. These wear types manifest on the primary and secondary clearance (flank) faces, as well as on the rake face of the tool. Flank and crater wear are progressive types that naturally occur during machining. In contrast, notch wear can be mitigated in different scenarios, primarily by adjusting cutting parameters (Dearnley & Trent, 1982; Klocke, 2011; Machado et al., 2015; Trent & Wright, 2000). **Figure 2-52** depicts parameters for measuring wear of cutting tools according to standard (ISO 3685, 1993)[132].

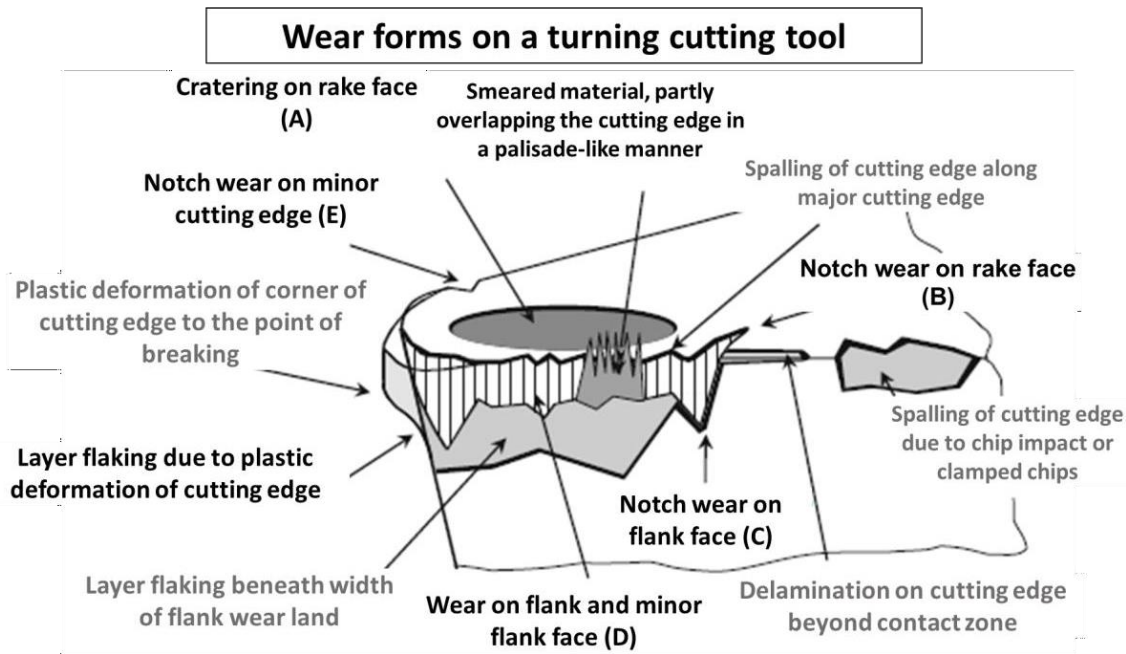


Figure 2-51: Wear forms on a turning cutting tool

Source: [37]

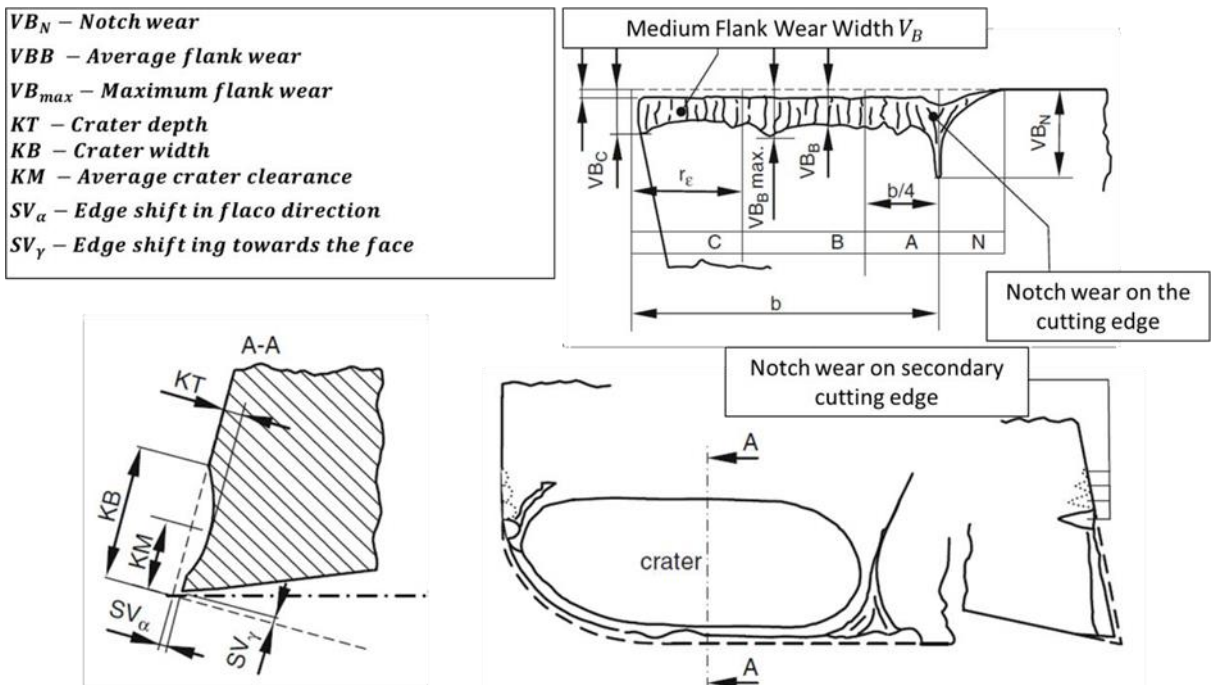


Figure 2-52: Parameters for measuring wear of cutting tools according to standard (ISO 3685, 1993)

Source: (ISO 3685, 1993)



High tool wear can harm the machining process, leading to increased cutting forces, higher energy consumption, compromised dimensional accuracy, surface integrity issues, and amplified vibrations. The ISO 3685 (1993) standard provides measurement methods and recommended criteria to determine the end of tool life. It should be noted that plastic deformation, although an unpredictable type of wear, is not quantified in the standard as its occurrence depends on the specific machining process. As per ISO 3685 (1993):

- **Crater depth ( $KT$ ):** is an inevitable consequence of chip friction with the tool rake surface. It is primarily caused by abrasion and oxidation mechanisms, with diffusion playing a significant role at higher cutting speeds. In tools made of high-speed steel, carbide, and ceramics, the criterion for tool life is determined based on this type of wear. The formula (Eq. 16) provides the basis for assessing tool life concerning this wear mechanism:

$$KT = 0.06 + 0.3fc \quad (16)$$

Where:  $fc$  is the feed in mm/rev.

- **Notch wear ( $VB_N$  or  $VB_C$ ):** can be prevented by carefully managing the machining parameters and controlling the environment. This type of wear occurs at the apex of the V-shaped depth of cut, where the primary or secondary clearance face meets the tool's rake face. It is predominantly caused by the combined effects of high oxidation, mechanical, and thermal stress, particularly in materials with high heat generation rates like Inconel 718. For tools made of high-speed steel, carbide, and ceramics, the tool life criterion is determined using the following value:

$$VB_N \text{ or } VB_C < 1.0 \text{ mm}$$

- **Flank wear:** refers to the gradual formation of wear at the intersection of a tool's flank and outlet surfaces, specifically at the primary and secondary cutting edges. This wear is primarily caused by the rubbing and scraping between two or more surfaces, resulting in abrasion and friction. Additionally, adhesion may also contribute to the formation of flank wear, while diffusion and oxidation can occur at higher temperatures. In practical terms, flank wear reduces the tool's ability to

cut effectively. For HSS, carbide, and ceramic tools, the expected lifespan is determined by the following criteria, as represented by the values:

$$VB_B < 0.3 \text{ mm}$$

$$VB_{Bmax} < 0.6 \text{ mm}$$

During the machining process of Inconel 718, several wear mechanisms are observed, including oxidation, diffusion, abrasion, and adhesion. These alloys possess a low coefficient of thermal conductivity (Inconel 718: 11.2 W/m.K; AISI Steel 1020: 51.1 W/m.K), causing heat to concentrate on the cutting tool and leading to high temperatures, even at low cutting speeds. Notch wear is considered a significant and major issue among the various types of wear, while flank wear is also commonly observed. However, crater wear is not as problematic since the other types tend to occur first [79]. **Table 2-8** provides an overview of studies conducted on wear in cutting tools during the machining of Inconel 718 [79].

**Table 2-8:** Summary of wear types and their causes in different machining processes of Inconel 718

Reference	Types of wear	Cutting tool	Machining operation	Remarks
(Grzesik et al., 2018)	Notch wear	Coated Carbide (AlTiN/AlTiN)	Turning	Due to the abrasive wear mechanism at the trailing cutting edge
(Çelik et al., 2017)	Flank wear rake	SiAlON milling cutter	Milling	Due to severe adhesion of the workpiece with flank and rake surface of the tool
(Cantero et al., 2013)	Notch and Flank wear	Coated carbide (TiAl/TiAlN)	Turning	Due to high work hardening of the workpiece and high machining temperature
(D'addona et al., 2017)	Flank Wear	Coated Carbide(CVD)	Turning	Due to the low thermal conductivity of the workpiece and high machining speed
(Zhuang et al., 2014)	Notch Wear	<i>Kennametal roundtype</i>	Turning	Due to the hardened layer beneath the workpiece surface
(Y. C. Chen & Liao, 2003)	Flank wear and chipping at outer machining edge	Coated Carbide(TiAlN)	Drilling	Due to friction between the tool and the workpiece
(Xavior et al., 2017)	Notch wear, Crater wear, Flank wear	Coated Carbide(TiAlN, PVD) Ceramic (Al <sub>2</sub> O <sub>3</sub> - TiC) CBN inserts	Turning	Due to adhesion, thermal softening, notching, diffusion, and thermal cracking

Source: [79]

### 2.3.1.4. Tools materials for Inconel 718<sup>®</sup> machining

A wide range of tool materials can be utilized for machining Inconel 718 alloys. The key physical and mechanical characteristics required for such materials, including: (i) excellent toughness, (ii) high hardness, (iii) chemical inertness, (iv) high mechanical strength, (v) thermal stability, (vi) resistance to thermal and mechanical shock, and (vii) good thermal conductivity. The most used tools have been high-speed steel (HSS) and carbides for many years [77,119,128].

Tungsten carbides are typically used at low cutting speeds within the range of  $10 < v_c < 50 \text{ m/min}$  [79]. High cutting speeds should be avoided as they result in concentrated heat in the cutting zone, leading to severe flank and notch wear. Catastrophic failures such as chipping and breaking of inserts are commonly observed, particularly when cutting conditions are harsh (refer to **Figure 2-12**). In order to mitigate these issues, Ezugwu et al. (1999) proposed a ramp machining strategy. This approach involves continuously and gradually altering the depth of cut, allowing notch and flank wear to develop uniformly along the entire cutting edge. Consequently, the wear initially observed in the notches transforms into flank wear over time.

In addition to tungsten carbides, other tool materials commonly used for turning Inconel 718 include aluminum oxide ( $\text{Al}_2\text{O}_3$ ) and silicon nitride ( $\text{Si}_3\text{N}_4$ )-based ceramics. However, pure  $\text{Al}_2\text{O}_3$  tools are characterized by poor conductivity and fragility. Additional elements are incorporated in weight percentages to enhance their thermal properties and toughness to form reinforced structures [79]. For example, adding zirconium oxide ( $\text{ZrO}_2$ ) improves toughness, while titanium carbide (TiC) enhances thermal resistance and hardness. These tools have demonstrated the ability to machine nickel superalloys at speeds ranging from 120 to 240 m/min [134]. However, it is essential to note that the tool life is considerably limited at such high speeds due to notch and flank wear [119].

According to Choudhury & El-Baradie (1998), the highest productivity in machining Inconel 718 was achieved using ceramic alumina tools reinforced with whiskers at cutting speeds ranging from 200 to 750 m/min [134]. On the other hand, Cubic Boron Nitride tools showed poor performance at speeds between 120 and 240 m/min. However, it should be noted that these specific tools are expensive and fragile, and their usage can

only be justified when economically viable [30]. **Table 2-9** provides information on each tool type's mechanical and physical properties.

**Table 2-9:** Properties of different types of tool materials in Inconel 718 machining

Material properties	Tool material					
	Tungsten carbide (K10) 94% WC + 6% Co (pp%)	Alumina 90 ~95% Al <sub>2</sub> O <sub>3</sub> + 5 ~ 10% ZrO <sub>2</sub>	Alumina mixture Al <sub>2</sub> O <sub>3</sub> +30% TiC + 5~10% ZrO <sub>2</sub> , Al <sub>2</sub> O <sub>3</sub> +30% TiN + 5 ~10% ZrO <sub>2</sub>	Alumina enhanced with Whiskers 75% Al <sub>2</sub> O <sub>3</sub> + 25% SiC	Sialon 77% Si <sub>3</sub> N <sub>4</sub> +13% Al <sub>2</sub> O <sub>3</sub> + 1% Y <sub>2</sub> O <sub>3</sub>	Boron Cubic Nitride 50 ~ 90% CBN + 50 ~10% TiN - TiC
Grain size (μm)	1 - 2	1 - 2	1 - 2	*	1	1 - 3
Density (g/cm <sup>3</sup> )	14.8	3.9 - 4.0	4.2 - 4.3	3.7	3.2	3.1
Hardness (HV) to 20°C	1 700	1 700	1 900	2 000	1 600	3 000 - 4 500
Hardness (HV) to 1,000 °C	400	650	800	*	900	1 800
Fracture resistance (MN/m <sup>3/2</sup> )	10	1.9	2	8	6	10
Young Module (kN/mm <sup>-2</sup> )	630	380	420	390	300	680
Thermal conductivity (W/m°C)	100	8 - 10	12 - 18	32	23	100
Thermal expansion coefficient (x 10 <sup>-6</sup> /°C)	5 - 6	8.5	8	*	3.2	5
Cutting speed (m/min)	10 < v <sub>c</sub> < 50	*	120 < v <sub>c</sub> < 240	200 < v <sub>c</sub> < 750	*	120 < v <sub>c</sub> < 240

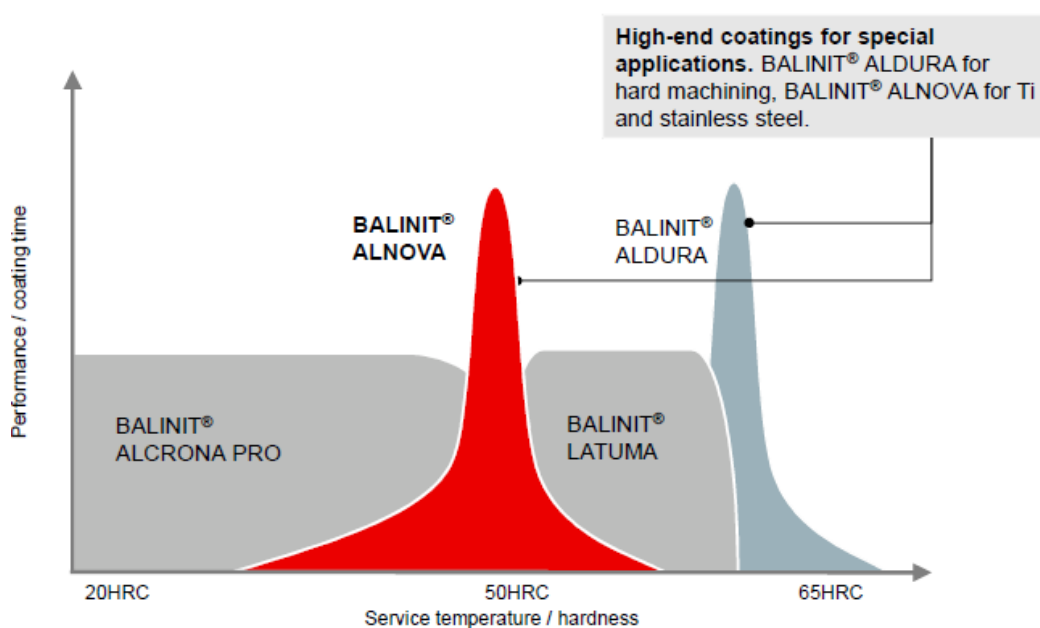
Source: [134,135]

The cutting edge and tool geometry are crucial in both tool life and the quality of machined parts. Ezugwu et al. (1999) emphasized that tools with rhomboid geometry (W) or other shapes with small tooltip angles ( $\epsilon_r$ ) are not recommended for machining superalloys due to the fragility of the cutting edge. As a result, square format (S) or round (R) tools tend to perform better in terms of tool life and surface finish[119]. Selecting the optimal geometry involves carefully considering the strength ratio and specific cutting pressure to ensure optimal performance, beyond tooltip radius, format, etc.

The Inconel 718 alloy exhibits remarkable shear resistance, even at elevated temperatures, and possesses good ductility. These properties form long chips that are challenging to control during machining. Therefore, employing positive insert tools with chip breakers becomes crucial for effectively managing chip formation and controlling the machining process. Additionally, it is vital to consider the environmental conditions during the machining of Inconel 718, as highlighted in the studies by Ezugwu et al., 1999, and Roy et al. (2018).

In the case of carbides and high-speed steel, coatings play a crucial role in enhancing the machining performance of Inconel 718. Coatings like the triple-layer (TiN, TiCN, TiN) have demonstrated excellent resistance properties and can effectively increase cutting speeds. Kamata & Obikawa (2007) observed a significant reduction in the tool life of carbide tools when increasing the cutting speed from 60 m/min to 90 m/min in Inconel 718 machining. The authors also noted that adding coatings allows for improvement in tool life; however, there are limitations at low speeds due to the high machining forces that can cause premature coating detachment [136].

An AlCrN coating, known by the trade name BALINIT® ALNOVA, has emerged as a potential coating for Inconel 718 alloys. The AlCrN coating has been systematically enhanced by a company in the field, as highlighted in a publication by Balzers (2013) [137]. This high-performance coating offers several advantages, including improved adhesivity and high reliability, high stability against thermal shocks suitable for both dry and wet machining, a significant increase in tool life, and excellent stability on cutting edges with efficient chip removal. The application of BALINIT® ALNOVA is recommended explicitly for materials within a specific hardness range, as illustrated in **Figure 2-53**.



**Figure 2-53:** Application range by hardness of BALINITI® coating material AlCrN

Source: adapted from [137]

According to the information provided by Balzers (2013), BALINIT® ALNOVA coating outperforms other types of coatings in various applications. The key advantages of BALINIT® ALNOVA include: (i) superior tool life performance when machining Inconel 718 turbine blades; (ii) increased productivity in titanium roughing milling operations; (iii) reduction of wear width in stainless steel milling; (iv) extended tool life in H13 steel roughing milling. These benefits are summarized in **Table 2-10**, which provides an overview of the newsletters shared by Balzers (2013) [137].

**Table 2-10:** Various operations and results using BALINITI ® ALNOVA

Operation	Material	Tool	Cutting conditions	Remarks
Finishing/ Milling	Inconel 718	<ul style="list-style-type: none"> <li>• Carbide (AlTiN)</li> <li>• Carbide (BALINIT® ALNOVA)</li> <li>• <math>\varnothing = 16 \text{ mm}</math></li> </ul>	<ul style="list-style-type: none"> <li>• <math>v_c = 40 \text{ m/min}</math></li> <li>• <math>f_z = 0.045 \text{ mm/rev}</math></li> <li>• <math>a_p = 22 \text{ mm}</math></li> <li>• <math>a_e = 2 \text{ mm}</math></li> <li>• Emulsion</li> </ul>	BANIT® ALNOVA tool life gain 28%
Roughing/ Milling	TiAl6V4	<ul style="list-style-type: none"> <li>• Carbide (ALNOVA)</li> <li>• Carbide (BALINIT® ALNOVA)</li> </ul>	<ul style="list-style-type: none"> <li>• <math>v_c = 70 \text{ m/min}</math></li> <li>• <math>a_p = 25 \text{ mm}</math></li> <li>• <math>a_e = 7.5 \text{ mm}</math></li> <li>• Emulsion 8%</li> </ul>	125% more parts produced with BALINIT® ALNOVA
Finishing/ Milling	Stainless steel	<ul style="list-style-type: none"> <li>• Carbide (ALNOVA)</li> <li>• Carbide (BALINIT® ALNOVA)</li> <li>• <math>\varnothing = 6 \text{ mm}</math></li> </ul>	<ul style="list-style-type: none"> <li>• <math>v_c = 31 \text{ m/min}</math></li> <li>• <math>a_p = 2 \text{ mm}</math></li> <li>• <math>a_e = 1.9 \text{ mm}</math></li> <li>• Emulsion</li> </ul>	Reduced wear width when milling stainless steel with BALINIT® ALNOVA
Roughing/ Milling	Aço AISI H13	<ul style="list-style-type: none"> <li>• Carbide (AlTiN)</li> <li>• Carbide (ALNOVA)</li> <li>• Carbide (BALINIT® ALNOVA)</li> <li>• <math>\varnothing = 10 \text{ mm}</math></li> </ul>	<ul style="list-style-type: none"> <li>• <math>v_c = 150 \text{ m/min}</math></li> </ul>	Increased tool life by 106% with BALINIT® ALNOVA compared to AlTiN
Roughing/ Milling	AISI 5115	<ul style="list-style-type: none"> <li>• Carbide (TiAlN, Wettbewerb)</li> <li>• Carbide (BALINITI® ALNOVA)</li> <li>• <math>\varnothing = 16 \text{ mm}</math></li> </ul>	<ul style="list-style-type: none"> <li>• <math>v_c = 181 \text{ m/min}</math></li> <li>• <math>f_z = 0.03 \text{ mm/rev}</math></li> <li>• Emulsion 5 %</li> </ul>	Number of workpiece increase (100%) using BALINIT® ALNOVA
Finishing/ Milling	AISI H13 (HRC 45)	<ul style="list-style-type: none"> <li>• Carbide (AlTiN)</li> <li>• Carbide (BALINIT® ALNOVA)</li> <li>• <math>\varnothing = 16 \text{ mm}</math></li> </ul>	<ul style="list-style-type: none"> <li>• <math>v_c = 250 \text{ m/min}</math></li> </ul>	Increased tool life by 106% with BALINIT® ALNOVA compared to AlTiN

Source: adapted from [137]

### 2.3.1.5. Lubri-cooling techniques - Inconel 718®

As a general practice, cemented carbide tools are commonly used for machining nickel-based superalloys, and a technique called cutting fluid in abundance is employed. The main objective of using CFA is to keep the tool cooled due to the significant heat generated during machining. The temperature at the tool tip can reach extremely high levels, exceeding 1,000 °C [62].

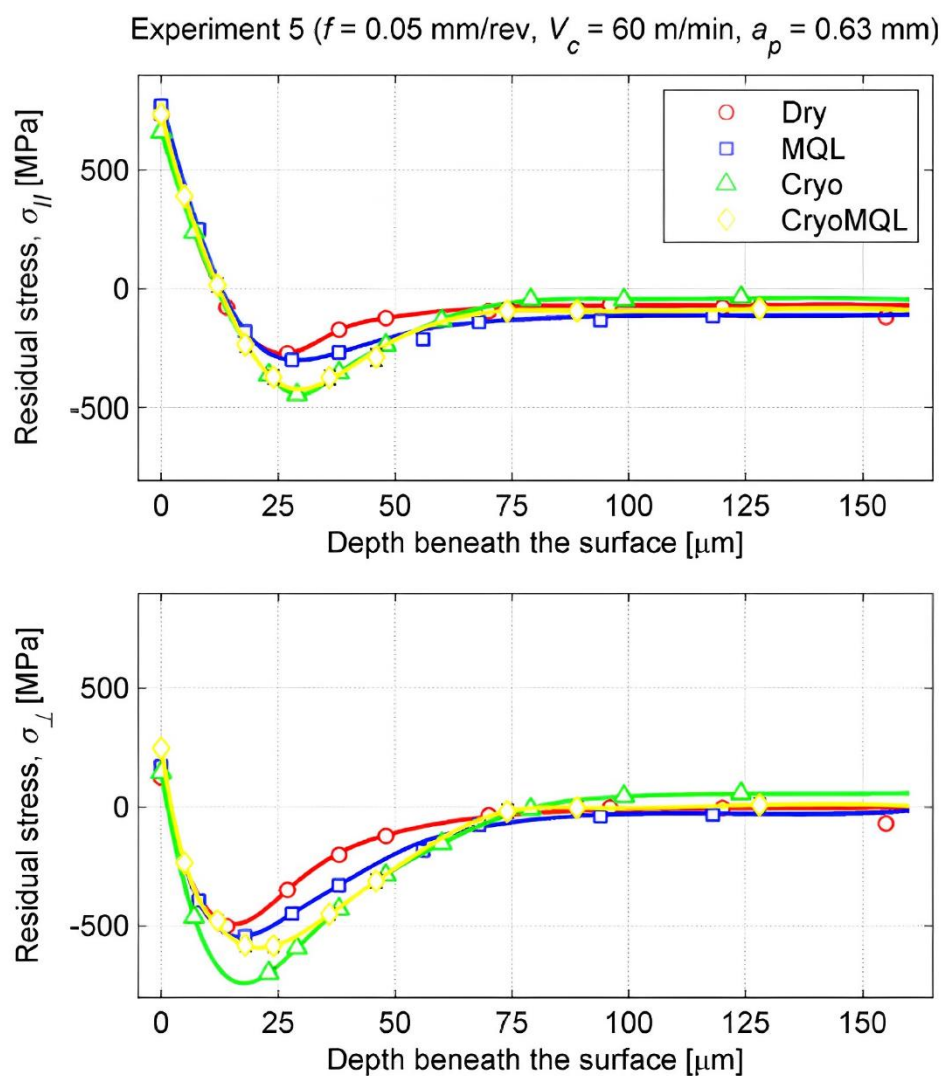
Several studies have explored unconventional cooling methods to enhance machinability and improve productivity. Hegab et al. (2018) specifically investigated the impact of incorporating carbon nanotubes and aluminum oxide nanoparticles ( $\text{Al}_2\text{O}_3$ ) into the oil used in minimum quantity lubrication (MQL) to enhance its cooling effectiveness and overall thermal conductivity [61]. The researchers compared the performance of a conventional MQL with the addition of nanoparticles during the machining of Inconel 718. They evaluated the tool performance and chip morphology. They found that the conventional MQL resulted in more significant flank wear, notch wear, crater wear, adhesive plastically deformed chip, BuE formation, and higher oxidation than the MQL with nanoparticles.

Khanna et al. (2020) conducted a study to assess the wear and hole quality in the drilling process of Inconel 718 using cryogenic cooling compared to a dry process [139]. They utilized helical carbide drills coated with TiAlN and analyzed various variables, including tool life, chip morphology, and hole quality parameters such as roundness, cylindricity, and surface roughness (Ra). The findings revealed significant improvements when employing cryogenic cooling, including a drastic reduction in temperature, a 30% reduction in torque, an 87.50% increase in tool life, reduced deviations in roundness (up to 51%), cylindricity (up to 77%), and surface roughness (up to 48%).

In a study conducted by Shokrani et al. (2017), an unconventional hybrid cooling method known as CryoMQL (MQL with cryogenic fluids) was investigated for the milling of Inconel 718 [140]. The researchers compared the performance of CryoMQL with that of MQL and cryogenics used separately. A 12 mm diameter solid tungsten carbide end mill was employed for the experiments. The results revealed that the hybrid CryoMQL system

outperformed the other cooling methods, doubling the tool's life and improving surface roughness by 18%.

Another study by Kenda et al. (2011) analyzed the residual stresses resulting from turning Inconel 718 using four different lubri-cooling atmospheres: dry, MQL, cryogenics, and cryoMQL [141]. Carbide tools, precisely ISO CNMG 120404 with chip breakers in MF1 format, were utilized in the experiments. The researchers employed X-ray diffraction as the technique for measuring residual stresses. **Figure 2-54** depicts the levels of stresses observed in different directions under various machining environments.



**Figure 2-54:** Residual stresses in two directions (a) radial and (b) longitudinal, under different environments: dry, MQL, cryogenic and *CryoMQL*

Source: adapted from [141]



The results demonstrate that the atmosphere had a significant impact over the residual stresses. Note that cryoMQL atmosphere had the best performance in this concern, reaching lower values for residual stresses, meaning compression tension in the surface.

Ezugwu & Bonney (2004) investigated the impact of high-pressure cutting fluids on the turning process of Inconel 718 [17]. They used a triple-layer coated carbide tool (TiC/Al<sub>2</sub>O<sub>3</sub>/TiN) and cutting speeds of up to 50 m/min, comparing it with conventional flood coolant application. The study measured tool life, wear, surface integrity, and residual stresses.

The results revealed a significant improvement in tool life, with a gain of approximately 740% observed at a pressure of 20.3 MPa. Moreover, the tool life tended to increase with higher fluid pressures. This improvement was attributed to two main factors. Firstly, the high-pressure cutting fluids facilitated the enhanced penetration of the liquid film at the tool/chip interface. Additionally, the fluid's ability to bend and break the chip reduced the contact area, thereby reducing the coefficient of friction on the rake surface. These combined effects contributed to the overall improvement in tool life and machining performance.

In a study conducted by Zhang et al. (2012), the focus was on the tool life and cutting forces in milling Inconel 718 under different cooling conditions: dry machining, cryogenic-cooled MQL, and biodegradable oil [12]. The experimental results demonstrated that MQL was effective in enhancing machinability, resulting in a 57% increase in tool life compared to dry machining.

Additionally, the study observed a reduction in all three components of cutting forces when MQL was used. This reduction indicates that MQL, by acting on the tool/chip interface, facilitated the cutting process and contributed to a decrease in the coefficient of friction. These findings suggest that MQL is a promising technique for improving tool life and cutting force characteristics during the milling of Inconel 718.

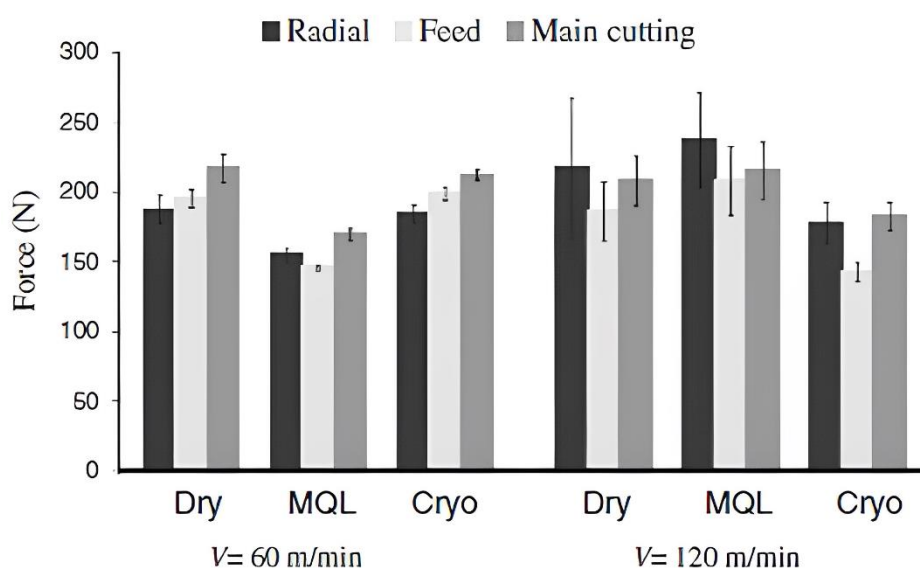
In his research, Kaynak (2014) conducted a comprehensive experimental study to compare the performance of different lubricating atmospheres, namely dry machining, cryogenic cooling, and MQL, in the machining of Inconel 718 [142]. The study examined

various variables: cutting forces, flank wear, notch wear, tool crater wear, cutting temperatures, chip morphology, and surface roughness.

Carbide tools, specifically uncoated ISO CNMG120408 inserts, were used for the turning operation [142]. The study's results indicated that cryogenic cooling offered the best tool life and surface integrity compared to the other cooling methods. Additionally, injector nozzles' number and positioning were crucial in controlling machining forces and temperature.

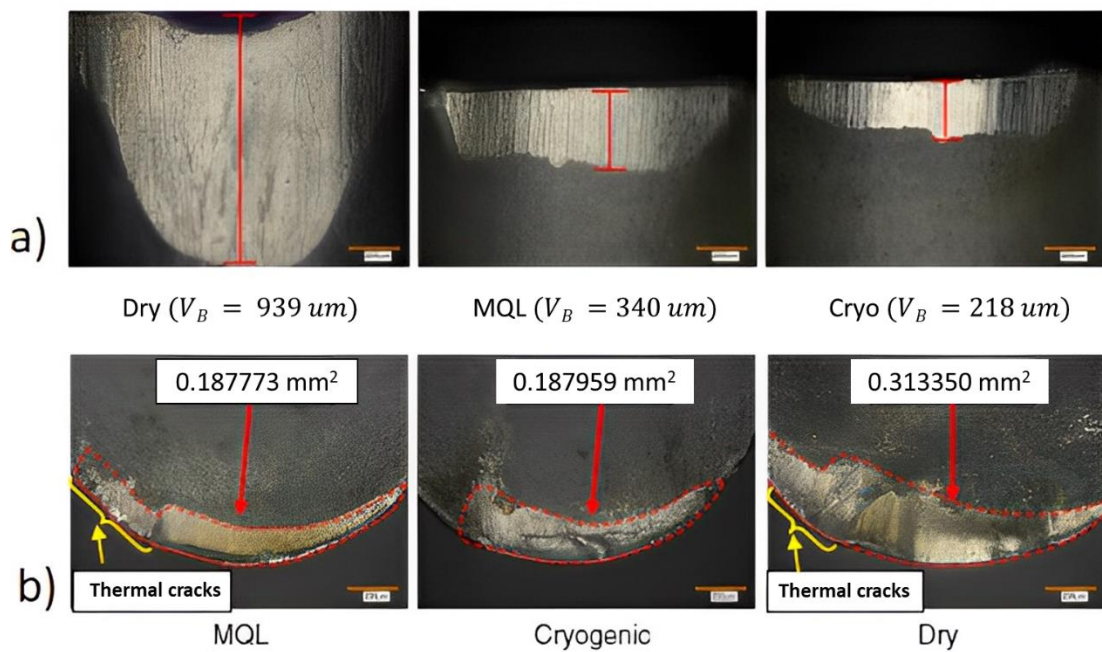
**Figure 2-55** illustrates the machining forces for the three cooling atmospheres at different cutting speeds. **Figure 2-56** displays photographs of the crater and flank wear observed during the experiments. Lastly, **Figure 2-57** presents the maximum temperature measured on chips formed under different cutting atmospheres.

Overall, the study emphasized the importance of selecting an appropriate lubricating atmosphere and optimizing nozzle placement to improve machining performance, tool life, and surface quality in Inconel 718 machining operations.



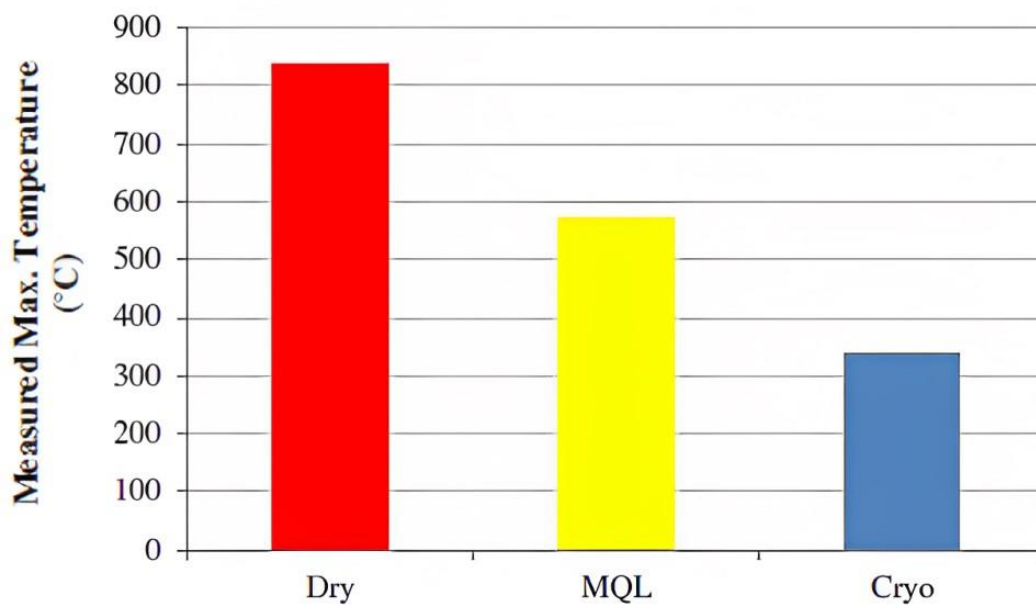
**Figure 2-55:** Main machining forces under different environments and cutting speeds.

Source: [142]



**Figure 2-56:** Wear for speed  $v_c = 120$  m/min, cutting time of 30 s, in different environments. a) Flank wear and b) Crater wear

Source: [142]



**Figure 2-57:** Maximum temperature measured on chips generated under different environments.

Source: [142]

Finally, Roy et al. (2018) conducted a literature review on various machining atmospheres employed in machining Inconel 718 superalloys. The review encompassed

studies that utilized different cooling and lubrication methods such as MQL, dry machining, cryogenics, compressed air cooling, and n-MQL, among others. These studies' findings and key details are summarized in **Table 2-11**, providing a comprehensive overview of the different machining atmospheres employed in Inconel 718 machining.

**Table 2-11: Lubri-cooling techniques used in the machining of Inconel 718**

Reference	Ambient	Machining process	Remarks
[143]	Dry and Cryogenic (LN2)	Milling	Cryogenic cooling proved more efficient and generated better surface roughness
[144]	Dry and Cryogenic (LN2)	Milling	Cryogenic cooling showed better potential for machinability as compared to dry condition
[145]	Dry and Cryogenic (LN2)	Turning	Lower tensile stresses were developed on the workpiece surface using cryogenic cooling
[146]	MQL (synthetic ester and palm oil)	Drilling	Palm oil surpassed synthetic ester in every machining performance
[70]	Flooded and Cryogenic + MQL	Turning	Combining Cryogenic and MQL machining provided better machining performance only for short machining time
[147]	DM, CFA e MQL	Turning	MQL generated a better surface finish
[140]	MQL, Cryogenic and Hybrid cryogenic and MQL (Cryo + MQL)	Turning	The longer life of the tool and better surface roughness was achieved using (Cryo + MQL) condition
[148]	MQL and WS2 solid lubricant MQL	Turning	Lower wear of the tool and better surface finish was obtained using WS2 solid lubricant
[23]	Dry, MQL (50 ml/h) and MQL (100 ml/h)	Turning	Better surface roughness using MQL

Source: [79]

### 2.3.1.6. Surface integrity - Inconel 718®

Surface integrity encompasses several variables crucial in defining the quality and quantifying the characteristics of a material's surface or subsurface. These variables include roughness and its parameters (such as  $R_a$ ,  $R_z$ ,  $R_q$ , etc.), hardness or microhardness, residual stresses, microstructure, crack analyses, color, reflectivity, and emissivity [4]. These variables are significant as they are often used as criteria for acceptance or rejection in production lines, indicating the quality and suitability of the machined surface.

According to Machado et al. (2015), machining results in inevitable changes to the condition of the newly formed surface due to various physical-chemical processes. These processes encompass elastoplastic deformations, shearing, high thermal inputs, residual stresses, chemical reactions, diffusion, and oxidation. In addition, Ezugwu et al. (1999) identify several defects associated with the build-up edge (BUE), including micro and macro hardness changes, the occurrence of micro and macro cracks, as well as marks and distortions. Furthermore, they note that metallurgical transformations, such as phase changes, hardening, or annealing, can occur during machining.

In the aeronautical industry, where reliability is paramount, superalloys like Inconel 718 find extensive application. Surface integrity plays a critical role in manufacturing parts for this industry. Structural parts and aircraft turbines are subjected to harsh operating conditions, including cyclic loads, wide temperature ranges, vibrations, and oxidation. To ensure the longevity and performance of these components, it is crucial to minimize tensile residual stresses that can contribute to crack initiation and propagation. Machined parts should possess compressive residual stresses to enhance their fatigue resistance. Therefore, when machining Inconel 718, addressing the issue of residual stresses becomes a significant consideration (Ezugwu et al., 2003).

According to Ezugwu et al. (1999), the tool wear level significantly impacts the machined parts' surface integrity during the turning of nickel superalloys. When using new tools with a positive insert geometry, the generated surfaces tend to have fewer residual stresses and less plastic deformation. The authors suggest that even better surface finishes, with reduced roughness and minimal surface damage, can be achieved by using rounded inserts. In the case of Inconel 718, the work-hardening effect can be

severe. As a result, it is often recommended to opt for a single pass with a greater depth of cut instead of two consecutive passes. This approach helps mitigate the adverse effects of work hardening and ensures improved surface integrity during machining operations.

The surface hardness of Inconel 718 increases during prolonged machining. This increase in hardness results from the severe flank wear that tools experience during the machining process. Increased wear, higher cutting forces, and elevated temperatures contribute to more significant tool wear, creating a positive feedback loop that ultimately leads to tool breakage.

It is crucial to carefully select the machining process to address surface integrity issues associated with machining Inconel 718. The negative impact on surface integrity can be minimized by choosing the appropriate machining techniques, including tool selection, cutting parameters, and cooling methods (refer to **Figure 2-12**).

**Table 2-12** provides a comprehensive overview of various studies conducted on the surface integrity of Inconel 718 alloys and their respective conclusions. These studies have examined different surface integrity aspects, offering valuable insights for optimizing machining processes and achieving the desired surface quality.

**Table 2-12:** Several studies on the roughness of Inconel 718

Reference	Tool	Atmosphere	Operation	Findings
[150]	Coated insert (Tool S) (TiCN/Al <sub>2</sub> O <sub>3</sub> /TiN) and uncoated insert (Tool H)	Flood (5% solution of semi-synthetic emulsion)	Turning	Worn out tool produced higher surface roughness due to the location of the wear scar
[80]	CVD TiCN-Al <sub>2</sub> O <sub>3</sub> -TiN	Dry and Flood	Turning	Surface roughness was lower using flood cooling
[23]	PVD (TiAlN)	Dry and MQL	Turning	MQL condition produces better surface roughness than dry condition
[151]	CVD Coated Carbide insert	Dry	Turning	Surface roughness was found similar for both high and low cutting speeds
[152]	Cemented Carbide (Al-TiN-TiCN-Tin)	Dry	Turning	Surface roughness was mostly affected by cutting speed and feed rate.
[153]	Cemented Carbide Tool	Wet	Turning	Surface roughness was affected by machining time
[154]	Uncoated Carbide insert	Dry	Turning	Feed rate was the most affecting factor for surface roughness followed by spindle speed and depth of cut

Source: [79]

---

---

## Chapter 3: Experimental procedures

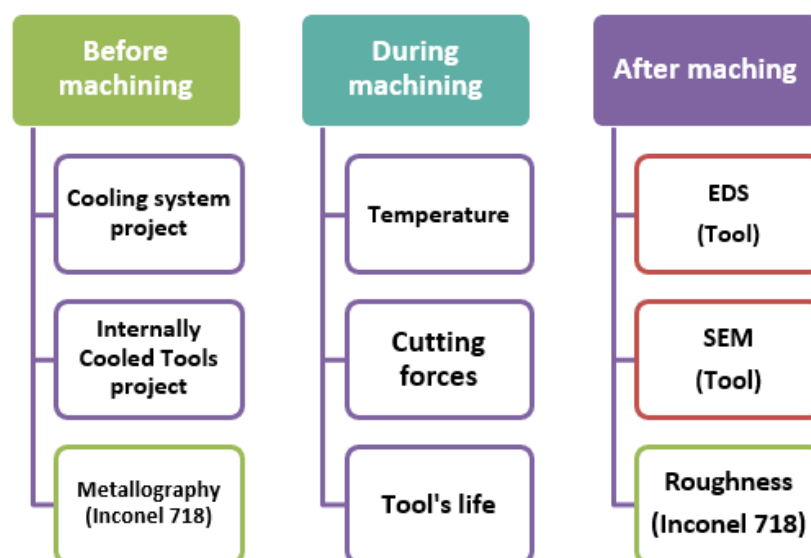
---

---

This chapter systematically explores the experimental procedures critical to the study. Beginning with an examination of the cooling system and Internally Cooled Tools (ICT), it proceeds to delve into Inconel 718® characterization. The chapter covers machinery and fluids used, followed by a detailed analysis of temperature measurements. Finally, it scrutinizes machining and wear mechanisms, offering comprehensive insights into the research. Chapter 3 is pivotal in facilitating rigorous data collection and advancing scientific excellence.

### 3.1. Logical sequencing of experimental procedures

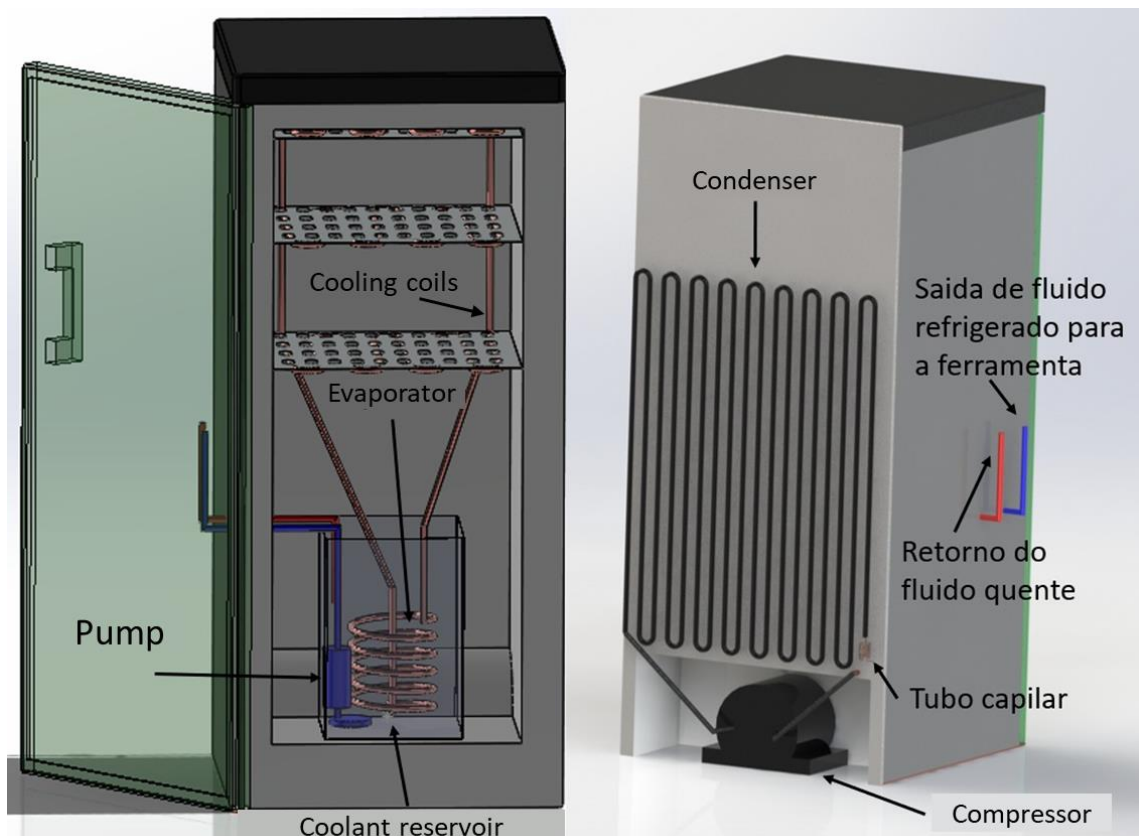
This research project consisted with activities before, during, and after machining to achieve the proposed objectives, as shown in **Figure 3-1**. In the pre-machining stage, refrigeration systems and cutting tools were designed. Metallography tests on Inconel 718 were also performed, aiming at characterization. During machining, tests were done to measure temperature, cutting force ( $F_c$ ), and tool life. Finally, after machining tests, analyses of the worn tools within the scanning electron microscope (SEM) equipped with electron dispersion spectroscopy (EDS) were performed after machining tests to verify the tool wear mechanisms present.



**Figure 3-1:** Diagram of experimental procedures at three levels: before, during, and after machining of Inconel 718

### 3.1.1. Cooling system & Internally Cooled Tools – ICT

To provide cooling during the cutting process, a chiller was utilized. Then, a conventional refrigerator was modified to accommodate the specific cooling requirements. To hold a chilled mixture of water and mono-ethylene glycol as the internal coolant for the tools a device was adapted. Throughout the experiments, the temperature inside the tools was consistently maintained at approximately  $-5\text{ }^{\circ}\text{C}$ . For a visual representation of the refrigeration system, please refer to **Figure 3-2**. Further details and specifications of the cooling systems can be found in **Table 3-1**.



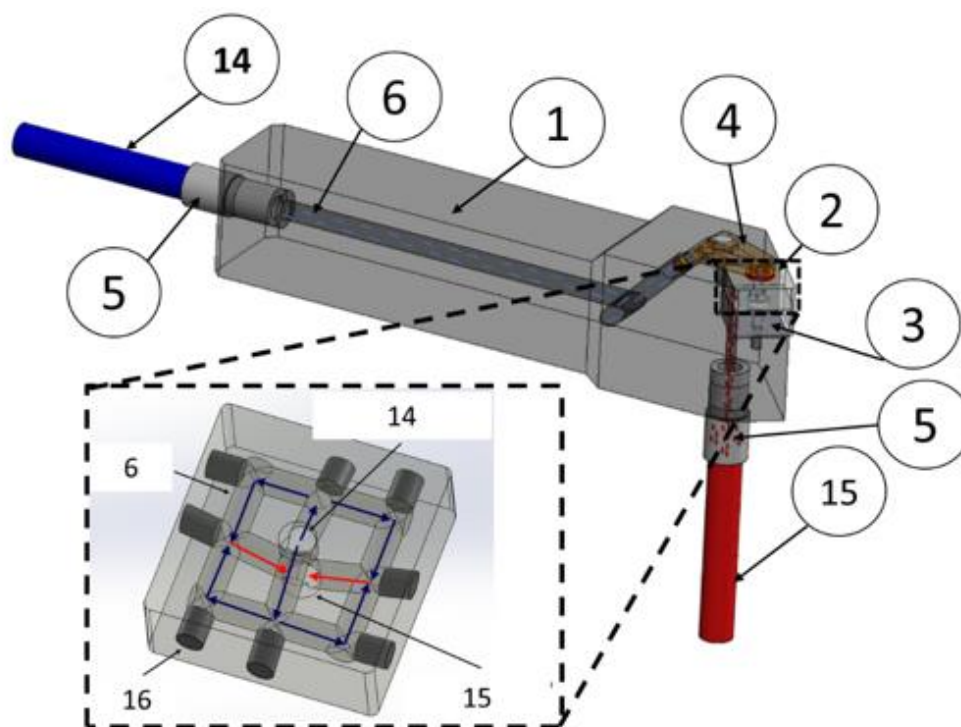
**Figure 3-2:** Details of the components of the cooling system

An wire electric discharge machine (EDM) was employed during manufacturing to create internal cooling channels within the tools, diameter of 1.5 mm. The tools utilized in the experiments were commercially available carbide inserts, Ceratizit Brand, with designation ISO code SNMG 120408EN-M34 CTPX710. These inserts were paired with a Walter-branded tool holder, model DSSNR2525X12-P, specifically modified to enable internal fluid circulation during machining. In **Figure 3-3** is schematically represents the tool holder/insert set with internal cooling channels.



**Table 3-1:** Specifications of the cooling system

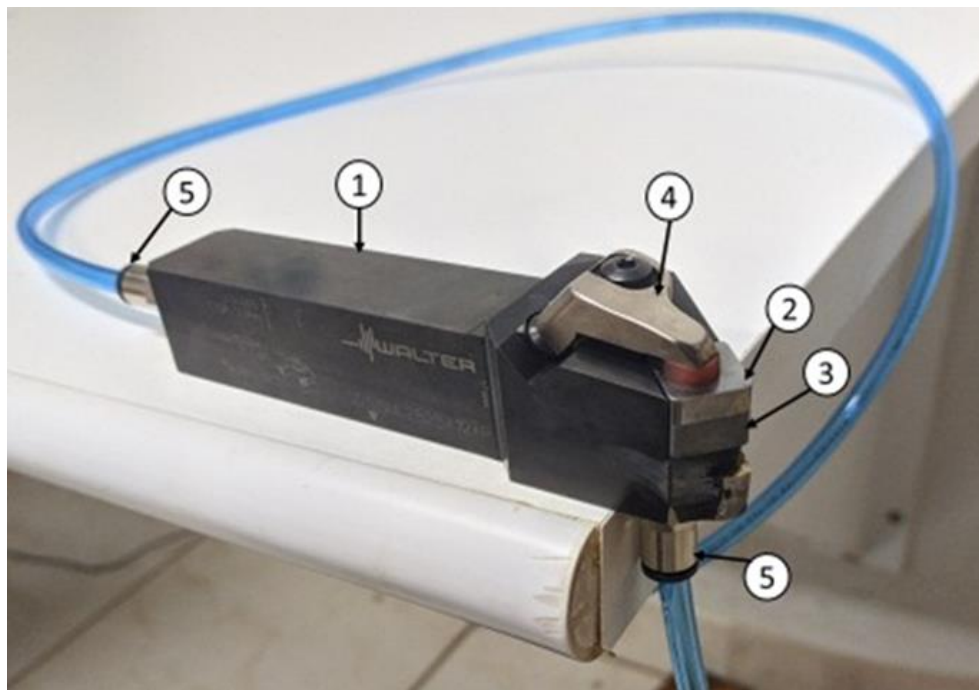
Commercial Freezer (Make/model)	Prosdócimo/04180CBC201
Cooling capacity [W]	146
Coolant	R 134
D.d.p. [V]	220
Coolant (R 134) pressure [kPa]	52
Coolant	Water (90%) Mono ethylene glycol (10%)
Minimum temperature [°C]	~ - 5 °C
Reservoir capacity [l]	60
Pump (type/model)	Micro diaphragm pump
Flow [l/min]	~1.02
D.d.p. [V]	12
Coolant pressure [kPa]	700

**Figure 3-3:** Tool holder set, and cemented carbide insert made by EDM.

Based on **Figure 3-3**, the components of tool holder following are: the hot duct (15) and cold duct (14) are connected to the tool holder (1) using connectors (5) or nipples. The coolant is introduced into the tool holder (1) through its back, where it flows through internal channels (6) until it reaches the clamp (4). From the clamp (4), the coolant is injected into the top of the adapted tool (2), facilitating the exchange of heat generated

during the machining process. As a result, the temperature of the coolant increases, and it is then directed to the shim (3). The sealing parts are represented in (16). The heated coolant begins its return process to the reservoir, completing the cycle within a closed-loop cooling system.


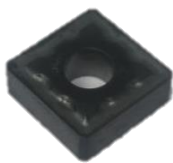
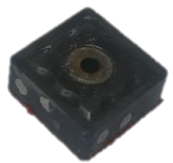
The coolant used in this setup is a mixture of demineralized water with 10% mono ethylene glycol, and it was maintained at -5 °C. In **Figure 3-4** is an real photograph of the assembly, which includes the tool holder (1), connectors (5), clamp (4), cutting tool (2), and shim (3).



**Figure 3-4:** Tool and tool holder set.

**Table 3-2** provides the specifications of the tool used in the study, while **Table 3-3** presents the details of the tool holder. For a comprehensive understanding of the tool in its original state, the complete specification sheet can be found in Appendix D. Appendix E contains specific details of the tool holder, and Appendix F provides the technical design of the tool after it was adapted with internal cooling channels (ICCs).

**Table 3-2: Cemented carbide tool inserts specifications**

Tool				
Standard ISO Code	SNMG 120408EN-M34 CTPX710			
Internally Cooled Tool	No	Yes	No	Yes
Coating	TiNAl	TiNAl	Balinit® ALNOVA	Balinit® ALNOVA
Available cutting edge	8			
Insert angle [ ° ]	90			
Inscribed circle diameter [mm]	12.7			
Cutting edge length [mm]	12.9			
Fixing hole diameter [mm]	5.76			
Insert width [mm]	4.76			
Tip radius ( $r_e$ ) [mm]	0.8			
Feed ( $f$ ) [mm]	0.1 – 0.35			
Depth of cut ( $doc$ ) [mm]	0.1 – 3.5			
Cutting speed ( $v_c$ ) [m/min]	40			
Chip breaker	M34			
Weight (g)	9.5	8.4	9.5	8.4
Estimated cost (US\$)	5	46	13	55

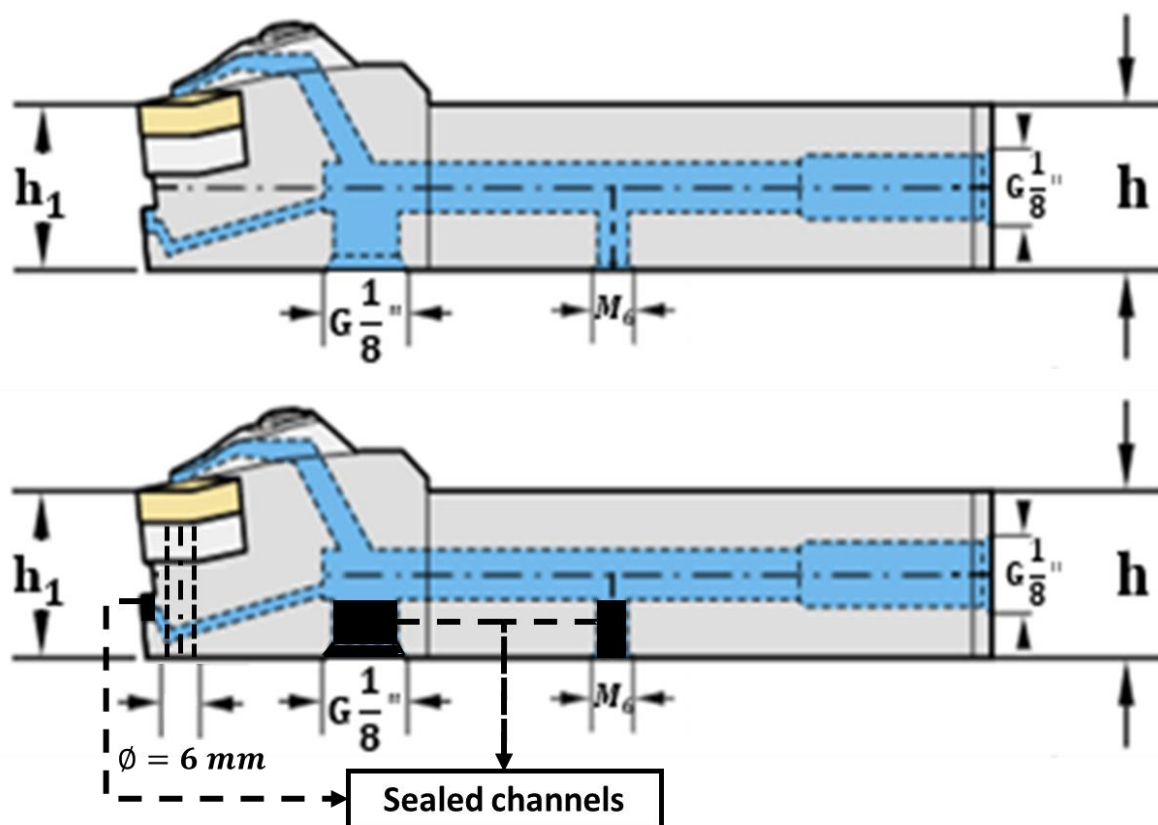
Source: adapted from [155]

**Table 3-3: Toolholder specifications (in conjunction with Table 3-2)**

Description	Symbol	Value
Standard ISO code	DSSNR2525X12-P	***
Height [mm]	$h = h_1$	25
Width [mm]	$b$	25
Functional width 1 [mm]	$f$	32
Functional width 2 [mm]	$f_1$	23.7
Functional length [mm]	$l_1$	130
Maximum balance [mm]	$l_4$	48
Total length [mm]	$l_{20}$	138.7
Orthogonal rake angle [°]	$\gamma$	-8

Source: adapted from [156]

**Figure 3-5** provides a draft of the original design (top) and the adapted tool holder (bottom). Mechanical devices such as an M6 screw, a thread, G 1/8" connector, and silver welding fill were utilized in the adaptation process. Additionally, a 6 mm diameter hole was created using wire electrical discharge machining (WEDM) to facilitate the return of the hot fluid. The clamp was also modified with silver weld fill to redirect the fluid initially directed toward the rake surface of the tool. Furthermore, a blind hole with a diameter of 2 mm was incorporated to enable the circulation of the coolant in a closed loop. Appendix E contains comprehensive details of the adapted tool holder.

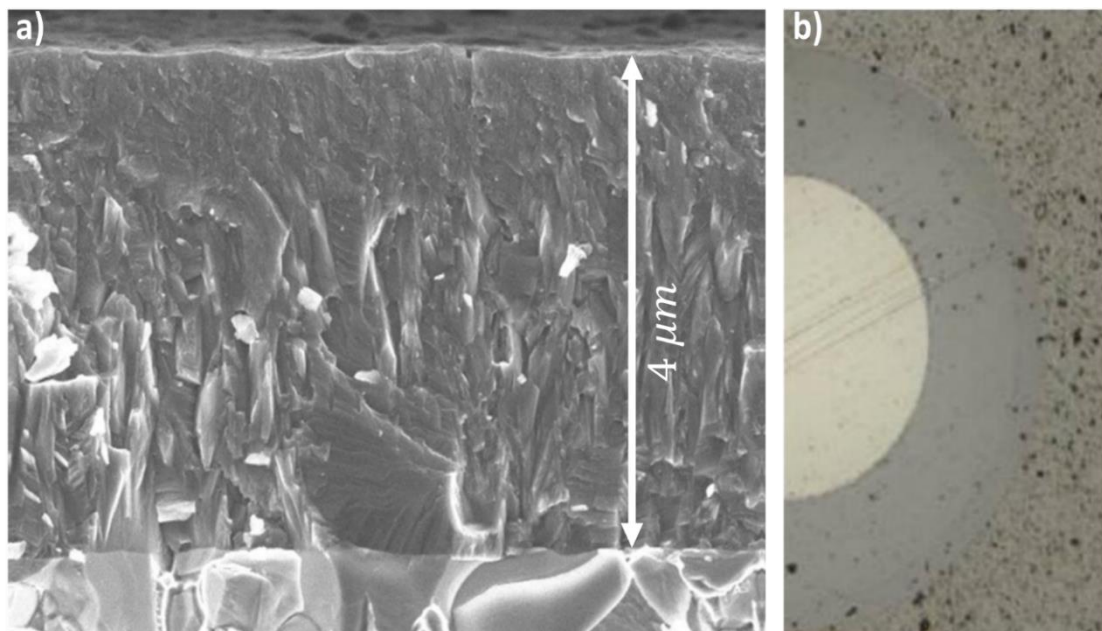


**Figure 3-5:** Side view of the original tool holder (above) and adapted (below)

Source: [156]

Typically, SNMG 120408EN-M34 CTPX710 tools are coated with TiAlN. However, for the specific machining of Inconel 718, a more suitable coating, such as AlCrN, can be used [137]. Hence, one of the objectives of this study was to evaluate the ICT system using both TiAlN and a double-coated AlCrN over TiAlN (referred to as AlCrN+). To achieve this, 20 out of the 40 inserts were coated with AlCrN+ by a specialized company. **Figure 3-6 (a)** provides an enlarged photo with a side-cut view of the  $4 \mu\text{m}$  thick coating. **Figure 3-6 (b)**

reveals micro-abrasion marks on the coating, exposing the underlying substrate **Table 3-4** presents the specifications of the BALINIT® AlCrN+ coating. Unfortunately, the manufacturer did not provide additional information due to industrial protection measures.



**Figure 3-6:** (a) Side-cut view of AlCrN coating (BALINIT® ALNOVA) with thickness of 4  $\mu\text{m}$  on hard metal substrate and (b) micro-abrasion marks until reveal the substrate

Source: [137]

**Table 3-4:** Coating specifications (BALINIT® ALNOVA & Dragon Skin)

Commercial name	BALINIT® ALNOVA +	DragonSkin®
Structure	AlCrN - TiNAl double coated	TiNAl
Hardness (HV 0.05)	3,200	1,820
Residual stresses (GPa)	- 3.0	***
Maximum service temperature (°C)	1,100	800
Coefficient of friction against steel ( <i>CoF</i> )	0.3	0.6
Carbide applications (milling/finishing)	<ul style="list-style-type: none"> <li>• Steels &gt; 1,000 <math>\text{N}/\text{mm}^2</math></li> <li>• Steels &gt; 45 ~52 HRC</li> <li>• Stainless steel</li> <li>• Cast gray iron</li> <li>• Titanium and its alloys</li> <li>• Inconel family</li> </ul>	<ul style="list-style-type: none"> <li>• Steels</li> <li>• Stainless steel</li> <li>• Non ferrous alloys</li> <li>• Heat resistant alloys</li> </ul>

Source: [137,155]

### 3.1.2. Inconel 718 characterization

Two bars of Inconel 718® VAT718 A, supplied by Villares Metals S.A., were utilized in the study. These alloys underwent a thermal treatment process involving precipitation and aging, as detailed in *section 0*. The cylindrical bars initially had dimensions of  $l=300$  mm and  $\varnothing=140$  mm. For detailed information regarding the composition, mechanical properties, and physical-chemical properties of the bars, please refer to **Table 3-5**.

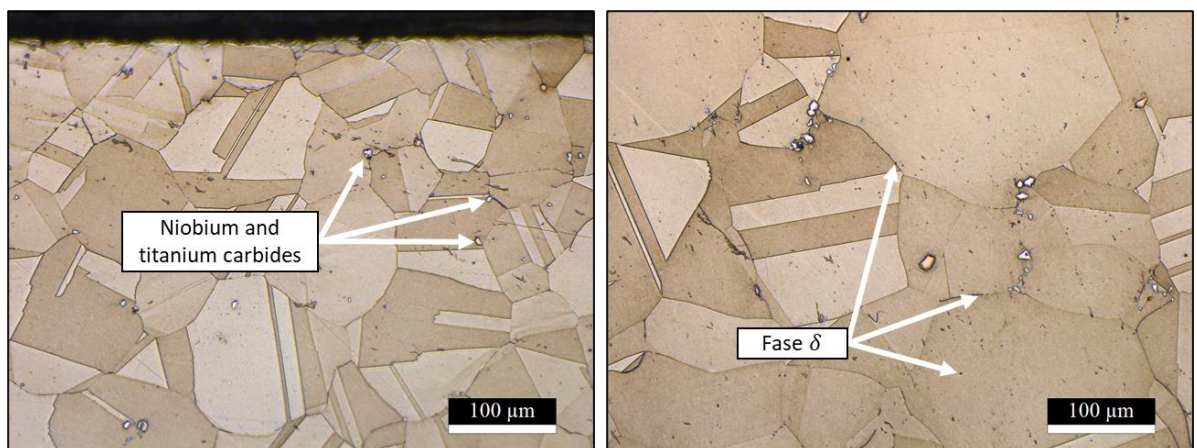
**Table 3-5:** Composition, mechanical and physical-chemical properties of Inconel 718

Composition		Ni	Cr	Fe	Nb	Mo	Ti	Al	C	Co
Inconel 718 (aged/precipitated)		52.90	18.48	18.88	5.11	2.94	0.98	0.54	0.032	0.04
Mechanical properties										
Alloy	Ultimate tensile strength (MPa)	Yielding limit (0.2%) (MPa)	deformation in 50 mm	Modulus of elasticity (GPa)	Hardness (HRC)	Descriptions and applications				
Inconel 718 (aged/Precipitated)	1,240	1,036	12	211	40	A precipitation-hardened nickel-chromium alloy containing significant amounts of iron, niobium, and molybdenum, along with smaller amounts of aluminum and titanium. It combines corrosion resistance and high mechanical strength with good weldability, including post-weld crack resistance. However, it has extraordinarily little machinability. The alloy has good crack resistance to vibration at temperatures up to 700 ° C. Used in gas turbines, rocket engines, spacecraft, nuclear reactors, pumps, and tools, among others.				
Physico-chemical properties										
		Density ( $g/cm^3$ )	Melting pint range (°C)	Specific heat (J/kg.K)	Average thermal expansion coefficient ( $\mu m/m.K$ )	Thermal conductivity ( $W/m.K$ )	Electrical resistivity ( $\eta\Omega m$ )	Curie temperature (°C)		
Inconel 718 (aged/precipitated)		8.19	1,260 ~ 1,336	435	13.0	11.4	1 250	-112		

Source: [111,112]

To examine the microstructure of Inconel 718, a metallographic experiment was conducted. The specimens were prepared at the Metallographic Testing Laboratory of FEMEC-UFU. The preparation process involved sequentially numbered sandpaper of particle of mesh in the sequence of 80, 120, 220, 320, 400, 600, 800, and 1,200 to ensure a smooth surface. Subsequently, the samples were polished using diamond paste with a granulometry of 1  $\mu\text{m}$  and 3  $\mu\text{m}$ . For a chemical attack, an etchant named Nital 3 % with 80 mL of HCl was used, and the samples were immersed in it for 30 seconds.

**Figure 3-7** illustrates the resulting microstructure of Inconel 718, allowing verification of the presence of niobium and titanium carbides (indicated by white points). However, the delta phase (indicated by dark points) did not exhibit a significant presence in the microstructure.



**Figure 3-7:** Microstructure of Inconel 718® VAT718 A produced by Villares Mettals.

### 3.1.3. Machine tool & Fluids

The machining operations were conducted at Laboratory for Teaching and Research in Machining (LEPU) at the Federal University of Uberlândia. Inside the LEPU there is a lathe IMOR MAX II, where the temperature tests were performed. It is a universal lathe with a swing over a bed of 400 mm and a swing over a cross slide of 240 mm. It has a center height of 200 mm and a distance between centers of 1,000 mm. The lathe features a wide spindle speed range from 40 to 2,000 RPM, powered by a 5.5 kW motor. It is equipped with a three-jaw chuck and a quick-change tool post. The lathe may include additional features such as a coolant system, thread-cutting capability, taper-turning attachment, and digital readouts.

The laboratory also has a CNC lathe manufactured by ROMI S.A., known as the MULTIPLIC 35-D model. The CNC was used to run the cutting forces, tools live, and roughness tests. The CNC lathe is equipped with cutting-edge numerical control technology, specifically the series 21i-TB, provided by GE FANUC. The lathe's power capacity has 11 kW (15 CV) on the tree axis. It has variable spindle speed, which ranges from 3 to 3,000 rpm.

A 100% synthetic emulsion named as ECO COOL P 1977 BF was utilized during the machining process with the CFA system. This emulsion is specially formulated to provide good cooling and lubrication properties and enhance machining performance [157]. The specifications of the ECO COOL P 1977 BF mixture can be found in **Table 3-6**.

The refractometer is a precision instrument that measures the refractive index of a liquid, which is directly related to its concentration. Using the Pocket PAL-1 refractometer, the concentration of the emulsion mixture could be accurately monitored throughout the machining process. This ensured that the emulsion maintained the desired concentration (25 % in water), refraction factor of 1.7, guaranteeing consistent performance and optimal cooling and lubrication effects.

In the internal cooling system, a mixture of water and mono ethylene glycol (MEG) was used to provide fluid to the cutting tool. The mixture was composed of 90% water and 10% MEG. The primary purpose of adding MEG to the mixture was to act as an anticorrosive agent, safeguarding the machine tool set against potential damage caused



by corrosion. MEG also served as an anti-freezing agent, enabling the cooling system to function with a coolant temperature below 0°C. Detailed specifications and properties of this mixture can be found in **Table 3-7**.

**Table 3-6: ECOCOOL P 1977 BF specifications**

Tests	Methods	ECOCOOLSYN 1977 BF
Density (20 °C) (g/cm <sup>3</sup> )	ASTMD 1298	1.040
Emulsion pH (2% in water) *	MR 125	9.70
Emulsion aspect (2 % in water) *	MR 079	clear, colorless
Bosch test GG (2 % in water)	DIN 51 360-2	0
Emulsion stability (2 % in water) (min. 15h)*	MR 015	Stable
Product stability (4 to 40 °C) (min. 15h)	MR 017	Stable
Refraction factor	MR 044	1,70
	Product code	315021

\*Emulsion made with tap water pH close to 7 and hardness ca. of 3 °d ( $\pm 54$  mg/l CaCO<sub>3</sub>). The tests are carried out at concentrations lower than recommended as we adopt more severe conditions.

Source: [157]

**Table 3-7: Properties of mono ethylene glycol**

Properties	Value
Color	Light orange
Aspect	Clear
Density (4°C ~20°C) (g/cm <sup>3</sup> )	1.1150
Boiling point (°C)	170
pH 10%	8.5
Alkaline Reserve 10%, ml HCl 0,1 N	6.7
Water K.F.	2.5
Nitrites	absent
Aminas Phosphate	absent
Specifications	ASTM D-3306; ASTM D-4985; NBR15297; FIAT 9.55523-2

Source: [158,159]

### 3.1.4. Temperature measurements

Initially, the experimental planning focused on analyzing temperature using two methods simultaneously: a thermocamera and a tool-workpiece thermocouple system. The first Design of Experiments (DoE) employed a fractionated factorial design, specifically a  $2^{5-1}$ . The variables considered in this DoE are listed in **Table 3-8**, which include cutting speed with levels of 47 and 94 mm/rev, feed rate, 0.1 and 0.2 mm/rev, and depth of cut, 0.25 and 0.5 mm.

Subsequently, a second fractionated DoE, again employing a  $2^{5-1}$  design, was conducted, this time varying only the cutting atmosphere between internally cooled tools and cutting fluid in abundance. Important to state that for the thermocamera tests, only DM and ICT conditions were performed since this method is not appropriate for CFA conditions.

Forty-eight experiments were performed for temperature analysis, comprising initial tests (T1) and one replica (T2). The specific details of each test can be found in **Table 3-9**.

**Table 3-8: Temperature fractionated DoE ( $2^{5-1}$ )**

Planning 01 (Temperatures) ( $2^{5-1}$ )				
Factors	Variables	Levels		
		(-)	(+)	
Cutting speed ( $v_c$ ) [m/min]	$\gamma_1$	47	94	
Feed rate (f) [mm/volt]	$\gamma_2$	0.1	0.2	
Tool coating	$\gamma_3$	AlCrN +	TiAl	
Cutting atmosphere	$\gamma_4$	ICT	DM	
Depth of cut [mm]	$\gamma_5$	0.25	0.50	
Planning 02 (Temperatures) ( $2^{5-1}$ )				
Cutting speed ( $v_c$ ) [m/min]	$\gamma_1$	47	94	
Feed rate (f) [mm/volt]	$\gamma_2$	0.1	0.2	
Tool coating	$\gamma_3$	AlCrN +	TiAl	
Cutting atmosphere	$\gamma_4$	ICT	CFA	
Depth of cut [mm]	$\gamma_5$	0.25	0.50	

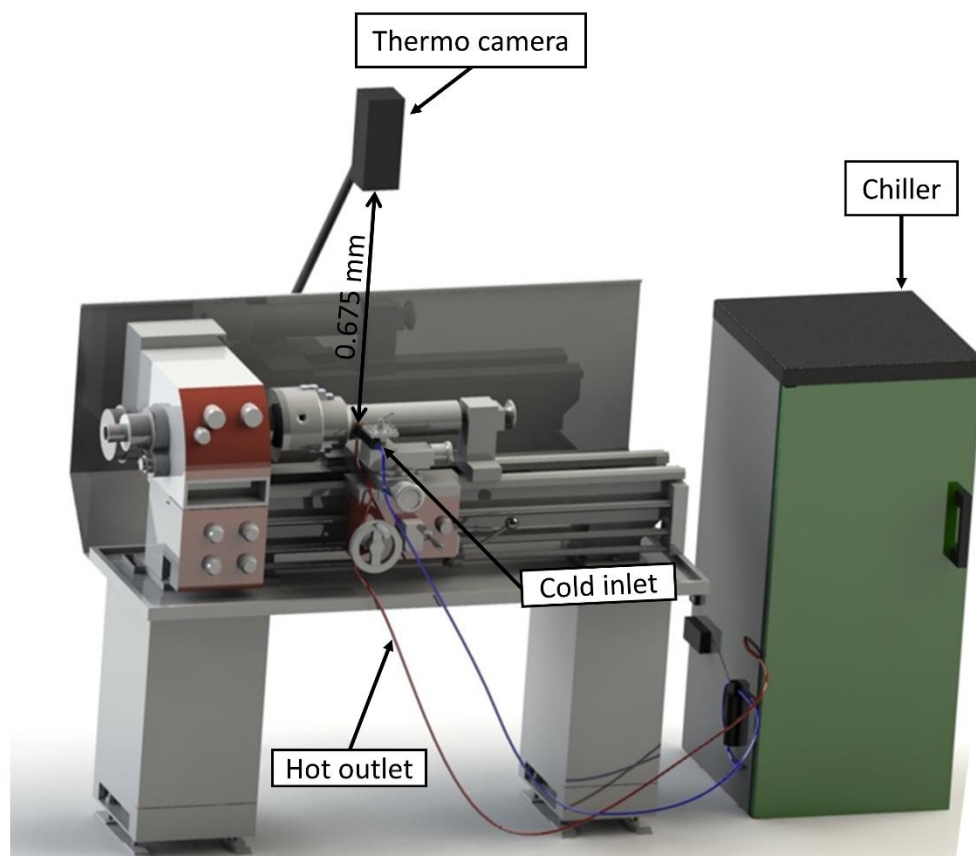
**Table 3-9:** Fractionated factorial experiment design  $2 \times (2^{5-1})$ 

Test	Atmosphere	Coating	Depth of cut [mm]	Feed [mm/rev]	Cutting speed [m/min]
1	DM	TINAL	0.25	0.103	47
2	ICT	TINAL	0.25	0.103	94
3	ICT	TINAL	0.50	0.103	47
4	DM	TINAL	0.50	0.103	94
5	ICT	TINAL	0.25	0.297	47
6	DM	TINAL	0.25	0.297	94
7	DM	TINAL	0.50	0.297	47
8	ICT	TINAL	0.50	0.297	94
9	ICT	AlCrN +	0.25	0.103	47
10	DM	AlCrN +	0.25	0.103	94
11	DM	AlCrN +	0.50	0.103	47
12	ICT	AlCrN +	0.50	0.103	94
13	DM	AlCrN +	0.25	0.297	47
14	ICT	AlCrN +	0.25	0.297	94
15	ICT	AlCrN +	0.50	0.297	47
16	DM	AlCrN +	0.50	0.297	94
17	CFA	TINAL	0.25	0.103	47
18	CFA	TINAL	0.50	0.103	94
19	CFA	TINAL	0.25	0.297	94
20	CFA	TINAL	0.50	0.297	47
21	CFA	AlCrN +	0.25	0.103	94
22	CFA	AlCrN +	0.50	0.103	47
23	CFA	AlCrN +	0.25	0.297	47
24	CFA	AlCrN +	0.50	0.297	94
25 to 48 as replica					

Temperature measurements were conducted using a FLIR Tools® thermal camera, specifically the A325 model. The camera possesses a resolution of 320 x 240 pixels and a temperature range of 300 to 1,200 °C, with an accuracy of  $\pm 2$  °C. A sampling rate of 30 frames per second was utilized for data acquisition.

To ensure accurate readings for the nickel alloy, an emissivity value of  $\varepsilon=0.35$  was employed, as specified in the FLIR manual. Maintenance of the maximum flank wear below 0.1 mm ( $V_{Bmax} < 0.1$  mm) was taken by utilizing new tools throughout the measurements.

The thermocamera was positioned with the focus directed at the root of the chip, with a measurement time of 45 seconds. The FLIR ThermoCAM researcher professional 2.10 software was employed to calculate the average maximum temperature per frame. The camera's focal distance was adjusted to 0.675 m, as depicted in **Figure 3-8**.



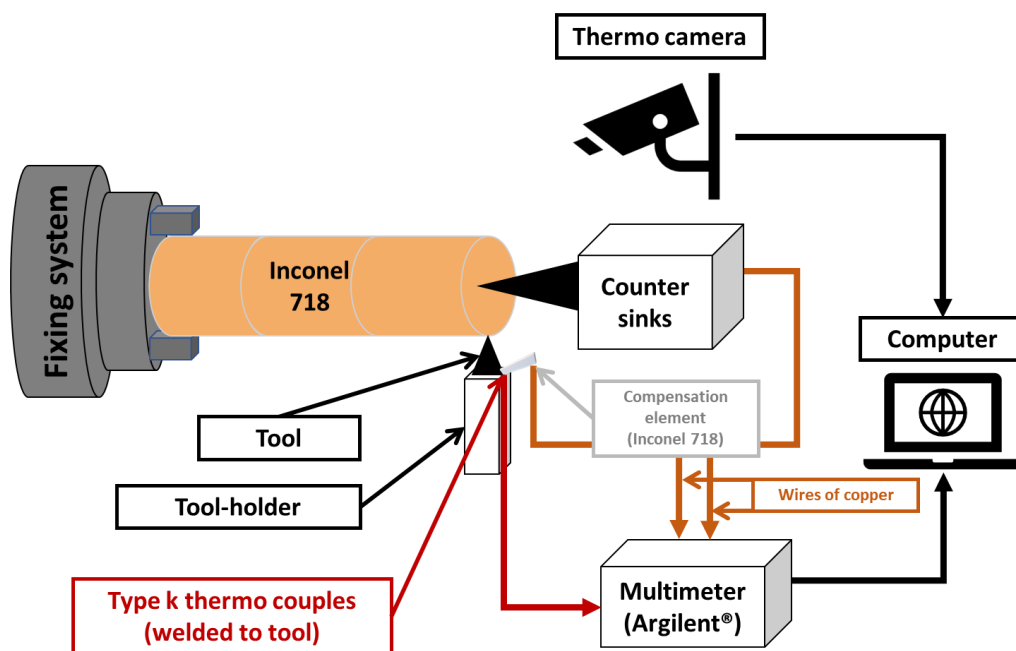
**Figure 3-8:** A lathe and thermocamera experiment position

The thermocouple method was run with the thermo camera, as described in **section 2.1.2**. All tests were performed on an IMOR MAX II universal lathe, described in **section 3.1.3**. Beyond the ICT and DM, the CFA condition was verified, too, as the tool-work method allows it. Each machining test took 45 seconds, more than enough for the temperature to reach its maximum value. A tool's life condition  $V_{Bmax} = 0.1$  mm was adopted to the wear does not interfere with the results.

An Agilent® 34901A data acquisition board was employed to capture the data signals generated during machining. This board offers a resolution of  $1 \mu\text{V}$  and a measurement uncertainty of  $0.3 \text{ }^\circ\text{C}$ . The data acquisition frequency was set at 2 Hz, as specified in **section 2.1.2**. The signals were acquired using the two copper wires connected to the thermoelectric circuit of the tool-work thermocouple. These wires were connected to the modified rotation counter tip and the compensation element.

**Figure 3-9** illustrates the experimental setup, scheming the temperature measurement tests using the two methods. Electrical isolation was implemented for the

bar and the tool holder in the tool-workpiece thermocouple method to ensure accurate measurements and avoid signal loss. This precautionary step was taken to maintain the integrity of the signals and minimize any potential interference.

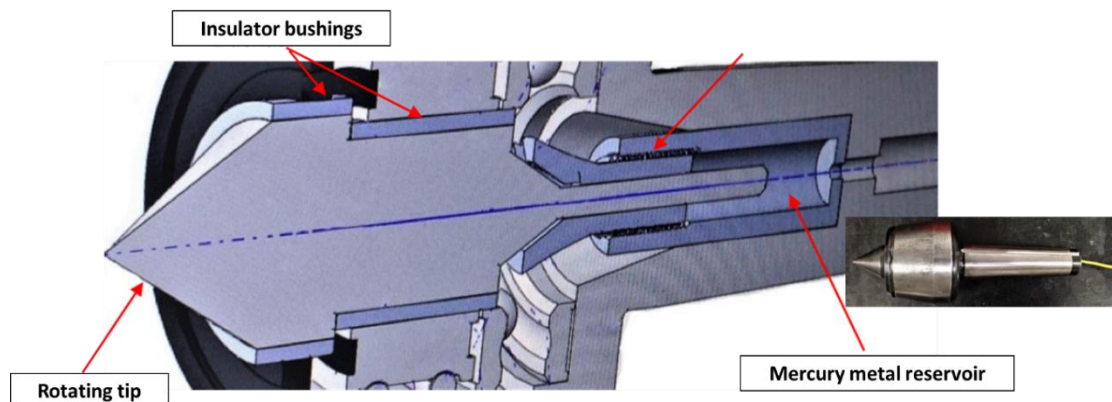


**Figure 3-9:** Experimental assembly diagram for temperature measurement

To enable the transfer of electrical signals from the rotating workpiece, an internally modified live center was utilized in the lathe's tailstock. Within this live center, a Teflon® capsule was installed to house liquid mercury. The liquid mercury establishes contact with the rotating conical point inside the live center, ensuring the continuity of the electrical signal during the tests.

The rotating conical point, constructed from SAE 1050 Steel, captures the electrical signal from the rotating workpiece and transmits it to the liquid mercury. The liquid mercury then transfers the electrical signal to an embedded copper wire, effectively closing the circuit for the measurement system. **Figure 3-10** illustrates a similar adapted tailstock for visual reference, demonstrating the abovementioned arrangement.

A thermocouple, a piece of Inconel 718 chip and a cemented carbide stick for the calibration scheme. Copper wires were soldered at the ends of the junction, and a K-type thermocouple (Nickel-Chromium/Nickel-Alumel) with a temperature measuring range of  $-200\text{ }^{\circ}\text{C}$  to  $1,260\text{ }^{\circ}\text{C}$  was positioned very close to the tip of the chip-tool.



**Figure 3-10:** Modified mandril of the tailstock for capturing the signal of a rotating part used

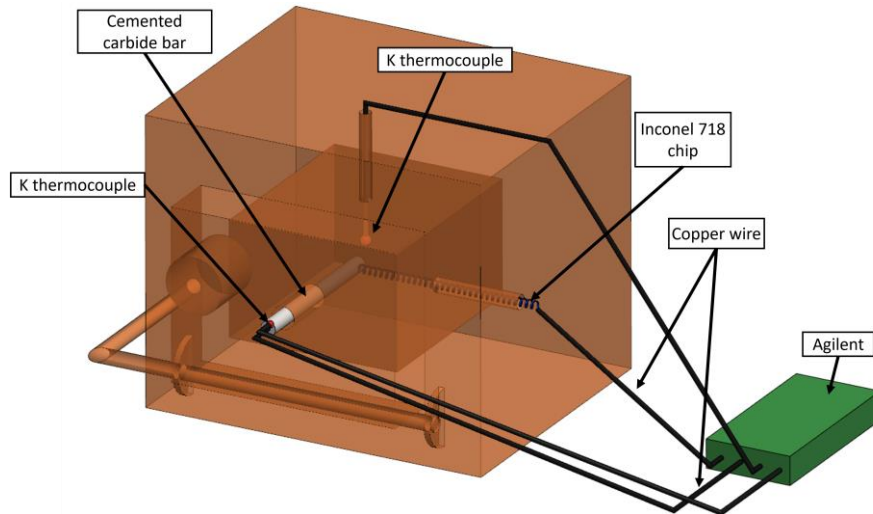
Source: [160]

The cemented carbide stick and the k thermocouples were placed in an electric induction oven, specifically a Mufla-type oven, with a power rating of 7,500 W. The oven was heated up to the desired temperature. This calibration method provides an excellent correlation between temperatures and electromotive forces (voltage). For a visual representation, **Figure 3-11** illustrates the schematic of the experimental setup used for the calibration process.

The Inconel 718 chip was isolated and securely fixed in the tool, ensuring pressure contact with the isolated cemented carbide bar for calibration. This combination formed the reference joint, known as the "hot joint," placed inside the oven. Adjacent to this contact, a separate thermocouple of type K was inserted to measure the calibration temperatures, specifically at the hot joint of the system.

The electrical signals generated by the Seebeck effect in the chip-tool thermocouple were collected through the copper wires by closing the electrical circuit. These signals were then correlated with the temperature readings provided by the K-type thermocouple, which served as a reference for the hot joint temperature. The entire system was electrically closed and insulated to ensure accurate calibration.

Although the calibration was not performed in the same experimental machining equipment, it was still possible to represent machining temperatures accurately. This is because all the equipment involved in the calibration process adheres to Seebeck's law, which governs the relationship between temperature and the generated electrical signals in thermocouples.



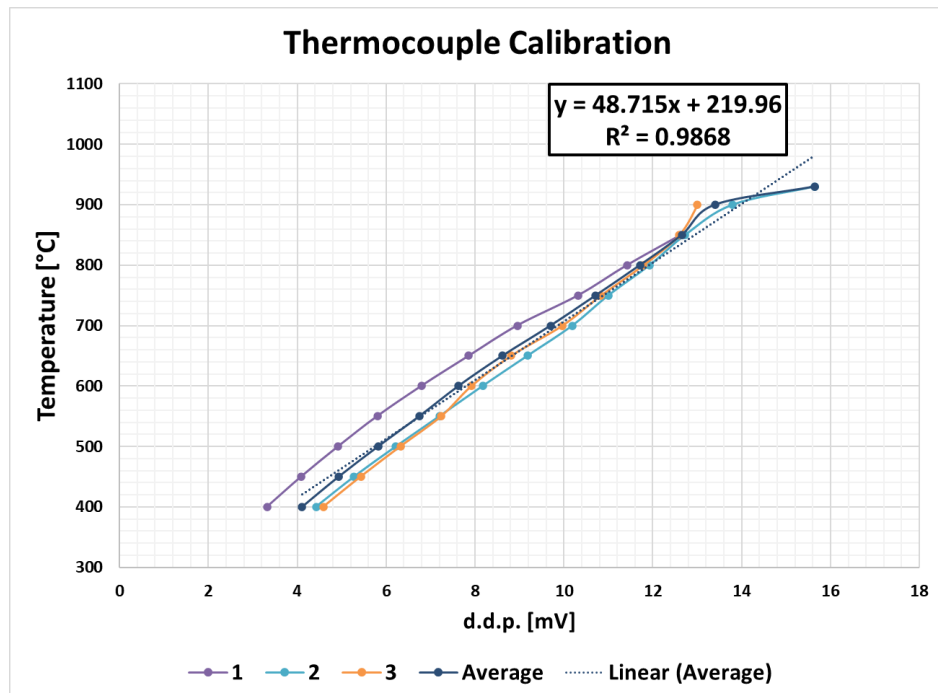
**Figure 3-11:** Schematic draw of the calibration of the tool-workpiece thermocouple in an oven.

The temperatures were measured at the beginning of the tool's life ( $V_{Bmax} < 0.1$  mm) using the resulting calibration equation (Eq.17), derived from the curves presented in **Figure 3-12:**

$$Temp(x) = 48.715x + 220 \text{ [}^\circ\text{C]} + T_2 \quad (17)$$

Where:  $x$  is the voltage in [mV]

$T_2$  is the temperature at cold tool junction



**Figure 3-12:** Tool-work thermocouple calibration curve

### 3.1.5. Machining and wear mechanisms analysis.

A full factorial experimental design, specifically ( $2^2$ ), was used to investigate machining by the meaning of cutting forces ( $F_c$ ), tool life, and surface roughness. The design included two input variables: tool coating (TiNAl and AlCrN+) and cutting atmosphere (DM and ICT). A second experiment was also conducted to evaluate a third cutting atmosphere condition (ICT and CFA). The details of the input variables and their levels for these two experimental designs (DoE) can be found in **Table 3-10** and **Table 3-11**. For the machining analysis, a total of 18 experiments were performed. This included initial tests (T1) and two additional replicas (T2 and T3). The cutting speed ( $v_c = 45$  m/min), feed rate ( $f = 0.103$  mm/rev) and depth of cut ( $a_p = 0.5$  mm) were kept constant in a finishing condition.

A third experiment included the analyses of the wear mechanisms. The input variables were the cutting atmospheres in three levels (ICT, CFA, and DM) and the tool's coating in two levels (TiNAl and AlCrN +). The cutting speed ( $v_c = 45$  m/min), feed rate ( $f = 0.103$  mm/rev), and depth of cut ( $a_p = 0.5$  mm) were kept constant in a finishing condition. After the tests, only one tool of each condition, cutting atmosphere and coating, were analyzed using scanning electron microscopy (SEM) equipped with energy-dispersive spectroscopy (EDS) to determine the wear mechanisms. A total of six tools were taken for wear investigation.

**Table 3-10:** Two full factorial Desing of Experiment ( $2^2$ )

Planning 01 ( $2^2$ )			
Factors	Variables	Levels	
		(-)	(+)
Coating	$x_1$	TiNAl	AlCrN+
Atmosphere	$x_2$	ICT	CFA
Planning 02 ( $2^2$ )			
Factors	Variables	Levels	
		(-)	(+)
Coating	$x_1$	TiNAl	AlCrN +
Atmosphere	$x_2$	ICT	DM



**Table 3-11:** Two full factorial Design of Experiment ( $2^2$ )

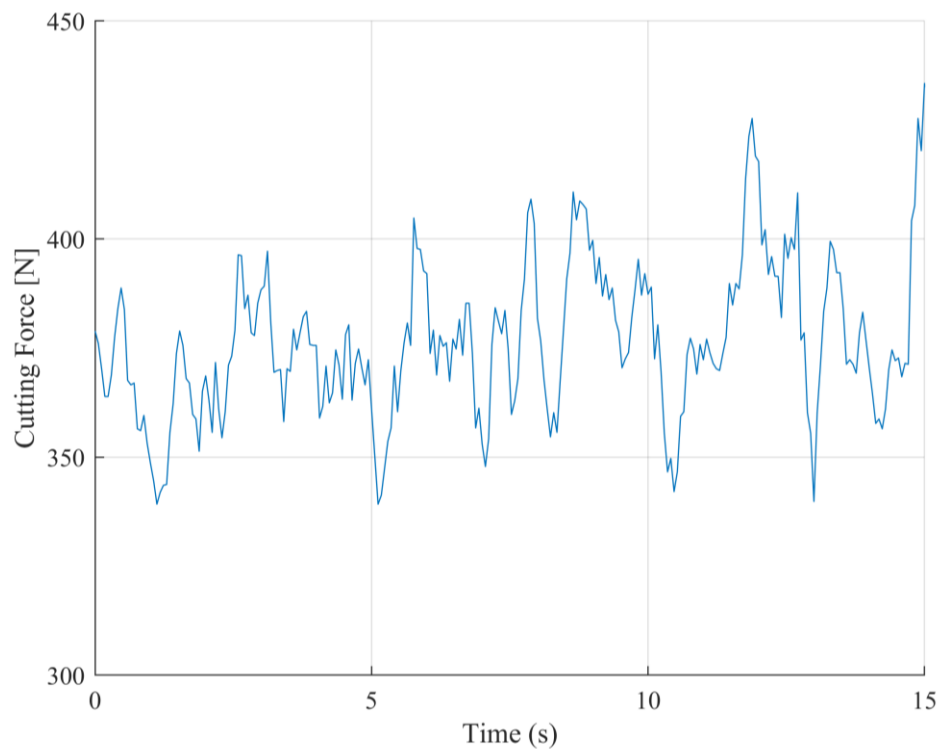
	Tests	Coating ( $x_1$ )	Atmosphere ( $x_2$ )
Roughness, tool's life, and cutting forces	1	TiNAl	ICT
	2	TiNAl	CFA
	3	TiNAl	DM
	4	AlCrN +	ICT
	5	AlCrN +	CFA
	6	AlCrN +	DM
	7	TiNAl	ICT
	8	TiNAl	CFA
	9	TiNAl	DM
	10	AlCrN +	ICT
	11	AlCrN +	CFA
	12	AlCrN +	DM
	13	TiNAl	ICT
	14	TiNAl	CFA
	15	TiNAl	DM
	16	AlCrN +	ICT
	17	AlCrN +	CFA
	18	AlCrN +	DM

The machining tests were carried out in a CNC lathe, described in **section 3.1.3**. Cutting force was measured using a Kistler dynamometer, specifically the model 9265B. This dynamometer was attached to the tool carrier of the lathe. A Kistler charge amplifier, model 5070, was utilized to amplify the signals. A signal acquisition board managed the amplified signals, the National Instruments USB-6251 DaqPad, controlled by LabView® software.

When the tool reached half-life time ( $V_B = 0.3$  mm) the cutting forces were measured. The measuring time took precisely 15 seconds. The acquisition rate was set at 100 Hz to ensure sufficient data for analysis.

The obtained signal was processed using mathematical software, and an overall average of the highest interval was calculated, as illustrated in **Figure 3-13**. To correct the sign of the cutting force measured by the dynamometer ( $F_c$ , measured), a calibration curve provided by Eq. (18) was applied.

$$F_c = 0.935 \cdot F_{c,measured} - 21.34655 \pm 15 N \quad (18)$$

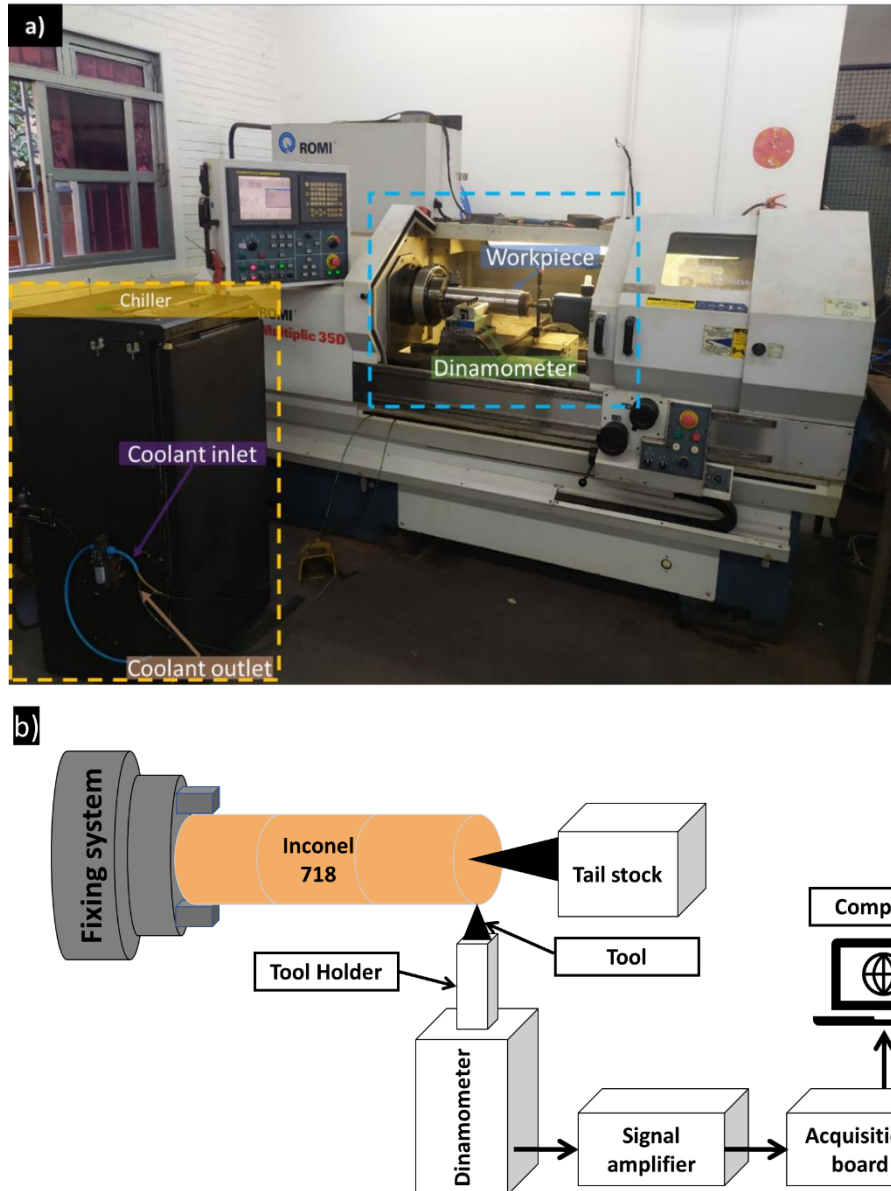


**Figure 3-13:** Example of the cutting force ( $F_c$ ) signal where the average was calculated

The end-of-life test criteria was total failure, which occurred when the tools could no longer perform the cutting operation. This criterion was chosen to push the tools to their maximum capacity and enable a comparison between the behavior of regular and adapted inserts.

Tool wear evolution was monitored at each cutting pass, covering approximately 150 mm. The main flank surfaces of the tools were analyzed using an Olympus stereomicroscope, model SZ61. The wear was measured with the assistance of Image Pro-Express software. The stereo microscope had a brand-specific amplification of 4.5x.

**Figure 3-14** visually represents the machining setup (a) and a schematic diagram of the cutting forces acquisition system (b).

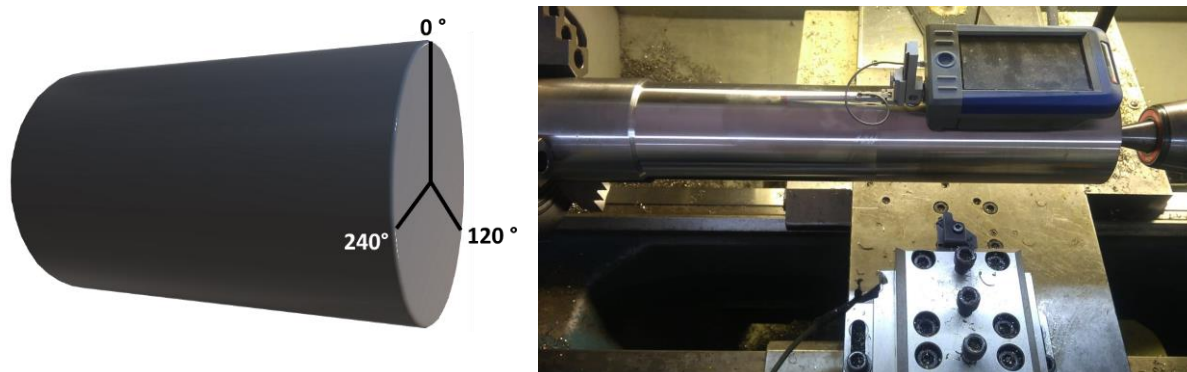


**Figure 3-14:** a) Photo of the force measurement experimental set up and b) schematical draw

The evaluation of surface roughness was based on the  $R_a$  parameter, as specified in the NBR ISO 4288 (2008) standard, which was discussed in *section 2.3.1.6*. A calibrated Mitutoyo SJ-201 P roughness meter was used for the measurements.

The measurement methodology involved taking three measurements for each section of the bar, which was rotated at  $120^\circ$  intervals, as depicted in **Figure 3-15**. Three measurements were taken at each angle, and an average value was calculated. All the roughness measurements were conducted when the tools reached half-life conditions ( $V_B = 0.3$  mm) at a position of near 75 mm from the border.

**Figure 3-15** comprehensively summarizes the roughness measurements taken along the bar. It is important to note that the study of surface roughness was performed in conjunction with the tool life studies, utilizing the same experimental setup.



**Figure 3-15:** Axial bar rotation for three different positions to assess roughness.

**Table 3-12:** Two Full factorial design ( $2^2$ ) for roughness measurement

Roughness test	Coating	Atmosphere	Roughness Measurements (Ra) [ $\mu\text{m}$ ]		
			0°	120°	240°
Replicate 1	TiNAL	ICT	M1	M2	M3
	TiNAL	CFA	M4	M5	M6
	TiNAL	DM	M7	M8	M9
	AlCrN +	ICT	M10	M11	M12
	AlCrN +	CFA	M13	M14	M15
	AlCrN +	DM	M16	M17	M18
Replicate 2	TiNAL	ICT	M19	M20	M21
	TiNAL	CFA	M22	M23	M24
	TiNAL	DM	M25	M26	M27
	AlCrN +	ICT	M28	M29	M30
	AlCrN +	CFA	M31	M32	M33
	AlCrN +	DM	M34	M35	M36
Replicate 3	TiNAL	ICT	M37	M38	M39
	TiNAL	CFA	M40	M41	M42
	TiNAL	DM	M43	M44	M45
	AlCrN +	ICT	M46	M47	M48
	AlCrN +	CFA	M49	M50	M51
	AlCrN +	DM	M52	M53	M54

---

---

## Chapter 4: Results and Discussions

---

---

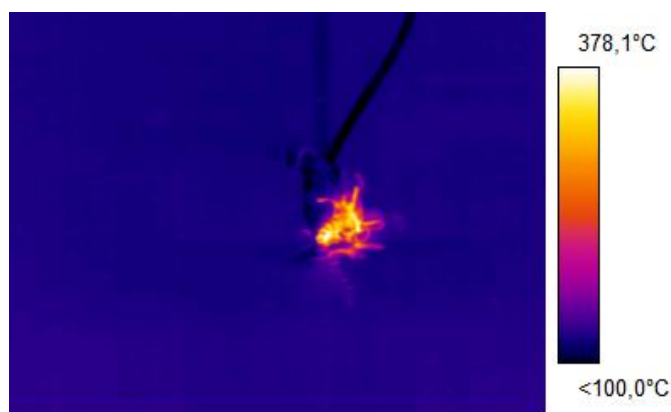
Chapter 4 presents the experimental results and their in-depth analysis. It covers cutting temperatures, including thermocamera and tool-work thermocouple analysis, shedding light on the temperature aspects. Additionally, the chapter explores cutting forces, roughness, and tool life evaluation. Furthermore, it scrutinizes wear mechanisms, offering comprehensive insights into the research findings. Chapter 4 plays a crucial role in elucidating the outcomes of the experimental investigations and their implications.

### 4.1. Cutting temperatures

Chapter 4.1 delves into the analysis of cutting temperatures, employing two distinct methods: thermocamera analysis and tool-work thermocouple analysis. This comprehensive examination of temperature-related aspects provides valuable insights into the machining process and its thermal effects, forming a crucial foundation for the subsequent analyses and discussions within this chapter.

#### 4.1.1. Temperature results *via* thermocamera

The temperatures were measured at the chip's root for forty-five seconds of machining in each cutting condition tested, deeply described in **section 3.1.4**. Considering all the frames recorded, the average maximum temperature registered per frame, 30 per second, was calculated. **Figure 4-1** shows an experiment example with the software (ThermaCAM researcher PRO 2.09) analysis. **Table 4-1** and **Figure 4-2** present the results. It is essential to state that the CFA condition was not used for temperature tests with a thermocamera, as the cutting fluids would block the camera view.



**Figure 4-1:** Chip-back temperature analysis with software

Table 4-1: Thermocamera temperature results

	Atmosphere	Coating	Depth of Cut [mm]	Feed rate [mm/rev]	Cutting speed [m/min]	Temperature (T)[°C]	Temperature (Replicate) [°C]	Average (T1 and T2) [°C]	Standard dev.
1	DM	TINAL	0.25	0.103	47	609	632	621	16
2	ICT	TINAL	0.25	0.103	94	612	617	615	4
3	ICT	TINAL	0.50	0.103	47	673	656	665	12
4	DM	TINAL	0.50	0.103	94	673	692	683	13
5	ICT	TINAL	0.25	0.297	47	613	634	624	15
6	DM	TINAL	0.25	0.297	94	697	663	680	24
7	DM	TINAL	0.50	0.297	47	674	682	678	6
8	ICT	TINAL	0.50	0.297	94	673	654	664	13
9	ICT	AlCrN+	0.25	0.103	47	636	647	642	8
10	DM	AlCrN+	0.25	0.103	94	652	669	661	12
11	DM	AlCrN+	0.50	0.103	47	653	664	659	8
12	ICT	AlCrN+	0.50	0.103	94	652	648	650	3
13	DM	AlCrN+	0.25	0.297	47	692	704	698	8
14	ICT	AlCrN+	0.25	0.297	94	611	650	631	28
15	ICT	AlCrN+	0.50	0.297	47	696	669	683	19
16	DM	AlCrN+	0.50	0.297	94	748	743	746	4

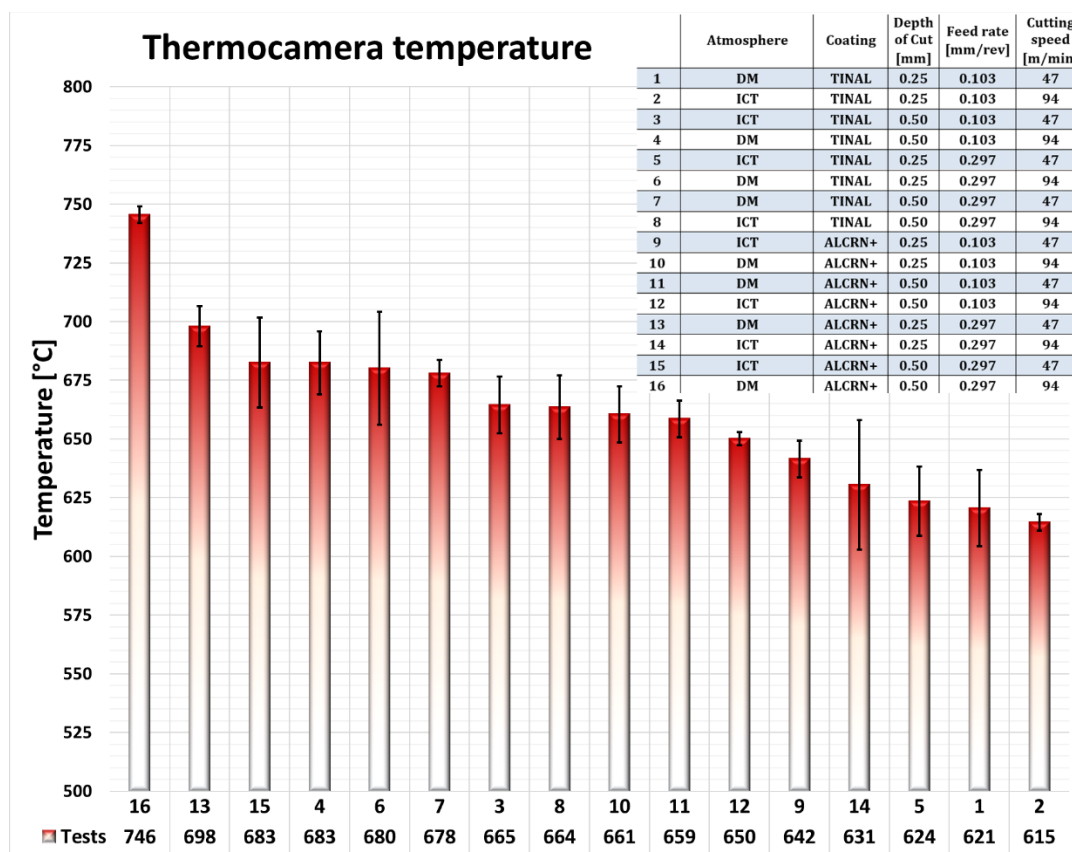
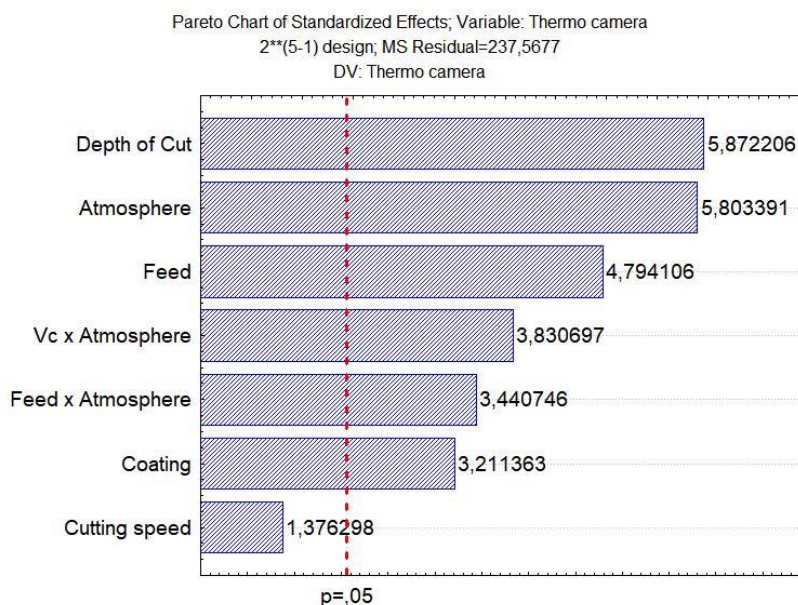


Figure 4-2: Temperature results in descending order via thermocamera

**Table 4-2** presents the ANOVA results for the temperature measured by the thermocamera considering a reliability index of 95 % and a confidence level of 5 %, and **Figure 4-3** shows Pareto's chart indicating the significant input variables.

**Table 4-2:** Thermo camera temperature ANOVA

Temperature – ICT x DM					
	SS	df	MS	F	p-value
Cutting speed (vc)	450.00	1	450.000	2.32558	0.146785
Depth of cut (DoC)	8192.00	1	8192.000	42.33592	0.000007
Feed rate (F)	5460.13	1	5460.125	28.21770	0.000070
Tool coating	2450.00	1	2450.000	12.66150	0.002620
Cutting atmosphere	8001.13	1	8001.125	41.34948	0.000008
Vc x DoC	392.00	1	392.000	2.02584	0.173851
Vc x F	28.12	1	28.125	0.14535	0.708035
Vc x Coating	288.00	1	288.000	1.48837	0.240147
Vc x Atmosphere	3486.12	1	3486.125	18.01615	0.000618
DoC x F	45.12	1	45.125	0.23320	0.635699
DoC x Coating	242.00	1	242.000	1.25065	0.279939
DoC x Atmosphere	253.13	1	253.125	1.30814	0.269556
F x Coating	861.13	1	861.125	4.45026	0.051000
F x Atmosphere	2812.50	1	2812.500	14.53488	0.001532
Coating x Atmosphere	496.13	1	496.125	2.56395	0.128881
Error	3096.00	16	193.500		
Total SS	450.00	1	450.000	2.32558	0.146785



**Figure 4-3:** Pareto chart results for the cutting temperature measured by the thermocamera.

Firstly, it will be considered exclusively the results provided by **Figure 4-2** and **Table 4-1**. In general, the results obtained in the study were consistent with expectations. As the cutting parameters increased, such as cutting speed, feed rate, and depth of cut, they had significance in the temperature, increasing it. This can be attributed to an increase in mechanical energy leading to higher heat generation, resulting in elevated temperatures during machining. These findings are in line with previous studies conducted by Korkut et al. (2007) [162], O'Sullivan and Cotterell (2002) [163], and J. Zhao et al. (2018) [51].

Regarding the specific temperature values, as shown in **Figure 4-2** and **Table 4-1**, a comparison between different tool coatings and cutting atmospheres revealed that the lowest temperatures, measuring  $615 \pm 4$  °C, were recorded when using a TiAlN coated tool and ICT cutting atmosphere. On the other hand, dry machining with an AlCrN+ coated tool resulted in the highest temperature of  $746 \pm 4$  °C. These temperature values align with the findings of Zhao et al. (2018), who conducted turning experiments on Inconel 718 using ceramic tools reinforced with whiskers. They reported a temperature of approximately 750 °C under similar cutting conditions, specifically using a cutting speed of 80 m/min, feed rate of 0.085 mm/rev, and depth of cut of 0.5 mm [51].

About the coating effects, TiAlN coating exhibits excellent thermal conductivity, allowing for efficient dissipation of heat, while AlCrN+ coating acts as a thermal insulator, leading to a higher concentration of heat. This distinction explains why TiAlN-coated tools generally produce lower temperatures during machining than AlCrN+-coated tools. As discussed in the extensive review by Zhao et al. (2021), the thermal barrier formed by tool coatings effectively protects the substrate from excessive heat [164].

In terms of the cutting atmosphere, dry machining is known for its limited cooling and lubrication capabilities, resulting in increased temperatures in the cutting atmosphere. França (2022) studied ICT when turning grey cast iron and demonstrated its ability to remove heat effectively [53]. Compared to dry machining, the author observed a temperature reduction of nearly 22 % at the chip-tool interface when ICT was used. Other studies that utilized indirect cooled tools also discovered significant temperature differences with this innovative method. For example, Minton et al. (2013) used a cooling chamber (block) to work with titanium grade 2 [71]. Using a thermocamera, the authors found an approximate temperature reduction of 8 % when using cooled PCD (Polycrystalline Diamond) compared to dry machining with PCD. Similarly, Li et al. (2018)



conducted turning experiments on AISI 1045 steel and achieved a temperature reduction of approximately 80% by employing optimized cooled tools instead of dry machining [92]. This finding establishes the cutting atmosphere as a statistically significant factor influencing temperature.

In the face of the statistical analysis depicted in **Table 4-2** and **Figure 4-3**, it revealed that nearly all input variables significantly influenced the cutting temperature, except for cutting speed, which yielded surprising results. Hypotheses regarding this unexpected outcome will be explored and discussed in detail. The interaction effects between variables, explicitly cutting speed x cutting atmosphere and feed rate x cutting atmosphere significantly influenced the cutting temperature.

Among the input variables analyzed, the depth of cut emerged as the most influential factor. The transition from a depth of cut of 0.25 mm (level -1) to 0.50 mm (level +1) resulted in an average temperature increase of 2.1%. This can be attributed to the higher depth of cuts corresponding to larger cutting section areas, which consequently lead to increased cutting forces. These elevated forces necessitate more power and energy from the machine, which is generally converted into heat, raising the temperature.

Similar effects were observed concerning the feed rate ( $f$ ) and the interaction between the feed rate and cutting atmosphere. Changes in the feed rate also contributed to temperature variations. Additionally, the interaction between the cutting speed and cutting atmosphere demonstrated a significant influence on the cutting temperature,

These findings further highlight the complex interplay of various parameters in determining the cutting temperature. The depth of cut, feed rate, and their interactions with the cutting atmosphere were identified as key factors influencing temperature variations during machining.

Regarding the cutting speed, it brought an unexpected result. It is generally observed that higher cutting speeds result in higher temperatures and lower cutting forces during machining. However, an interesting finding by Peixoto (2021) while using the ICT system in turning grey cast iron with uncoated tools challenges this general observation [166]. The study showed that increasing the cutting speed led to an increase in the cutting forces. This unexpected result suggests a plausible hypothesis that the high cooling capacity of the ICT system might effectively mitigate the cutting temperature increase associated

with higher speeds, thereby canceling the typical influence of this variable on temperature. Further investigations are necessary to have a conclusive finding.

Supporting this hypothesis, the strong influence of the cutting atmosphere variable on chip temperature further reinforces the role of cooling in temperature control. Dry machining, characterized by the absence of cooling or lubrication, significantly increased the chip temperature as depicted in **Figure 4-2**.

Furthermore, the existing literature presents conflicting findings regarding the relationship between temperature and cutting parameters, suggesting that the behavior of cutting temperature is closely tied to the specific combination of machine, workpiece, and tool used. For example, in a study conducted by Korkut et al. (2007), the temperature at the chip root was examined using a FLIR thermocamera during the turning of AISI 1117 [162]. The researchers employed an uncoated carbide tool with a chip-breaker and varied the depth of cut, feed rate, and cutting speed. Their findings indicated that as these variables were increased, the chip-root temperature increased, with cutting speed being the most influential parameter.

Similar results were observed by Kus et al. (2015) in their investigation of machining parameters [48]. They utilized a thermocouple and an infrared sensor to measure the temperature during the dry turning of AISI 4140 alloy (hardened, 50 HRC) with PVD TiAl-TiN coated tools. The main findings demonstrated a proportional increase in temperature with the rise in cutting parameters, with cutting speed being the most influential parameter in promoting temperature elevation.

In contrast, O'Sullivan & Cotterell (2002) examined the workpiece temperature during the turning operation of aluminum alloy 6082-T6 [163]. They employed K-type thermocouples and an Inframetrics ThermaCAM (model PM380E) camera to determine the temperature of the machined surface. Their results revealed a decrease in the temperature of the machined surface at higher feed rates.

Adding to the previous information, Barbosa (2021) conducted a study using the same ICT system while turning D6 hardened steel with a PCBN tool [16]. Surprisingly, the study found that neither the basic cutting parameters nor the cutting atmosphere influenced the machining temperature.

Still analyzing the statics (**Figure 4-3**) outcomes for temperature, the second most significant variable was the cutting atmosphere, which exhibited nearly the same level of influence as the depth of cut. The results demonstrated that dry machining (level 1) increased the temperature compared to ICT (level -1). This was explained earlier with vast literature examples of how internally cooled tools effectively reduce temperature.

Finally, the tool coating was identified as a significant variable, although it had the least influence. The temperature increased when using the double-coating AlCrN+ (level +1) instead of the single-coating TiNAl (level -1). This can be attributed to the fact that AlCrN+ is a thermal insulator and tends to concentrate more heat at the cutting zone, whereas TiNAl, with its superior heat dissipation properties, directs the heat flow towards the tool substrate rather than concentrating it on the chip. Also, it must be considered that the coating AlCrN+ is a double coating type, which naturally has a thicker layer contributing to heat concentration.

Kusiak et al. (2005) proposed an analytical solution for heat conduction in a coated insert, comparing different coating types such as TiNAl, TiN, and Al<sub>2</sub>O<sub>3</sub> [167]. They found that Al<sub>2</sub>O<sub>3</sub> exhibited the best thermal insulation properties, while the other coatings had no significant impact on heat flux within the tool. This finding aligns with the results obtained, where TiNAl, an excellent thermal conductor, effectively dissipates heat, reducing the cutting temperature.

Summarizing the findings of the thermocamera measurements, minimum temperature values were  $615 \pm 4$  °C (TiNAl and ICT),  $621 \pm 16$  °C (TiNAl and DM), and the maximum was  $746 \pm 4$  °C (AlCrN+ and DM) and  $683 \pm 19$  °C (AlCrN+ and ICT). Tool coating and cutting atmosphere were the most significant variables, with TiNAl and ICT effectively contributing to decreasing the temperature. The feed rate and the depth of cut were also statistically significant variables, considering 95 % of the reliability index; surprisingly, the cutting speed was not significant.

#### 4.1.2. Temperature results via tool-work thermocouple

**Table 4-3** and **Figure 4-4** show the results of the chip-tool interface temperatures measured by this method during the tests (T1) and replicas (R1).

**Table 4-3: Tool-work thermocouple temperature results**

Test	Atmosphere	Coating	Depth of cut [mm]	Feed [mm/rev]	Cutting speed [m/min]	Temperature T1 [°C]	Temperature Replica 1 [°C]	Average (T1 and T2) [°C]	Std. Dev.
1	DM	TINAL	0.25	0.103	47	922	930	926	6
2	ICT	TINAL	0.25	0.103	94	1046	1040	1043	4
3	ICT	TINAL	0.50	0.103	47	948	922	935	18
4	DM	TINAL	0.50	0.103	94	1110	1141	1126	22
5	ICT	TINAL	0.25	0.297	47	976	952	964	17
6	DM	TINAL	0.25	0.297	94	1197	1195	1196	1
7	DM	TINAL	0.50	0.297	47	1055	1031	1043	17
8	ICT	TINAL	0.50	0.297	94	1191	1190	1191	1
9	ICT	AlCrN+	0.25	0.103	47	876	896	886	14
10	DM	AlCrN+	0.25	0.103	94	1058	1033	1046	18
11	DM	AlCrN+	0.50	0.103	47	963	970	967	5
12	ICT	AlCrN+	0.50	0.103	94	1121	1112	1117	6
13	DM	AlCrN+	0.25	0.297	47	988	1001	995	9
14	ICT	AlCrN+	0.25	0.297	94	1178	1202	1190	17
15	ICT	AlCrN+	0.50	0.297	47	1034	1062	1048	20
16	DM	AlCrN+	0.50	0.297	94	1243	1255	1249	8
17	CFA	TINAL	0.25	0.103	47	844	868	856	17
18	CFA	TINAL	0.50	0.103	94	1077	1066	1072	8
19	CFA	TINAL	0.25	0.297	94	1150	1163	1157	9
20	CFA	TINAL	0.50	0.297	47	1032	1053	1043	15
21	CFA	AlCrN+	0.25	0.103	94	1070	1079	1075	6
22	CFA	AlCrN+	0.50	0.103	47	941	940	941	1
23	CFA	AlCrN+	0.25	0.297	47	953	949	951	3
24	CFA	AlCrN+	0.50	0.297	94	1207	1207	1207	0

The analyses of variance ANOVA were performed with the input of the results obtained by pairs of cutting atmospheres and considering a reliability index of 95 % and a confidence level of 5%. ANOVA of the results of comparing ICT x DM cutting atmospheres are presented in **Table 4-4** and **Figure 4-5** shows Pareto's chart with significant variables.

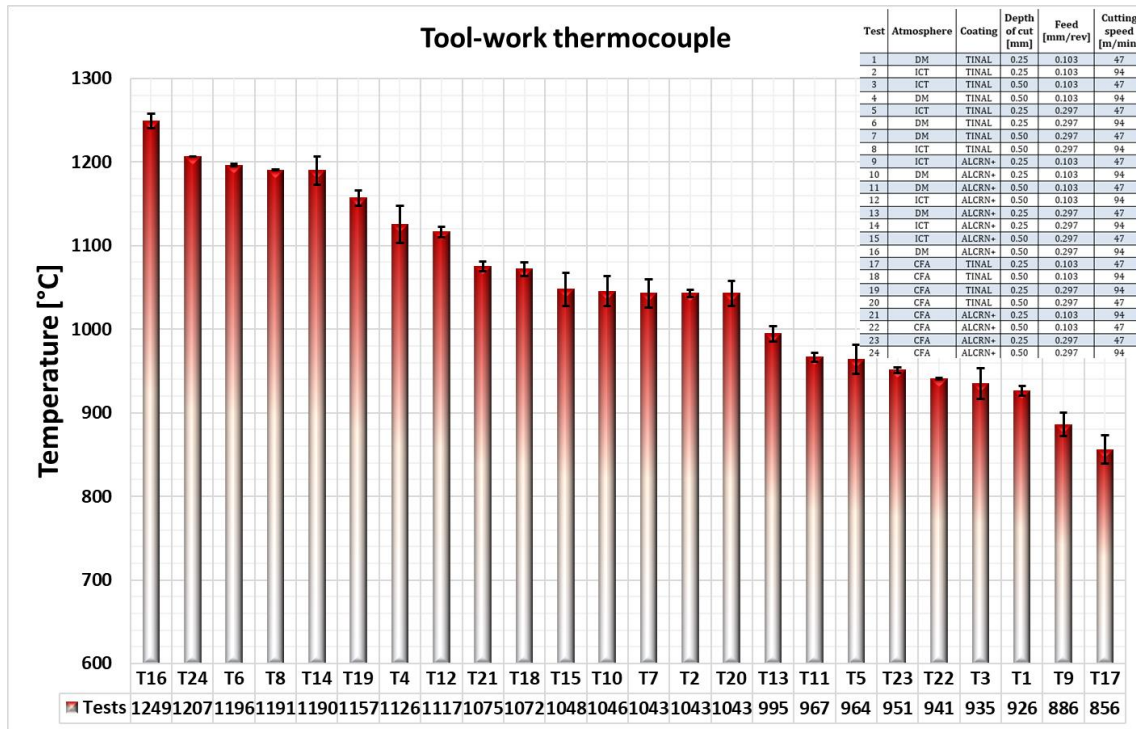
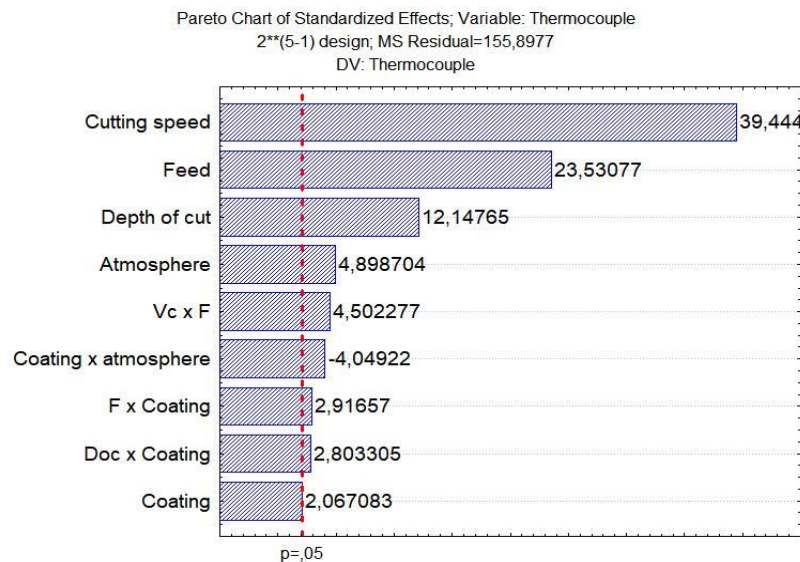


Figure 4-4: Tool-work thermocouple temperature results.

Table 4-4: ANOVA of the temperature measured by the tool-workpiece thermocouple method (ICT x DM).

Temperature – ICT x DM					
	SS	df	MS	F	p-value
Cutting speed (vc)	242556.1	1	242556.1	1356.483	0.000000
Depth of cut (DoC)	23005.1	1	23005.1	128.655	0.000000
Feed rate (f)	86320.1	1	86320.1	482.741	0.000000
Tool coating	666.1	1	666.1	3.725	0.071518
Cutting atmosphere	3741.1	1	3741.1	20.922	0.000312
Vc x DoC	28.1	1	28.1	0.157	0.696906
Vc x f	3160.1	1	3160.1	17.673	0.000673
Vc x Coating	45.1	1	45.1	0.252	0.622262
Vc x Atmosphere	55.1	1	55.1	0.308	0.586415
DoC x f	406.1	1	406.1	2.271	0.151284
DoC x Coating	1225.1	1	1225.1	6.851	0.018664
DoC x Atmosphere	28.1	1	28.1	0.157	0.696906
f x Coating	1326.1	1	1326.1	7.416	0.015037
f x Atmosphere	6.1	1	6.1	0.034	0.855494
Coating x Atmosphere	2556.1	1	2556.1	14.295	0.001638
Error	2861.0	16	178.8		
Total SS	367985.9	31			

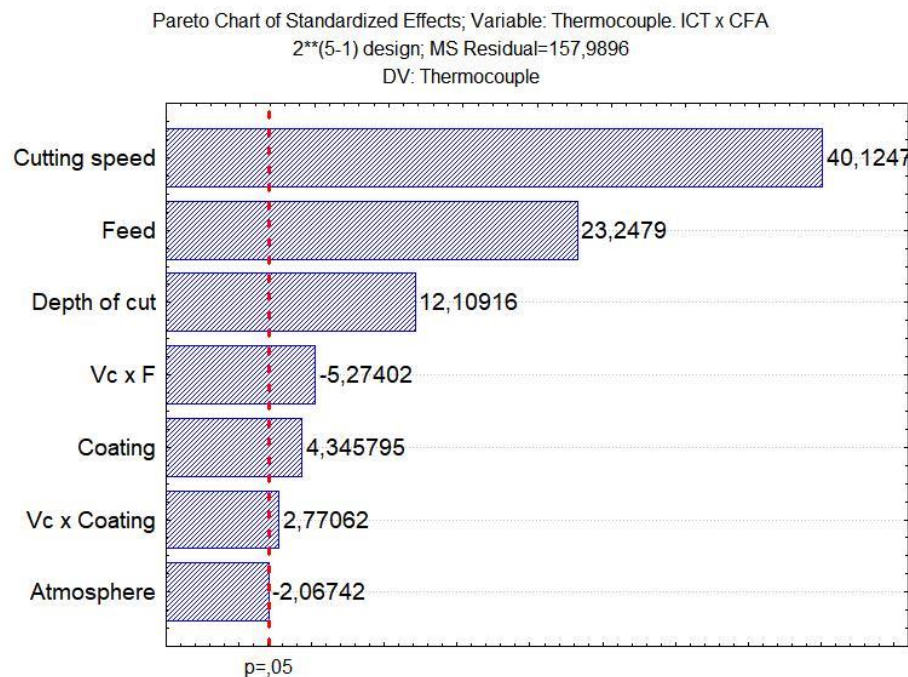


**Figure 4-5:** Pareto Chart for tool-work thermocouple temperature, ICT x DM

ANOVA of the results for the comparison of ICT x CFA cutting atmospheres are presented in **Table 4-5**, and **Figure 4-6** shows Pareto's chart with significant variables.

**Table 4-5:** ANOVA of the temperature measured by the tool-workpiece thermocouple method (ICT x CFA)

Temperature - ICT x CFA					
	SS	df	MS	F	p-value
<b>Cutting speed (vc)</b>	254362.8	1	254362.8	1794.842	<b>0.000000</b>
<b>Depth of cut (DoC)</b>	23166.3	1	23166.3	163.467	<b>0.000000</b>
<b>Feed rate (f)</b>	85387.8	1	85387.8	602.516	<b>0.000000</b>
<b>Tool coating</b>	2983.8	1	2983.8	21.054	<b>0.000303</b>
<b>Cutting atmosphere</b>	675.3	1	675.3	4.765	<b>0.044291</b>
<b>Vc x DoC</b>	4394.5	1	4394.5	31.009	<b>0.000042</b>
<b>Vc x f</b>	318.8	1	318.8	2.249	0.153140
<b>Vc x Coating</b>	1212.8	1	1212.8	8.558	<b>0.009906</b>
<b>Vc x Atmosphere</b>	19.5	1	19.5	0.138	0.715331
<b>DoC x f</b>	63.3	1	63.3	0.447	0.513514
<b>DoC x Coating</b>	11.3	1	11.3	0.080	0.781453
<b>DoC x Atmosphere</b>	34.0	1	34.0	0.240	0.630762
<b>f x Coating</b>	603.8	1	603.8	4.260	0.055618
<b>f x Atmosphere</b>	0.8	1	0.8	0.006	0.941734
<b>Coating x Atmosphere</b>	472.8	1	472.8	3.336	0.086494
<b>Error</b>	2267.5	16	141.7		
<b>Total SS</b>	375975.0	31			

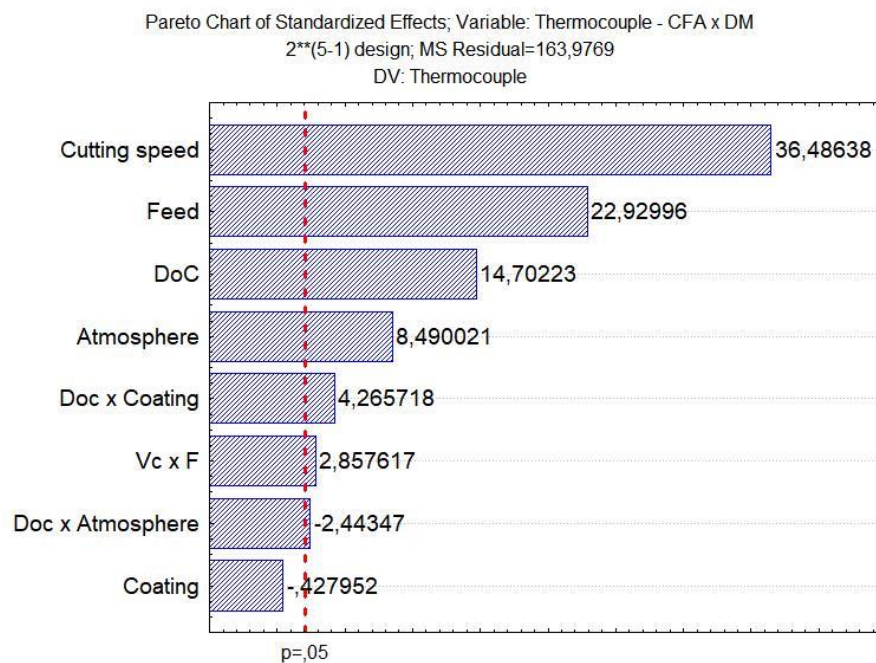


**Figure 4-6:** Pareto Chart of the temperatures measured by the tool-workpiece thermocouple method, ICT x CFA

ANOVA of the results of comparing CFA x DM cutting atmospheres are presented in **Table 4-6**, and **Figure 4-7** shows Pareto's chart with significant variables.

**Table 4-6:** ANOVA of the temperature measured by the tool-workpiece thermocouple method (CFA x DM)

Temperature - CFA x DM					
	SS	df	MS	F	p-value
<b>Cutting speed (vc)</b>	218295.3	1	218295.3	1427.058	<b>0.000000</b>
<b>Depth of cut (DoC)</b>	35444.5	1	35444.5	231.711	<b>0.000000</b>
<b>Feed rate (f)</b>	86216.3	1	86216.3	563.620	<b>0.000000</b>
<b>Tool coating</b>	30.0	1	30.0	0.196	0.663638
<b>Cutting atmosphere</b>	11819.5	1	11819.5	77.268	<b>0.000000</b>
<b>Vc x DoC</b>	108.8	1	108.8	0.711	0.411498
<b>Vc x f</b>	1339.0	1	1339.0	8.754	<b>0.009243</b>
<b>Vc x Coating</b>	42.8	1	42.8	0.280	0.604175
<b>Vc x Atmosphere</b>	318.8	1	318.8	2.084	0.168148
<b>DoC x f</b>	47.5	1	47.5	0.311	0.584950
<b>DoC x Coating</b>	2983.8	1	2983.8	19.506	<b>0.000432</b>
<b>DoC x Atmosphere</b>	979.0	1	979.0	6.400	<b>0.022292</b>
<b>f x Coating</b>	427.8	1	427.8	2.797	0.113907
<b>f x Atmosphere</b>	7.0	1	7.0	0.046	0.832947
<b>Coating x Atmosphere</b>	371.3	1	371.3	2.427	0.138806
<b>Error</b>	2447.5	16	153.0		
<b>Total SS</b>	360879.0	31			



**Figure 4-7:** Pareto Chart of the temperatures measured by the tool-workpiece thermocouple method, CFA x DM

The study demonstrated a clear relationship between cutting parameters and the temperature at the tool-chip interface, indicating that increasing the cutting parameters resulted in higher temperatures. Temperature measurements obtained using the tool-workpiece thermocouple system, as shown in **Figure 4-4** and **Table 4-5**, compared different tool coatings and cutting atmospheres. The combination of TiNAl coating with CFA yielded the lowest temperature of  $856 \pm 17$  °C, while dry machining with AlCrN+ coating recorded the highest temperature of  $1,249 \pm 8$  °C.

These temperature values' magnitude follows the results recorded in the work developed by Marques (2015). The author machined Inconel 718 in turning operation using different cutting atmospheres, such as MQL, CFA, MQL, and solid lubricants. The tools used were uncoated cemented carbide. The author found that increasing the cutting speed from 20 m/min to 70 m/min, the temperatures varied from 550 to 900 °C. Itakura et al. (1999) used the same method for machining Inconel 718, turning operation, using multilayer coating carbide tools, P20 grade [168]. They also found that increasing the cutting speed, the temperature increased too. At 30 m/min, it was  $\sim 717$  °C, and at 100 m/min,  $1,046$  °C.



As expected, dry machining exhibited the highest temperatures among all tested cutting conditions. However, CFA and ICT showed similar results, with a slight advantage of ICT over CFA at higher removal rates and larger machining parameters ( $a_p$ ,  $v_c$ , and  $f$ ). In contrast, CFA outperformed ICT at lower cutting conditions. This observation is in agreement with the literature about machining that cutting fluid's lubricating ability is more effective at lower removal rates while cooling becomes crucial at higher material removal rates [4,37]. This was surprising as the cutting fluids contain lubricating and cooling capacities acting together. Thus, CFA was expected to have a lower temperature as the ICT only has a cooling capacity.

Two hypotheses were proposed to explain the observed phenomenon. The first hypothesis suggests that at high cutting speeds, thin film lubrication struggles to reach the tool-chip interface due to the absolute contact zone between the tool and chip, as well as the dynamic nature of the cutting process [3]. Cutting fluids serve two main purposes: lubrication and cooling. Lubrication is more effective at lower cutting conditions [169], while cooling becomes crucial at higher speeds [170].

The performance comparison between CFA and ICT supports the hypothesis that CFA exhibits better lubrication capacity at lower speeds but performs worse at higher speeds [5,171,172]. This can be attributed to the increasing pressure between the tool and chip as machining parameters increase, forming a stronger adhesion zone characterized by absolute contact. Consequently, the cutting fluid faces challenges accessing the tool-chip interface, resulting in reduced performance [4].

ICT demonstrates its effectiveness as a highly efficient cooling method in such scenarios. This finding aligns with the second hypothesis, which states that ICT compensates for the lack of lubrication by providing excellent heat removal capabilities, as discussed by Neto et al. [95]. Both hypotheses complement each other, suggesting that both phenomena likely coincide.

Regarding the cutting atmospheres, dry machining presented the highest values in practically all cutting conditions because the air lacks cooling or lubricating abilities. CFA and ICT had quite similar results, with a slight advantage for ICT over CFA at high removal rates or bigger basic machining parameters ( $a_p$ ,  $v_c$ , and  $f$ ). In opposition, CFA performed better at lower values, and the reason for this was discussed earlier.

Generally, the AlCrN+ coating exhibited higher temperatures compared to the TiNAl coating. The explanation for these results follows what was stated for the thermocamera analysis, and it is worth to be mentioned again. The AlCrN+ coating is known for its superior thermal insulation properties, contributing to its performance in high-temperature applications. These thermal insulation properties can be attributed to the unique microstructure and composition of the coating [137]. Compared to other coatings, such as TiNAl, AlCrN+ exhibits enhanced resistance to heat flow. This characteristic enables the AlCrN+ coating to act as a thermal barrier, reducing heat dissipation from the cutting zone and resulting in higher temperatures at the tool-chip interface. These results are consistent with the findings in the existing literature [55,173–175].

Regarding the statistical analysis, comparing the cutting atmospheres ICT x DM,  
**Table 4-4**

**Table 4-4** and **Figure 4-5**. the most significant variables were cutting speed, feed, depth of cut, and atmosphere. Furthermore, significant interactions were observed between several variables that affected the meaning of temperature increase. In summary, the use of DM contributed to an increase in the chip-tool interface temperature, particularly when combined with the AlCrN+ coating and higher levels of basic cutting parameters such as cutting speed, feed rate, and depth of cut ( $v_c$ ,  $f$ , and  $a_p$ ).

Considering ICT and DM, the results were under the literature [176], where generally, the  $v_c$  was the most influential parameter. Dry machining is critical when machining nickel-based superalloys because it has poor cooling and lubricating ability. It undoubtedly impacts the temperature by increasing it. Meanwhile, ICT has high heat removal capacity, as proven by França [165]. The author found a temperature reduction at the tool-chip interface of almost 25% compared to dry cut when turning grey cast iron. He also found the atmosphere a significant influencing variable.

Considering ICT x CFA, **Table 4-5**, and **Figure 4-6**, similar findings were verified. The cutting speed, feed rate, and depth of cut were significant variables for the chip-tool interface temperatures, as were the interactions between cutting speed x feed rate and cutting speed x tool coating. The tool coating was a critical variable, with AlCrN+ increasing the temperature. The cutting atmosphere had a marginal significance, i.e., almost was not significant. In this comparison, the ICT increased the chip-tool interface

temperature as compared to CFA, however, only slightly. This is an exciting result, and the reasons were described previously.

Finally, for CFA x DM conditions, **Table 4-6** and **Figure 4-7** showed that all the basic machining parameters (cutting speed, feed rate, and depth of cut, in this order) and the cutting atmosphere were statistically significant. Cutting atmosphere had an essential contribution with DM increasing the overall chip-tool interface temperature. Tool coating, in this comparison, was not significant. The interaction depth of cut x tool coating, cutting speed x feed rate, and depth of cut x cutting atmosphere were also statistically significant. Again, AlCrN+ coating contributed to the increase in the temperature, but not significantly.

Last but certainly not least, it has been demonstrated that internally cooled tools (ICT) have a superior ability to remove heat compared to dry machining and cutting fluid application (CFA). ICT tools maintain significantly lower temperatures than dry machining and are comparable to CFA. It is important to note that internally cooled tools are considered a form of dry machining, as highlighted by Neto et al. [95] and Fernandes et al. [85]. Consequently, ICT lacks the lubricating capacity of CFA. In cutting fluids, the oil acts as a lubricant on the rake face, facilitating sliding and reducing temperature. Therefore, it is reasonable to infer that ICT compensates for the lack of lubrication by having a much higher heat removal capacity, which ultimately results in comparable interface temperatures despite the absence of lubricating oil.

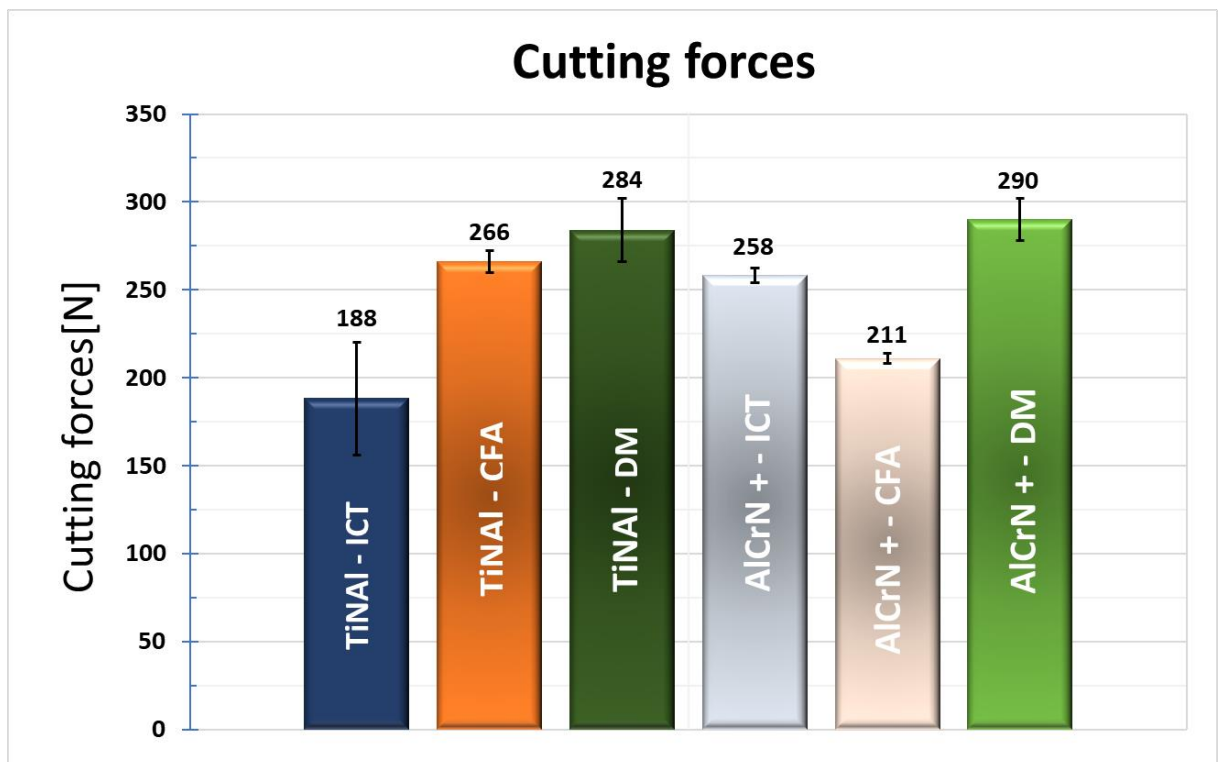
To summarize, the higher the basic machining parameters ( $v_c$ ,  $f$ , and  $doc$ ), the higher the mechanical energy dispended, and the temperature will increase [4]. The results showed that the basic parameters were the most significant variables and had the higher parcel of contributions to increase the temperature at the tool-work interface. These are supported by Kumar et al. [177] and Marques [111].

## 4.2. Cutting forces

Table 4-7 shows the results for the cutting force, and Figure 4-8 shows the average of their values in block diagrams.

**Table 4-7:** Cutting forces measured at the beginning of the tool's life

Cutting Force Test	Coating	Atmosphere	Cutting Forces [N]
Replica 1	TiNAL	ICT	186
	TiNAL	CFA	261
	TiNAL	DM	270
	AlCrN+	ICT	258
	AlCrN+	CFA	211
	AlCrN+	DM	277
Replica 2	TiNAL	ICT	158
	TiNAL	CFA	272
	TiNAL	DM	277
	AlCrN+	ICT	254
	AlCrN+	CFA	208
	AlCrN+	DM	294
Replica 3	TiNAL	ICT	221
	TiNAL	CFA	264
	TiNAL	DM	304
	AlCrN+	ICT	261
	AlCrN+	CFA	213
	AlCrN+	DM	300

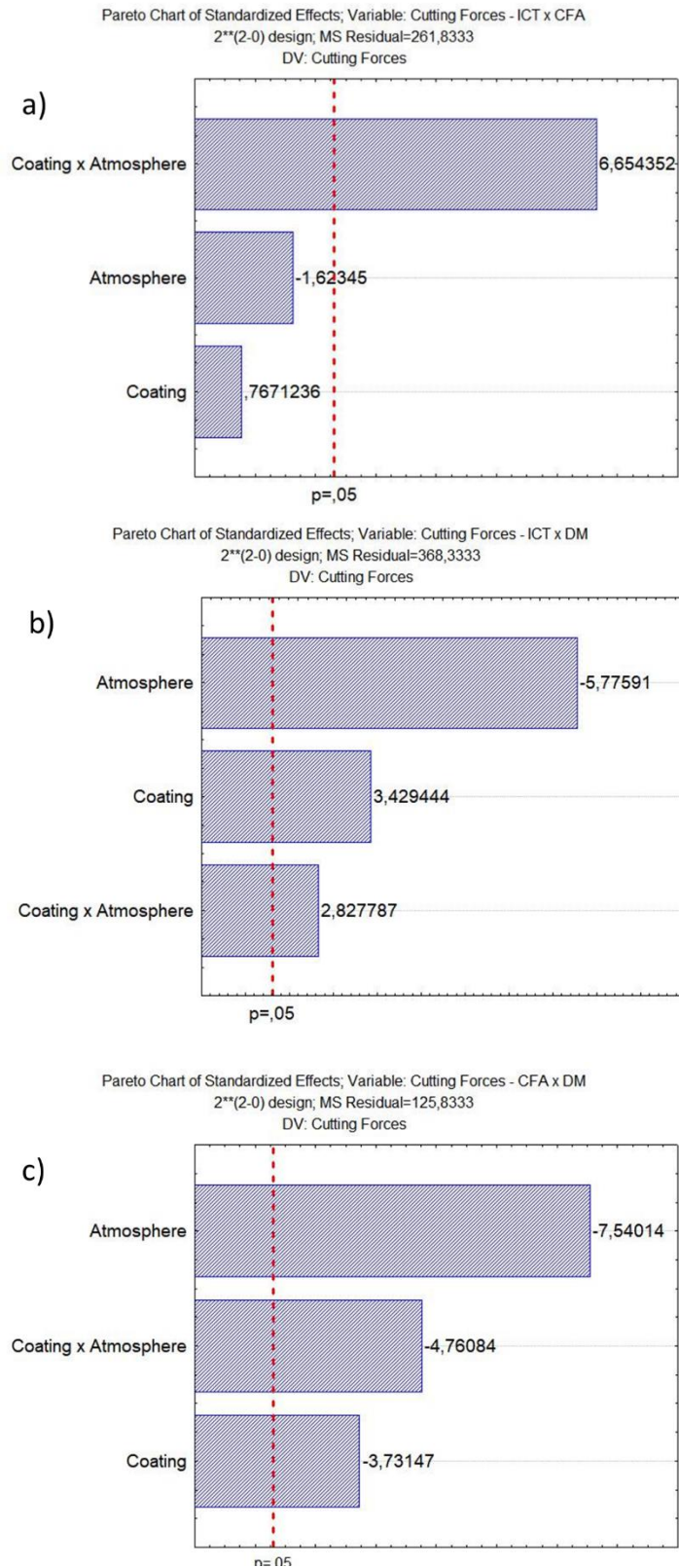


**Figure 4-8:** Cutting forces with different tool coatings and atmosphere conditions.

**Table 4-8** contains the analysis of variance for the cutting forces comparing the atmospheres, while **Figure 4-9** contains the Pareto diagram with the significance variables considering a 95% confidence interval.

**Table 4-8: Cutting Forces ANOVA**

Cutting Forces - ICT x CFA					
	SS	df	MS	F	p-value
Coating	154.08	1	154.08	0.58848	0.465043
Atmosphere	690.08	1	690.08	2.63558	0.143150
Coating x Atmosphere	11594.08	1	11594.08	44.28039	0.000160
Error	2094.67	8	261.83		
Total SS	14532.92	11			
Cutting Forces - ICT x DM					
	SS	df	MS	F	p-value
Coating	4332.00	1	4332.00	11.76109	0.008962
Atmosphere	12288.00	1	12288.00	33.36109	0.000416
Coating x Atmosphere	2945.33	1	2945.33	7.99638	0.022226
Error	2946.67	8	368.33		
Total SS	22512.00	11			
Cutting Forces - CFA x DM					
	SS	df	MS	F	p-value
Coating	4332.00	1	4332.00	11.76109	0.008962
Atmosphere	1752.08	1	1752.083	13.92384	0.005776
Coating x Atmosphere	7154.08	1	7154.083	56.85364	0.000067
Error	2852.08	1	2852.083	22.66556	0.001425
Total SS	1006.67	8	125.833		



**Figure 4-9:** Pareto chart results for cutting forces considering different atmospheres, ICT x CFA (a), ICT x DM (b), CFA x DM (c)

Comparing the results of the cutting forces –  $F_c$  for CFA atmosphere, when using the TiNAl coated tools, the ICT strategy presented the lowest values, while when using the AlCrN+ coating, it had highest values. Dry machining presented the highest cutting forces regardless of the tool coating and cutting atmosphere conditions. With the TiNAl-coated tools, the cutting force average values were  $188 \pm 32$ ,  $266 \pm 6$ , and  $284 \pm 18$  for ICT, CFA, and DM, respectively. With the AlCrN+, it was  $211 \pm 3$ ,  $258 \pm 4$ , and  $290 \pm 12$  for CFA, ICT, and DM.

It is known that high temperatures in the cutting zone tend to decrease the mechanical strength of the material and, consequently, the cutting forces. This is widely accepted in the literature (Klocke, 2011; Machado et al., 2011; Trent & Wright, 2000). On the other hand, a material with lower shear strength is more ductile and deforms more than fragile materials. So, this higher ductility could cause an increase in the tool-chip contact length; with this, the cutting forces tend to increase. So, the high heat removal offered by the cooling strategy cools the cutting region more efficiently and tends to change the shape of the chip, deforming it less, with reduced chip-tool contact area and consequently lower cutting forces. It is important to emphasize that this hypothesis is supported only by the TiNAl coating, which is a good conductor. In the case of ICT and the double AlCrN+ coated tool, which is thermal insulating, the shear force was higher than the CFA and lower than the DM. Bearing in mind that the cutting fluids also contain good lubricating capacity in addition to the heat removal capacity, that ICT strategy does not have.

Under the DM condition, the shear forces were higher in all analyzed situations. The explanation would be that the high temperature, which on the one hand favors the softening of the material, also deforms it further, increasing the chip-tool contact length that, in turn, enhances the machining force. This can even be observed in the machining of Inconel 718, either in dry machining or when the tools are already worn when the material tends to adhere further on the rake surface.

The Pareto's chart, **Figure 4-9**, showed the most significant input variables for the cutting force. When comparing ICT (level +1) x CFA (level -1), only the tool coating x cutting atmosphere interaction was significant, considering a 95 % reliability index **Figure 4-9 (a)**. The cutting force was higher for the tool coating AlCrN+ (level +1) and

ICT cooling strategy. The CFA atmosphere tended to decrease the cutting forces, although not statistically significant. With the TiNAl coating, the lowest cutting forces were found for ICT, 30% lower than CFA. However, for AlCrN+, CFA was 18 % lower.

Bazon (2020) monitored cutting forces during trials of turning cast gray iron with uncoated cemented carbide tools comparing two different atmospheres, ICT and CFA and varied cutting speed from 40 to 600 m/min [159]. The author found that ICT presented higher cutting forces than CFA for all tested cutting conditions, however, with a tendency to increase as the  $v_c$  increased. This reinforces the following hypothesis: increasing the cutting speed, the cutting fluid has more difficulty getting access to the cutting zone or the chip-tool workpiece interfaces; at low cutting speeds, it has the better lubricating ability; at high cutting speed, the cooling capacity becomes more relevant, and so, the ICT tends to perform better reducing the cutting forces.

For ICT (level +1) x DM (level -1), all the variables were significant, **Figure 4-9 (b)**. In this case, ICT performed much better than DM, having with the TiNAl coated tool 33 % and AlCrN+ 11 % lower cutting forces. Tool coating was the second most significant input variable. AlCrN+ contributed to the increase in the cutting forces, and the explanation is attributed to the high heat generation on this coating. Finally, the interaction of the tool coating x cutting atmosphere is significant, with the combination of AlCrN+ and DM conditions contributing to enhancing the cutting force.

Peixoto (2021) used the ICT when machining grey cast iron during turning with uncoated carbide tools and varied the cutting speed [166]. The author found that ICT's cutting forces were also lower than DM's. According to him, this result was because of the discontinuous chip type and the ICT strategy that could effectively reduce the temperature at the chip-tool interface, changing the tribological conditions. However, Barbosa (2021), when machining AISI D6 hardened steel with PCBN tools, found higher forces for ICT than DM [179]. Even with contradictory results, they are important because they prove that internally cooled tools influence the tribology of the chip-tool interface.

Neto et al. (2015) developed a particular type of internally cooled tool holder using a refrigerant fluid instead of water [95]. They performed a turning test with the proposed system using stainless-steel (SAE XEV-F), a challenging to cut with poor thermal



conductivity (14.5 W/m.K), a value close to Inconel 718. The tests were carried out with triple-coated cemented carbide tools (TiN, TiCN, Al<sub>2</sub>O<sub>3</sub>, and CVD). The author found the highest machining force values when using DM compared to CFA and ICT.

For CFA (level +1) x DM (level -1), all the input variables were significant, **Figure 4-9 (c)**. The cutting atmosphere was the most significant influence variable, with CFA considerably decreasing the cutting forces. Tool coating x cutting atmosphere interaction was the second most influential input variable, with the DM and AlCrN+ coated tool the most important variable, increasing the cutting force remarkably. With the TiNAl coated tool, the CFA presented 7% lower cutting forces, and with AlCrN+, 27 % lower than DM. The reason was already mentioned, which is part of this method's lubricant and cooling ability. The literature supports these findings since cutting fluids reduces the machining force components [12,14,180,181].

### 4.3. Roughness results

The measured of roughness was make with tool at half-life condition,  $V_B = 0.3$  m. **Tables 4.9 to 4.11** show the results of the workpiece surface roughness  $R_a$ ,  $R_z$ , and  $R_q$  parameters for the three cutting atmospheres, DM, CFA, and ICT. **Figure 4-10 to Figure 4-12** show these results graphically.

**Table 4-9:** Surface roughness  $R_a$  parameter

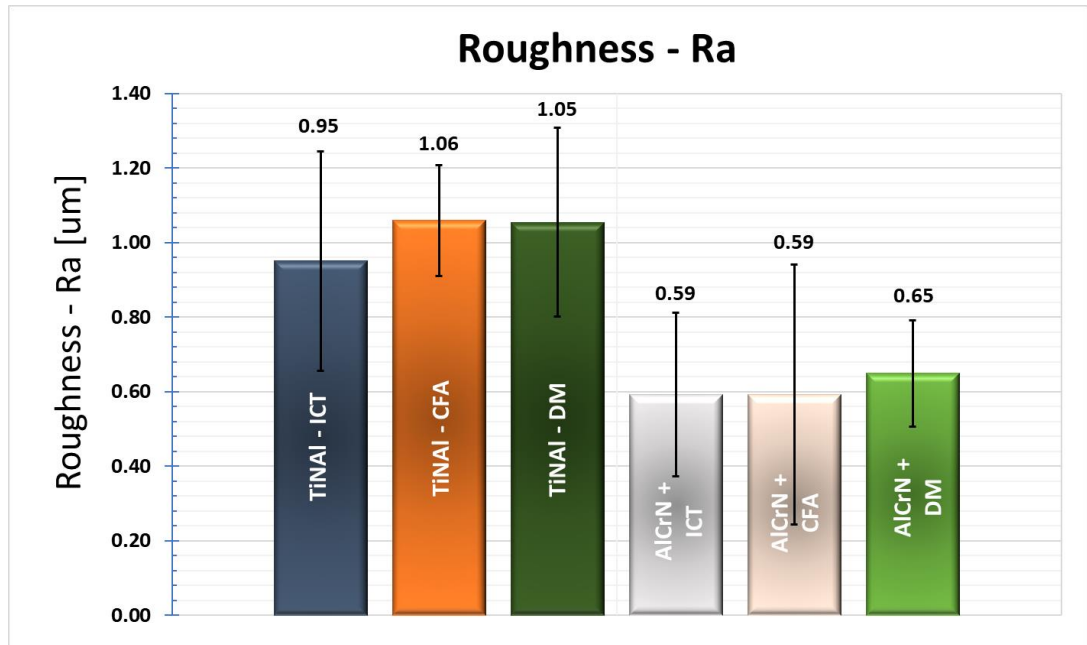
Roughness test	Coating	Atmosphere	Roughness Measurements ( $R_a$ ) [ $\mu m$ ]			Average ( $R_a$ ) [ $\mu m$ ]
			0°	120°	240°	
Replicate 1	TiNAL	ICT	1.07	1.35	0.96	1.13
	TiNAL	CFA	1.17	1.20	1.18	1.18
	TiNAL	DM	1.02	0.97	0.96	0.98
	AlCrN+	ICT	0.45	0.51	0.55	0.50
	AlCrN+	CFA	0.38	0.36	0.38	0.37
	AlCrN+	DM	0.60	0.46	0.43	0.50
Replicate 2	TiNAL	ICT	1.15	1.08	1.17	1.13
	TiNAL	CFA	0.89	1.01	0.94	0.95
	TiNAL	DM	0.88	0.87	0.70	0.82
	AlCrN+	ICT	0.43	0.37	0.44	0.41
	AlCrN+	CFA	0.43	0.33	0.31	0.36
	AlCrN+	DM	0.65	0.60	0.79	0.68
Replicate 3	TiNAL	ICT	0.51	0.61	0.65	0.59
	TiNAL	CFA	1.06	0.84	1.24	1.05
	TiNAL	DM	1.38	1.38	1.33	1.36
	AlCrN+	ICT	0.75	1.04	0.79	0.86
	AlCrN+	CFA	1.26	0.93	0.95	1.05
	AlCrN+	DM	0.71	0.77	0.83	0.77

**Table 4-10:** Surface roughness  $R_z$  parameter

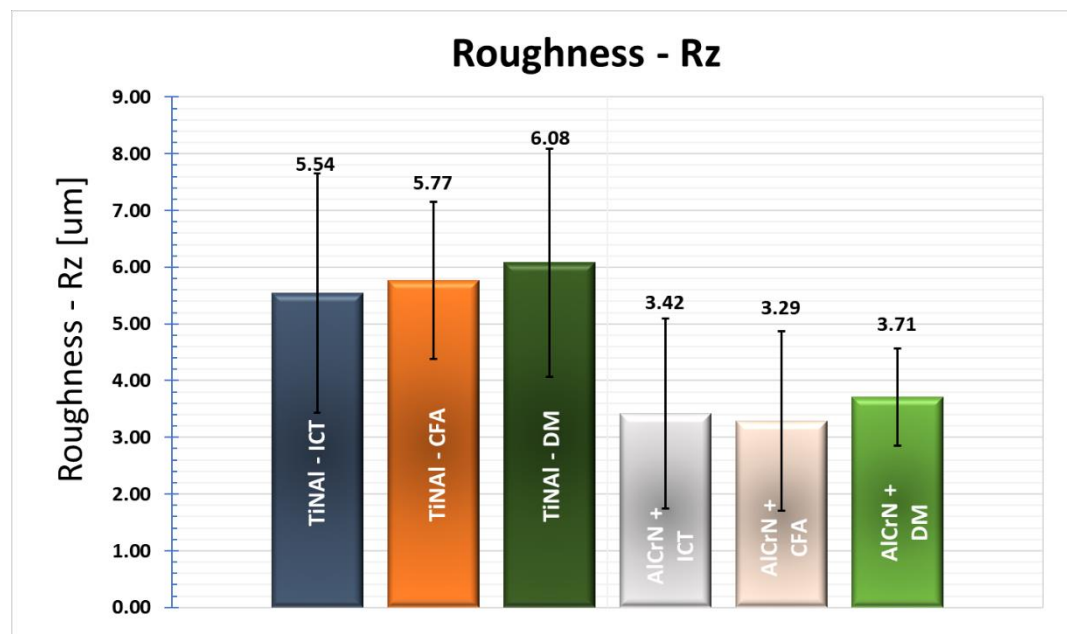
Roughness test	Coating	Atmosphere	Roughness Measurements			Average $(R_z)$ [ $\mu m$ ]
			$(R_z)$ [ $\mu m$ ]			
			0°	120°	240°	
Replicate 1	TiNAL	ICT	5.40	8.70	4.70	6.27
	TiNAL	CFA	5.90	6.20	6.10	6.07
	TiNAL	DM	5.30	4.80	4.80	4.97
	ALCRN+	ICT	2.80	3.10	2.30	2.73
	ALCRN+	CFA	2.30	2.20	2.40	2.30
	ALCRN+	DM	3.80	2.70	2.30	2.93
Replicate 2	TiNAL	ICT	5.80	7.30	8.10	7.07
	TiNAL	CFA	4.70	4.90	4.80	4.80
	TiNAL	DM	6.50	4.30	3.80	4.87
	ALCRN+	ICT	2.60	2.60	2.40	2.53
	ALCRN+	CFA	2.70	2.10	2.40	2.40
	ALCRN+	DM	4.40	3.60	3.50	3.83
Replicate 3	TiNAL	ICT	3.10	3.60	3.20	3.30
	TiNAL	CFA	4.70	5.50	9.10	6.43
	TiNAL	DM	6.90	9.50	8.80	8.40
	ALCRN+	ICT	4.00	3.30	7.70	5.00
	ALCRN+	CFA	4.20	4.60	6.70	5.17
	ALCRN+	DM	3.80	4.40	4.90	4.37

**Table 4-11:** Surface roughness  $R_q$  parameter

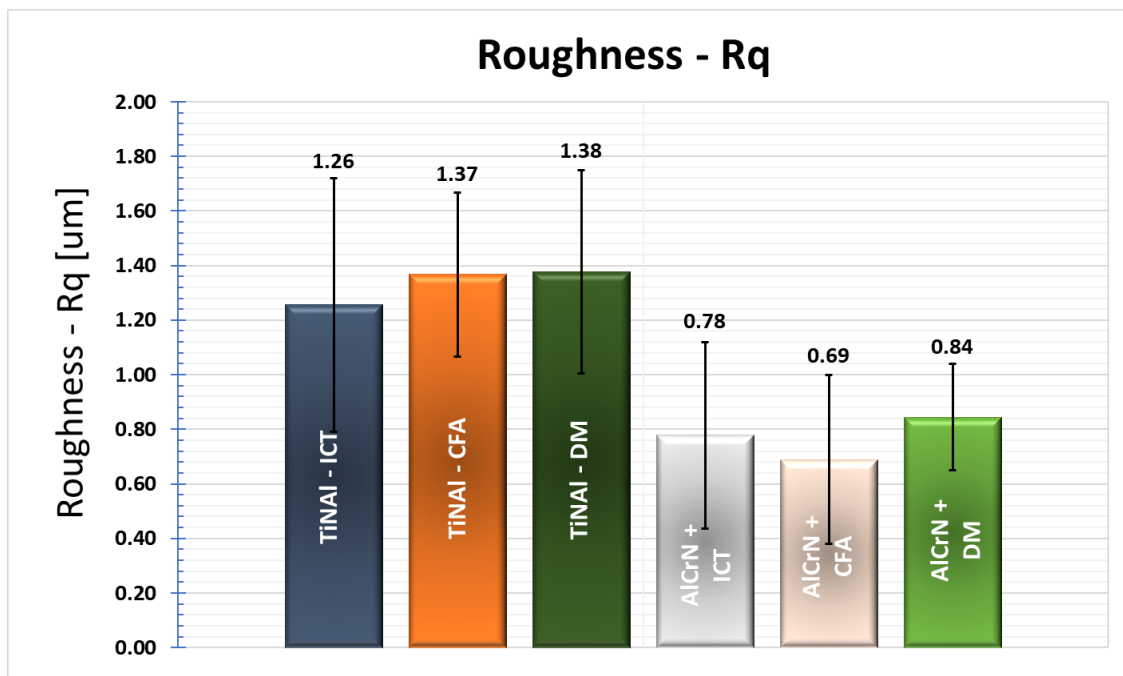
Roughness test	Coating	Atmosphere	Roughness Measurements			Average $(R_q)$ [ $\mu m$ ]
			$(R_q)$ [ $\mu m$ ]			
			0°	120°	240°	
Replicate 1	TiNAL	ICT	1.30	2.0	1.20	1.50
	TiNAL	CFA	1.40	1.40	1.40	1.40
	TiNAL	DM	1.20	1.10	1.20	1.17
	ALCRN+	ICT	0.70	0.70	0.60	0.67
	ALCRN+	CFA	0.50	0.50	0.50	0.50
	ALCRN+	DM	0.50	0.60	0.80	0.63
Replicate 2	TiNAL	ICT	1.30	1.60	1.70	1.53
	TiNAL	CFA	1.10	1.20	1.10	1.13
	TiNAL	DM	1.40	1.10	0.90	1.13
	ALCRN+	ICT	0.50	0.60	0.50	0.53
	ALCRN+	CFA	0.50	0.40	0.50	0.47
	ALCRN+	DM	1.00	0.80	0.90	0.90
Replicate 3	TiNAL	ICT	0.60	0.80	0.80	0.73
	TiNAL	CFA	2.10	1.30	1.30	1.57
	TiNAL	DM	1.70	1.90	1.90	1.83
	ALCRN+	ICT	0.90	0.90	1.60	1.13
	ALCRN+	CFA	1.10	1.10	1.10	1.10
	ALCRN+	DM	0.90	1.00	1.10	1.00



**Figure 4-10:** Surface roughness  $R_a$  average (R1, R2, and R3) for various cutting atmospheres and tool coatings.  
 $v_c = 45$  m/min,  $a_p = 0.5$  and  $f = 0.103$  mm/rev



**Figure 4-11:** Surface roughness  $R_z$  average (R1, R2, and R3) for various cutting atmospheres and tool coatings.  
 $v_c = 45$  m/min,  $a_p = 0.5$  and  $f = 0.103$  mm/rev.



**Figure 4-12:** Surface roughness  $R_q$  average (R1, R2, and R3) for various cutting atmospheres and tool coatings.

$vc = 45$  m/min,  $ap = 0.5$  and  $f = 0.103$  mm/rev.

Considering the dispersion bars, the tool coating input variable significantly influenced the surface roughness  $R_a$ ,  $R_z$ , and  $R_q$  parameters. The AlCrN+ coating presented lower surface roughness than TiNAl, regardless of the cutting atmosphere used. These results can be explained in the face of the coating. AlCrN + was specially developed for superalloys, such as Inconel 718. TiNAl is the standard coating from the manufacturer, CERATIZIT®. Its datasheet informs that this coating suits various applications, from cast irons, non-ferrous, etc., to super-alloy materials. So, it is reasonable to expect a non-optimized performance for Inconel 718. While it may seem counterintuitive that the AlCrN+ coating, which resulted in higher temperatures, could lead to improved surface roughness, this phenomenon can be attributed to the coating's unique suitability for machining Inconel 718. The compensatory effect of this coating's superior performance on Inconel 718 contributed to the overall improvement in surface roughness, despite the elevated temperatures.

Ramanujam et al. (2018) studied the performance of several tool coatings in the turning of Inconel 825 alloy [182]. The authors compared TiNAl, AlCrN, TiNAl-AlCrN, and uncoated tools. The best  $R_a$  roughness results were obtained with the TiNAl-AlCrN tool. According to the authors: “good surface morphology, high thermal stability, high adhesion

strength, low coefficient of friction, and better wear resistance of TiAlN/AlCrN coating could be the reasons for a better surface finish of the workpiece.” This author’s arguments are sustained by the study of Sampath Kumar et al. (2014) [183]. They characterized TiAlN, AlCrN, and AlCrN/TiAlN coatings and found that double coating (AlCrN-TiAlN) had higher hardness (32.75 GPa), higher Young’s modulus (561.97 GPa), and superior scratch resistance (LCN = 46 N) than the counterpart.

The analyses of variance results for the  $R_a$ ,  $R_z$ , and  $R_q$  roughness parameters are presented in **Table 4-12** when the pair ICT x CFA was compared. **Figure 4-13** contains the Pareto diagram showing the most statistically significant input variables on the workpiece surface roughness, considering a 95% of confidence level.

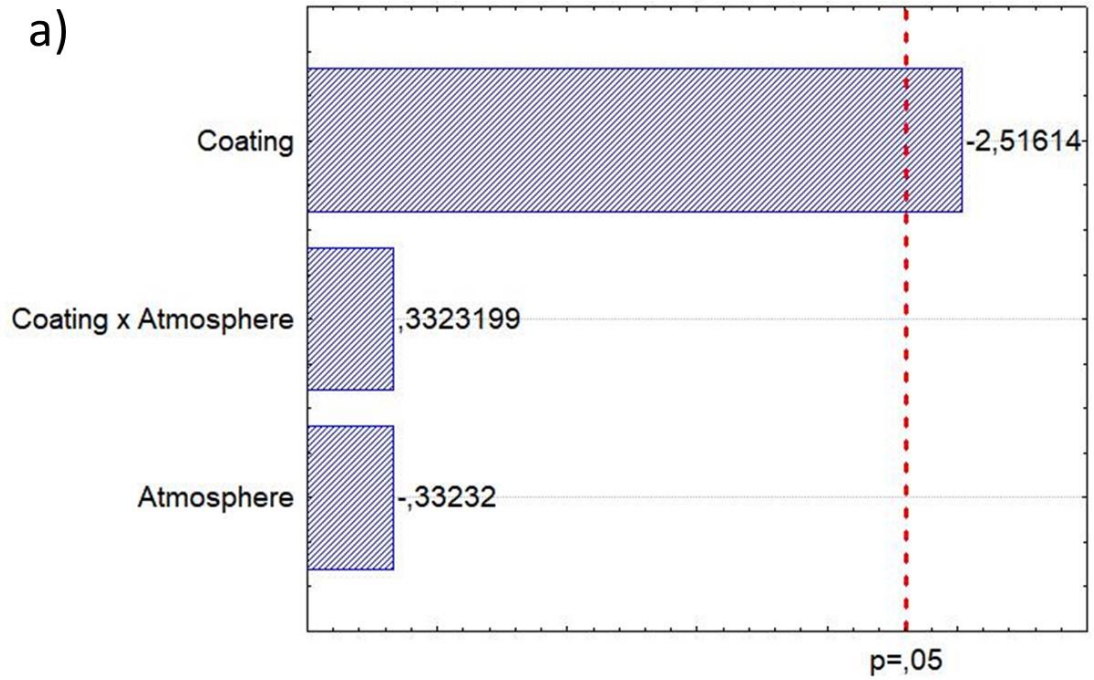
**Table 4-12:** Roughness  $R_a$ ,  $R_z$ , and  $R_q$  ANOVA comparing ICT x CFA

Roughness - $R_a$					
	SS	df	MS	F	p value
Tool coating	0.509781	1.000000	0.509781	6.330942	0.036025
Cutting atmosphere	0.008893	1.000000	0.008893	0.110437	0.748188
Coating x Atmosphere	0.008893	1.000000	0.008893	0.110437	0.748188
Error	0.644178	8.000000	0.080522		
Total SS	1.171744	11.000000			
Roughness - $R_z$					
Tool coating	15.870000	1.000000	15.870000	6.902501	0.030307
Cutting atmosphere	0.005926	1.000000	0.005926	0.002577	0.960755
Coating x Atmosphere	0.094815	1.000000	0.094815	0.041239	0.844148
Error	18.393333	8.000000	2.299167		
Total SS	34.364074	11.000000			
Roughness - $R_q$					
Tool coating	1.001481	1.000000	1.001481	8.365043	0.020130
Cutting atmosphere	0.000370	1.000000	0.000370	0.003094	0.957009
Coating x Atmosphere	0.030000	1.000000	0.030000	0.250580	0.630146
Error	0.957778	8.000000	0.119722		
Total SS	1.989630	11.000000			

Pareto Chart of Standardized Effects; Variable: Ra

2\*\*(2-0) design; MS Residual=,0805222

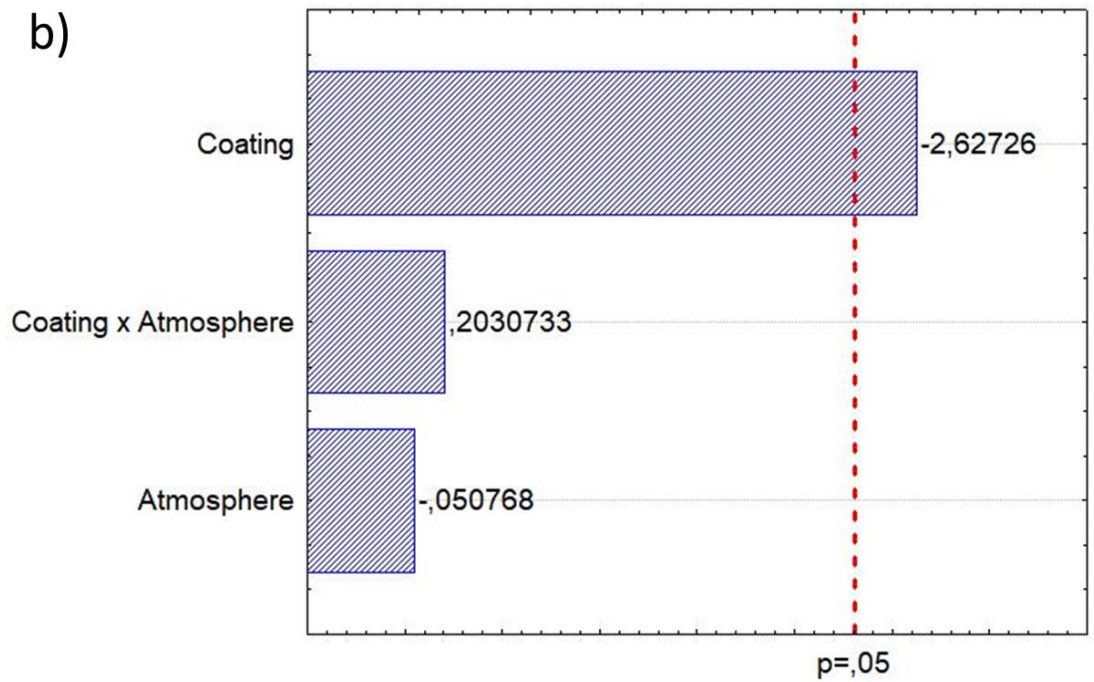
DV: Ra

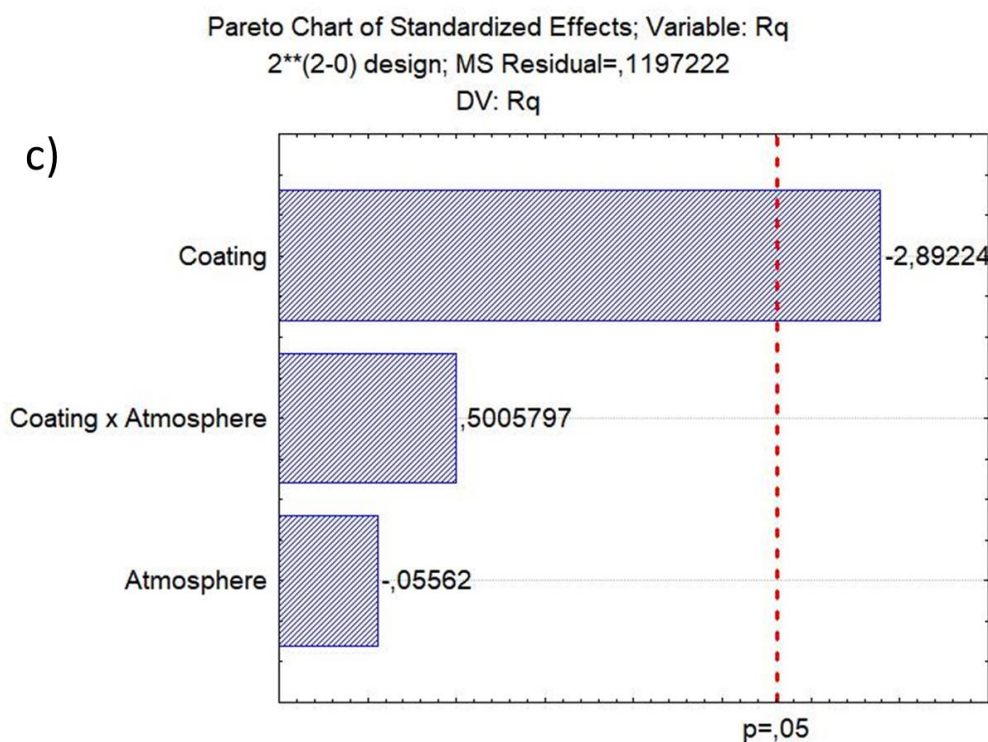


Pareto Chart of Standardized Effects; Variable: Rz

2\*\*(2-0) design; MS Residual=2,299167

DV: Rz





**Figure 4-13:** Pareto chart results for (a)  $R_a$ ; (b)  $R_z$  and (c)  $R_q$  - ICT x CFA

For the ICT x CFA comparison, only the tool coating significantly influenced the surface roughness  $R_a$ ,  $R_z$ , and  $R_q$  parameters, and AlCrN+ coating presented a better surface finish than TiNAl. Although the cutting atmosphere was not statistically significant, the CFA atmosphere presented better results than ICT and DM. This can be associated with the lubricating capacity lacking in ICT and DM. It is not clear how much cutting fluids could penetrate chip-tool-workpiece interfaces. At the tool's rake face, the cutting zone is formed with high pressure and high temperatures, and the theory indicates the presence of a seizure zone, of absolute contact between the chip and the tool where no fluid can gain access [4,5].

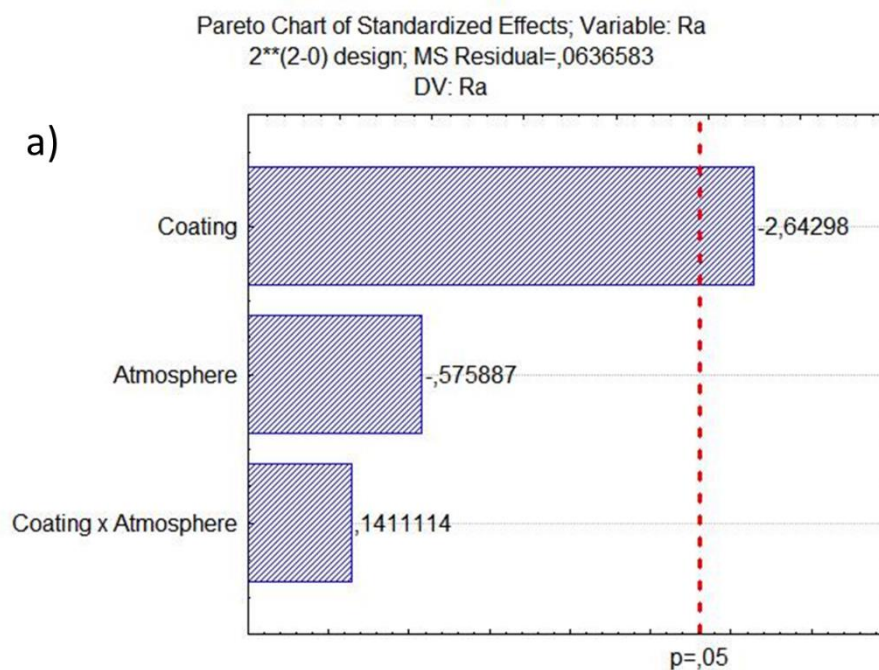
Nevertheless, the seizure zone is followed by the sliding zone, where the pressure is less and with room for cutting fluid penetration. In the sliding zone, the CFA strategy allows a liquid film formation that eases the chip sliding over the rake face, reducing the CoF at the chip-tool interface [4,5,37]. The results demonstrate the possibility of using ICT, at least concerning the workpiece surface roughness, as it presented statically the same behavior as CFA, the standard technique used for Inconel 718 turning with cemented carbide tools.

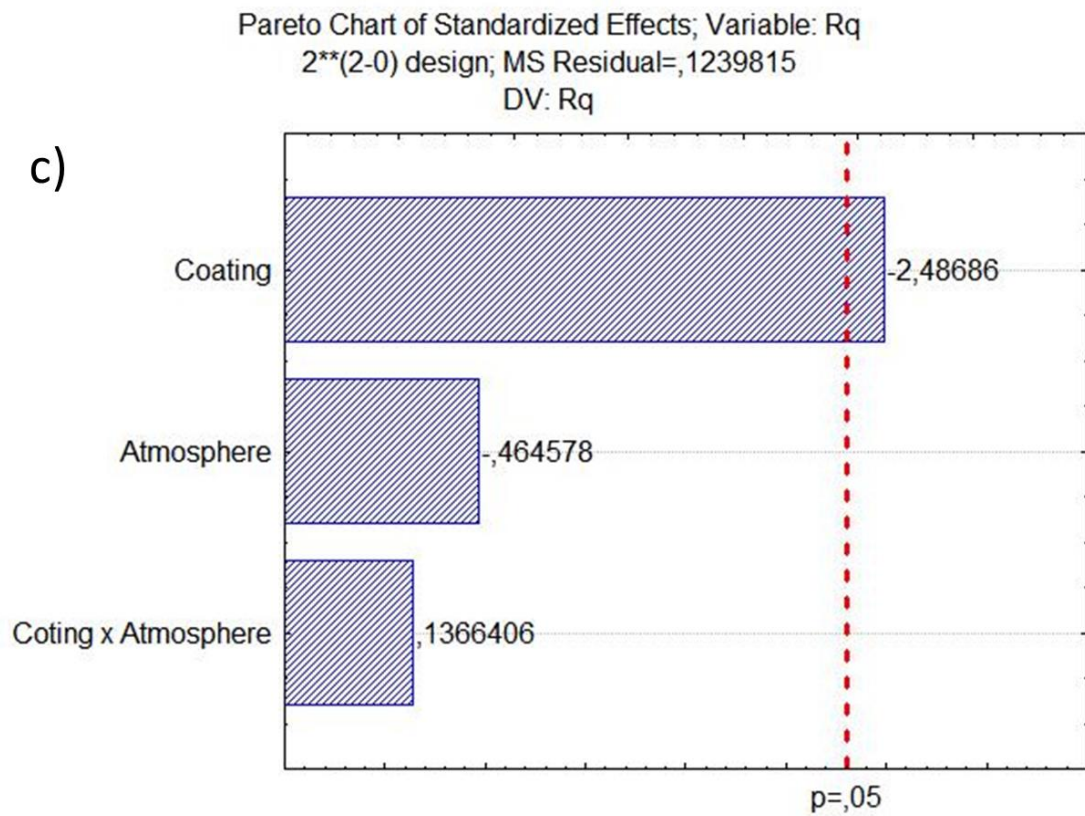
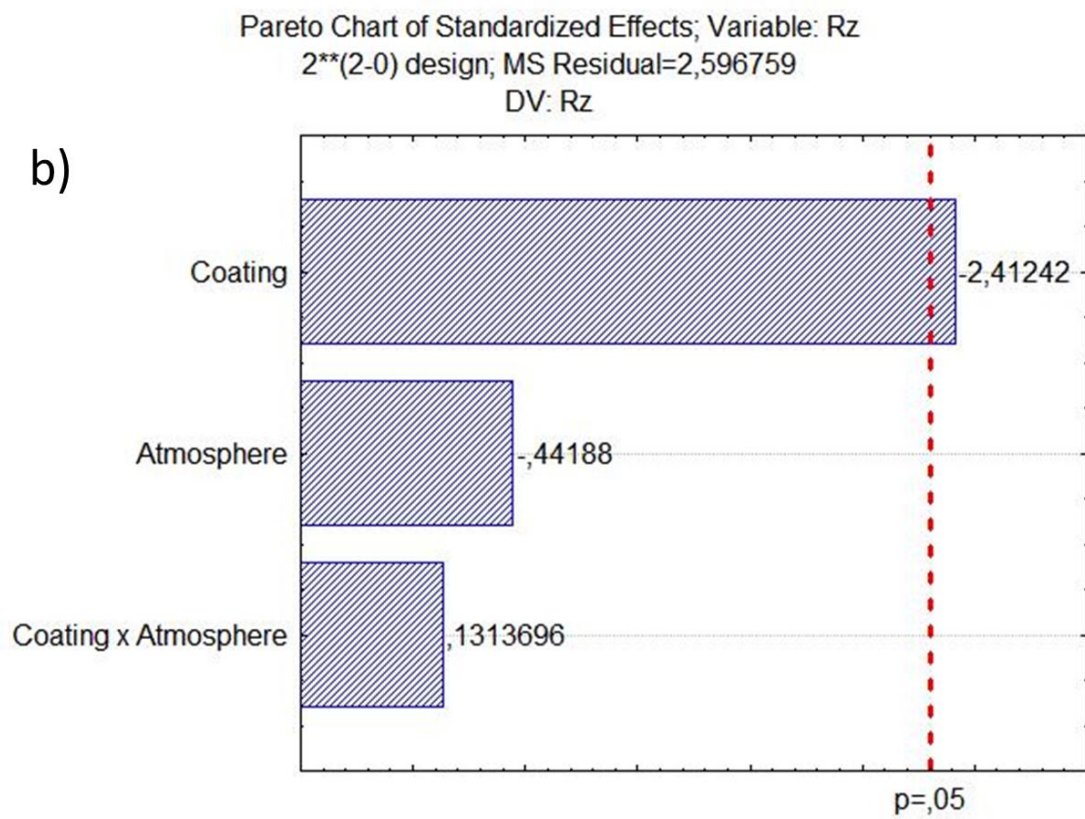


The analyses of variance for the  $R_a$ ,  $R_z$ , and  $R_q$  roughness parameters for the comparison between ICT x DM are presented in **Table 4-13**. **Figure 4-14** contains the Pareto diagram showing the most statistically significant input variables on the workpiece surface roughness, considering a 95% of confidence level.

**Table 4-13: Roughness  $R_a$ ,  $R_z$ , and  $R_q$  ANOVA comparing ICT x DM**

Roughness - $R_a$					
	SS	df	MS	F	p-value
Tool coating	0.444675	1	0.444675	6.985338	0.029576
Cutting atmosphere	0.021112	1	0.021112	0.331646	0.580526
Coating x Atmosphere	0.001268	1	0.001268	0.019912	0.891270
Error	0.509267	8	0.063658		
Total SS	0.976321	11			
Roughness - $R_z$					
Tool coating	15.11259	1	15.11259	5.819790	0.042348
Cutting atmosphere	0.50704	1	0.50704	0.195258	0.670277
Coating x Atmosphere	0.04481	1	0.04481	0.017258	0.898727
Error	20.77407	8	2.59676		
Total SS	36.43852	11			
Roughness - $R_q$					
Tool coating	0.766759	1	0.766759	6.184466	0.037706
Cutting atmosphere	0.026759	1	0.026759	0.215833	0.654616
Coating x Atmosphere	0.002315	1	0.002315	0.018671	0.894691
Error	0.991852	8	0.123981		
Total SS	1.787685	11			





**Figure 4-14:** Pareto chart results for roughness (a) Ra, (b) Rz and (c) Rq, respectively (from top to bottom) comparing ICT x DM

For the ICT x DM comparison, only the tool coating input variable significantly influenced the roughness  $R_a$ ,  $R_z$ , and  $R_q$  parameters, as occurred in the comparison of ICT x CFA. AlCrN+ coating presented better results than TiNAl. Although the cutting atmosphere was not statistically significant, the ICT strategy tended to decrease the surface roughness. The ICT's high heat removal capacity can contribute to reducing the temperature at the cutting zone, avoiding its harmful effects.

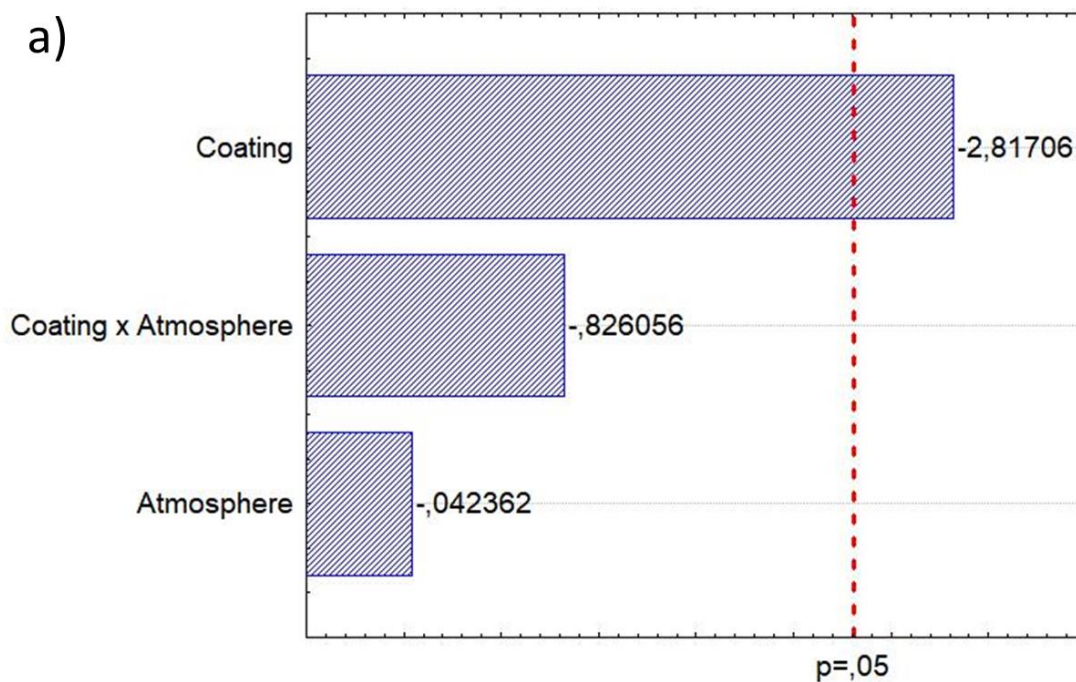
Many studies indicate lower temperatures improve surface finishing [2,30,125]. Temperature plays a multifaceted role in machining processes, significantly impacting surface roughness. Elevated temperatures can lead to thermal expansion of the workpiece, potentially causing dimensional changes and rougher surfaces. Tool wear accelerates with increased temperatures, resulting in tool-related irregularities and roughness. The material properties of workpieces can be affected, with some materials becoming more susceptible to deformation and smearing at higher temperatures. Chip formation and evacuation can also be influenced, potentially leading to chip adhesion and surface imperfections. Effective cooling can mitigate these effects, maintaining smoother surface finishes. Additionally, the choice of tool coating can modulate the impact of temperature on surface roughness. Achieving the desired surface finish in machining processes requires a careful balance of temperature control and optimization [7]. Dry machining, though, presented a poor surface finish with almost no lubricating and cooling capacity.

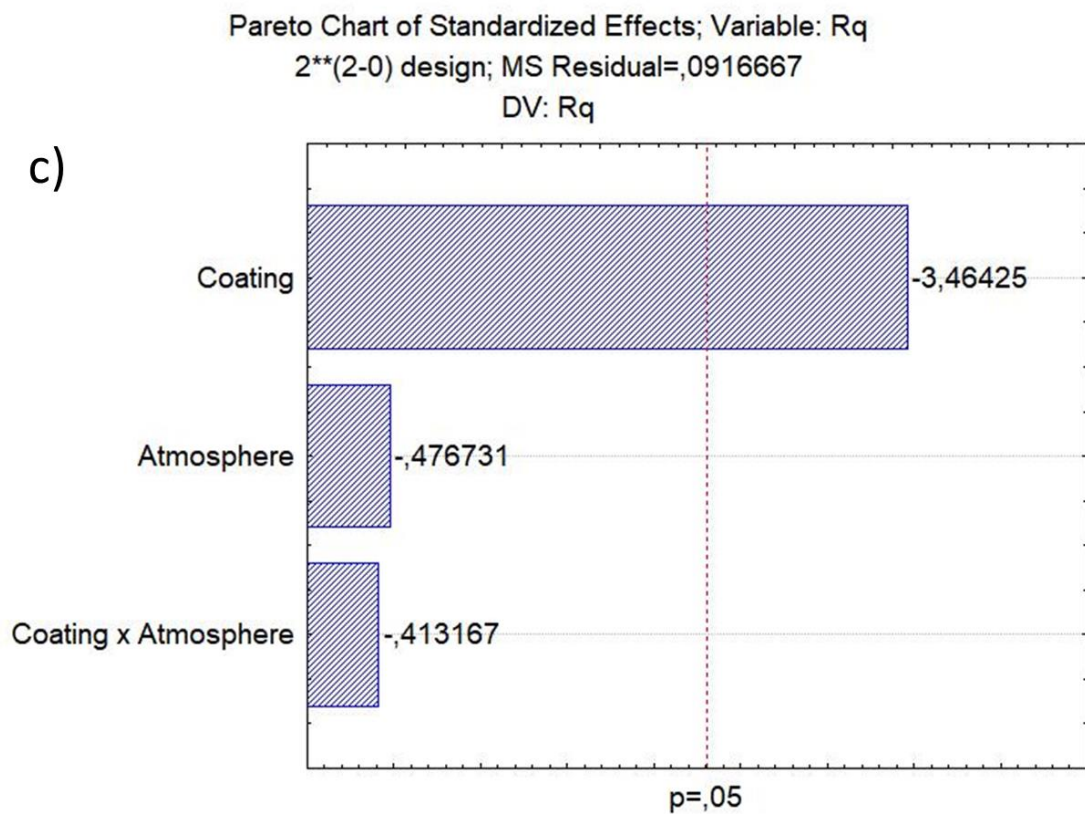
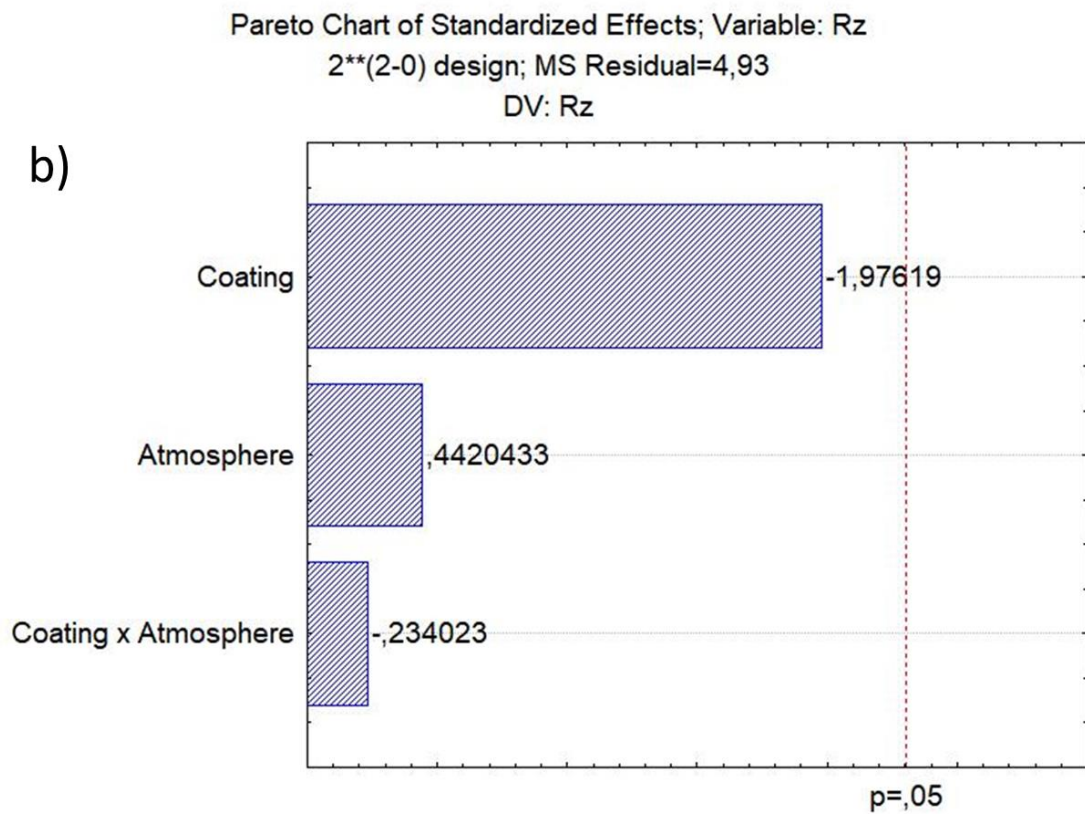
Finally, ANOVA results for the  $R_a$ ,  $R_z$ , and  $R_q$  roughness parameters for comparing CFA x DM are presented in **Figure 4-13**. **Figure 4-15** contains the Pareto diagram showing the most statistically significant input variables on the workpiece surface roughness, considering a 95% of a confidence interval.

**Table 4-14:** Roughness Ra, Rz, and Rq ANOVA comparing CFA x DM

Roughness - Ra					
	SS	df	MS	F	p-value
Tool coating	0.589633	1.000000	0.589633	7.935846	0.022596
Cutting atmosphere	0.000133	1.000000	0.000133	0.001795	0.967248
Error	0.594400	8.000000	0.074300		
Total SS	1.234867	11.000000			
Roughness - Rz					
Tool coating	19.253333	1.000000	19.253333	3.905341	0.083539
Cutting atmosphere	0.963333	1.000000	0.963333	0.195402	0.670164
Coating x Atmosphere	0.270000	1.000000	0.270000	0.054767	0.820845
Error	39.440000	8.000000	4.930000		
Total SS	59.926667	11.000000			
Roughness - Rq					
Tool coating	1.100093	1.000000	1.100093	12.001010	0.008514
Cutting atmosphere	0.020833	1.000000	0.020833	0.227273	0.646303
Coating x Atmosphere	0.015648	1.000000	0.015648	0.170707	0.690337
Error	0.733333	8.000000	0.091667		
Total SS	1.869907	11.000000			

Pareto Chart of Standardized Effects; Variable: Ra  
 2\*\*(2-0) design; MS Residual=,0743  
 DV: Ra





**Figure 4-15:** Pareto chart results for roughness (a) Ra, (b) Rz and (c) Rq, respectively (from top to bottom) comparing CFA x DM

When comparing CFA x DM atmospheres, results followed the same trends, with the tool coating being the most influential input variable on the surface roughness. However, in this comparison, none of the input variables presented statistical influence over the Rz roughness parameter, **Figure 4-15 (b)**.

Rz often exhibits a higher statistical dispersion compared to other roughness parameters due to its specific method of measurement. Unlike parameters such as Ra (average roughness) or Rq (root mean square roughness), which consider the entire roughness profile, Rz focuses on the distance between the highest peak and the lowest valley within each sampling length. This localized measurement can be more sensitive to isolated irregularities or abrupt changes in the surface texture, leading to greater variability in the data. Additionally, Rz may capture unique features that other parameters overlook, contributing to its tendency for higher statistical dispersion in certain cases. Again, AlCrN+ coating presented better workpiece surface roughness than TiNAl, and DM atmosphere tended to increase it for not having either cooling or lubricating capacity.

Barbosa (2021), using the same ICT cooling strategy proposed in this work, found similar results, i.e., the cutting atmosphere did not influence roughness  $R_a$ ,  $R_z$ , and  $R_q$  parameters. The author machined D6 hardened steel in turning operation using PCBN tools internally cooled compared to DM. Bazon (2020), using the same ICT but machining grey cast iron in turning operation, found that the cutting atmosphere was not a significant variable for the surface roughness.

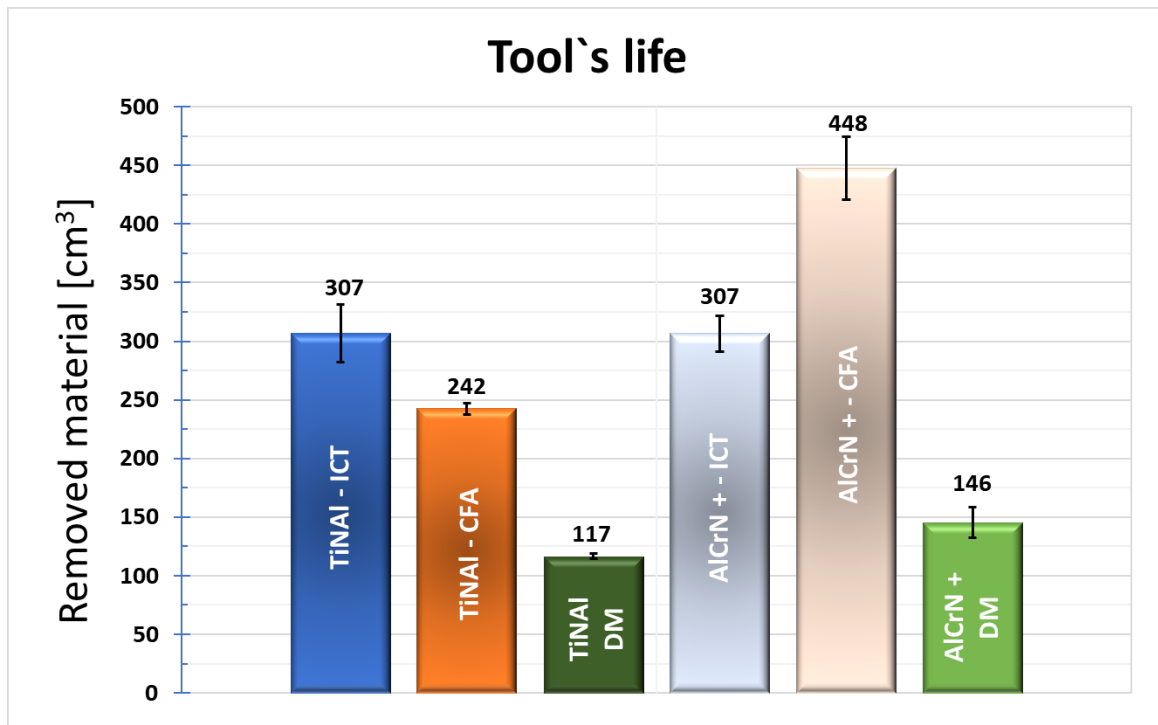
Therefore, these results are a positive aspect since they demonstrate the possibility of using ICT, at least concerning the surface roughness, as it presented similar behavior of the CFA strategy, the standard technique used for Inconel 718 turning with cemented carbide tools.

#### 4.4. Tools life

**Table 4-15** shows the results for the tool's life, and **Figure 4-16** shows the average of these variables. The tool's end-of-life criterion was when the tool had no more cutting capacity, i.e., failure.

**Table 4-15:** Tool's life for different machining conditions

Tool Coating	Cutting Atmosphere	Material removed Replica 1 [cm <sup>3</sup> ]	Material removed Replica 2 [cm <sup>3</sup> ]	Material removed Replica 3 [cm <sup>3</sup> ]	Average [cm <sup>3</sup> ]	Stand. Deviation
TiNAL	ICT	330	310	280	307	25.00
TiNAL	CFA	245	237	245	242	4.61
TiNAL	DM	115	119	116	117	2.080
AlCrN+	ICT	291	321	308	307	15.00
AlCrN+	CFA	418	458	467	448	26.00
AlCrN+	DM	161	135	141	146	16.60



**Figure 4-16:** Average (Replica 1, 2, and 3) for tool's life for each machining condition

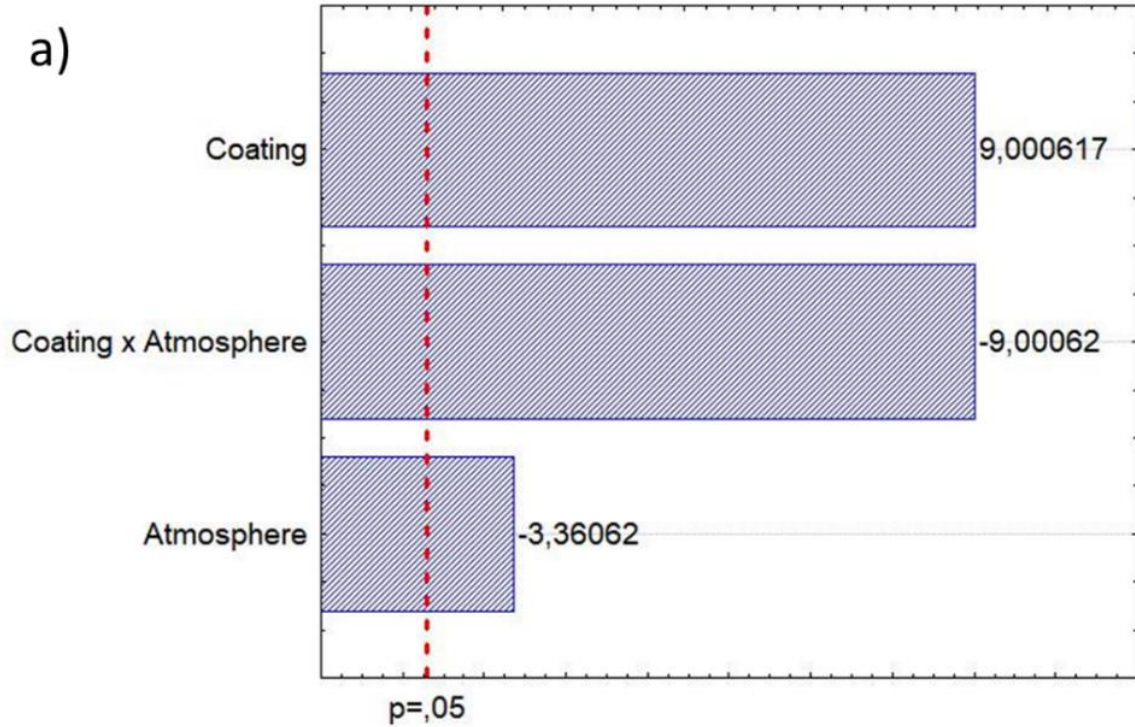
The ANOVA of the tool life results was performed in pairs of comparisons, considering all three cutting atmospheres tested. The results are presented in **Figure 4-15** and **Figure 4-17**, which contain the Pareto diagram showing the influence of the input variables considering a 95% confidence level.

**Table 4-16: ANOVA of the tool life tests**

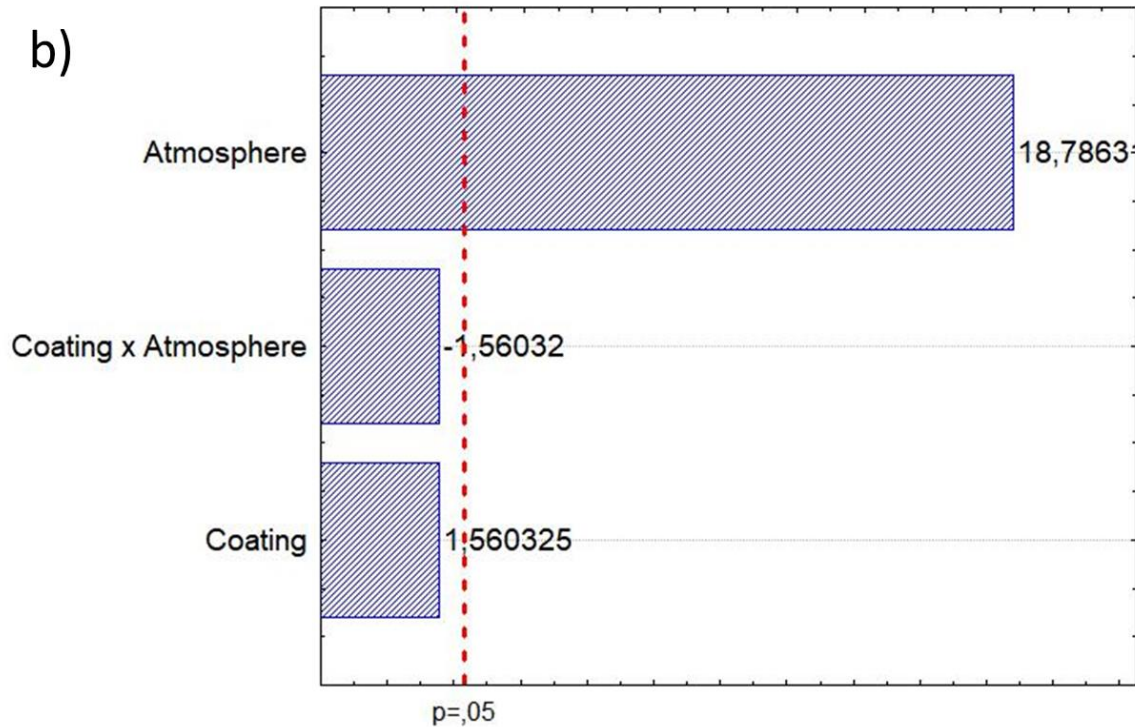
Tool's life - ICT x CFA					
	SS	df	MS	F	p-value
Tool coating	3,162133E+10	1	3,162133E+10	81,01110	0,000019
Cutting atmosphere	4,408333E+09	1	4,408333E+09	11,29377	0,009923
Coating x Atmosphere	3,162133E+10	1	3,162133E+10	81,01110	0,000019
Error	3,122667E+09	8	3,903333E+08		
Total SS	7,077367E+10	11			
Tool's life - ICT x DM					
	SS	df	MS	F	p-value
Tool coating	6.380208E+08	1	6.380208E+08	2.4346	0.157304
Cutting atmosphere	9.248852E+10	1	9.248852E+10	352.9254	0.000000
Coating x Atmosphere	6.380208E+08	1	6.380208E+08	2.4346	0.157304
Error	2.096500E+09	8	2.620625E+08		
Total SS	9.586106E+10	11			
Tool's life - CFA x DM					
	SS	df	MS	F	p-value
Tool coating	5,182133E+10	1	4,196133E+10	54,05110	0,000001
Cutting atmosphere	4.124269E+10	1	4.124269E+10	185.3083	0.000001
Coating x Atmosphere	1.372810E+11	1	1.372810E+11	616.8201	0.000000
Error	2.327602E+10	8	2.327602E+10		
Total SS	1.780500E+09	11			

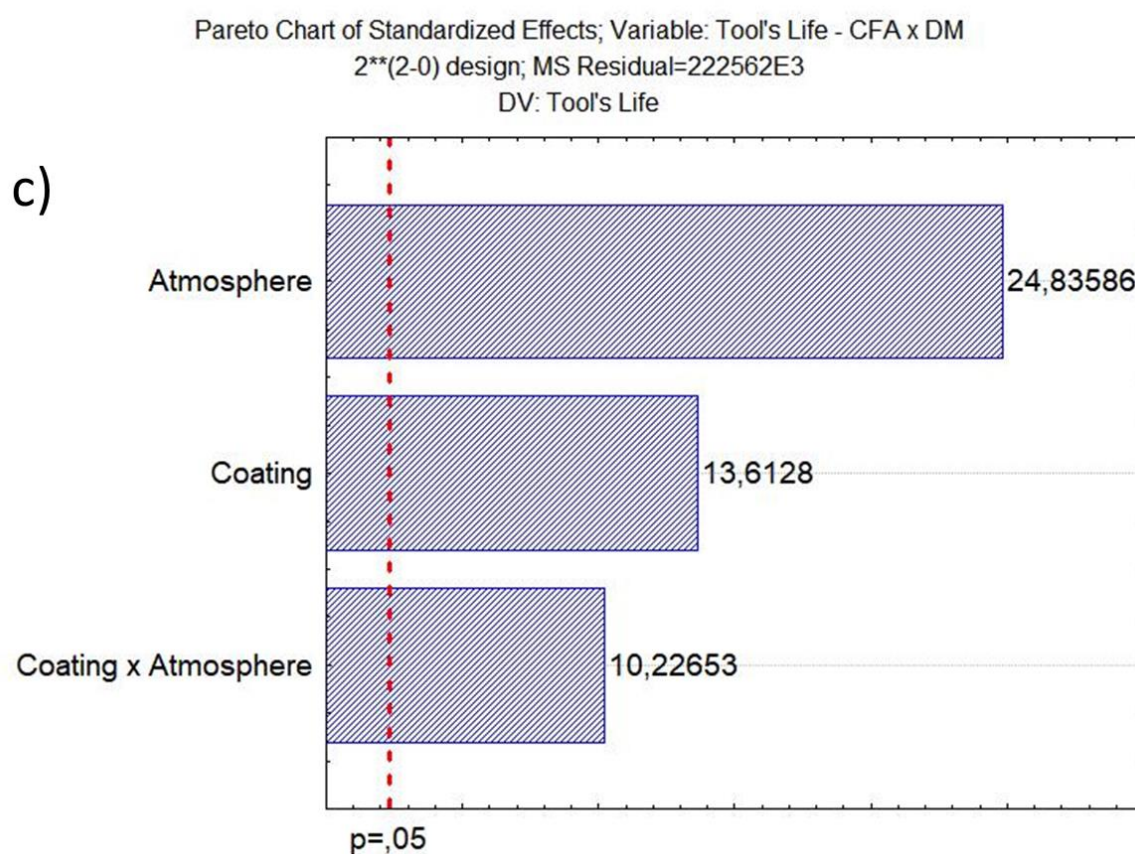


Pareto Chart of Standardized Effects; Variable: Tool's Life - ICT x CFA  
2\*\*(2-0) design; MS Residual=390333E3  
DV: Tool's Life



Pareto Chart of Standardized Effects; Variable: Tool's Life - ICT x DM  
2\*\*(2-0) design; MS Residual=262062E3  
DV: Tool's Life





**Figure 4-17:** Pareto's charts of the for tool's life results, (a) ICT x CFA, (b) ICT x DM and (c) CFA x DM.

Observing the results of **Figure 4-16**, both the cutting atmosphere and the tool coating significantly affect the tools' life. The ANOVA of the tool life results was performed in pairs of comparisons, considering all three cutting atmospheres tested. The results are presented in **Figure 4-15** and **Figure 4-17**, which contain the Pareto diagram showing the influence of the input variables considering a 95% confidence level.

In this regard, the AlCrN+ coating has proven its superiority over TiNAl across a spectrum of cutting conditions. This distinction holds particular significance when dealing with Inconel, a material known for its propensity to produce continuous chips that entail extensive contact between the chip, tool, and workpiece.

The formation of continuous chips during Inconel machining introduces challenges such as heightened friction and thermal stress at the tool-chip interface. Consequently, the selection of an appropriate tool coating becomes imperative to mitigate wear and friction in such demanding scenarios. The double layered AlCrN+ coating not only surpasses TiNAl but also fortifies the tool by adding extra protective layers over the

WC+Co substrate. This reinforcement significantly enhances tool durability and overall performance, making it particularly well-suited for machining high-strength materials like Inconel 718.

This correlation underscores the pivotal role played by tool coatings in addressing the unique demands imposed by the chip type generated during Inconel machining. Given Inconel's tendency to produce continuous chips characterized by higher chip-tool-workpiece contact compared to the segmented chips of titanium alloys, the choice of a double-coated (AlCrN+) tool emerges as a robust solution, bolstering resistance and protection through multiple layers over the WC+Co substrate.

The tool's results life when using the tool coated with AlCrN+ better performance was obtained with CFA, followed by ICT and DM, with the average tool's lives being  $448 \pm 26$ ,  $306 \pm 15$ , and  $146 \pm 15$  cm<sup>3</sup>, respectively. Cutting fluids applied by flooding usually have good heat removal and lubricating capacity, which is lacking in the ICT system. The CFs form a film on the rake face where the chip slides over, facilitating the cutting and less stressing the tool. It also cools the tool preserving it.

The AlCrN+ is double-coated with TiNAl forming a thermal insulating layer between the substrate and the chip. Since ICT has a cooling action inside the tool, the AlCrN+ will probably reduce the heat removal creating a thermal barrier because of its low thermal conductivity. This hypothesis can be sustained because, for TiNAl single coating, the ICT presented the highest tool's life,  $307 \pm 25$ , compared to CFA and DM,  $242 \pm 5$  and  $117 \pm 2$ , respectively.

The Pareto's chart, **Figure 4-17**, showed the most significant variables for the tool's life. When comparing ICT (level +1) x CFA (level -1), tool coating, cutting atmosphere, and their interaction was statistically significant, considering a 95 % confidence level. AlCrN+ (level +1) and CFA contributed equally to increasing the tool's performance, followed by their interaction. Again, AlCrN+ with CFA had the highest tool's life, + 46% in comparison. However, for TiNAl (level -1), ICT presented the highest performance, + 27%, compared to CFA. Important to note that ICT has no lubricating capacity, only cooling of the tool, while CFA has both capacities. Thus, it is concluded that ICT demonstrates good heat removal capacity.

Only the cutting atmosphere significantly affected ICT (level +1) x DM (level -1) comparison. In this case, ICT performed much better than DM. Because Inconel 718 has very high mechanical resistance, more mechanical energy is dispended for shearing. It is well known that most of this energy is converted into heat at the cutting zone (L. R. R. Da Silva et al., 2018; Fernandes et al., 2021; Klocke, 2011; Trent & Wright, 2000). Thus, DM machining is practically impossible for turning this work material since it has no cooling effects, while ICT is the opposite. ICT tool's life was higher for both AlCrN+ (level +1) and TiNAl (level -1), being 210 % and 262 %, respectively, compared to DM. Barbosa (2021), when machining D6 hardened steel using a PCBN tool internally cooled, found 35% higher tool life compared to DM.

All input variables were statistically significant for the comparison of CFA (level +1) x DM (level -1). The cutting atmosphere was the most important, with CFA considerably increasing the tool's life. The reason was already mentioned, which is part of this method's lubricant and cooling ability. The tool coating was also an essential factor, with the AlCrN+ (level +1) with CFA having much better performance, 307% in comparison to DM. For TiNAl (level -1) and CFA, it was 207 % higher than DM.

The tool's life results align with many other works where tool indirectly cooled was studied, which shows that this system has promising perspectives. For instance, Neto et al. (2015) performed turning tests with the proposed system in SAE XEV-F, a type of stainless steel challenging to cut with poor thermal conductivity (14.5 W/m. K), a value close to Inconel 718. The tests were carried out with triple-coated carbide tools (TiN, TiCN, Al<sub>2</sub>O<sub>3</sub>, CVD). The authors found intermediary tool's life for their system; the highest values were obtained for CFA while the lowest for DM. According to the authors, the lack of lubrication in their system could be improved (using a hybrid method, for example) to achieve better results.

Minton et al. (2013) used a similar system with a cooling chamber (block) replacing the cutting tool shim. They used mono ethylene glycol at room temperature (~26°C) in a closed circuit. The machined material was titanium, grade 2, using cemented carbide inserts coated with Polycrystalline Diamond - *PCD* (Chemical Vapor Deposition - CVD). The authors observed that the internal cooling system of the tool holder acted efficiently, showing that the PCD coating dissipates heat quickly on the surface, which is

subsequently removed by the internal cooling. The refrigeration system achieved better tool life results and lower temperatures.

Rozzi et al. (2011) developed a system of exchanging heat removal made by microchannels in the tool shim through which liquid nitrogen (LN<sub>2</sub>) circulated to cool the tool indirectly during cutting. They conclude that the LN<sub>2</sub>-cooled microchannel heat exchanger is a viable system capable of significantly improving tool life compared to the traditional CFA environment.

## 4.5. Wear mechanisms analysis

**Figure 4-19** shows the perspective view, **Figure 4-20** the lateral view (flank face), and **Figure 4-21** the top view (rake face) for all the tool coatings and the atmosphere conditions. Regarding the wear mechanisms, the five most common in machining were observed: adhesion (attrition), abrasion, oxidation, diffusion, and plastic deformation. However, they were present regardless of the tool coating or cutting atmosphere used in different intensities. For Inconel 718 machining, these five wear mechanisms are widely observed, and the findings follow the literature [111,117,119,143,168,185]. Lima [115] investigated the tool wear on ceramics (SiAlON, mixed, and whiskers) when turning Inconel 751 and 718. The author varied the cutting speed from 150 to 300 m/min and could observe an intense adhesion wear mechanism on the tool surfaces for all the cutting conditions tested. Although using cemented carbide tools, in the present work, the same was observed. The adhesion wear mechanism was present in all the cutting conditions tested.

Adhesion is a wear mechanism in which the work material adheres to the tool's surface and slides over it, pulling out grains from the tool. Adhered work material on the worn tools indicates an adhesion wear mechanism may have occurred. With the help of EDS analysis shown in **Figure 4-22** and **Figure 4-23**, together with a visual inspection, adhered work material can be certified. For instance, nickel (Ni), iron (Fe), and chrome (Cr), basic elements of Inconel 718, were observed on the tool, even after the chemical attack, especially over the cutting zone. EDS is a semi-quantitative analysis that can help to estimate the elements presented. Thus, **Table 4-17** is a supportive tool to help to identify the wear mechanisms present in the tool after machining. It shows a semi-quantitative presence of each element.

Regarding the cutting atmospheres, it was not observed notable differences between them. However, a difference in adhesion between TiAlN and AlCrN+ coatings was observed. The nickel and iron content sum at AlCrN+ coating was superior to TiAlN, **Table 4-17**. **Figure 4-18** graphically shows the elements' content comparing flank and rake faces obtained by EDS analysis. Nickel and iron elements are absent in the tools and come from the workpiece material. The transference is associated either with diffusion or adhesion. This could happen due to the affinity between the coatings and the work

material.

**Table 4-17:** Semi-quantitative elements analysis at tools rake and flank faces

<b>Rake face</b>										
Coating	Atmosphere	N	Al	Ti	Cr	Fe	Co	Ni	W	Total
AlCrN +	ICT	22.73	24.26	1.46	24.18	15.78	0.44	0.97	10.19	100
AlCrN +	CFA	23.90	27.49	1.42	29.86	3.91	0	7.23	6.19	100
AlCrN +	DM	25.08	24.15	1.59	28.09	3.93	0.71	9.44	7.00	100
TiNAl	ICT	34.91	6.66	10.11	0.40	9.97	1.65	0.83	35.47	100
TiNAl	CFA	26.92	17.76	21.02	1.22	2.00	0.57	2.88	27.63	100
TiNAl	DM	28.09	20.31	25.68	0.86	1.01	0.30	1.90	21.86	100
<b>Flank face</b>										
Coating	Atmosphere	N	Al	Ti	Cr	Fe	Co	Ni	W	Total
AlCrN +	ICT	28.00	25.99	0.60	23.18	9.33	1.61	1.23	10.07	100
AlCrN +	CFA	30.59	25.82	0.62	23.94	2.44	0.13	4.98	11.47	100
AlCrN +	DM	23.57	19.09	3.99	19.47	6.34	0.29	10.94	16.30	100
TiNAl	ICT	34.67	27.14	28.77	0.32	1.80	1.34	0.59	5.37	100
TiNAl	CFA	32.69	29.32	31.96	0.89	1.19	0	2.10	1.85	100
TiNAl	DM	32.40	24.22	27.34	0.74	0.90	0.18	1.43	12.79	100

Another difference is related to the content of tungsten (W), the major element of the tool substrate. For the rake face, where the chip sliding effects occur, **Table 4-17** shows that much higher W is observed on the TiNAl coated tool than AlCrN +, indicating that the latter resisted more to abrasion wear than the former. It also must be considered that AlCrN + is a double coating with AlCrN + over TiNAl. However, the opposite effect happened in the flank face, where more wear was obtained for the AlCrN+ coating. This is probably due to the dynamics of chip forming. While it tends to slide at the rake face, at the flank, the tool tends to attrit with the newly formed workpiece surface.

The wear occurred more uniformly at the AlCrN + coating than TiNAl. It was more concentrated in small regions, with a more significant presence of nickel, iron, and chromium at the tip of the cutting tools. In turn, for TiNAl, there was chipping, cracking, and greater crater wear, causing the chip-tool contact area to be greater, thus increasing the dispersion of these elements, as observed in **Figure 4-22** and **Figure 4-23**.

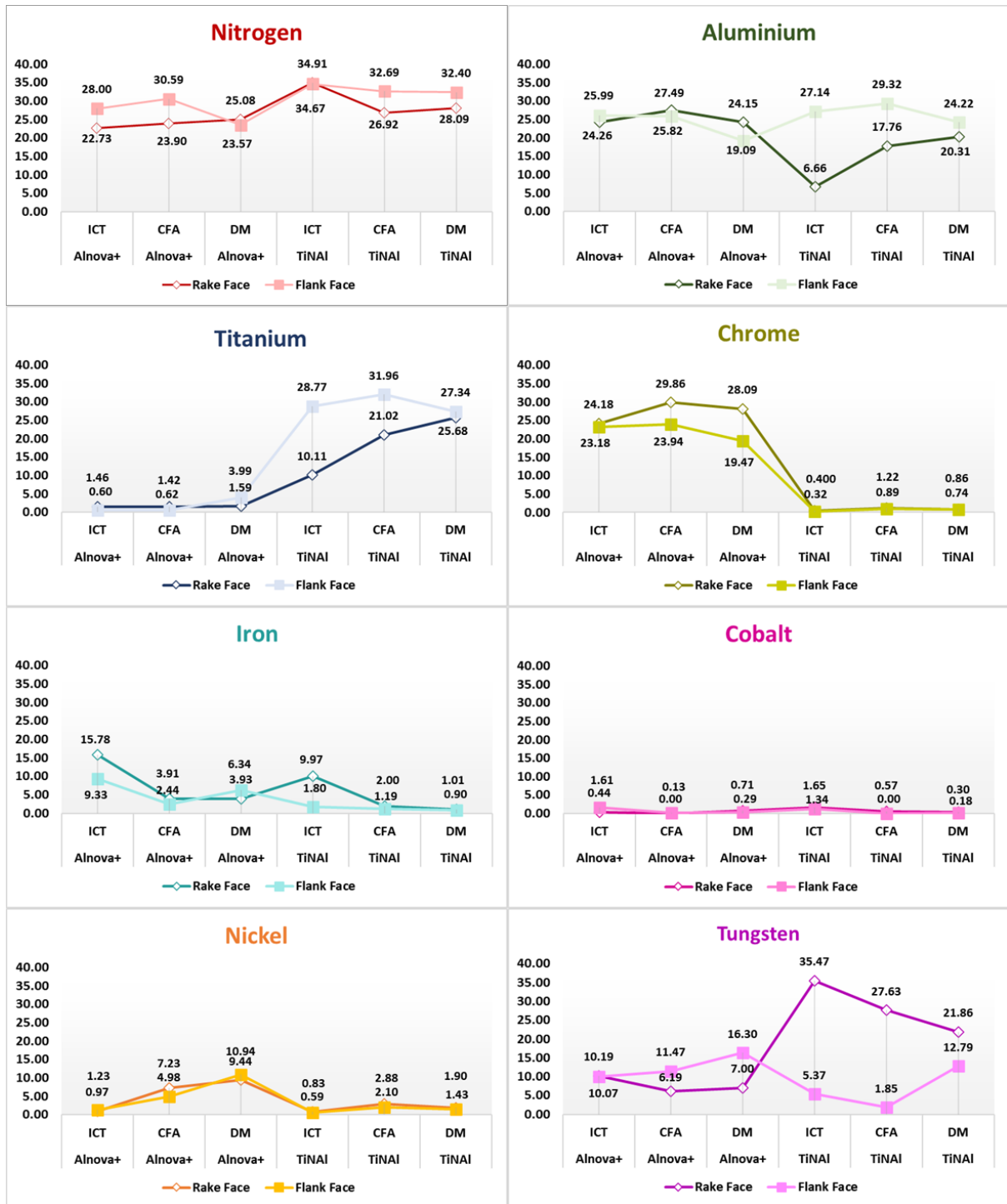


Figure 4-18: Semi-quantitative graphic elements analysis at tools rake and flank faces

Abrasion is a wear mechanism that generates grooves caused by hard particles on the work material like oxides, nitrides, and carbides or by hard particles lost from the tools by adhesion or microchipping, for example. It involves sub-classifications, such as



two or three bodies, generating grooves or micro grooves, etc. In the present work, these details were not considered, and abrasion was simplified as parallel and uniform grooves or micro grooves observed in the direction of the material flow. They are observed in all the cutting conditions tested, as shown in **Figure 4-19** to **Figure 4-21**. Regarding the abrasion wear mechanism, no noticeable differences were found between tool coatings or cutting atmospheres. For Inconel 718 machining, this wear mechanism is widely noted by many authors [84,111,117,143,186].

Diffusion occurs at the interatomic level on the rake and clearance surfaces. The interaction between materials (tool/chip/workpiece) strongly influences its intensity, which involves solubility of the elements, which depends on the size of the atoms involved, the kind of solid solution (interstitial or substitutional), etc. At the microscope, it has a smooth appearance and is thermally activated. It often happens during Inconel 718 machining [21,119,185].

The present study observed diffusion for all the cutting conditions tested. A concentration gradient of nickel, iron, and chromium atoms was found to be more intense for AlCrN+ and dispersed for TiNAl, as shown in EDS **Figure 4-22** and **Figure 4-23**. The reason is the same for adhesion, i.e., the wear is more uniform at AlCrN+ condition and tends to be concentrated at the tool tip. While for TiNAl, diffusion was more dispersed on a more extensive worn area. Regarding the cutting atmosphere, tools used in the tests with dry and ICT presented bigger crater wear than CFA. This was probably due to CFA's lubricating + cooling ability that acts on the rake face, especially at the sliding zone, thus creating a liquid film facilitating the chip removal.

Concerning the tool damages and wear types, chipping, microchipping, flank, crater wear, and coating detachments, comparing the AlCrN+ and TiNAl, it was observed that the former tended to have much less intensity of wear and damage. For example, in AlCrN+, **Figure 4-19 (right)**, the crater and flank wear are more uniform. Coating detachments, microchipping, and cracks were also observed. However, in the TiNAl coated tools, **Figure 4-20 (left)**, the wear was much more severe, with intense crater and flank wear, chipping, and cracks. These damages, wear types, and mechanisms can be seen in more detail in **Figure 4-20** and **Figure 4-21**.

It was observed that all cooling strategies caused intense microchipping, chipping, and micro cracks on the tools. These damages were predominant for dry machining due to the high temperatures that weakened the tool. This is characteristic of superalloys machining, mainly because of their mechanical resistance and hardness even at high temperatures [187]. Comparatively, the damages were more severe on the TiNAl-coated tools than on AlCrN+, as seen in **Figure 4-19**.

Notch wear was also present, especially at the beginning of machining at the level of the depth of cut, as observed by Marques (2015). This was expected because the contact impact between the tool and workpiece occurs at a depth of cut level, with the access of atmosphere, creating the conditions for the notch wear. Crater wear also occurred, associated with the diffusion mechanism [108,111,188]. This was notable for the ICT condition, **Figure 4-21**. Finally, the flank wear used as the end-of-tool-life criterion was prominent and more uniform for CFA, **Figure 4-20**.

The coating detachment was also a type of damage observed for all cutting conditions tested, especially on the cutting edges of the tools. Slightly more severe was observed in the dry condition due to the lack of lubrication and cooling, in addition to the higher temperatures that diminish the adhesion of the coatings [137], **Figure 4-19**.

Other works had similar results concerning the wear mechanisms and types. For instance Marques (2015) machined Inconel 718, varying the lubri-cooling conditions (CFs, CFs with solid lubricant, etc.) and using carbide and ceramic SIALON and whiskers reinforced tools. The author observed the exact wear mechanisms and types identified here, such as abrasion, adhesion, attrition, oxidation, and diffusion. In addition, it was observed notch at the depth of cut and intense crater wear. Furthermore, the same wear behavior when machining Inconel 718 was observed by Itakura et al. (1999)[168], Bhatt et al. (2010)[189], Roy et al. (2018) [79].

The present study identified plastic deformation in all cutting conditions, with a notable concentration gradient of nickel, iron, and chromium atoms. AlCrN+ coatings exhibited a more concentrated distribution of plastic deformation, primarily localized at the tool's tip, while TiNAl coatings displayed dispersed plastic deformation over a broader worn area. The cutting atmosphere also influenced plastic deformation, with dry and ICT conditions resulting in more substantial crater wear, possibly due to the cooling and

lubricating effects of CFA mitigating this form of wear. Plastic deformation is a critical wear mechanism to consider when optimizing machining processes for Inconel 718. The intensity of plastic deformation is strongly influenced by the interactions between materials, including the tool, chip, and workpiece. Plastic deformation is a common occurrence when machining Inconel 718, consistent with previous research [21,119,185]

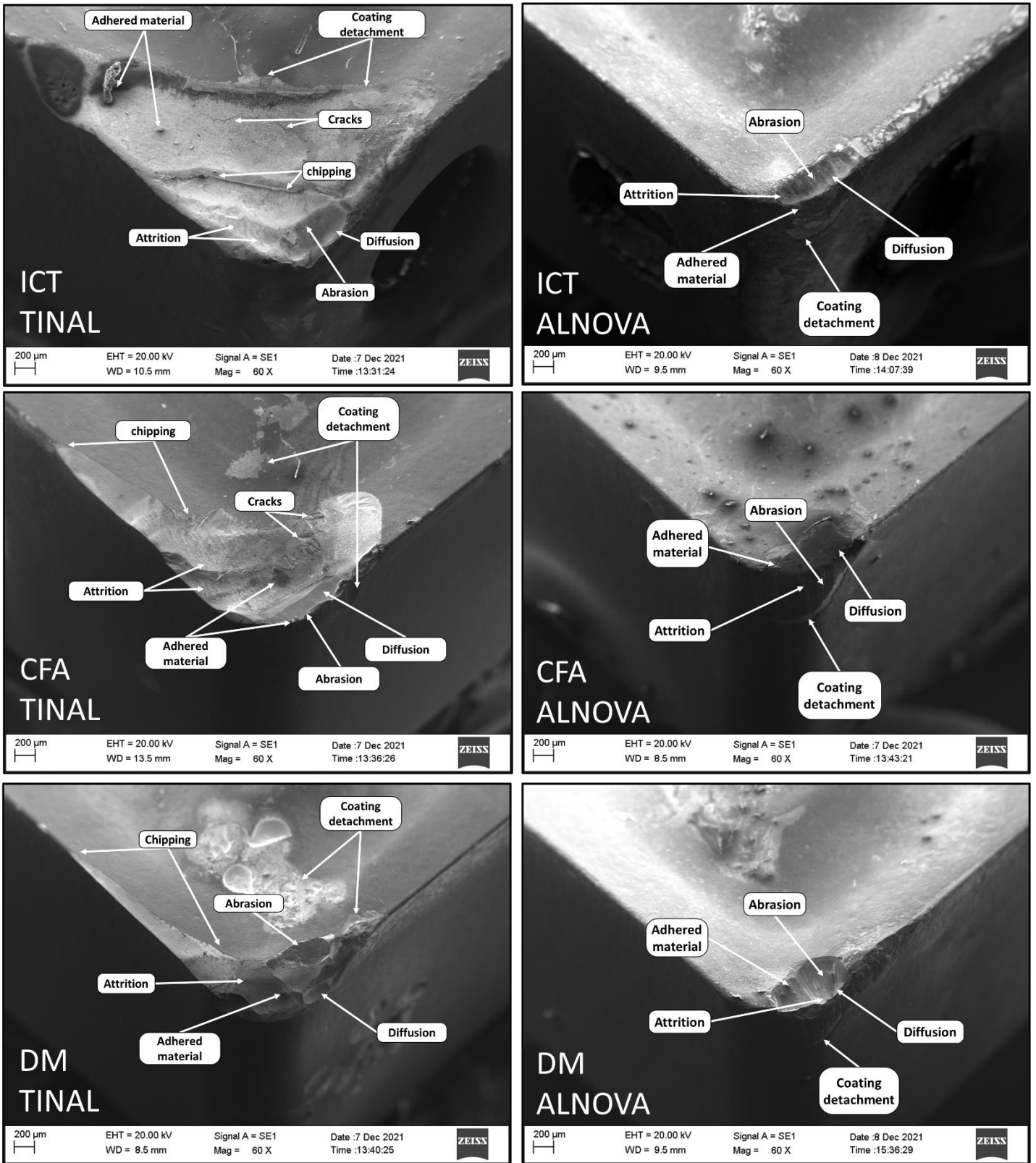
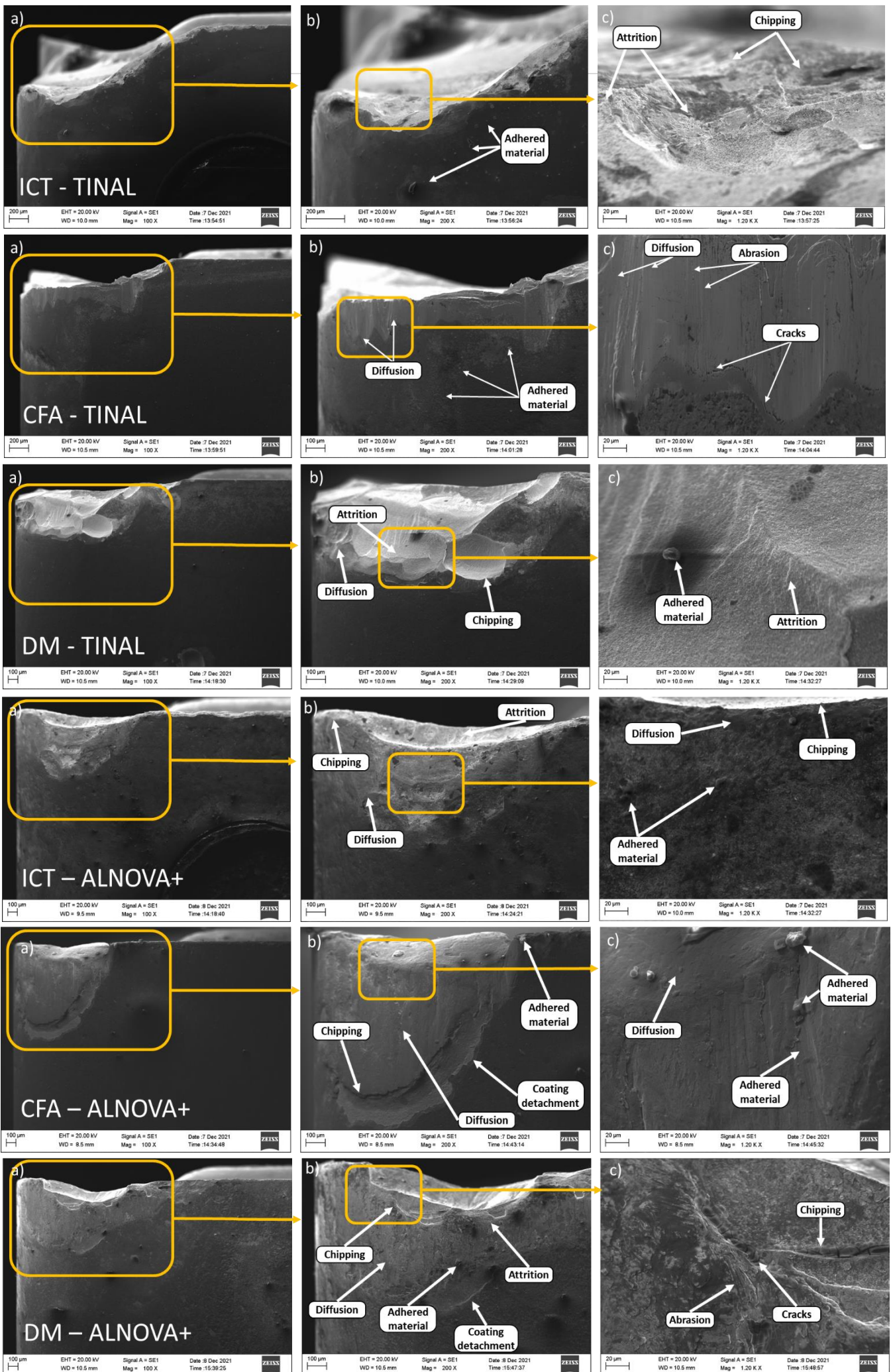
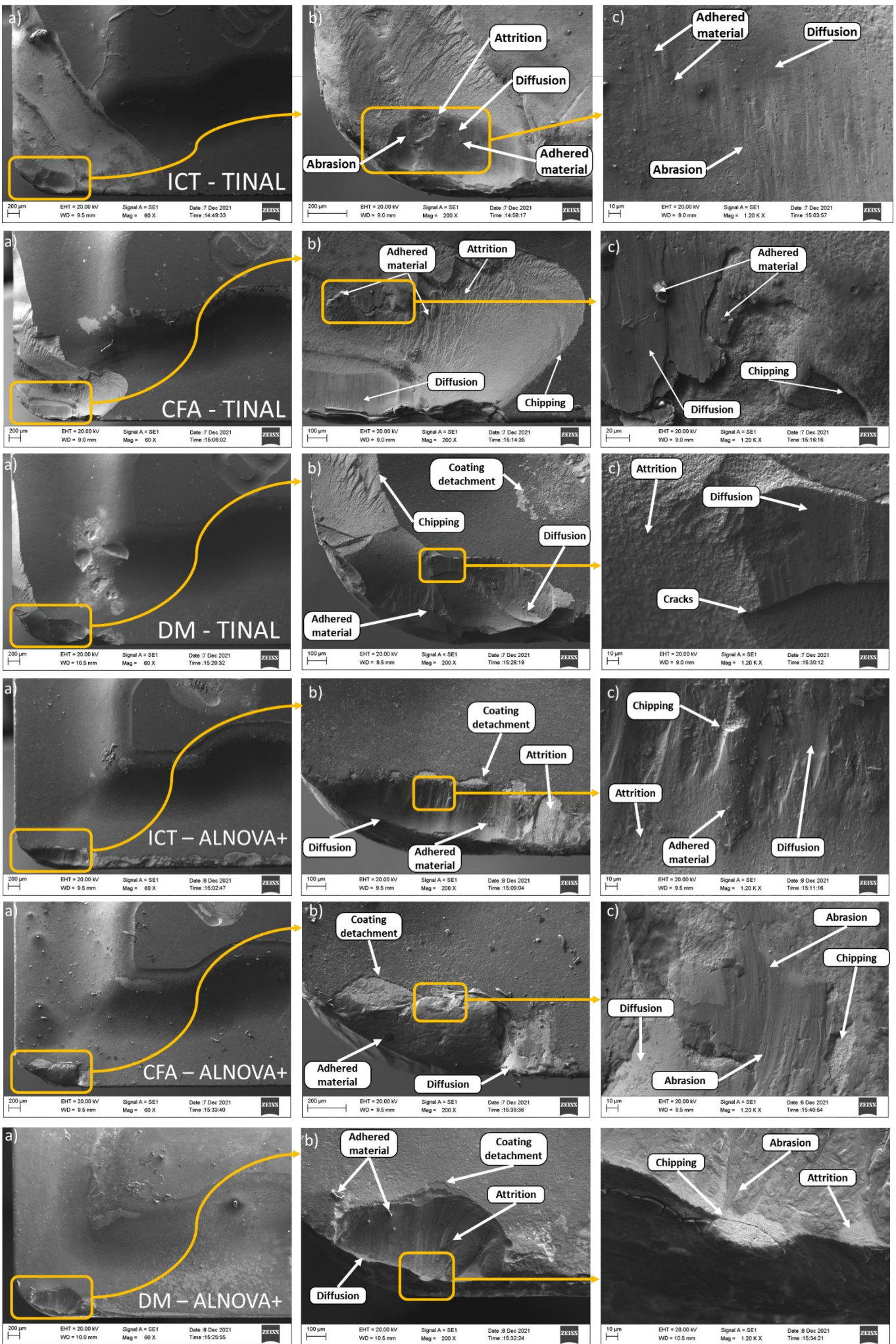


Figure 4-19: Perspective tool view for coating and atmosphere conditions

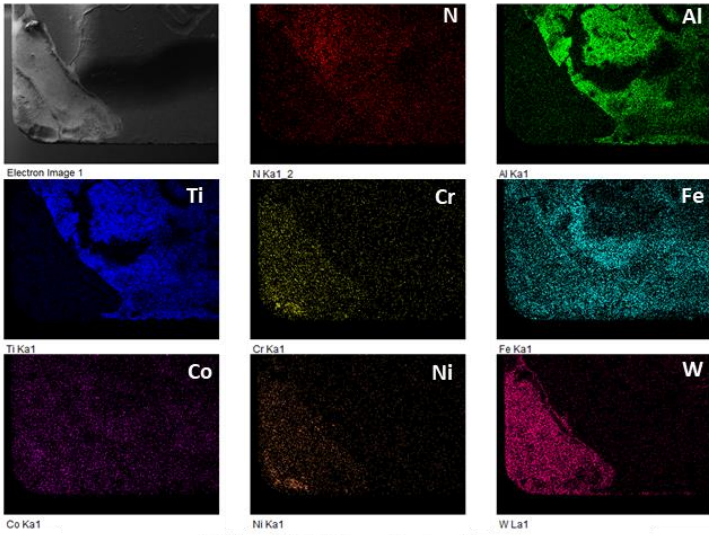


**Figure 4-20:** Lateral view (flank face) of the worn tools used under all cutting atmospheres tested. (a) 100 X, (b) 200 X and (c) 1 200 X

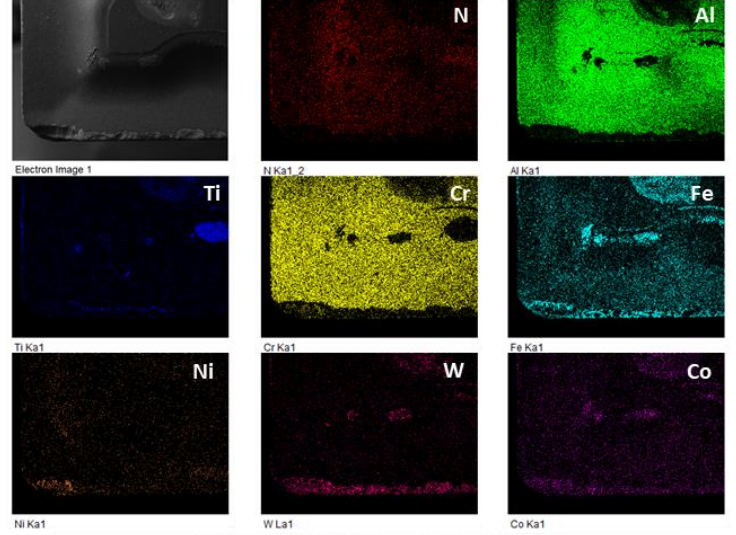


**Figure 4-21:** Top view (rake face) of the worn tools used under all cutting atmospheres tested (a) 100 X, (b) 200 X and (c) 1,200 X

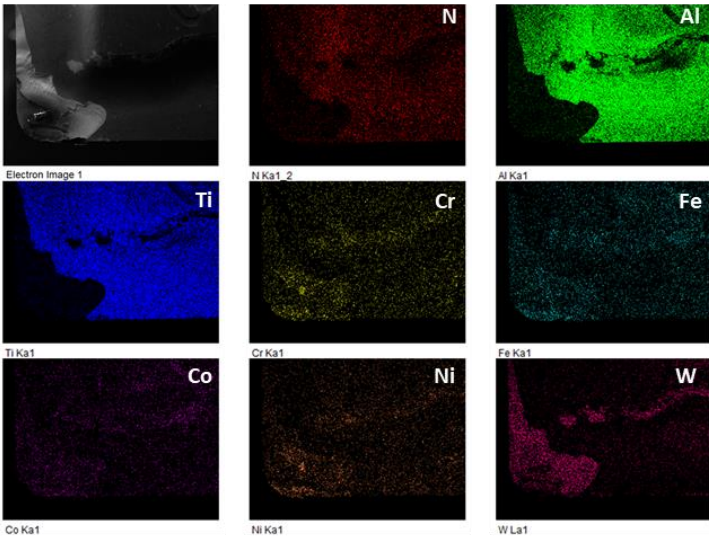
ICT – TINAL – Rake face



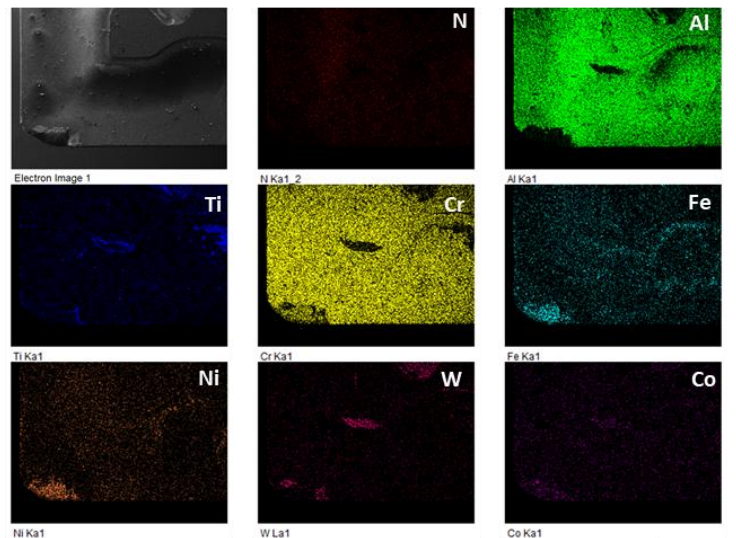
ICT – ALNOVA – Rake face



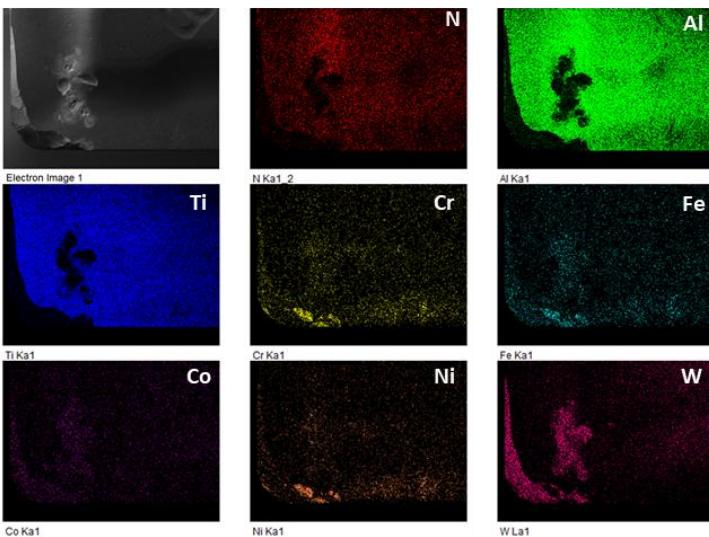
CFA – TINAL – Rake face



CFA – ALNOVA – Rake face



DM – TINAL – Rake face



DM – ALNOVA – Rake face

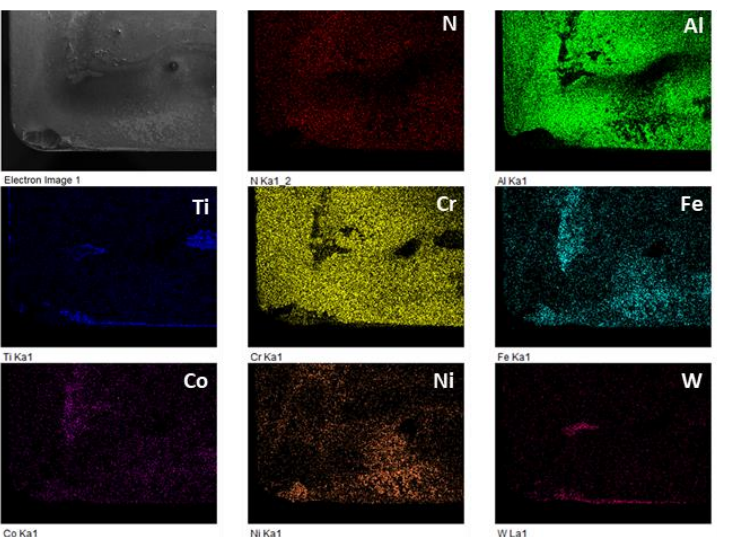
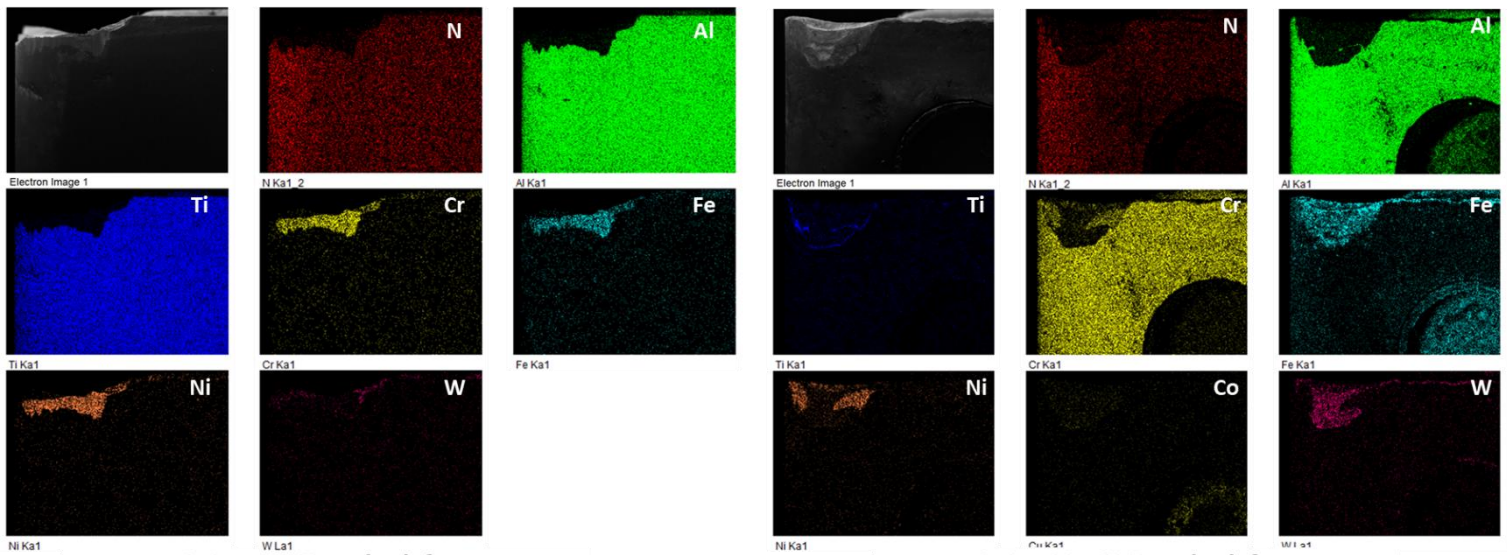


Figure 4-22: Top view (rake face) EDS analysis on the worn tools used under several cutting atmospheres

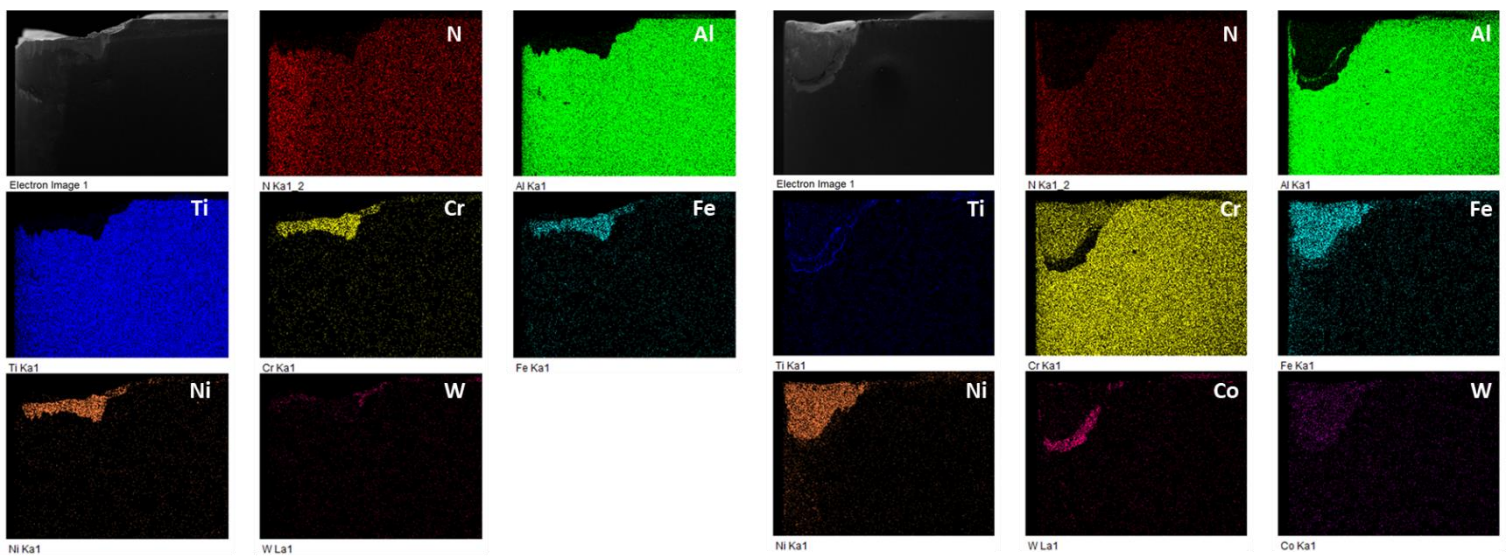
ICT – TINAL – Flank face

ICT – ALNOVA – Flank face



CFA – TINAL – Flank face

CFA – ALNOVA – Flank face



DM – TINAL – Flank face

DM – ALNOVA – Flank face

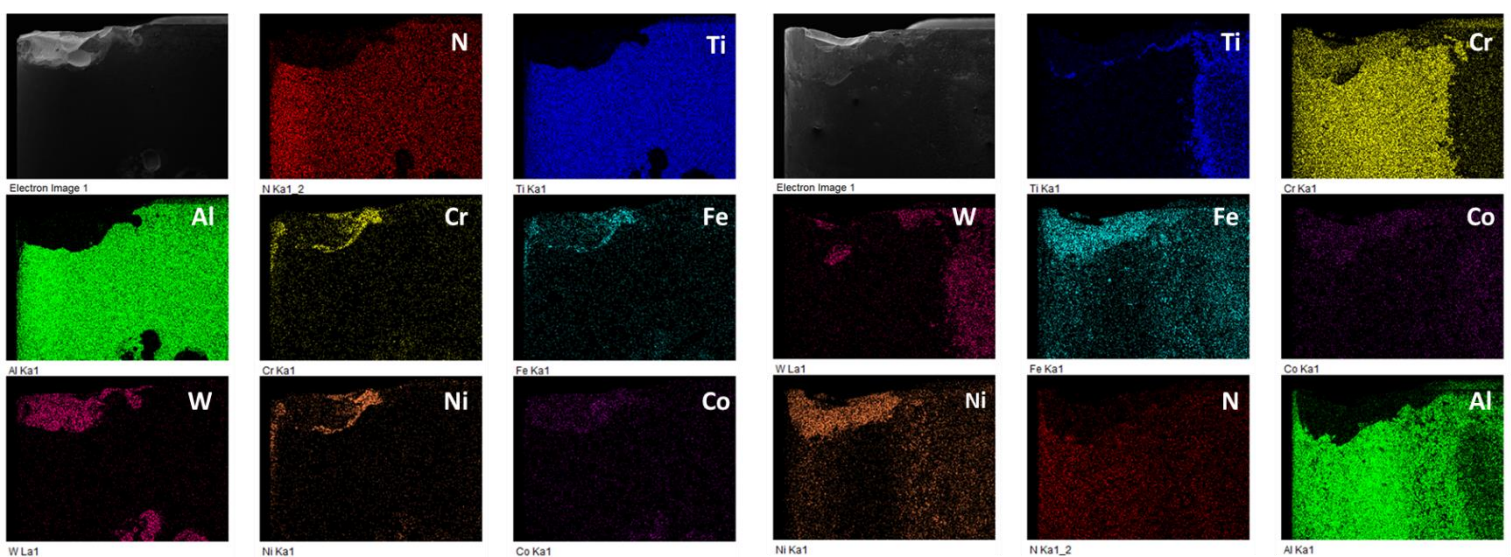


Figure 4-23: Lateral view (flank face) EDS analysis on the worn tools used under several cutting atmospheres



---

---

## Chapter 5: Conclusions

---

---

### 5.1. Conclusions

The main objective of this work was to develop, apply, and validate the internally cooled tool - ICT for the machining of Inconel 718. For this end, coated cemented carbide tools (TiNAl and AlCrN+) were adapted with the tool holder with internal channels able to circulate a cooling fluid inside and remove heat from the tool during the machining time. Machining tests with the ICT strategy were performed to validate the newly proposed method. The conventional cooling method, cutting fluid in abundance – CFA and dry machining – DM were also tested for comparisons. The machining tests were divided into two steps. A statistical Design of Experiment was performed in the first step to test and validate this technique. Two fractionated planning  $2 \times (2^{(5-1)})$  were used to evaluate temperature as the response variable, using two measuring methods, a thermocamera, and a tool-workpiece thermocouple system. The input variables were cutting speed ( $v_c = 47$  and  $94$  m/min), depth of cut ( $a_p = 0.25$  or  $0.50$  mm), feed rate ( $f = 0.103$  or  $0.297$  mm/rev), cutting atmosphere (DM, CFA, or ICT) and tool coating (TiNAl or AlCrN+). In the second step, two full factorial planning,  $2 \times (2^2)$  the input variables were used for the tool coating (TiNAl and AlCrN+) and the cutting atmosphere (DM, ICT, and CFA). The output variables included cutting forces, workpiece surface roughness, and tool life. The mains conclusions achieved are:

- ✚ *The temperature measured by the thermocamera indicated that the minimum values were  $615 \pm 4$  °C (TiNAl and ICT),  $621 \pm 16$  °C (TiNAl and DM), and the maximum were  $746 \pm 4$  °C (AlCrN+ and DM), and  $683 \pm 19$  °C (AlCrN+ and ICT). Tool coating and cutting atmosphere were the most significant variables, with TiNAl and ICT effectively contributing to decreasing the temperature. The feed rate and the depth of cut were also statistically significant variables, considering 95 % of the reliability index; surprisingly, the cutting speed was not significant.*

- ✚ *The tool-workpiece thermocouple system measured the temperature, and comparing ICT x DM, it was found that the minimum values were  $886 \pm 14$  °C (TiNAl and ICT) and  $926 \pm 6$  °C (DM and TiNAl); the maximum was  $1,249 \pm 8$  °C (AlCrN+ and DM) and  $1,196 \pm 1$  °C (TiNAl and DM). All the basic machining parameters ( $v_c$ ,  $f$ , and  $a_p$ ) increased the temperature at the chip-tool interface. The cutting atmosphere was also statistically significant, and ICT decreased it. Tool coating was marginally significant, with AlCrN+ tending to increase the temperature.*
  
- ✚ *With the tool-work thermocouple system and comparing ICT x CFA, the minimum temperatures found were  $856 \pm 14$  °C (TiNAl and CFA) and  $886 \pm 14$  °C (TiNAl and ICT); the maximum was  $1,207 \pm 10$  °C (TiNAl and CFA) and  $1,191 \pm 1$  °C (TiNAl and ICT). The basic machining parameters ( $v_c$ ,  $f$ , and  $a_p$ ) were the most significant for this comparison. The cutting atmosphere was not statistically significant, with 95 % of the reliability index being very near to being so. This means that, statistically, there was no difference between CFA and ICT. This proves the high heat removal capacity of internally cooled tools, although it has no lubrication capacity. So, it is reasonable to infer that ICT's cooling ability is so high that it permits it to be equal to CFA in terms of cutting temperature, a method that has both cooling and lubricating capacity.*
  
- ✚ *Regarding the cutting forces, when using tools coated with TiNAl, the average values were  $188 \pm 32$  [N],  $266 \pm 6$  [N], and  $284 \pm 18$  [N] for ICT, CFA, and DM, respectively. With AlCrN+ coated tools, the average cutting forces were  $211 \pm 3$  [N],  $258 \pm 4$  [N], and  $290 \pm 12$  [N] for CFA, ICT, and DM. TiNAl contributed to increasing the cutting forces, despite the lower temperatures. So, probably there is the effect of interaction between Inconel 718 chip and the coating to be considered. All the other variables were statistically significant, affecting the cutting force.*
  
- ✚ *In comparing ICT x DM, the cutting atmosphere, tool coating, and the interaction of the tool coating x cutting atmosphere were statistically significant, considering 95 % of the reliability index. Dry machining contributed the highest*

to increasing the cutting forces, and TiNAl coating also raised it. Dry machining showed to not be a suitable practice for Inconel 718.

- ✚ For the ICT x CFA comparison, only the interaction between tool coating x cutting atmosphere presented significant influence. This was a positive indication for internally cooling tools - ICT because considering only the cutting forces, it would be suitable for substituting the CFA cooling strategy.
- ✚ Surface roughness analyses demonstrated that only the tool coating was a statistically significant variable. Statistically, the cutting atmosphere (DM, CFA, or ICT) presented the same surface roughness qualities.
- ✚ Considering the tool's life, tools coated with AlCrN+ TiNAl presented better performance than TiNAl, with the average tool's life being  $448 \pm 26 \text{ cm}^3$  (CFA),  $306 \pm 15 \text{ cm}^3$  (ICT) and  $146 \pm 15$  (DM)  $\text{cm}^3$  of the volume of material removed. When using the tools coated with TiNAl, the average tool's life was  $306 \pm 18 \text{ cm}^3$  (ICT),  $242 \pm 36 \text{ cm}^3$  (CFA), and  $117 \pm 13 \text{ cm}^3$  (DM).
- ✚ The tool coated with AlCrN+ and using a CFA cooling strategy was far superior to TiNAl, reaching almost double the tool life (85 %). Thus, the coating AlCrN + showed a higher lifespan, more appropriate to Inconel 718 + machining. It is vital to bear that it is a double-layer coating.
- ✚ When using the TiNAl coated tools, surprisingly, the ICT cooling strategy presented the best performance compared to the other cooling strategies. This may be because of its good heat removal ability that performs better with TiNAl, which has high thermal conductivity.
- ✚ The tool life results showed that DM presented the worst performance in all the scenarios, making it unsuitable for turning Inconel 718 with cemented carbide tools. However, when cutting dry (DM), AlCrN+ was better than TiNAl, with 25 % of increment.

- ✚ *All four wear mechanisms widely accepted in the literature, abrasion, adhesion, oxidation, and diffusion, were found in the worn tools, independently of tool coating or cutting atmosphere conditions. This was expected since Inconel 718 is a difficult-to-cut material that reaches high temperatures, as proven, which favors the thermally activated mechanisms, such as oxidation and diffusions, and has high mechanical strength and toughness, that favors the appearance of adhesion and abrasion wear mechanisms.*
- ✚ *The AlCrN+ coated tools presented smoother and more uniform flank and crater wear. Coating detachment, microchipping, and microcracks were also observed.*
- ✚ *It was evident in the SEM analysis that TiNAl coated tools presented much more severe wear than AlCrN+. There was an intense crater and flank wear, chipping, cracks, and coating detachment. This is an explanation for the tool's life being worse for TiNAl.*
- ✚ *Finally, the ICT system is a promising eco-friendly technique that has a very high cooling capacity. This technique has prominent potential social and environmental improvements. Even technically it was even better than cutting fluids when used with TiNAl coated tools. Important to mention that it needs further studies and development as a new technique. A problem of the ICT system is the lack of lubrication, considered a dry cut, which hybrid techniques, such as solid lubricants, textured tools, MQL, etc, could surpass.*

## 5.2. Further works proposals

It was observed that the ICT system presented a promising performance for machining Inconel 718 with cemented carbide tools. In order to improve this technique, the following proposals can be developed:

- ✓ To design improvement and thermal optimization analysis to find the best internal channel geometry and solve leakage problems.
- ✓ To perform thermal and fluid dynamics simulations.
- ✓ To combine the use of ICT system with other techniques (hybrid systems), such as Minimum Quantity Lubrication, to give it some lubricating capacity that was observed to be lacking.
- ✓ To test this ICT system with other workpieces and tool materials and try it on rotating tools.

---

---

## References

---

---

- [1] Ueda T, Hosokawa A, Yamada K. Effect of oil mist on tool temperature in cutting 2006. <https://doi.org/10.1115/1.2039099>.
- [2] Yildiz Y, Nalbant M. A review of cryogenic cooling in machining processes. *Int J Mach Tools Manuf* 2008;48:947–64. <https://doi.org/10.1016/j.ijmachtools.2008.01.008>.
- [3] Fernandes GHN, Barbosa LMQ. HEAT IN MACHINING. In: Fernandes GHN, Barbosa LMQ, editors. *Mach. Cool. Tech. an Introd.* 1st ed., Recife: Even3; 2022, p. 10–24. <https://doi.org/10.29327/559427.1-1>. <https://doi.org/10.29327/559427.1-1>.
- [4] Machado AR, Abrao AM, Coelho RT, Silva MB Da. *Teoria da usinagem dos materiais*. Editora Blucher; 2015.
- [5] Trent EM, Wright PK. *Metal cutting*. 4th ed. Butterworth-Heinemann; 2000. <https://doi.org/10.1016/B978-075067069-2/50007-3>.
- [6] Almeida Carvalho DO, da Silva LRR, de Souza FCR, França PHP, Machado ÁR, Costa ES, et al. Flooding Application of Vegetable-and Mineral-Based Cutting Fluids in Turning of AISI 1050 Steel. *Lubricants* 2022;10:309. <https://doi.org/10.3390/lubricants10110309>.
- [7] Fernandes GHN, Barbosa LMQ. *Machining cooling techniques: an introduction*. 1st ed. Recife: Even3; 2022. <https://doi.org/10.29327/559427>.
- [8] Said Z, Gupta M, Hegab H, Arora N, Khan AM, Jamil M, et al. A comprehensive review on minimum quantity lubrication (MQL) in machining processes using nano-cutting fluids. *Int J Adv Manuf Technol* 2019;105:2057–86. <https://doi.org/10.1007/s00170-019-04382-x>.
- [9] Benedicto E, Carou D, Rubio EM. Technical, economic and environmental review of the lubrication/cooling systems used in machining processes. *Procedia Eng* 2017;184:99–116. <https://doi.org/10.1016/j.proeng.2017.04.075>.
- [10] Sen B, Mia M, Krolczyk GM, Mandal UK, Mondal SP. Eco-friendly cutting fluids in minimum quantity lubrication assisted machining: a review on the perception of sustainable manufacturing. *Int J Precis Eng Manuf Technol* 2019:1–32. <https://doi.org/10.1007/s40684-019-00158-6>.
- [11] Singh T, Singh P, Dureja JS, Dogra M, Singh H, Bhatti MS. A review of near dry machining/minimum quantity lubrication machining of difficult to machine alloys. *Int J Mach Mach Mater* 2016;18:213–51. <https://doi.org/10.1504/IJMMM.2016.076276>.
- [12] Zhang S, Li JF, Wang YW. Tool life and cutting forces in end milling Inconel 718 under dry and minimum quantity cooling lubrication cutting conditions. *J Clean Prod* 2012;32:81–7. <https://doi.org/10.1016/j.jclepro.2012.03.014>.
- [13] Sartori S, Ghiotti A, Bruschi S. Solid lubricant-assisted minimum quantity lubrication and cooling strategies to improve Ti6Al4V machinability in finishing turning. *Tribol Int* 2018;118:287–94. <https://doi.org/10.1016/j.triboint.2017.10.010>.

- [14] Debnath S, Reddy MM, Yi QS. Environmental friendly cutting fluids and cooling techniques in machining: a review. *J Clean Prod* 2014;83:33–47. <https://doi.org/10.1016/j.jclepro.2014.07.071>.
- [15] Sharma VS, Dogra M, Suri NM. Cooling techniques for improved productivity in turning. *Int J Mach Tools Manuf* 2009;49:435–53. <https://doi.org/10.1016/j.ijmachtools.2008.12.010>.
- [16] Fernandes GHN, Lopes GHF, Barbosa LMQ, Martins PS, Machado ÁR. WEAR MECHANISMS OF DIAMOND-LIKE CARBON COATED TOOLS IN TAPPING OF AA6351 T6 ALUMINIUM ALLOY. *Procedia Manuf* 2021;53:293–8. <https://doi.org/10.1016/j.promfg.2021.06.032>.
- [17] Ezugwu EO, Bonney J. Effect of high-pressure coolant supply when machining nickel-base, Inconel 718, alloy with coated carbide tools. *J Mater Process Technol* 2004;153:1045–50. <https://doi.org/10.1016/j.jmatprotec.2004.04.329>.
- [18] Öjmertz KMC, Oskarson H-B. Wear on SiC-whiskers reinforced ceramic inserts when cutting Inconel with waterjet assistance. *Tribol Trans* 1999;42:471–8. <https://doi.org/10.1080/10402009908982243>.
- [19] Nandy AK, Gowrishankar MC, Paul S. Some studies on high-pressure cooling in turning of Ti–6Al–4V. *Int J Mach Tools Manuf* 2009;49:182–98. <https://doi.org/10.1016/j.ijmachtools.2008.08.008>.
- [20] Kaminski J, Alvelid B. Temperature reduction in the cutting zone in water-jet assisted turning. *J Mater Process Technol* 2000;106:68–73. [https://doi.org/10.1016/S0924-0136\(00\)00640-3](https://doi.org/10.1016/S0924-0136(00)00640-3).
- [21] Ezugwu EO, Bonney J. Finish machining of nickel-base Inconel 718 alloy with coated carbide tool under conventional and high-pressure coolant supplies. *Tribol Trans* 2005;48:76–81. <https://doi.org/10.1080/05698190590899958>.
- [22] de Carvalho PP, Fernandes GHN, Barbosa LMQ, de Sousa JAG, Martins PS, Ba ECT, et al. Different cooling strategies applied during the process of aluminum alloy boring. *Int J Adv Manuf Technol* 2023. <https://doi.org/10.1007/s00170-023-11840-0>.
- [23] Yazid MZA, CheHaron CH, Ghani JA, Ibrahim GA, Said AYM. Surface integrity of Inconel 718 when finish turning with PVD coated carbide tool under MQL. *Procedia Eng* 2011;19:396–401. <https://doi.org/10.1016/j.proeng.2011.11.131>.
- [24] Fleischer J, Pabst R, Kelemen S. Heat flow simulation for dry machining of power train castings. *CIRP Ann* 2007;56:117–22. <https://doi.org/10.1016/j.cirp.2007.05.030>.
- [25] Verma AK. Sustainable development and environmental ethics. *Int J Environ Sci* 2019;10:1–5.
- [26] Shashidhara YM, Jayaram SR. Vegetable oils as a potential cutting fluid—an evolution. *Tribol Int* 2010;43:1073–81. <https://doi.org/10.1016/j.triboint.2009.12.065>.
- [27] Ozcelik B, Kuram E, Cetin MH, Demirbas E. Experimental investigations of vegetable based cutting fluids with extreme pressure during turning of AISI 304L. *Tribol Int* 2011;44:1864–71. <https://doi.org/10.1016/j.triboint.2011.07.012>

- [28] Pervaiz S, Anwar S, Qureshi I, Ahmed N. Recent advances in the machining of titanium alloys using minimum quantity lubrication (MQL) based techniques. *Int J Precis Eng Manuf Technol* 2019;6:133–45. <https://doi.org/10.1007/s40684-019-00033-4>.
- [29] Naveed M, Arslan A, Javed HMA, Manzoor T, Quazi MM, Imran T, et al. State-of-the-Art and Future Perspectives of Environmentally Friendly Machining Using Biodegradable Cutting Fluids. *Energies* 2021;14:4816. <https://doi.org/10.3390/en14164816>.
- [30] Dhar NR, Kamruzzaman M. Cutting temperature, tool wear, surface roughness and dimensional deviation in turning AISI-4037 steel under cryogenic condition. *Int J Mach Tools Manuf* 2007;47:754–9. <https://doi.org/10.1016/j.ijmachtools.2006.09.018>.
- [31] Bagaber SA, Yusoff AR. Sustainable optimization of dry turning of stainless steel based on energy consumption and machining cost. *Procedia CIRP* 2018;77:397–400. <https://doi.org/10.1016/j.procir.2018.08.300>.
- [32] Demirbas E, Kobya M. Operating cost and treatment of metalworking fluid wastewater by chemical coagulation and electrocoagulation processes. *Process Saf Environ Prot* 2017;105:79–90. <https://doi.org/10.1016/j.psep.2016.10.013>.
- [33] Luchesi VM, Coelho RT. An inverse method to estimate the moving heat source in machining process. *Appl Therm Eng* 2012;45:64–78. <https://doi.org/10.1016/j.applthermaleng.2012.04.014>.
- [34] Singh A, Dubey V, Sharma AK. Thermal modelling of cutting tool under different cutting environment in turning. *Mater Today Proc* 2023. <https://doi.org/10.1016/j.matpr.2023.04.193>.
- [35] Knight WA, Boothroyd G. *Fundamentals of metal machining and machine tools*. vol. 198. CRC Press; 2005.
- [36] Abukhshim NA, Mativenga PT, Sheikh MA. Heat generation and temperature prediction in metal cutting: A review and implications for high speed machining. *Int J Mach Tools Manuf* 2006;46:782–800. <https://doi.org/10.1016/j.ijmachtools.2005.07.024>.
- [37] Klocke F. *Manufacturing Processes 1 Cutting* Translated by Aaron Kuchle. *Libr. Congr. Control*, 2011. <https://doi.org/10.1007/978-3-642-11979-8>.
- [38] Xiang W, Yan S, Wu J. Dynamic analysis of planar mechanical systems considering stick-slip and Stribeck effect in revolute clearance joints. *Nonlinear Dyn* 2019;95:321–41. <https://doi.org/10.1007/s11071-018-4566-6>.
- [39] YEŞİLKAYA KK, Yaman K. Heat partition effect on cutting tool morphology in orthogonal metal cutting using finite element method. *Mechanics* 2019;25:326–34. <https://doi.org/10.5755/j01.mech.25.4.22745>.
- [40] Habibnia M, Sheikholeslami M, Tabarhoseini SM, Taheri A, Sheykhi M. Cooling improvement for the machining process with the inclusion of nanoparticles using the experimental approach. *J Mol Liq* 2023;370:120985. <https://doi.org/10.1016/j.molliq.2022.120985>.



- [41] Kazeem RA, Fadare DA, Ikumapayi OM, Adediran AA, Aliyu SJ, Akinlabi SA, et al. Advances in the Application of Vegetable-Oil-Based Cutting Fluids to Sustainable Machining Operations—A Review. *Lubricants* 2022;10:69. <https://doi.org/10.3390/lubricants10040069>.
- [42] Singh G, Pruncu CI, Gupta MK, Mia M, Khan AM, Jamil M, et al. Investigations of machining characteristics in the upgraded MQL-assisted turning of pure titanium alloys using evolutionary algorithms. *Materials (Basel)* 2019;12:999. <https://doi.org/10.3390/ma12060999>.
- [43] Balic J. Intelligent CAD/CAM systems for CNC programming—an overview. *Adv Prod Eng Manag* 2006;1:13–22.
- [44] Fernandes GHN, Barbosa LMQ. *Machining cooling techniques*. vol. 1. 1st ed. Recife: Even3 Publicações; 2022. <https://doi.org/10.29327/559427>.
- [45] Tu L, Lin L, Liu C, Zheng T, Deng Y, Han L, et al. Tool wear characteristics analysis of cBN cutting tools in high-speed turning of Inconel 718. *Ceram Int* 2023;49:635–58. <https://doi.org/10.1016/j.ceramint.2022.09.034>.
- [46] Albertelli P, Mussi V, Monno M. Development of generalized tool life model for constant and variable speed turning. *Int J Adv Manuf Technol* 2022:1–17. <https://doi.org/10.21203/rs.3.rs-487913/v1>.
- [47] Meola C, Carlomagno GM. Recent advances in the use of infrared thermography. *Meas Sci Technol* 2004;15:R27. <https://doi.org/10.1088/0957-0233/15/9/R01>.
- [48] Kus A, Isik Y, Cakir MC, Coşkun S, Özdemir K. Thermocouple and infrared sensor-based measurement of temperature distribution in metal cutting. *Sensors* 2015;15:1274–91. <https://doi.org/10.3390/s150101274>.
- [49] Davoodi B, Hosseinzadeh H. A new method for heat measurement during high speed machining. *Measurement* 2012;45:2135–40. <https://doi.org/10.1016/j.measurement.2012.05.020>.
- [50] Dubey V, Sharma AK, Singh RK. A Technological Review on Temperature Measurement Techniques in Various Machining Processes. *Adv Metrol Meas Eng Surfaces* 2020:55–67. [https://doi.org/10.1007/978-981-15-5151-2\\_6](https://doi.org/10.1007/978-981-15-5151-2_6).
- [51] Zhao J, Liu Z, Wang B, Hua Y, Wang Q. Cutting temperature measurement using an improved two-color infrared thermometer in turning Inconel 718 with whisker-reinforced ceramic tools. *Ceram Int* 2018;44:19002–7. <https://doi.org/10.1016/j.ceramint.2018.07.142>.
- [52] Díaz-Álvarez J, Tapetado A, Vázquez C, Miguélez H. Temperature measurement and numerical prediction in machining inconel 718. *Sensors* 2017;17:1531. <https://doi.org/10.3390/s17071531>.
- [53] França PHP, Barbosa LMQ, Fernandes GHN, da Silva LRR, Machado ÁR, Martins PS, et al. Thermal analysis of a proposed internally cooled machining tool system. *Int J Adv Manuf Technol* 2022. <https://doi.org/10.1007/s00170-022-10602-8>.
- [54] Kaminise AK, Guimarães G, da Silva MB. Development of a tool–work thermocouple calibration system with physical compensation to study the influence of tool-holder material on cutting temperature in machining. *Int J Adv Manuf Technol* 2014;73:735–47. <https://doi.org/10.1007/s00170-014-5898-0>.

- [55] Byers JP. Metalworking fluids. crc Press; 2016. <https://doi.org/10.1201/9781420017731>.
- [56] Krolczyk GM, Maruda RW, Krolczyk JB, Wojciechowski S, Mia M, Nieslony P, et al. Ecological trends in machining as a key factor in sustainable production – A review. *J Clean Prod* 2019;218:601–15. <https://doi.org/10.1016/j.jclepro.2019.02.017>.
- [57] Sen B, Yadav SK, Kumar G, Mukhopadhyay P, Ghosh S. Performance of eco-benign lubricating/cooling mediums in machining of superalloys: A comprehensive review from the perspective of Triple Bottom Line theory. *Sustain Mater Technol* 2023:e00578. <https://doi.org/10.1016/j.susmat.2023.e00578>.
- [58] Yıldırım ÇV. Experimental comparison of the performance of nanofluids, cryogenic and hybrid cooling in turning of Inconel 625. *Tribol Int* 2019;137:366–78. <https://doi.org/10.1016/j.triboint.2019.05.014>.
- [59] Rubaiee S, Danish M, Gupta MK, Ahmed A, Yahya SM, Yildirim MB, et al. Key initiatives to improve the machining characteristics of Inconel-718 alloy: Experimental analysis and optimization. *J Mater Res Technol* 2022;21:2704–20. <https://doi.org/10.1016/j.jmrt.2022.10.060>.
- [60] Deiab I, Raza SW, Pervaiz S. Analysis of lubrication strategies for sustainable machining during turning of titanium Ti-6Al-4V alloy. *Procedia CIRP* 2014;17:766–71. <https://doi.org/10.1016/j.procir.2014.01.112>.
- [61] Hegab H, Kishawy HA. Towards sustainable machining of Inconel 718 using nano-fluid minimum quantity lubrication. *J Manuf Mater Process* 2018;2:50. <https://doi.org/10.3390/jmmp2030050>.
- [62] Marques, Narala SKR, Machado AR, Gunda RK, Josyula SK, Da Silva RB, et al. Performance assessment of MQL: Minimum quantity solid lubricant during turning of Inconel 718. *Proc Inst Mech Eng Part B J Eng Manuf* 2017;231:1144–59. <https://doi.org/10.1177/0954405415592128>.
- [63] Singh K, Singh AK, Chattopadhyay KD. Effect of machining parameters and MQL parameter on material removal rate in milling of Aluminium alloy. *Adv. Prod. Ind. Eng.*, Springer; 2021, p. 359–68. [https://doi.org/10.1007/978-981-15-5519-0\\_27](https://doi.org/10.1007/978-981-15-5519-0_27).
- [64] Gajrani KK, Suvin PS, Kailas SV, Sankar MR. Hard machining performance of indigenously developed green cutting fluid using flood cooling and minimum quantity cutting fluid. *J Clean Prod* 2019;206:108–23. <https://doi.org/10.1016/j.jclepro.2018.09.178>.
- [65] Shokrani A, Dhokia V, Newman ST. Environmentally conscious machining of difficult-to-machine materials with regard to cutting fluids. *Int J Mach Tools Manuf* 2012;57:83–101. <https://doi.org/10.1016/j.ijmachtools.2012.02.002>.
- [66] Gajrani KK, Sankar MR. Role of eco-friendly cutting fluids and cooling techniques in machining. *Mater Forming, Mach Post Process* 2020:159–81. [https://doi.org/10.1007/978-3-030-18854-2\\_7](https://doi.org/10.1007/978-3-030-18854-2_7).
- [67] Kumar P, Jain AK, Chaurasiya PK, Tiwari D, Gopalan A, Arockia Dhanraj J, et al. Sustainable Machining Using Eco-Friendly Cutting Fluids: A Review. *Adv Mater Sci Eng* 2022;2022. <https://doi.org/10.1155/2022/5284471>.

- [68] Stephenson DA, Agapiou JS. Metal cutting theory and practice. CRC press; 2016. <https://doi.org/10.1201/b19559>.
- [69] Vieira JM, Machado AR, Ezugwu EO. Performance of cutting fluids during face milling of steels. *J Mater Process Technol* 2001;116:244–51. [https://doi.org/10.1016/S0924-0136\(01\)01010-X](https://doi.org/10.1016/S0924-0136(01)01010-X).
- [70] Iturbe A, Hormaetxe E, Garay A, Arrazola PJ. Surface integrity analysis when machining inconel 718 with conventional and cryogenic cooling. *Procedia Cirp* 2016;45:67–70. <https://doi.org/10.1016/j.procir.2016.02.095>.
- [71] Minton T, Ghani S, Sammler F, Bateman R, Fürstmann P, Roeder M. Temperature of internally-cooled diamond-coated tools for dry-cutting titanium. *Int J Mach Tools Manuf* 2013;75:27–35. <https://doi.org/10.1016/j.ijmachtools.2013.08.006>.
- [72] de Sousa JAG, Sales WF, Machado AR. A review on the machining of cast irons. *Int J Adv Manuf Technol* 2018;94:4073–92. <https://doi.org/10.1007/s00170-017-1140-1>.
- [73] Luiz NE, Machado ÁR. Development trends and review of free-machining steels. *Proc Inst Mech Eng Part B J Eng Manuf* 2008;222:347–60. <https://doi.org/10.1243/09544054JEM861>.
- [74] Akyuz B. Machinability of magnesium and its alloys. *TOJSAT Online J Sci Technol* 2011;1:31–8.
- [75] Santos MC, Machado AR, Sales WF, Barrozo MAS, Ezugwu EO. Machining of aluminum alloys: a review. *Int J Adv Manuf Technol* 2016;86:3067–80. <https://doi.org/10.1007/s00170-016-8431-9>.
- [76] Goindi GS, Sarkar P. Dry machining: a step towards sustainable machining—challenges and future directions. *J Clean Prod* 2017;165:1557–71. <https://doi.org/10.1016/j.jclepro.2017.07.235>.
- [77] Mahesh K, Philip JT, Joshi SN, Kuriachen B. Machinability of Inconel 718: A critical review on the impact of cutting temperatures. *Mater Manuf Process* 2021;36:753–91. <https://doi.org/10.1080/10426914.2020.1843671>.
- [78] Yin Q, Liu Z, Wang B, Song Q, Cai Y. Recent progress of machinability and surface integrity for mechanical machining Inconel 718: a review. *Int J Adv Manuf Technol* 2020;109:215–45. <https://doi.org/10.1007/s00170-020-05665-4>.
- [79] Roy S, Kumar R, Panda A, Das RK. A brief review on machining of Inconel 718. *Mater Today Proc* 2018;5:18664–73. <https://doi.org/10.1016/j.matpr.2018.06.212>
- [80] Devillez A, Le Coz G, Dominiak S, Dudzinski D. Dry machining of Inconel 718, workpiece surface integrity. *J Mater Process Technol* 2011;211:1590–8. <https://doi.org/10.1016/j.jmatprotec.2011.04.011>.
- [81] Ginting A, Nouari M. Surface integrity of dry machined titanium alloys. *Int J Mach Tools Manuf* 2009;49:325–32. <https://doi.org/10.1016/j.ijmachtools.2008.10.011>.
- [82] Meyers PG. TOOL COOLING APPARATUS. 3,137,184, 1964.
- [83] Jeffries NP, Zerkle RD. Thermal analysis of an internally-cooled metal-cutting tool. *Int J Mach Tool Des Res* 1970;10:381–99. [https://doi.org/10.1016/0020-7357\(70\)90019-3](https://doi.org/10.1016/0020-7357(70)90019-3).

- [84] Fernandes G, Barbosa L, França P, Martins P, Machado A. Towards green machining: wear analysis of a novel eco-friendly cooling strategy for Inconel 718. *Int J Adv Manuf Technol* 2023. <https://doi.org/10.1007/s00170-023-12207-1>.
- [85] Nazareno Fernandes GH, Bazon VT, Queiroz Barbosa LM, Pires França PH, da Silva MB, Uddin M, et al. Performance comparison between internally cooled tools and flood cooling during grey cast iron turning. *J Manuf Process* 2023;85:817–31. <https://doi.org/10.1016/j.jmapro.2022.11.040>.
- [86] Fernandes G, Barbosa L, França P, Ferreira E, Martins P, Machado Á. ENHANCING SUSTAINABILITY IN INCONEL 718 MACHINING: TEMPERATURE CONTROL WITH INTERNALLY COOLED TOOLS. *Int J Adv Manuf Technol* 2023. <https://doi.org/10.1007/s00170-023-12296-y>.
- [87] Barbosa LMQ, França PHP, Fernandes GHN, Costa ES, da Silva MB, Martins PS, et al. COMPARISON OF THE PERFORMANCE OF THE INTERNALLY COOLED TOOL IN CLOSED CIRCUIT AGAINST STANDARD PCBN TOOLS IN TURNING AISI D6 HARDENED. *J Manuf Process* 2023;\*:.\*.
- [88] Zerkle RD. United States Patent 72) 1971.
- [89] Ferri C, Minton T, Ghani SBC, Cheng K. Internally cooled tools and cutting temperature in contamination-free machining. *Proc Inst Mech Eng Part C J Mech Eng Sci* 2014;228:135–45. <https://doi.org/10.1177/0954406213480312>.
- [90] Li T, Wu T, Ding X, Chen H, Wang L. Design of an internally cooled turning tool based on topology optimization and CFD simulation. *Int J Adv Manuf Technol* 2017;91:1327–37. <https://doi.org/10.1007/s00170-016-9804-9>.
- [91] Su Y, Li Z, Li L, Wang J, Gao H, Wang G. Cutting performance of micro-textured polycrystalline diamond tool in dry cutting. *J Manuf Process* 2017;27:1–7. <https://doi.org/10.1016/j.jmapro.2017.03.013>.
- [92] Li T, Wu T, Ding X, Chen H, Wang L. Experimental study on the performance of an internal cooled turning tool with topological channel. *Int J Adv Manuf Technol* 2018;98:479–85. <https://doi.org/10.1007/s00170-018-2278-1>.
- [93] Rozzi JC, Sanders JK, Chen W. The experimental and theoretical evaluation of an indirect cooling system for machining. *J Heat Transfer* 2011;133. <https://doi.org/10.1115/1.4002446>.
- [94] Rozzi C, Chen W, Archibald EE. Indirect Cooling Of A Cutting Tool, 2011.
- [95] Neto RRI, Fragelli RL, Fiochi AA, Scalón VL, de Angelo Sanchez LE. Toolholder Internally Cooled by a Phase Change Fluid in Turning of SAE. *Appl Mech Mater* 2015;798:486–90. <https://doi.org/10.4028/www.scientific.net/AMM.798.486>.
- [96] FIOCHI AA, SANCHEZ LEDÂ, NETO RRI, Scalón VL. PORTA-FERRAMENTAS COM SISTEMA INTERNO DE TRANSFERENCIA DE CALOR COM FLUIDO EM MUDANÇA DE FASE. BR 102013018189-7 A2, 2016.
- [97] Judd RL, MacKenzie HS, Elbestawi MA. An investigation of a heat pipe cooling system for use in turning on a lathe. *Int J Adv Manuf Technol* 1995;10:357–66. <https://doi.org/10.1007/BF01179398>.

- [98] Zhao H, Barber GC, Zou Q. A study of flank wear in orthogonal cutting with internal cooling. *Wear* 2002;253:957–62. [https://doi.org/10.1016/S0043-1648\(02\)00248-X](https://doi.org/10.1016/S0043-1648(02)00248-X).
- [99] Jen TC, Gutierrez G, Eapen S, Barber G, Zhao H, Szuba PS, et al. Investigation of heat pipe cooling in drilling applications.: part I: preliminary numerical analysis and verification. *Int J Mach Tools Manuf* 2002;42:643–52. [https://doi.org/10.1016/S0890-6955\(01\)00155-9](https://doi.org/10.1016/S0890-6955(01)00155-9).
- [100] Zhao H, Barber GC, Zou Q, Gu R. Effect of internal cooling on tool-chip interface temperature in orthogonal cutting. *Tribol Trans* 2006;49:125–34. <https://doi.org/10.1080/05698190500544163>.
- [101] Zhu L, Jen T-C, Yin C-L, Yen Y-H, Zhu M, Zhang J. Investigation of Heat Pipe Cooling in Drilling Applications: Part 2—Thermal, Structural Static, and Dynamic Analyses. *ASME Int. Mech. Eng. Congr. Expo.*, vol. 43826, 2009, p. 2027–34. <https://doi.org/10.1115/IMECE2009-10314>.
- [102] Chiou RY, Lu L, Chen JSJ, North MT. Investigation of dry machining with embedded heat pipe cooling by finite element analysis and experiments. *Int J Adv Manuf Technol* 2007;31:905–14. <https://doi.org/10.1007/s00170-005-0266-8>.
- [103] Shu S, Chen S, Cheng K. Investigation of a novel green internal cooling in turning application. *Proc. 2011 Int. Conf. Electron. Mech. Eng. Inf. Technol.*, vol. 3, IEEE; 2011, p. 1156–9. <https://doi.org/10.1109/EMEIT.2011.6023299>.
- [104] Liang L, Quan Y, Ke Z. Investigation of tool-chip interface temperature in dry turning assisted by heat pipe cooling. *Int J Adv Manuf Technol* 2011;54:35–43. <https://doi.org/10.1007/s00170-010-2926-6>.
- [105] Sun X, Bateman R, Cheng K, Ghani SC. Design and analysis of an internally cooled smart cutting tool for dry cutting. *Proc Inst Mech Eng Part B J Eng Manuf* 2012;226:585–91. <https://doi.org/10.1177/0954405411424670>.
- [106] Pavlovich KV, Gorgots GV, Sergeevich SA, Viktorovich AA. Tool cutting plate cooling system II. RU182799U1, 2017.
- [107] Pavlovich KV, Gorgots GV, Sergeevich SA, Viktorovich AA, Georgievich GV, Sergeevich SA, et al. Tool cutting plate cooling system. RU182799U1, 2017.
- [108] Barbosa LMQ. Torneamento de aço endurecido ABNT-D6 com ferramenta de PCBN refrigerada através de galerias internas 2021.
- [109] Hayyat MS, Adnan M, Awais M, Bilal HM, Khan B, Rahman HA. Effect of heavy metal (Ni) on plants and soil: A review. *Int J Appl Res* 2020;6:313–8.
- [110] Davis JR, Mills KM, Lampman SR. *Metals handbook*. Vol. 1. Properties and selection: irons, steels, and high-performance alloys. ASM Int Mater Park Ohio 44073, USA, 1990 1063 1990.
- [111] Marques A. TORNEAMENTO DE INCONEL 718 COM APLICAÇÃO DE LUBRIFICANTES SÓLIDOS. Universidade Federal de Uberlândia, 2015.
- [112] ASM International. *ASM Handbook, Volume 2, Properties and Selection: Nonferrous Alloys and Special-Purpose Materials*. 1990.

- [113] Committee ASMIH. ASM Handbook, Volume 16-Machining. ASM International; 1989.
- [114] Davis JR. ASM specialty handbook: heat-resistant materials. Asm International; 1997.
- [115] Lima F de F. ESTUDO DO DESGASTE DE FERRAMENTAS DE METAL DURO E CERÂMICAS NO TORNEAMENTO DO INCONEL® 751 E INCONEL® 718. 2012.
- [116] Durand-Charre M. The microstructure of superalloys. Routledge; 2017. <https://doi.org/10.1201/9780203736388>.
- [117] Oliveira D. EFEITO ESCALA E INTEGRIDADE SUPERFICIAL NO MICROFRESAMENTO DA LIGA DE NÍQUEL. Universidade Federal de Uberlândia - UFU, 2019.
- [118] da Veiga FL, Faria MIST, Coelho GC. Superliga Inconel-718: Caracterização microestrutural e validação da base de dados termodinâmicos. Cad UniFOA 2017;7:77–85. <https://doi.org/https://doi.org/10.47385/cadunifoa.v7.n1%20Esp.2185>.
- [119] Ezugwu, Wang ZM, Machado AR. The machinability of nickel-based alloys: a review. J Mater Process Technol 1999;86:1–16. [https://doi.org/10.1016/S0924-0136\(98\)00314-8](https://doi.org/10.1016/S0924-0136(98)00314-8).
- [120] Reed RC. The superalloys: fundamentals and applications. Cambridge university press; 2008.
- [121] Azadian S, Wei L-Y, Warren R. Delta phase precipitation in Inconel 718. Mater Charact 2004;53:7–16. <https://doi.org/10.1016/j.matchar.2004.07.004>.
- [122] Rao GA, Kumar M, Srinivas M, Sarma DS. Effect of standard heat treatment on the microstructure and mechanical properties of hot isostatically pressed superalloy inconel 718. Mater Sci Eng A 2003;355:114–25. [https://doi.org/10.1016/S0921-5093\(03\)00079-0](https://doi.org/10.1016/S0921-5093(03)00079-0).
- [123] Ezugwu EO. Key improvements in the machining of difficult-to-cut aerospace superalloys. Int J Mach Tools Manuf 2005;45:1353–67. <https://doi.org/10.1016/j.ijmachtools.2005.02.003>.
- [124] Patel SJ, Smith GD. The role of niobium in wrought superalloys. Int. Symp. Niobium 2001, 2001, p. 1081–108.
- [125] Pusavec F, Hamdi H, Kopac J, Jawahir IS. Surface integrity in cryogenic machining of nickel based alloy—Inconel 718. J Mater Process Technol 2011;211:773–83. <https://doi.org/10.1016/j.jmatprotec.2010.12.013>.
- [126] Tabernero I, Lamikiz A, Martínez S, Ukar E, Figueras J. Evaluation of the mechanical properties of Inconel 718 components built by laser cladding. Int J Mach Tools Manuf 2011;51:465–70. <https://doi.org/10.1016/j.ijmachtools.2011.02.003>.
- [127] Kuo C-M, Yang Y-T, Bor H-Y, Wei C-N, Tai C-C. Aging effects on the microstructure and creep behavior of Inconel 718 superalloy. Mater Sci Eng A 2009;510:289–94. <https://doi.org/10.1016/j.msea.2008.04.097>.

- [128] Mustafa G, Anwar MT, Ahmed A, Nawaz M, Rasheed T. Influence of Machining Parameters on Machinability of Inconel 718—A Review. *Adv Eng Mater* 2022;24. <https://doi.org/10.1002/adem.202200202>.
- [129] Vieregge G. *Zerspanung der Eisenwerkstoffe [Machining of ferrous material]*. Stahleisen, Düsseldorf 1970.
- [130] Trent EM, Wright PK. *Metal cutting*. Butterworth-Heinemann; 2000. <https://doi.org/10.1016/B978-075067069-2/50007-3>.
- [131] Dearnley PA, Trent EM. Wear mechanisms of coated carbide tools. *Met Technol* 1982;9:60–75. <https://doi.org/10.1179/030716982803285909>.
- [132] Iso 3685. Tool-life testing with single-point turning tools 1993.
- [133] ISO 3685 IO for S, S O for. Tool-life testing with a single-point turning tools. Switzerland: 1993.
- [134] Choudhury IA, El-Baradie MA. Machinability of nickel-base super alloys: a general review. *J Mater Process Technol* 1998;77:278–84. [https://doi.org/10.1016/S0924-0136\(97\)00429-9](https://doi.org/10.1016/S0924-0136(97)00429-9).
- [135] Richards N, Aspinwall D. Use of ceramic tools for machining nickel based alloys. *Int J Mach Tools Manuf* 1989;29:575–88. [https://doi.org/10.1016/0890-6955\(89\)90072-2](https://doi.org/10.1016/0890-6955(89)90072-2).
- [136] Kamata Y, Obikawa T. High speed MQL finish-turning of Inconel 718 with different coated tools. *J Mater Process Technol* 2007;192:281–6. <https://doi.org/10.1016/j.jmatprotec.2007.04.052>.
- [137] Balzers O. BALINIT ® ALNOVA For ambitious milling applications 2013.
- [138] Hegab H, Umer U, Soliman M, Kishawy HA. Effects of nano-cutting fluids on tool performance and chip morphology during machining Inconel 718. *Int J Adv Manuf Technol* 2018;96:3449–58. <https://doi.org/10.1007/s00170-018-1825-0>.
- [139] Khanna N, Agrawal C, Gupta MK, Song Q. Tool wear and hole quality evaluation in cryogenic Drilling of Inconel 718 superalloy. *Tribol Int* 2020;143:106084. <https://doi.org/10.1016/j.triboint.2019.106084>.
- [140] Shokrani A, Dhokia V, Newman ST. Hybrid cooling and lubricating technology for CNC milling of Inconel 718 nickel alloy. *Procedia Manuf* 2017;11:625–32. <https://doi.org/10.1016/j.promfg.2017.07.160>.
- [141] Kenda J, Pusavec F, Kopac J. Analysis of residual stresses in sustainable cryogenic machining of nickel based alloy—Inconel 718. *J Manuf Sci Eng* 2011;133. <https://doi.org/10.1115/1.4004610>.
- [142] Kaynak Y. Evaluation of machining performance in cryogenic machining of Inconel 718 and comparison with dry and MQL machining. *Int J Adv Manuf Technol* 2014;72:919–33. <https://doi.org/10.1007/s00170-014-5683-0>.
- [143] Musfirah AH, Ghani JA, Haron CHC. Tool wear and surface integrity of inconel 718 in dry and cryogenic coolant at high cutting speed. *Wear* 2017;376:125–33. <https://doi.org/10.1016/j.wear.2017.01.031>.

- [144] Aramcharoen A, Chuan SK. An experimental investigation on cryogenic milling of Inconel 718 and its sustainability assessment. *Procedia Cirp* 2014;14:529–34. <https://doi.org/10.1016/j.procir.2014.03.076>.
- [145] He Z-H, Zhang X-M, Ding H. Comparison of residual stresses in cryogenic and dry machining of Inconel 718. *Procedia Cirp* 2016;46:19–22. <https://doi.org/10.1016/j.procir.2016.03.130>.
- [146] Rahim EA, Sasahara H. An analysis of surface integrity when drilling inconel 718 using palm oil and synthetic ester under MQL condition. *Mach Sci Technol* 2011;15:76–90. <https://doi.org/10.1080/10910344.2011.557967>.
- [147] Kumar S, Singh D, Kalsi NS. Experimental investigations of surface roughness of Inconel 718 under different machining conditions. *Mater Today Proc* 2017;4:1179–85. <https://doi.org/10.1016/j.matpr.2017.01.135>.
- [148] Paturi UMR, Maddu YR, Maruri RR, Narala SKR. Measurement and analysis of surface roughness in WS2 solid lubricant assisted minimum quantity lubrication (MQL) turning of Inconel 718. *Procedia Cirp* 2016;40:138–43. <https://doi.org/10.1016/j.procir.2016.01.082>.
- [149] Ezugwu EO, Bonney J, Yamane Y. An overview of the machinability of aeroengine alloys. *J Mater Process Technol* 2003;134:233–53. [https://doi.org/10.1016/S0924-0136\(02\)01042-7](https://doi.org/10.1016/S0924-0136(02)01042-7).
- [150] Sharman ARC, Hughes JI, Ridgway K. Workpiece surface integrity and tool life issues when turning Inconel 718™ nickel based superalloy. *Mach Sci Technol* 2004;8:399–414. <https://doi.org/10.1081/MST-200039865>.
- [151] D'addona DM, Raykar SJ, Narke MM. High speed machining of Inconel 718: tool wear and surface roughness analysis. *Procedia CIRP* 2017;62:269–74. <https://doi.org/10.1016/j.procir.2017.03.004>.
- [152] Cai X, Qin S, Li J, An Q, Chen M. Experimental investigation on surface integrity of end milling nickel-based alloy—Inconel 718. *Mach Sci Technol* 2014;18:31–46. <https://doi.org/10.1080/10910344.2014.863627>.
- [153] Jafarian F, Umbrello D, Golpayegani S, Darake Z. Experimental investigation to optimize tool life and surface roughness in inconel 718 machining. *Mater Manuf Process* 2016;31:1683–91. <https://doi.org/10.1080/10426914.2015.1090592>.
- [154] Thirumalai R, Senthilkumaar JS, Selvarani P, Arunachalam RM, Senthilkumaar KM. Investigations of surface roughness and flank wear behaviour in machining of Inconel 718. *Aust J Mech Eng* 2012;10:157–68. <https://doi.org/10.7158/M12-040.2012.10.2>.
- [155] Ceratizit. CNMG. Webpage 2022. <https://cuttingtools.ceratizit.com/ie/en/products/7500363000.html?referrer=https://www.google.com/> (accessed April 11, 2022).
- [156] Walter. Walter Tools 2021. <https://www.walter-tools.com/pt-pt/search/pages/default.aspx#/product/DSSNR2525X12-P> (accessed April 4, 2021).
- [157] Fuchs. *Informações técnicas* 2017:6612.
- [158] Petronas. *Petronas coolant up*. vol. 18. 2005.



- [159] Bazon VT. Estudo da aplicabilidade de ferramentas refrigeradas internamente na usinagem de ferro fundido cinzento 2020:81.
- [160] Favaretto VA. Desenvolvimento de um medidor de temperatura em usinagem pelo método do termopar ferramenta peça. Pontifícia Universidade Católica do Paraná, 2017.
- [161] NBR ISO 4288. NBR ISO\_4288 2008.
- [162] Korkut I, Boy M, Karacan I, Seker U. Investigation of chip-back temperature during machining depending on cutting parameters. *Mater Des* 2007;28:2329–35. <https://doi.org/10.1016/j.matdes.2006.07.009>.
- [163] O’Sullivan D, Cotterell M. Workpiece temperature measurement in machining. *Proc Inst Mech Eng Part B J Eng Manuf* 2002;216:135–9. <https://doi.org/10.1243/0954405021519645>.
- [164] Zhao J, Liu Z, Wang B, Hu J, Wan Y. Tool coating effects on cutting temperature during metal cutting processes: Comprehensive review and future research directions. *Mech Syst Signal Process* 2021;150:107302. <https://doi.org/10.1016/j.ymsp.2020.107302>.
- [165] França P. Estudo da temperatura em ferramentas de usinagem com canais de refrigeração internos no torneamento do ferro fundido cinzento. Universidade Federal de Uberlândia, 2021. <https://doi.org/10.14393/ufu.di.2021.283>.
- [166] Peixoto ACS. Análise da força de corte e rugosidade no torneamento de ferro fundido cinzento utilizando sistemres 2021.
- [167] Kusiak A, Battaglia J-L, Rech J. Tool coatings influence on the heat transfer in the tool during machining. *Surf Coatings Technol* 2005;195:29–40. <https://doi.org/10.1016/j.surfcoat.2005.01.007>.
- [168] Itakura K, Kuroda M, Omokawa H, Itani H, Yamamoto K, Ariura Y. Wear mechanism of coated cemented carbide tool in cutting of inconel 718 super-heat-resisting alloy. *Int J Japan Soc Precis Eng* 1999;33:326–32. <https://doi.org/10.2493/jjspe.65.976>.
- [169] Kelly JF, Cotterell MG. Minimal lubrication machining of aluminium alloys. *J Mater Process Technol* 2002;120:327–34. [https://doi.org/10.1016/S0924-0136\(01\)01126-8](https://doi.org/10.1016/S0924-0136(01)01126-8).
- [170] Amigo FJ, Urbikain G, Pereira O, Fernández-Lucio P, Fernández-Valdivielso A, de Lacalle LNL. Combination of high feed turning with cryogenic cooling on Haynes 263 and Inconel 718 superalloys. *J Manuf Process* 2020;58:208–22. <https://doi.org/10.1016/j.jmapro.2020.08.029>.
- [171] Machado AR, Abrão AM, Coelho RT, Silva MB Da. Theory of machining of materials. Ed Edgard Blücher, São Paulo 2009;384.
- [172] Klocke, Eisenblätter. Dry cutting. *Cirp Ann* 1997;46:519–26. [https://doi.org/10.1016/S0007-8506\(07\)60877-4](https://doi.org/10.1016/S0007-8506(07)60877-4).
- [173] Haapala KR, Zhao F, Camelio J, Sutherland JW, Skerlos SJ, Dornfeld DA, et al. A review of engineering research in sustainable manufacturing. *J Manuf Sci Eng* 2013;135. <https://doi.org/10.1115/1.4024040>.

- [174] OECD PB. Sustainable manufacturing and eco-innovation: towards a green economy. Policy Brief-OECD Obs 2009.
- [175] Hsien WLY. Towards green lubrication in machining. Springer; 2015.
- [176] Palanikumar K, Boppana SB, Natarajan E. Analysis of chip formation and temperature measurement in machining of titanium alloy (Ti-6Al-4V). *Exp Tech* 2023;47:517–29. <https://doi.org/10.1007/s40799-021-00537-2>.
- [177] Kumar S, Kumar S, Kiran GU, Mukhopadhyay A, Barman M. A Simplistic Regression-Based Genetic Algorithm Optimization of Tool-Work Interface Temperature. *Eng Trans* 2022;70:141–56.
- [178] Machado AR, Abrão AM, Coelho RT, Silva MB Da. *Teoria da Usinagem dos Materiais [Theory of Materials' Machining]* 2011.
- [179] Barbosa LMQ. Torneamento de aço endurecido ABNT D6 com ferramenta de PCBN refrigerada com galerias internas. Universidade Federal de Uberlândia, 2021. <https://doi.org/10.14393/ufu.di.2021.282>.
- [180] Revuru RS, Posinasetti NR, VSN VR, Amrita M. Application of cutting fluids in machining of titanium alloys—a review. *Int J Adv Manuf Technol* 2017;91:2477–98. <https://doi.org/10.1007/s00170-016-9883-7>.
- [181] Gupta MK, Jamil M, Wang X, Song Q, Liu Z, Mia M, et al. Performance evaluation of vegetable oil-based nano-cutting fluids in environmentally friendly machining of inconel-800 alloy. *Materials (Basel)* 2019;12:2792. <https://doi.org/10.3390/ma12172792>.
- [182] Ramanujam R, Vignesh M, Tamiloli N, Sharma N, Srivastava S, Patel A. Comparative evaluation of performances of TiAlN, AlCrN, TiAlN/AlCrN coated carbide cutting tools and uncoated carbide cutting tools on turning Inconel 825 alloy using Grey Relational Analysis. *Sensors Actuators A Phys* 2018;279:331–42. <https://doi.org/10.1016/j.sna.2018.06.041>.
- [183] Sampath Kumar T, Balasivanandha Prabu S, Manivasagam G, Padmanabhan KA. Comparison of TiAlN, AlCrN, and AlCrN/TiAlN coatings for cutting-tool applications. *Int J Miner Metall Mater* 2014;21:796–805. <https://doi.org/10.1007/s12613-014-0973-y>.
- [184] Da Silva LRR, Filho AF, Costa ES, Marcucci Pico DF, Sales WF, Guessier WL, et al. Cutting Temperatures in End Milling of Compacted Graphite Irons. *Procedia Manuf.*, vol. 26, Elsevier B.V.; 2018, p. 474–84. <https://doi.org/10.1016/j.promfg.2018.07.056>.
- [185] Ezugwu EO, Pashby IR. High speed milling of nickel-based superalloys. *J Mater Process Technol* 1992;33:429–37. [https://doi.org/10.1016/0924-0136\(92\)90277-Y](https://doi.org/10.1016/0924-0136(92)90277-Y).
- [186] Khanna N, Agrawal C, Dogra M, Pruncu CI. Evaluation of tool wear, energy consumption, and surface roughness during turning of inconel 718 using sustainable machining technique. *J Mater Res Technol* 2020. <https://doi.org/10.1016/j.jmrt.2020.03.104>.

- [187] Sarıkaya M, Gupta MK, Tomaz I, Pimenov DY, Kuntoğlu M, Khanna N, et al. A state-of-the-art review on tool wear and surface integrity characteristics in machining of superalloys. *CIRP J Manuf Sci Technol* 2021;35:624–58. <https://doi.org/10.1016/j.cirpj.2021.08.005>.
- [188] Astakhov VP. *Tribology of metal cutting* 2006.
- [189] Bhatt A, Attia H, Vargas R, Thomson V. Wear mechanisms of WC coated and uncoated tools in finish turning of Inconel 718. *Tribol Int* 2010;43:1113–21. <https://doi.org/10.1016/j.triboint.2009.12.053>.
- [190] Walter EK. *Catálogo Geral - Torneamento, usinagem de furos, rosqueamento, fresamento e adaptadores* 2017.
- [191] Balki N, Nelge B. EXPERIMENTAL INVESTIGATION OF COOLING METHODS FOR DIFFERENT MACHINING CONDITIONS. 2015.
- [192] Schey JA. Tribology in metalworking: Friction. *Lubr Wear, Am Soc Met* 1983:573–616.
- [193] Khan SA, Soo SL, Aspinwall DK, Sage C, Harden P, Fleming M, et al. Tool wear/life evaluation when finish turning Inconel 718 using PCBN tooling. *Procedia Cirp* 2012;1:283–8. <https://doi.org/10.1016/j.procir.2012.04.051>.



<b>Alloy C~22</b>	51.6	21.5	5.5	2.5	13.5	4.0	***	***	***	0.01	1.00	0.10	***	***	***	0.30 V
<b>Alloy C~276</b>	bal	14.5~16.5	4.0 ~ 7.0	2.5	15 ~ 17	3.0 ~ 4.5	***	***	***	0.01	1.00	0.08	***	***	***	0.35 V
<b>Alloy G3</b>	bal	21 ~ 24	18 ~ 21	5.0	6.0 ~ 8.0	1.5	0.5 <sup>(c)</sup>	***	***	0.02	1.00	1.00	***	1.5 ~ 2.5	***	***
<b>Alloy HX</b>	bal	20.5 ~ 23	17 ~ 20	0.5 ~ 2.5	8.0 ~ 10.0	0.2 ~ 1.0	***	***	***	0.05~0.15	1.00	1.00	***	***	***	***
<b>Alloy S</b>	bal	14.5 ~ 17	3.0	2.0	14 ~ 16.5	1.0	***	***	0.1 ~ 0.5	0.02	0.3 ~ 1.0	0.2 ~ 0.75	0.015	0.35	***	0.01 ~ 0.10 La
<b>Alloy W</b>	63.0	5.0	6.0	2.5	24.0	***	***	***	***	0.12	1.00	1.00	***	***	***	***
<b>Alloy X</b>	bal	20.5~23	17 ~ 20	0.5 ~ 2.5	8.0 ~ 10.0	0.2 ~ 1.0	***	0.15	0.5	0.05~0.15	1.00	1.00	0.008	0.5	***	***

### Iron-nickel-chromium alloys

<b>Alloy 556</b>	20.0	22.0	bal	18.0	3.0	2.5	***	***	0.20	0.1	1.0	0.4	***	***	***	0.6 Ta. 0.02 La. 0.02 Zr
<b>Alloy 800</b>	30 ~ 35.0	19 ~ 23.0	39.5 min	***	***	***	***	0.15 ~ 0.6	0.15 ~ 0.6	0.1	1.5	1.0	***	***	***	***
<b>Alloy 800HT</b>	30 ~ 35.0	19 ~ 23.0	39.5 min	***	***	***	***	0.15 ~ 0.6	0.15 ~ 0.6	0.06 ~ 0.1	1.5	1.0	***	***	***	0.85 ~ 1.20 Al + Ti
<b>Alloy 825</b>	38 ~ 46.0	19.5~23.5	22.0 min	***	2.5 ~ 3.5	***	***	0.60 ~ 1.2	0.2	0.1	1.0	0.5	***	***	***	***
<b>Alloy 925</b>	44.0	21.0	28.0	***	3.0	***	***	2.10	0.3	0.0	***	***	***	***	***	***
<b>Alloy 20Cb3</b>	32 ~ 38.0	19 ~ 21.0	bal	***	2.0 ~ 3.0	***	1.0	***	***	0.1	2.0	1.0	***	3.0 ~ 4.0	***	***
<b>20Mo~4</b>	35 ~ 40.0	22.5 ~ 25	bal	***	3.5 ~ 5.0	***	0.2~0.4	***	***	0.0	1.0	0.5	***	0.5 ~ 1.5	***	***
<b>20Mo~6</b>	33~37.20	22 ~ 26.0	bal	***	5.0 ~ 6.7	***	***	***	***	***	1.0	0.5	***	2.0 ~ 4.0	***	***

### Alloys of controlled expansion (Fe-Ni-Cr. Fe-Ni-Co)

<b>Alloy 902</b>	41 ~ 43.5 <sup>(b)</sup>	4.9 ~ 5.75	bal	***	***	***	***	2.2 ~ 2.75	0.3 ~ 0.8	0.06	0.8	1.00	***	***	***	***
<b>Alloy 903</b>	38.0	***	42	15	***	***	3.0	1.40	0.90	***	***	***	***	***	***	***
<b>Alloy 907</b>	38.0	***	42	13	***	***	4.7	1.50	0.03	***	***	0.15	***	***	***	***
<b>Alloy 909</b>	38.0	***	42	13	***	***	4.7	1.50	0.03	0.01	***	0.40	***	***	***	***
<b>Alloy 902</b>	41 ~ 43.5	4.9 ~ 5.75	bal	***	***	***	***	2.2 ~ 2.75	0.3 ~ 0.8	0.06	0.8	1.00	***	***	***	***

### Alloys of Nickel-Iron

<b>Alloy 36</b>	35 ~ 38.0	0.50	bal	1.0	0.5	***	***	***	***	0.10	0.6	0.35	***	***	***	***
<b>Alloy 42</b>	42.0 <sup>(e)</sup>	0.50	bal	1.0	0.5	***	***	***	0.15	0.05	0.8	0.30	***	***	***	***
<b>Alloy 48</b>	48.0 <sup>(e)</sup>	0.25	bal	1.0	***	***	***	***	0.10	0.05	0.8	0.30	***	***	***	***

- a) Unique values are maximum values. Unless otherwise indicated.  
b) Nickel plus cobalt content.  
c) Niobium plus tantalum content.  
d) Alloy mechanically enhanced by dispersion. Alloy made by powdered metallurgy.  
e) Nominal value; adjusted to meet expansion requirements.

Source: adapted from (ASM International. 1990)

## Appendix B - Mechanical properties (at room temperature) characteristics and applications of nickel-based alloys[112]

Alloy	Ultimate tensile strength (MPa)	Yield strength (0.2 %) (MPa)	Elongation in 50 mm (%)	Elastic modulus (GPa)	Hardness	Description/Major applications
<b>Commercially pure and low-alloy nickels</b>						
Nickel 200	462	148	47	204	109 HB	Commercially pure wrought nickel with good mechanical properties and excellent resistance to many corrosives. Nickel 201 has low carbon (0.02% max) for applications over 315 °C (600 °F). Used for food processing equipment, chemical shipping drums, caustic handling equipment, and piping, electronic parts, aerospace and missile components, rocket motor cases, and magneto strictive devices
Nickel 201	403	103	50	207	129 HB	
Nickel 205	345	90	45	***	***	Wrought nickel like Nickel 200 but with compositional adjustments to enhance performance in electrical and electronic applications. Used for the anodes and grids of electronic valves, magneto strictive transducers, lead wires, transistor housings, and battery cases
Nickel 211	530	240	40	***	***	Nickel-manganese alloy is slightly harder than Nickel 200. The manganese addition provides resistance to sulfur compounds at elevated temperatures. Used as fuses in light bulbs, as grids in vacuum tubes, and in assemblies where sulfur is present in heating flames
Nickel 212	483	***	***	***	***	Wrought nickel strengthened with an addition of manganese. Used for electrical and electronic applications such as lead wires, supporting components in lamps and cathode-ray tubes, and electrodes in glow discharge lamps
Nickel 222	380					Wrought nickel with an addition of magnesium for electronic applications. The magnesium provides activation for cathodes of thermionic devices. Used for sleeves of indirectly heated oxide-ALNOVA cathodes
Nickel 270	345	110	50	***	30 HRC	A high-purity grade of nickel made by powder metallurgy. It has low base hardness and high ductility. Its extreme purity is useful for components of hydrogen. Thyratrons. Also used for electrical resistance thermometers
Duranickel 301 (precipitation hardened)	1170	862	25	207	30 ~40 HRC	Nickel-aluminum-titanium alloy is used for applications that require the corrosion resistance of commercially pure nickel but with greater strength or spring properties. These applications include diaphragms, springs, clips, press components for extrusion of plastics, and molds for the production of glass articles
<b>Nickel-copper alloys</b>						
Alloy 400	550	240	40	180	110 ~150 HB	A nickel-copper alloy with high strength and excellent corrosion resistance in various media, including seawater, hydrofluoric acid, sulfuric acid, and alkalis. Used for marine engineering, chemical and hydrocarbon processing equipment, valves, pumps, shafts, fittings, fasteners, and heat exchangers
Alloy 401	440	134	51	***	***	A copper-nickel alloy designed for specialized electrical and electronic applications. It has a very low-temperature coefficient of resistance and medium-range

						electrical resistivity. Used for wire-wound precision resistors and bimetal contacts
<b>Alloy R-405</b>	<b>550</b>	<b>240</b>	<b>40</b>	<b>180</b>	<b>110 ~140 HB</b>	The free-machining version of Alloy 400. A controlled amount of sulfur is added to the alloy to provide sulfide inclusions that act as chip breakers during machining. Used for meter and valve parts, fasteners, and screw machine products
<b>Alloy 450</b>	<b>385</b>	<b>165</b>	<b>46</b>	<b>***</b>	<b>***</b>	A copper-nickel alloy of the 70-30 types having superior weldability. It is resistant to corrosion and biofouling in seawater, has good fatigue strength, and has relatively high thermal conductivity. Used for seawater condensers, condenser plates, distiller tubes, evaporator and heat exchanger tubes, and saltwater piping
<b>Alloy K-500 (precipitation hardened)</b>	<b>1 100</b>	<b>790</b>	<b>20</b>	<b>180</b>	<b>300 HB</b>	A precipitation-hardenable nickel-copper alloy that combines the corrosion resistance of Alloy 400 with greater strength and hardness. It also has low permeability and is nonmagnetic to under -100 °C (-150 °F). Used for pump shafts, oil-well tools and instruments, doctor blades and scrapers, springs, valve trim, fasteners, and marine propeller shafts

### Nickel-chromium and nickel-chromium-iron alloys

<b>Alloy 230<sup>(a)</sup></b>	<b>860</b>	<b>390</b>	<b>47,7</b>	<b>211</b>	<b>92,5 HRB</b>	Nickel-chromium-tungsten alloy combines excellent high-temperature strength with resistance to oxidizing environments up to 1150 °C (2100 °F) and resistance to nitriding environments. Used for aerospace gas turbine components, chemical processing equipment, and heat-treating equipment
<b>Alloy 600</b>	<b>655</b>	<b>310</b>	<b>40</b>	<b>207</b>	<b>75 HRB</b>	A nickel-chromium alloy with good oxidation resistance at high temperatures and resistance to chloride-ion stress-corrosion cracking, corrosion by high-purity water, and caustic corrosion. Used for furnace components, in chemical and food processing, in nuclear engineering, and for sparking electrodes
<b>Alloy 601</b>	<b>620</b>	<b>275</b>	<b>45</b>	<b>207</b>	<b>65~80 HRB</b>	A nickel-chromium alloy with aluminum for outstanding resistance to oxidation and other forms of high-temperature corrosion. Its also high mechanical properties at elevated temperatures. Used for industrial furnaces; heat-treating equipment such as baskets, muffles, and retorts; petrochemical and other process equipment; and gas turbine components
<b>Alloy 617</b>	<b>755</b>	<b>350</b>	<b>58</b>	<b>211</b>	<b>173 HB</b>	A nickel-chromium-cobalt-molybdenum alloy with an exceptional combination of metallurgical stability, strength, and oxidation resistance at high temperatures. An aluminum addition enhances oxidation resistance. The alloy also resists a wide range of corrosive aqueous environments. Used in gas turbines for combustion cans, ducting, and transition liners; for petrochemical processing; for heat-treating equipment; and in nitric acid production
<b>Alloy 625</b>	<b>930</b>	<b>517</b>	<b>42,5</b>	<b>207</b>	<b>190 HB</b>	A nickel-chromium-molybdenum alloy with an addition of niobium acts with the molybdenum to stiffen the alloy's matrix and provide high strength without strengthening heat treatment. The alloy resists a wide range of severely corrosive environments and is especially resistant to pitting and crevice corrosion. Used in chemical processing, aerospace and marine engineering, pollution-control equipment, and nuclear reactors.
<b>Alloy 690</b>	<b>725</b>	<b>348</b>	<b>41</b>	<b>211</b>	<b>88 HRB</b>	A high-chromium-nickel alloy with excellent resistance to many aqueous media and high-temperature atmospheres. Used for various applications involving nitric or nitric/hydrofluoric acid solutions. Also useful for high-temperature service in gases containing sulfur
<b>Alloy 718 (precipitation hardened)</b>	<b>1 240</b>	<b>1 036</b>	<b>12</b>	<b>211</b>	<b>36 HRC</b>	A precipitation-hardenable nickel-chromium alloy containing significant amounts of iron, niobium, and molybdenum, along with lesser amounts of aluminum and titanium. It combines corrosion resistance and high strength with outstanding weldability, including resistance to post-weld cracking. The alloy has excellent creep-rupture strength at temperatures up to 700 °C (1300 °F). Used in gas turbines, rocket motors, spacecraft, nuclear reactors, pumps, and tooling
<b>Alloy X750</b>	<b>1 137</b>	<b>690</b>	<b>20</b>	<b>207</b>	<b>330 HB</b>	A nickel-chromium alloy similar to Alloy 600 but made precipitation hardenable by additions of aluminum and titanium. The alloy has good resistance to corrosion and oxidation and high tensile and creep-rupture properties at temperatures up to about 700 °C (1300 °F). Its excellent relaxation resistance is useful for high-temperature springs and bolts. Used in gas turbines, rocket engines, nuclear reactors, pressure vessels, tooling, and aircraft structures
<b>Alloy 751</b>	<b>1 310</b>	<b>976</b>	<b>22,5</b>	<b>214</b>	<b>352 HB</b>	A nickel-chromium alloy similar to Alloy X750 but with increased aluminum content for greater precipitation hardening. Designed for use as exhaust valves in internal combustion engines. In that application, the alloy offers high strength at operating temperatures, high hot hardness. For wear resistance and corrosion resistance in hot exhaust gases containing lead oxide, sulfur, bromine, and chlorine
<b>Alloy MA 754</b>	<b>965</b>	<b>585</b>	<b>22</b>	<b>***</b>	<b>***</b>	A mechanically alloyed nickel-chromium alloy with oxide dispersion strengthening. The strength, corrosion resistance, and microstructural stability of the alloy make it useful for gas turbine vanes and other extreme-service applications.

<b>Alloy C-22</b>	785	372	62	***	209 HB	A nickel-chromium-molybdenum alloy with outstanding resistance to pitting, crevice corrosion, and stress-corrosion cracking. It also exhibits high resistance to oxidizing media, including wet chlorine and mixtures containing nitric and oxidizing acids. Used for pollution control and pulp and paper equipment
<b>Alloy C-276</b>	790	355	61	205	90 HRB	A nickel-molybdenum-chromium alloy with an addition of tungsten having excellent corrosion resistance in a wide range of severe environments. The high molybdenum content makes the alloy especially resistant to pitting and crevice corrosion. The low carbon content minimizes carbide precipitation during welding to maintain corrosion resistance in as-welded structures. Used in pollution control, chemical processing, pulp, and paper production, and waste treatment
<b>Alloy G3</b>	690	320	50	199	79 HRB	A nickel-chromium-iron alloy with additions of molybdenum and copper. It has good weldability and resistance to intergranular corrosion in the welded condition. The low carbon content helps prevent sensitization and consequent intergranular corrosion of weld heat-affected zones. Used for flue gas scrubbers and for handling phosphoric and sulfuric acids
<b>Alloy HX (solution annealed)</b>	793	358	45,5	205	90 HRB	A nickel-chromium-iron-molybdenum alloy with outstanding strength and oxidation resistance at temperatures up to 1200 °C (2200 °F). Matrix stiffening provided by the molybdenum content results in high strength in a solid-solution alloy having good fabrication characteristics. Used in gas turbines, industrial furnaces, heat-treating equipment, and nuclear engineering
<b>Alloy S</b>	835	445	49	212	52 HRA	High-temperature alloy with excellent thermal stability, low thermal expansion, and oxidation resistance to 1095 °C (2000°F). Retains strength and ductility after aging at temperatures of 425 to 870 °C (800 to 1600 °F). Developed for applications involving severely cyclical heating conditions. Used extensively as seal rings in gas turbine engines
<b>Alloy W</b>	850	370	55	***	***	A solid-solution-strengthened alloy that was developed primarily for the welding of dissimilar alloys. It is available as straight cut-length wire for gas tungsten arc welding, layer-wound wire for gas metal arc welding, and ALNOVA electrodes for shielded metal arc welding. It has also been produced in sheet and plate for structural applications up to 760 °C (1400°F).
<b>Alloy X</b>	785	360	43	196	89 HRB	A nickel-chromium-iron-molybdenum alloy that possesses an exceptional combination of oxidation resistance, fabricability, and high-temperature strength. It has also been found to be exceptionally resistant to stress corrosion cracking in petrochemical applications. Exhibits good ductility after prolonged exposure at temperatures of 650, 760, and 870 °C (1200, 1400, and 1600 °F) for 16,000 h

### Iron-nickel-chromium alloys

<b>Alloy 556</b>	815	410	47,7	205	91 HB	An iron-nickel-chromium-cobalt alloy combines effective resistance to sulfurizing, carburizing, and chlorine-bearing environments at high temperatures with good oxidation resistance, good fabricability, and excellent high-temperature strength. It has also been found to resist corrosion by molten salts and is resistant to corrosion from molten zinc. Used for the waste incinerator, chemical process, and pulp and paper mill equipment
<b>Alloy 800</b>	600	295	44	193	138 HB	An iron-nickel-chromium alloy with good strength and excellent resistance to oxidation and carburization in high-temperature atmospheres. It also resists corrosion by many aqueous environments. The alloy maintains a stable, austenitic structure during prolonged exposure to high temperatures. Used for process piping, heat exchangers, carburizing equipment, heat in element sheathing, and nuclear steam-generator tubing
<b>Alloy 800 HT</b>	600	295	44	193	138 HB	An iron-nickel-chromium alloy having the same basic composition as Alloy 800 but with significantly higher creep-rupture strength. The higher strength results from close control of the carbon, aluminum, and titanium contents in conjunction with a high-temperature anneal. Used in chemical and petroleum processing, in power plants for superheater and reheater tubing, in industrial furnaces, and for heat-treating equipment.
<b>Alloy 825</b>	690	310	45	206	***	An iron-nickel-chromium alloy with additions of molybdenum and copper. It has excellent resistance to reducing and oxidizing acids, stress-corrosion cracking, and localized attacks such as pitting and crevice corrosion. The alloy is especially resistant to sulfuric and phosphoric acids. Used for Chemical processing, pollution-control equipment, oil and gas well piping, nuclear fuel reprocessing, acid production, and pickling equipment
<b>Alloy 925<sup>(b)</sup></b>	1 210	815	24	***	36.5 HRC	A precipitation-hardenable iron-nickel chromium alloy with additions of molybdenum and copper. The alloy has outstanding resistance to general corrosion, pitting, crevice corrosion, and stress corrosion cracking in many aqueous environments, including those containing sulfides and chlorides. Used for surface and down-hole hardware in sour gas wells and oil production equipment



<b>20Cb3</b>	<b>550</b>	<b>240</b>	<b>30</b>	<b>***</b>	<b>90 HRB</b>	A high-nickel austenitic stainless steel with excellent resistance to chemicals containing chlorides and sulfuric, phosphoric, and nitric acids. Resists pitting, crevice corrosion, and intergranular attack used for tanks, piping, heat exchangers, pumps, valves, and other chemical process equipment
<b>20Mo-4</b>	<b>615</b>	<b>262</b>	<b>41</b>	<b>186</b>	<b>80 HRB</b>	Alloy is designed for applications requiring improved resistance to pitting and crevice corrosion. It should be considered for acid environments where pitting and crevice corrosion problems are encountered. Applications include heat exchangers, chemical process piping and equipment, mixing tanks, and metal-cleaning and pickling tanks
<b>20Mo-6</b>	<b>607</b>	<b>275</b>	<b>50</b>	<b>186</b>	<b>***</b>	Austenitic stainless steel is resistant to corrosion in hot chloride environments with low pH. It has good resistance to pitting, crevice corrosion, and stress corrosion cracking in chloride environments. It is also resistant to oxidizing media. Applications include commercial fume scrubbers, offshore platforms, and equipment for pulp and paper mills.

### Controlled-expansion alloys

<b>Alloy 902 (precipitation hardened)</b>	<b>1 210</b>	<b>760</b>	<b>25</b>	<b>***</b>	<b>***</b>	A nickel-iron-chromium alloy made precipitation hardenable by additions of aluminum and titanium. The titanium content also helps provide a controllable thermoelastic coefficient, which is the outstanding characteristic of the alloy. The alloy can be processed to have a constant modulus of elasticity at temperatures from -45 to 65 °C (-50 to 150 °F). Used for precision springs, mechanical resonators, and other precision elastic components
<b>Alloy 903 (precipitation hardened)</b>	<b>1 310</b>	<b>1 100</b>	<b>14</b>	<b>***</b>	<b>***</b>	A nickel-iron-cobalt alloy with additions of niobium, titanium, and aluminum for precipitation hardening. The alloy combines high strength with a low and constant coefficient of thermal expansion at temperatures up to about 430 °C (800 °F). It also has a constant modulus of elasticity and is highly resistant to thermal fatigue and thermal shock. Used in gas turbines for rings and casings
<b>Alloy 907</b>	<b>1 310</b>	<b>1 100</b>	<b>14</b>	<b>***</b>	<b>***</b>	A nickel-iron-cobalt alloy with additions of niobium and titanium for precipitation hardening. It has the low coefficient of expansion and high strength of Alloy 903 but improved notch-rupture properties at elevated temperatures. Used for components of gas turbines, including seals, shafts, and casings
<b>Alloy 909 (precipitation hardened)</b>	<b>1 275</b>	<b>1 035</b>	<b>15</b>	<b>159</b>	<b>***</b>	A nickel-iron-cobalt alloy with a silicon addition and containing niobium and titanium for precipitation hardening. It is similar to Alloys 903 and 907 in that it has low thermal expansion and high strength. However, the silicon addition results in improved notch-rupture and tensile properties achieved with less restrictive processing and significantly shorter heat treatments. Used for gas turbine casings, shrouds, vanes, and shafts

- a) Cold-rolled and solution annealed at 1230 °C (2250 °F). Sheet thickness, 1.2 to 1.6 mm (0.048 to 0.063 in.).  
b) Annealed at 980 °C (1800 °F) for 30 min, air-cooled, and aged at 760 °C (1400 °F) for 8 h, furnace cooled at a rate of 55 °C (100 °F)/h, heated to 620 °C (1150 °F) for 8 h, air-cooled

Source: adapted from [112]

## Appendix C - Physical properties (at room temperature) of various nickel-based alloys [112]

Alloy	Density (g/cm <sup>3</sup> )	Melting point range (°C)	Specific heat (J/kg.K)	Average coefficient of thermal expansion (µm/m.K)	Thermal conductivity (W/m.K)	Electrical resistivity (nΩ. m)	Curie temperature (°C)
<b>Commercially pure and low-alloy nickels</b>							
Nickel 200	8.89	1 435 ~ 1 445	456	13.3	70	95	360
Nickel 201	8.89	1 435 ~ 1 445	456	13.1	79.9	85	360
Nickel 205	8.89	1 435 ~ 1 445	456	13.3	75.0	95	360
Nickel 211	8.72	1427	532	13.3	44.7	169	310
Nickel 212	8.86	1 435 ~ 1 445	430	12.9	44.0	109	***
Nickel 222	8.89	1 435 ~ 1 445	460	13.3	75	88	Ferromagnético
Nickel 270	8.89	1455	460	13.3	86	75	Ferromagnético
DuraNickel 301 (precipitation/hardened)	8.25	1438	435	13.0	23.8	424	16 ~ 50
<b>Nickel-copper alloys</b>							
Alloy 400	8.80	1 300 ~ 1 350	427	13.9	21.8	547	20 ~ 50
Alloy 401	8.89	***	***	13.7	19.2	489	<-196
Alloy R-405	8.80	1 300 ~ 1 350	427	13.7	21.8	510	20 ~ 50
Alloy 450	8.91	1 170 ~ 1 240	***	15.5	29.4	412	***
Alloy K-500 (precipitation/hardened)	8.44	1 315 ~ 1 350	419	13.7	17.5	615	-134
<b>Nickel-chromium and nickel-chromium-iron alloys</b>							
Alloy 230 <sup>(a)</sup>	8.83	1 300 ~ 1 370	397	12.6	8.9	1 250	***
Alloy 600	8.47	1 355 ~ 1 413	444	13.3	14.9	1 030	-124
Alloy 601	8.11	1 360 ~ 1 411	448	13.75	11.2	1 190	-196
Alloy 617 (solution/annealed)	8.36	1 330 ~ 1 380	419	11.6 <sup>(b)</sup>	13.6	1 220	***
Alloy 625	8.44	1 290 ~ 1 350	410	12.8	9.8	1 290	***
Alloy 690	8.19	1 343 ~ 1 377	450	14.06 <sup>(b)</sup>	13.5	1 148	***

<b>Alloy 718 (precipitation/hardened)</b>	8.19	1 260 ~ 1 336	435	13.0	11.4	1 250	-112
<b>Alloy X750</b>	8.28	1 390 ~ 1 430	431	12.6	12.0	1 220	-125
<b>Alloy 751</b>	8.222	1 390 ~ 1 430	431	12.6	12.0	1 220	-125
<b>Alloy C-276</b>	8.89	1325 ~ 1 370	427	11.2 <sup>(b)</sup>	9.8	1 300	***
<b>Alloy G3</b>	8.14	1 260 ~ 1 355	452	14.6	10.0	***	***
<b>Alloy HX (solution/annealed)</b>	8.23	1 260 ~ 1 355	461	13.3	11.6	1 160	***
<b>Alloy S (solution/annealed)</b>	8.75	1 335 ~ 1 380	398 <sup>(c)</sup>	11.5	14.0 <sup>(d)</sup>	1 280	***
<b>Alloy X (solution/annealed)</b>	8.22	1 260 ~ 1 355	486	13.9	9.1	1 180	***

### Iron-nickel-chromium alloys

<b>Alloy 556</b>	8.23	1 330 ~ 1 415	464	14.6	11.1	952	***
<b>Alloy 800</b>	7.94	1 357 ~ 1 385	460	14.4	11.5	989	-115
<b>Alloy 800HT</b>	7.94	1 357 ~ 1 385	460	14.4	11.5	989	-115
<b>Alloy 825</b>	8.14	1 370 ~ 1 400	440	14.0	11.1	1 130	-196
<b>Alloy 925<sup>(e)</sup></b>	8.14	1 311 ~ 1 366	435	13.2	***	1 166	***
<b>Alloy 20Cb3</b>	8.08	***	500	14.7	12.2 <sup>(f)</sup>	1 082	***
<b>20Mo-4</b>	8.106	***	458	14.9 <sup>(g)</sup>	12.1 <sup>(f)</sup>	1 056	***
<b>20Mo-6</b>	8.13	***	460	14.8 <sup>(b)</sup>	12.1 <sup>(f)</sup>	1 082	***

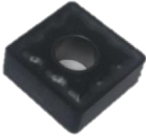

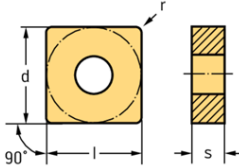
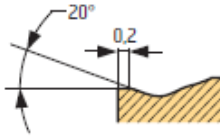
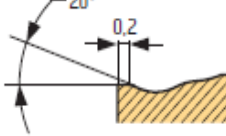
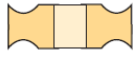
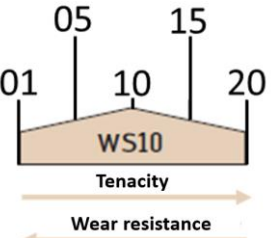
### Controlled-expansion alloys

<b>Alloy 902 (precipitation/hardened)</b>	8.05	1 455 ~ 1 480	500	7.6	12.1	1 020	190
<b>Alloy 903 (precipitation/hardened)</b>	8.25	1 318 ~ 1 393	435	7.65 <sup>(h)</sup>	16.7	610	415 ~ 470
<b>Alloy 907 (precipitation/hardened)</b>	8.33	1 335 ~ 1 400	431	7.7 <sup>(h)</sup>	14.8	697	400 ~ 455
<b>Alloy 909 (precipitation/hardened)</b>	8.30	1 395 ~ 1 430	427	7.7 <sup>(h)</sup>	14.8	728	400 ~ 455

- a) Cold-rolled and solution annealed at 1230 °C (2250 °F). Sheet thickness, 1.2-1.6 mm (0.048-0.063 in.).
- b) Average value at 25-100 °C (75-200 °F).
- c) Average value at 0 °C (32 °F).
- d) Average value at 200 °C (390 °F).
- e) Annealed at 980 °C (1800 °F) for 30 min, air-cooled, and aged at 760 °C (1400 °F) for 8 h, furnace cooled at a rate of 55 °C (100 °F)/h, heated to 620 °C (1150 °F) for 8 h, air-cooled. Valor médio a 50 °C (120 °F).
- f) Average value at 50 °C (120 °F).
- g) Average value at 25 to 200 °C (75 to 390 °F).
- h) Valor médio de 25 a 425 °C (75 a 800 °F).

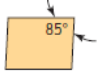
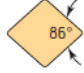
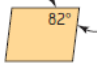

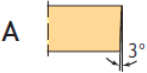



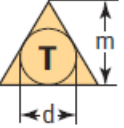
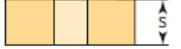
Source: adapted from [112]

## Appendix D - Tool Spec Sheet SNMG120412 -NRT WS10

Insert illustration	ISO denomination	$r_\epsilon (mm)$	$f (mm)$	$doc (mm)$	Coating	HW (WS10) S (superalloys)	Negative Square SNMG	Primary cutting edge	Corner radius	Characteristics of cutting and clamping geometry	Application field
	SNMG 120412 NRT WS10	1.2	0.25 – 0.50	0.8 – 6.0	Sem (HW)	Medium machining condition 					

### ISO 1832 CODING

<b>S</b>	<b>N</b>	<b>M</b>	<b>G</b>	<b>12</b>	<b>04</b>	<b>12</b>	<b>-</b>	<b>N</b>	<b>R</b>	<b>T</b>
1	2	3	4	5	6	7	-	12	13	14

1	2	3	6																								
Insert format	Clearance Angle	Tolerances	Insert thickness $S (mm)$																								
<div style="display: flex; justify-content: space-around;"> <div style="text-align: center;">  A                 </div> <div style="text-align: center;">  M                 </div> </div> <div style="display: flex; justify-content: space-around; margin-top: 10px;"> <div style="text-align: center;">  B                 </div> <div style="text-align: center;">  O                 </div> </div>	<div style="display: flex; justify-content: space-around;"> <div style="text-align: center;">  A                 </div> <div style="text-align: center;">  F                 </div> </div> <div style="display: flex; justify-content: space-around; margin-top: 10px;"> <div style="text-align: center;">  B                 </div> <div style="text-align: center;">  G                 </div> </div>	<div style="text-align: center; margin-bottom: 10px;">  T                 </div> <table border="1" style="width: 100%; border-collapse: collapse; margin-bottom: 10px;"> <thead> <tr> <th colspan="4" style="text-align: center;">Permissible deviation (mm)</th> </tr> </thead> <tbody> <tr> <td style="width: 15%; text-align: center;">A</td> <td style="width: 15%; text-align: center;">± 0.025</td> <td style="width: 15%; text-align: center;">± 0.005</td> <td style="width: 15%; text-align: center;">± 0.025</td> </tr> <tr> <td style="text-align: center;">B</td> <td style="text-align: center;">± 0.025</td> <td style="text-align: center;">± 0.013</td> <td style="text-align: center;">± 0.025</td> </tr> <tr> <td style="text-align: center;">E</td> <td style="text-align: center;">± 0.025</td> <td style="text-align: center;">± 0.025</td> <td style="text-align: center;">± 0.025</td> </tr> </tbody> </table>	Permissible deviation (mm)				A	± 0.025	± 0.005	± 0.025	B	± 0.025	± 0.013	± 0.025	E	± 0.025	± 0.025	± 0.025	<div style="display: flex; justify-content: space-between; align-items: center;">  <div style="text-align: right;"> <table border="1" style="width: 100%; border-collapse: collapse;"> <tr> <td style="width: 20%;">01</td> <td style="text-align: right;"><math>S = 1.59</math></td> </tr> <tr> <td>T1</td> <td style="text-align: right;"><math>S = 1.98</math></td> </tr> <tr> <td>02</td> <td style="text-align: right;"><math>S = 2.38</math></td> </tr> <tr> <td>T2</td> <td style="text-align: right;"><math>S = 2.78</math></td> </tr> </table> </div> </div>	01	$S = 1.59$	T1	$S = 1.98$	02	$S = 2.38$	T2	$S = 2.78$
Permissible deviation (mm)																											
A	± 0.025	± 0.005	± 0.025																								
B	± 0.025	± 0.013	± 0.025																								
E	± 0.025	± 0.025	± 0.025																								
01	$S = 1.59$																										
T1	$S = 1.98$																										
02	$S = 2.38$																										
T2	$S = 2.78$																										

			<b>F</b>	$\pm 0.013$	$\pm 0.005$	$\pm 0.025$		03	$S = 3.18$
			<b>G</b>	$\pm 0.025$	$\pm 0.025$	$\pm 0.130$		T3	$S = 3.97$
			<b>H</b>	$\pm 0.013$	$\pm 0.013$	$\pm 0.130$		04	$S = 4.76$
			<b>J<sup>1</sup></b>	$\pm 0.05 - 0.15^{\text{@}}$	$\pm 0.005$	$\pm 0.025$		05	$S = 5.56$
			<b>K<sup>1</sup></b>	$\pm 0.05 - 0.15^{\text{@}}$	$\pm 0.013$	$\pm 0.025$		06	$S = 6.35$
			<b>L<sup>1</sup></b>	$\pm 0.05 - 0.15^{\text{@}}$	$\pm 0.025$	$\pm 0.025$		07	$S = 7.94$
			<b>M</b>	$\pm 0.05 - 0.15^{\text{@}}$	$\pm 0.08 - 0.20^{\text{@}}$	$\pm 0.130$		09	$S = 9.52$
			<b>N</b>	$\pm 0.05 - 0.15^{\text{@}}$	$\pm 0.08 - 0.20^{\text{@}}$	$\pm 0.025$			
			<b>U</b>	$\pm 0.08 - 0.25^{\text{@}}$	$\pm 0.13 - 0.38^{\text{@}}$	$\pm 0.130$			
							<sup>1</sup> Inserts with flat and ground cutting edges @ Depending on the size of the insert (see ISO 1832)		

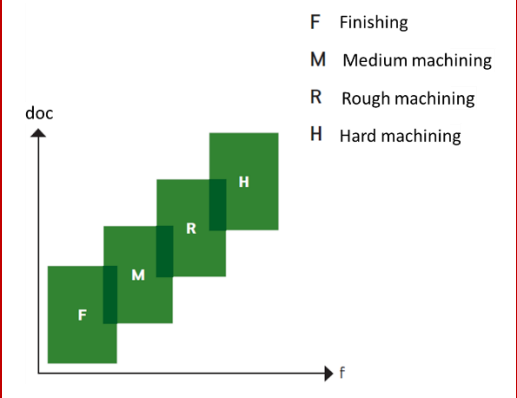
5

12

**Cutting edge length**

**Chip breaking range**

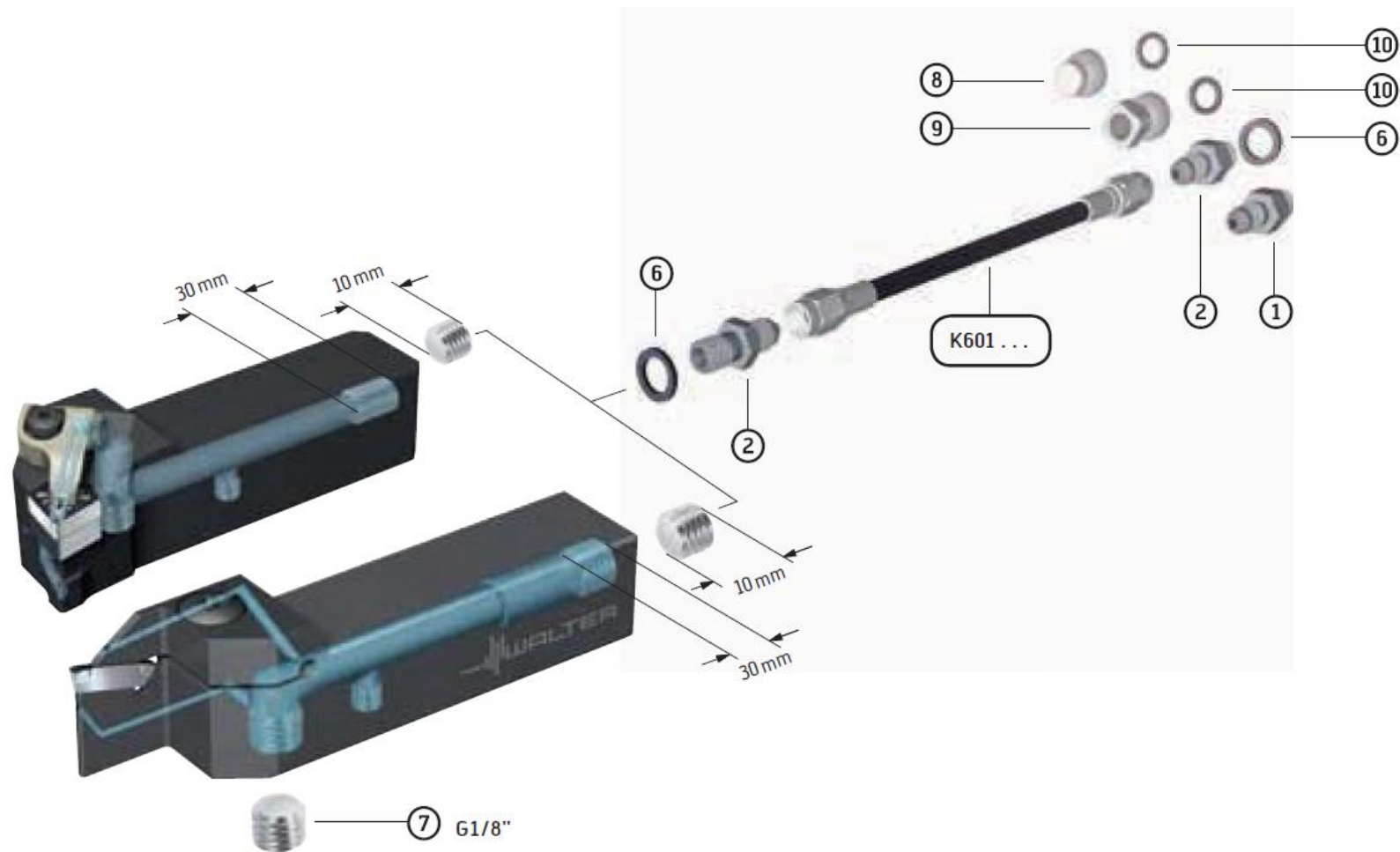
Internal diameter d		C		D		R		S		T		V		W	
mm	in	Size	l	Seize	l	Size	l	Size	l	Size	l	Size	l	Size	l
3.97	5/32									06	6.9				
5	0.197					05								03	3.8
5.56	7/32									09	9				
6	0.236					06									
6.35	2/8	06	6.4	0.7	7.7	06 <sup>1</sup>				11	11	11	11	04	4.3
8	0.315					08								05	5.2
9.525	3/8	09	9.6	11	11.6	09 <sup>1</sup>		09	9.5	16	16.5	16	16.5	06	6.5
10	0.394					10									
12	0.472					12									
12.7	4/8	12	12.9	15	15.5	12 <sup>1</sup>		12	12.7	22	22	22	22.1	08	8.7
15.875	5/8	16	16.1					15	15.8	27	27			10	10.8





## Appendix E - Tool Holder Spec Sheet DSSNR2525X12-P

### Tool holder with shank -P












**Comments:**





"All rod holders and precision coolers are equipped with 3 coolant connections. Before using the tools, make sure that the unused connections are sealed with the threaded pins included in the kit. Cooling kits K601... for shank tool holders are certified for pressures from 10 bar to a maximum of 275 bar.

The length of the tool shank can be shortened by up to 20 mm, as the tread depth on all Walter Turn and Walter Cut square shanks with precision cooling is 30 mm. "


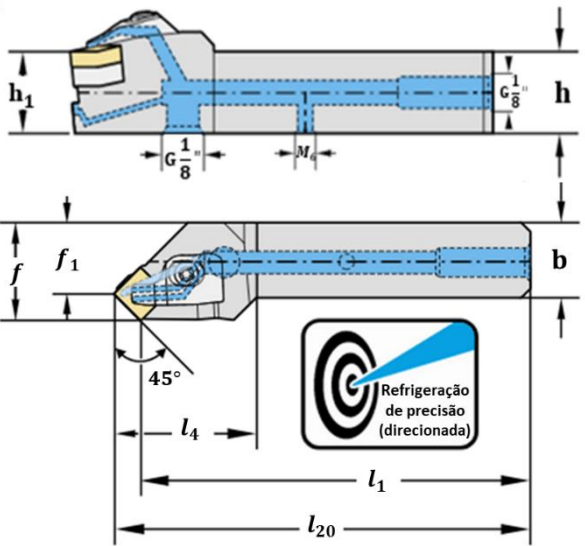
### Walter Cooling hose set -P


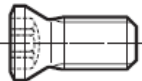





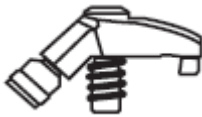
		Length (mm)				
		150	Set K601.01.150	Set K601.02.150	Set K601.03.150	
		250	Set K601.01.250	Set K601.02.250	Set K601.03.250	
<b>Individual components</b>		300	Set K601.01.300	Set K601.02.300	Set K601.03.300	
1		Connecting element M10	FS2252	Content per set		
				1 x	***	***
2		Connecting element double G1 / 8 "	FS2253	2 x	1 x	***
				***	1 x	1 x
3		G1 / 8 "elbow	FS2254	***	1 x	1 x
				***	1 x	1 x
4		G1 / 8 "elbow	FS2255	***	1 x	1 x
				***	1 x	1 x
5		G1 / 4 " -G1 / 8" reduction	FS2256	***	1 x	1 x
				***	1 x	1 x
6		Copper sealing	FS2257	2 x	3 x	4 x
				***	3 x	4 x



7		Threaded pin G1 / 8 "	FS2258	1 x	1 x	1 x
8		Blind brass plug	FS2259	1 x	1 x	1 x
9		Brass spout G1 / 8 "	FS2260	1 x	1 x	1 x
10		Sealing ring	FS2261	2 x	2 x	2 x

### Tool Holder Design

Tool holder illustration	ISO classification		$h = h_1$ mm	b mm	$b_1$ mm	f mm	$l_1$ mm	$l_4$ mm	$\gamma$	$\lambda_s$	Tipo
	DSSNR2525X12-P	12	25	25	0	23.7	138.7	48	-8 °	0°	SN..1204..
<p>Measured with the SN ..120408 master insert</p> <p>For more information on the exit angle <math>\gamma</math> (for indexed inserts without chip breakers) and with the inclination angle <math>\lambda_s</math>, see Technical Information - ISO Turning</p> <p>For the supply of refrigerant with G1 / 8 "in the connection set, see" Mounting parts and accessories."</p> <p>The maximum recommended refrigerant pressure should be 150 bar (2,175 psi)</p>											

<b>Mounting parts</b>		
<b>Types</b>		<b>SN..1204..</b>
	<b>Shim</b>	<b>AP308-SN12</b>
	<b>Screw for the shim</b> <b>Tightening torque</b>	<b>FS1461 (Torx 15IP)</b> <b>2,5 Nm</b>
	<b>Left clip</b> <b>Staple on the right</b>	<b>PK265L</b> <b>PK265R</b>
	<b>Clamp fixing screw</b> <b>Tightening torque</b>	<b>FS1473 (Torx 15IP)</b> <b>3,9 Nm</b>
	<b>Pressure spring</b>	<b>FS2188</b>
	<b>G1 / 8 "threaded plug</b>	<b>FS2258 (SW 5)</b>
	<b>Torx key</b>	<b>FS1465 (Torx15IP)</b>
<b>Accessories</b>		
	<b>Left clip</b> <b>(standard mounting parts)</b>	<b>PS265L-SET</b>
	<b>Staple on the right</b> <b>(standard mounting parts)</b>	<b>PS265R-SET</b>
Source: adapted from [156]		

## Appendix F - Technical drawing of the SNMG 120408EN-M34 CTPX710 Tool adapted with internal cooling channels

